THE DETERMINATION OF DYNAMIC INITIATION FRACTURE TOUGHNESS OF METALS USING THE HOPKINSON PRESSURE BAR LOADED INSTRUMENTED CHARPY TEST.

Thesis submitted in accordance with the requirements of the University of Liverpool for the degree of Doctor in Philosophy by:

ANDREW GEOFFREY DUTTON

Department of Mechanical Engineering
University of Liverpool

September 1989

ABSTRACT.

A review of instrumented impact testing, with particular reference to the instrumented Charpy test, shows that the measured hammer load and displacement histories are complex functions of the inertia and stiffness of both specimen and loading system. Specifically, the instant of maximum load measured at the hammer is not necessarily coincident with that of crack initiation and, due to inertia effects, this load cannot be directly used to characterise the fracture toughness of the specimen.

A one-dimensional lumped mass-spring model, developed for the instrumented Charpy test, is applied for the first time to the Hopkinson pressure bar instrumented impact test. The model shows that the loading rate experienced by a linear elastic specimen is essentially constant and the stress intensity factor history is then derived. A strain gauge mounted on the specimen close to the crack tip is used to detect crack initiation and hence the dynamic initiation fracture toughness can be determined.

The full test procedure is described and results are quoted for several tempers of En24 steel and two magnesium alloys (Magnesium Elektron ZCM 630-T6 and WE54) at a range of test temperature and impact velocity. Estimates are made of the effective contact stiffnesses at the impact point and the supports and these are found to be more compliant than theory predicts.

The model is also used to examine the frequency and force magnitude changes caused by shortening the specimen so that its overhang at the supports is reduced. Estimates of crack velocity at initiation are made from the load-time characteristics and found to have important implications for the effective identification of crack initiation.

Finally, an algorithm is introduced to extend the model to cover non-linear material behaviour based on a power law strain hardening relationship.

In loving memory
of my father
Arthur Raymond Dutton

'I do not know what I may appear to the world,
but to myself I seem to have been
only a boy playing on the seashore,
and diverting myself in now and then
finding a smoother pebble or a prettier shell
than the ordinary,
whilst the great ocean of truth lay
all undiscovered before me.'

Isaac Newton.

ACKNOWLEDGEMENTS.

The experimental work reported in this thesis was carried out in the Department of Mechanical Engineering at the University of Liverpool. Specimen preparation and the study of fracture surfaces using the scanning electron microscope were carried out in the Department of Materials Science. I am grateful to both departments and their staff for the help and assistance given over three years.

Specifically, I would like to thank Mr. F. Cummins for his detailed design of the Hopkinson pressure bar rig, Mr. S. Draper and Mr. G. Swallow for their help in assembling the rig, machining specimens, and general assistance in the laboratory, and Mr. C. Jackson for instruction in using the Amsler Vibrophone for pre-cracking specimens. Special thanks are due to Dr. R. Birch for his advice and assistance in setting up the rig and instrumentation, Dr. S. McParland for advice on the metallurgical aspects of the study and, in particular, her invaluable help in obtaining photographs of the fracture surfaces, and my supervisor, Dr. R. Mines for his guidance and encouragement throughout the project.

The magnesium alloy specimens were supplied by Magnesium Elektron Ltd.

The Department of Physics provided liquid nitrogen for the chilling of specimens below room temperature.

Photographs of the experimental apparatus were taken by the University of Liverpool Photographic Services, who also produced all the prints presented in the thesis.

Compositional analysis of the two batches of En24 steel were carried out by Amtac Laboratories, Altrincham.

All finite element numerical modelling was carried out using the ABAQUS finite element package accessed at the University of Manchester Regional Computing Centre.

I am grateful to all five of the above for enabling me to extend the scope of the study.

Finally I would like to thank my wife, Susan, for all the support and encouragement she has given me throughout the course of the project, which, to date, has only been two weeks shorter than our marriage.

The work was carried out between October 1986 and September 1989 under SERC grant number GR/E/00570.

TABLE OF CONTENTS.

LIST OF TABLES.

LIST OF FIGURES.

3.14. Data reduction procedure for the Hopkinson pressure bar instrumented impact test (En24 HC2 059 - T = 20°C : V_0 = 1.7 m/s):
(a) incident wave at strain gauge S1,
(b) stress wave interaction at strain gauge S2,
(c) specimen strain gauge measurement S3,
(d) calibrated S1 and S2 signals aligned by shifting S2 by $-t_{12}$ relative to S1,
(e) reflected wave at tip of incident bar.

3.15. Test En24 HC2 059 derived relationships:
(a) velocity-time,
(b) displacement-time,
(c) force-time and S3 strain-time.

3.16. Comparison of crack initiation criteria (En24 HC2 052 - T = 100°C : V_0 = 2.5 m/s):
(a) maximum specimen strain gauge reading,
(b) "first drop" on specimen strain gauge.

3.17. Comparison of crack initiation criteria (En24 HC2 053 - T = 100°C : V_0 = 2.5 m/s):
(a) maximum specimen strain gauge reading,
(b) "first drop" on specimen strain gauge.

Titles for figures 3.18 to 3.31

3.18. Force-time characteristics for En24 HC1 : the effect of test temperature (V_0 = 2.50 m/s).

3.19. Force-time characteristics for En24 HC1 : the effect of impact velocity (T = -20°C).

3.20. Force-time characteristics for En24 HC1 : the effect of test temperature (V_0 = 3.20 m/s).

3.21. Force-time characteristics for En24 HC2 : the effect of test temperature (V_0 = 2.50 m/s).

3.22. Force-time characteristics for En24 HC2 : the effect of impact velocity (T = 20°C) in the standard Charpy size specimens.

3.23. Force-time characteristics for En24 HC2 : the effect of impact velocity (T = 20°C) in the truncated specimens.

3.24. Force-time characteristics for En24 HC2 : the effect of low impact velocities (T = 20°C).

3.25. Force-time characteristics for En24 HC3 : the effect of impact velocity (T = 20°C).

4.3. Finite element model of the three point bend impact specimen with detail of crack tip quarter point and transition elements.

4.4. Finite element prediction of measured load (P_1) and support load (P_{sup}) for input real displacement function from test En24 HC1 027.

4.5. Finite element prediction of measured load (P_1) for constant displacement rate in a standard steel Charpy specimen (a) and truncated specimen (b).

4.6. Finite element prediction of measured load (P_1) for constant displacement rate function in magnesium alloy specimen.

4.7. Profiled end section of incident bar: geometry for stiffness calculation.

4.8. Contact stiffness and mean stress in the contact zone for En24 HC1/HC2 steel (a) and magnesium alloy (b).

4.9. Hopkinson pressure bar impact test results:
(a) velocity-time relationship input to the inertial model,
(b) force-time relationship for comparison with the derived force.

4.10. Inertial model results:
(a) derived forces P_1 and P_2,
(b) derived forces P_1 and wedge inertia,
(c) derived force F_p compared with measured force F_m.

Titles for figures 4.11 to 4.17.

4.11. Inertial model results for En24 HC1 with increasing test temperature (V_0 = 2.5 m/s).

4.12. Inertial model results for En24 HC1 with increasing impact velocity (T = -20°C).

4.13. Inertial model results for En24 HC1 at room temperature for impact velocity V_0 = 3.2 m/s.

4.14. Inertial model results for En24 HC2 with increasing test temperature (V_0 = 2.5 m/s) - maximum specimen strain criterion.

4.15. Inertial model results for En24 HC2 with increasing test temperature (V_0 = 2.5 m/s) - "first drop" initiation criterion.

5.5. Ramberg-Osgood characterisations of the stress-strain behaviour of magnesium alloys ZCM 630-T6 ($n = 6.9$, $\alpha = 0.36$) and WE54 ($n = 6.3$, $\alpha = 0.25$).

5.6. Yield stress-temperature data for AISI 4340 steel from:
(i) Lee and Kang [120] - tempers 350/450°C,
(ii) Tanimura and Duffy [52] - temper 425°C,
showing mean interpolation for temper 375°C with nominal yield stress for En24 [127].

5.7. Geometry for determination of the plastic component of contact stiffness.

5.8. Plastic components of contact stiffness for:
(a) En24 steel ($\sigma_Y = 1500$ MPa),
(b) Mg alloy WE54 ($\sigma_Y = 177$ MPa).

5.9. h_3 [32] and η_p functions for elasto-plastic analysis.

5.10. KE/SE v. time for En24 HC2 specimens:
(a) test 054 ($V_0 = 4.2$ m/s),
(b) test 060 ($V_0 = 0.95$ m/s).

5.11. KE/SE v. time for Mg alloy ZCM 630-T6 specimens:
(a) test 14 ($V_0 = 4.1$ m/s),
(b) test 01 ($V_0 = 1.2$ m/s).

Titles for figures 5.12 to 5.20.

5.12. Elasto-plastic inertial model results for En24 HC3 with increasing impact velocity (T = 20°C) - plane strain.

5.13. Elasto-plastic inertial model results for En24 HC3 with increasing impact velocity (T = 20°C). - plane stress.

5.14. Elasto-plastic inertial model results for En24 HC3 test 075: the effect of damping ($\zeta = 0.05$):
(a) damped model result,
(b) comparison of F_p forces,
(c) comparison of P_2^p forces.

5.15. Elasto-plastic inertial model results for En24 HC3 test 075: the effect of plasticity in the support contact stiffness:
(a) model result,
(b) comparison of F_p forces,
(c) comparison of P_2^p forces.

5.16. Elasto-plastic inertial model results for magnesium alloy ZCM 630-T6 with increasing test temperature (V_0 = 2.4 m/s).

5.17. Elasto-plastic inertial model results for magnesium alloy ZCM 630-T6 with increasing test temperature (V_0 = 4.1 m/s).

5.18. Elasto-plastic inertial model results for magnesium alloy ZCM 630-T6 using "first drop" initiation criterion.

5.19. Elasto-plastic inertial model results for magnesium alloy WE54 with increasing test temperature (V_0 = 1.5 m/s).

5.20. Elasto-plastic inertial model results for magnesium alloy WE54 with increasing test temperature (V_0 = 3.3 m/s).

5.21. Dynamic J-integral v. test temperature for magnesium alloy specimens.

Titles for figures 5.22 to 5.26.

5.22. Comparison of linear and elasto-plastic inertial model results for magnesium alloy WE54 test 15 (T = -75° C : V_0 = 3.3 m/s):
(a) linear model result,
(b) comparison of F_p forces,
(c) comparison of P_2^p forces.

5.23. Comparison of linear and elasto-plastic inertial model results for magnesium alloy WE54 test 18 (T = 125° C : V_0 = 3.3 m/s):
(a) linear model result,
(b) comparison of F_p forces,
(c) comparison of P_2^p forces.

5.24. Comparison of linear and elasto-plastic inertial model results for magnesium alloy WE54 test 13 (T = -75° C : V_0 = 1.5 m/s):
(a) linear model result,
(b) comparison of F_p forces,
(c) comparison of P_2^p forces.

5.25. Comparison of linear and elasto-plastic inertial model results for magnesium alloy ZCM 630-T6 test 10 (T = -75° C : V_0 = 2.4 m/s):
(a) linear model result,
(b) comparison of F_p forces,
(c) comparison of P_2^p forces.

5.26. Comparison of linear and elasto-plastic inertial model results for magnesium alloy ZCM 630-T6 test 08 ($T = 125^{o}$ C : $V_0 = 2.4$ m/s):
  (a) linear model result,
  (b) comparison of F_p forces,
  (c) comparison of P_2^p forces.

5.27. Inertial model results for Mg alloy ZCM 630-T6 test 10 with:
  (a) crack velocity $\dot{a} = 25$ m/s after initiation,
  (b) crack velocity $\dot{a} = 50$ m/s after initiation.

5.28. Inertial model results for Mg alloy ZCM 630-T6 test 15 with:
  (a) crack velocity $\dot{a} = 25$ m/s after initiation,
  (b) crack velocity $\dot{a} = 50$ m/s after initiation.

5.29. Inertial model results for Mg alloy WE54 with crack velocity $\dot{a} = 25$ m/s after initiation for:
  (a) test 13 ($V_0 = 1.5$ m/s),
  (b) test 18 ($V_0 = 3.3$ m/s).

NOTATION.

A area of cross-section

a crack length

$\dot{a}$ crack velocity

a_e effective crack length allowing for plastic zone size

B thickness of specimen

b half-width of contact zone in elastic problem

b uncracked ligament, $b = (W - a)$

C material constant in Cowper-Symonds relationship (equation 2.51)

c wavespeed in a given medium

c viscous damping coefficient

c_s specimen compliance c geometric constraint factor

d scalar quantity in the relationship between δ_t and J (equation 2.25)

d depth of penetration in plastic contact stiffness problem

E total energy

E Young's modulus

E_m emf in Wheatstone bridge network

e_{bc} potential difference across Wheatstone bridge

F force measured at end section of incident bar

G shear modulus

G strain energy release rate

G_d dynamic strain energy release rate

h length scale

h_1 scalar quantity in KGS elasto-plastic model (equation 5.2)

h_3 scalar quantity in KGS elasto-plastic model (equation 5.3)

I second moment of area

I_n normalisation constant in HRR field (equation 2.24)

J J-integral (equation 2.18)

$\dot{J}$ rate of change of J with time

J_{Ic} critical value of J-integral at fracture initiation in a static problem (mode I loading)

J_{Id} critical value of J-integral at fracture initiation in a dynamic problem (mode I loading)

K stress intensity factor

K_I stress intensity factor (mode I loading)

$\dot{K}_I$ rate of change of stress intensity factor with time

K_{Ic} plane strain fracture toughness (mode I)

K_{Id} dynamic plane strain fracture toughness (mode I)

K_{IJ} equivalent stress intensity factor derived from J-integral (equation 2.34)

K_Q critical value of stress intensity factor at fracture initiation where plane strain condition is invalid

k stiffness

k_a anvil stiffness

k_c contact stiffness

k_{cp} plastic component of contact stiffness

k_g strain gauge sensitivity

k_s specimen stiffness

k_{sup} support stiffness

k_w impactor stiffness

k_1 inertial model stiffness parameter (equation 4.1)

k_2 inertial model stiffness parameter (equation 4.2)

L length scale

L length of specimen

l_c critical length scale in ductile fracture criterion (equation 2.45)

l_f critical length scale in cleavage fracture criterion (equation 2.43)

M bending moment

m strain rate parameter (equation 2.52)

m' effective mass of specimen for inertial model

m_w mass of end section of incident bar

n strain hardening index in Ramberg-Osgood stress-strain relationship (equation 2.20)

$\underset{\sim}{n}$ normal vector

P load

P_0 limit load for perfectly plastic material

p material constant in Cowper-Symonds relationship (equation 2.51)

R size scale of HRR singularity

R electrical resistance

R radius

r distance from crack tip

r_Y plastic zone size

S surface energy

S distance between supports in impact test (span)

S_v voltage sensitivity of Wheatstone bridge network

s arc length

T temperature

T kinetic energy

$\underset{\sim}{T}$ traction vector

t time

t_f time to fracture

t_T transition time beyond which a J-dominated field may be said to exist

U strain energy U^* complementary strain energy

u specimen displacement

$\dot{u}$ specimen velocity

$\ddot{u}$ specimen acceleration

$\underset{\sim}{u}$ displacement vector from crack tip

u' specimen/support interface displacement

V velocity

V_0 travelling bar velocity at impact with incident bar

V_2 non-dimensional function of crack length (equation 4.26)

v measurement plane (surface A) displacement

W width of specimen

w natural frequency

x Cartesian coordinate

y Cartesian coordinate

y_0 half-width of contact zone in plastic contact problem

α material constant in Ramberg-Osgood stress-strain relationship (equation 2.20)

β strain rate parameter (equation 2.53)

β scalar quantity (= 2 plane stress, = 6 plane strain)

β' scalar quantity (= 1.072 plane stress, = 1.456 plane strain)

Γ contour in definition of J-integral

γ shear strain

γ surface energy density

δ_t crack tip opening displacement

ϵ strain

$\dot{\epsilon}$ axial strain rate

ϵ_c critical fracture strain (equation 2.45)

ϵ_Y effective strain at yielding, $\epsilon_Y = \sigma_Y/E$

ζ relative damping coefficient

η loading rate sensitivity of fracture toughness (equation 2.60)

η_e coefficient of elastic component of J-integral in deep-crack formulation (equation 2.39)

η_p coefficient of plastic component of J-integral in deep-crack formulation (equation 2.39)

θ angle, centred at crack tip, above and below plane of crack

ν Poisson's ratio

Π potential energy

ρ density

σ stress

σ_f critical fracture stress (equation 2.43)

σ_Y yield stress

σ_{Yd} dynamic yield stress

τ shear stress

τ period of oscillation

ϕ angle

ϕ factor in reducing plastic zone size correction in KGS elasto-plastic model (equation 5.9)

1. INTRODUCTION : WHY STUDY DYNAMIC FRACTURE MECHANICS?

1.1. The limitations of static, linear elastic fracture mechanics.

Linear elastic fracture mechanics is now a widely used design tool for defining load safety factors and critical flaw sizes for a given structure. It is founded on the concept that a crack represents a site of stress concentration within the structure. In the same way that stress function theory can be used to define the local elevation of stress caused by the presence of a circular hole, Westergaard [1] has defined the mathematical singularity in stress and strain which exists for a sharp crack in a linear elastic material. The strength of this singularity can be stated in terms of the local stress intensity factor, K_I, which has a limiting value, K_{Ic}, at which crack initiation takes place. This limiting value is known as the plane strain fracture toughness and is a temperature-dependent material property. It can be used to define the stress level, σ_{max}, to cause fracture in a structure with a given flaw size:

$$\sigma_{max} = \frac{K_{Ic}}{(\pi a)^{\frac{1}{2}}} \tag{1.1}$$

or, inversely, the limiting flaw size, a_{max}, at a given load:

$$a_{max} = \frac{1}{\pi}\left[\frac{K_{Ic}}{\sigma_{max}}\right]^2 \qquad (1.2)$$

Obviously, if failure is to be prevented then the minimum detectable crack size must be less than the limiting flaw size (allowing for a necessary safety factor). If the rate of stable growth of a sub-critical crack is known, then it is possible to define an inspection interval for any given component. This philosophy has been applied with considerable success, but it fails to take account of material plasticity or strain rate effects, both of which play an important part in determining the load-bearing capacity of a structure.

For many materials truly elastic behaviour is only exhibited at either very low loads or very low temperatures. The effect of significant amounts of non-elastic (plastic) deformation is to increase the resistance to fracture of a material and hence its fracture toughness. This elevation of fracture toughness may take place due to a loss of constraint at the crack tip (caused by local yielding) or due to changes in critical stress levels on a microstructural scale. If elasto-plastic behaviour is accounted for in designs subject to static loading then it is possible to design structures to take higher loads or to use less material for the same load-bearing capacity. In either case a material cost saving can be made at no expense to safety.

In the case of dynamic loading, however, there is evidence to suggest that statically determined toughness values are non-conservative. Klepaczko [2] has measured a fall of fracture toughness with increasing strain-rate in the linear range, while with the advent of small amounts of plasticity in materials such as steel it is well known that the effect of strain-rate is to promote (less tough) elastic behaviour.

A further reason for studying dynamic fracture originates in the laboratory. Theoretically, the material property, fracture toughness (K_{Ic}), is defined for the situation of "plane strain" loading which implies a test specimen of infinite thickness. In practice, it is possible to define geometries within which the plane strain approximation is valid. This results in a minimum specimen size for a given material such that [3]:

$$a,B,(W-a) > 2.5 \left[\frac{K_{Ic}}{\sigma_Y}\right]^2 \qquad (1.3)$$

where a is the crack length, B and W are specimen dimensions, and σ_Y is the material yield stress. For some materials at room temperature this condition requires very large and expensive specimens. However, since yield stress commonly rises with strain rate, the condition is less severe in a dynamic test and it is possible to define the material toughness-temperature relationship with smaller specimens at lower cost.

Unfortunately, as will be described in more detail in section 2.5, it is not as easy to obtain the required fracture toughness measurement from a dynamic test as from a static test and a major aim of this thesis is to examine the suitability of a Hopkinson pressure bar loaded impact rig for making just such a measurement. Furthermore, owing to the close relationship between dynamic and elasto-plastic effects it is desirable that the analysis technique should be capable of dealing with limited amounts of plasticity.

1.2. An approach to the characterisation of dynamic crack initiation in an elasto-plastic material.

The thesis is divided into four major sections.

Chapter 2 contains an extensive literature survey which defines the parameters most widely used to characterise crack initiation and examines their range of validity. Two parameters - K_{Ic}, for linear elastic materials, and the critical value of the J-integral at crack initiation, J_{Ic}, for elasto-plastic materials - are identified as being the most useful. Section 2.3 briefly describes the relationships between these parameters and the microstructure of the test material. The applicability of K_{Ic} and J_{Ic} in characterising dynamic crack initiation

is then examined, followed by a survey of the problems arising in dynamic fracture tests. Section 2.6 considers the application of finite element modelling techniques to fracture mechanics. They are generally time-consuming and expensive, but offer solutions to otherwise insoluble problems. For laboratory analysis of dynamic fracture tests, however, there is a need for simpler modelling techniques. Finally, section 2.7 reviews some dynamic fracture measurements reported in the literature.

Chapter 3 describes the Hopkinson pressure bar test apparatus and the test programme. Standard Charpy specimens (10 x 10 x 55 mm) are fractured in the three point bend load configuration and force-time and displacement-time characteristics derived for a range of temperature and impact velocity. The materials studied are different heat treatments (tempers) of En24 steel and two magnesium alloys. Techniques of detecting crack initiation are discussed.

Chapter 4 presents a lumped mass-spring model of the Hopkinson pressure bar loaded impact test. This kind of model was first used by Glover et al [4] and Williams and Adams [5] for the Charpy pendulum test, but is especially suited for application to the Hopkinson pressure bar test where the load point displacement is accurately measured. The various parameters in the model are considered in some depth. The most important finding is that, due to inertial

effects, remotely measured loads are not always suitable for characterising dynamic crack initiation. The model is favourably applied to those test results where the specimen behaviour is purely elastic and derived fracture toughness values are presented.

In chapter 5 the model is extended to allow for elasto-plastic behaviour of the specimen. There is further discussion of the applicability of the J-integral in dynamic testing. Some shortcomings are revealed in the material characterisation employed. Again the model is compared with experimental results.

2. THE CHARACTERISATION OF DYNAMIC CRACK INITIATION.

2.1. Linear elastic fracture mechanics (LEFM).

A cracked body may be loaded in three distinct ways (figure 2.1) - the opening mode (I), sliding mode (II), and tearing mode (III). This thesis will be concerned with mode I loading only.

The stress field near a crack tip loaded in the mode I configuration is given asymptotically by:

$$\begin{Bmatrix} \sigma_{11} \\ \sigma_{12} \\ \sigma_{22} \end{Bmatrix} = \frac{K_I}{(2\pi r)^{\frac{1}{2}}} \cos(\theta/2) \begin{Bmatrix} 1 - \sin(\theta/2)\sin(3\theta/2) \\ \sin(\theta/2)\cos(3\theta/2) \\ 1 + \sin(\theta/2)\sin(3\theta/2) \end{Bmatrix} \quad (2.1)$$

where K_I is the mode I stress intensity factor:

$$K_I = \lim_{r \to 0} \left[(2\pi r)^{\frac{1}{2}} \sigma_{22}|_{\theta=0} \right] \quad (2.2)$$

(see, for example, [6]). The loading may be further categorised as plane strain ($\epsilon_{33} = 0$) or plane stress ($\sigma_{33} = 0$) depending on the geometry of the structure.

In linear elastic fracture mechanics (LEFM) it is assumed that any non-linear material behaviour in the highly stressed region close to the crack tip is confined to an area which is small compared to the K-dominant region (ie the area where the asymptotic solution (2.1) is close to the full elastic solution). This condition is known as small scale yielding.

The size of the non-linear plastic zone can be estimated by assuming a yield condition such as the von Mises yield criterion:

$$(\sigma_1 - \sigma_2)^2 + (\sigma_2 - \sigma_3)^2 + (\sigma_3 - \sigma_1)^2 = 2\sigma_Y^2 \qquad (2.3)$$

For plane problems the principal stresses are given by:

$$\left.\begin{matrix}\sigma_1 \\ \sigma_2\end{matrix}\right\} = \frac{\sigma_{11} + \sigma_{22}}{2} \pm \left[\frac{(\sigma_{11} - \sigma_{22})^2}{4} + \sigma_{12}^2\right]^{\frac{1}{2}}$$

$$\sigma_3 = \begin{cases} 0 & \text{plane stress} \\ \nu(\sigma_1 + \sigma_2) & \text{plane strain} \end{cases} \qquad (2.4)$$

which can be rewritten in terms of the stress intensity factor, K_I, by using equation (2.1):

$$\left.\begin{matrix}\sigma_1 \\ \sigma_2\end{matrix}\right\} = \frac{K_I}{(2\pi r)^{\frac{1}{2}}} [1 \pm \sin(\theta/2)]\cos(\theta/2)$$

$$\sigma_3 = \begin{cases} 0 & \text{plane stress} \\ \dfrac{2\nu K_I}{(2\pi r)^{\frac{1}{2}}} \cos(\theta/2) & \text{plane strain} \end{cases} \qquad (2.5)$$

Substituting (2.5) in (2.3) provides the size of the plastic zone, $r = r_Y$, as:

$$r_Y(\theta) = \frac{K_I^2}{4\pi\sigma_Y^2} [(1 - 2\nu)^2(1 + \cos\theta) + \tfrac{3}{2}\sin^2\theta] \qquad (2.6a)$$

for plane strain, and:

$$r_Y(\theta) = \frac{K_I^2}{4\pi\sigma_Y^2} [1 + \cos\theta + \tfrac{3}{2}\sin^2\theta] \qquad (2.6b)$$

for plane stress. Figure 2.2 shows a comparison of these boundaries for $\nu = 0.3$.

For the purposes of many calculations it is

convenient to estimate equations (2.6a) and (2.6b) by:

$$r_Y = \frac{1}{\beta\pi}\left[\frac{K_I}{\sigma_Y}\right]^2 \qquad (2.7)$$

where $\beta = 2$ for plane stress and $\beta = 6$ for plane strain [7]. Within the region of this plastic zone the asymptotic solution (2.1) is no longer representative of the true stress field, material yielding takes place, and there is a reduction in stiffness of the body relative to the ideal elastic case. Irwin [7] suggested that this reduction in stiffness could be represented in the ideal elastic body by introducing a correction to the actual crack length, a, thus giving an effective crack length, a_e:

$$a_e = a + r_Y \qquad (2.8)$$

where r_Y is the plastic zone size given by equation (2.7). This is known as Irwin's plastic zone correction and is often used as a correction to the crack length when calculating the stress intensity factor - for example, see equation (2.13) below.

Griffith [8] suggested a second characteristic parameter which can be derived by considering the exchange of energy in a cracked body . He postulated that during an increment of crack growth, da, there can be no net change in the total energy, E, of the body. If U is the potential energy of deformation and S the surface energy, then:

$$dE = dU + dS = 0 \qquad (2.9)$$

If γ is the surface energy density per unit area, then:

$$dS = 2\gamma B\, da \tag{2.10}$$

and the strain energy release rate (or crack driving force), G, is defined as:

$$G = \frac{1}{B}\left[\frac{dU}{da}\right]_u = 2\gamma \tag{2.11}$$

It can be shown from stress function theory (see, for example, [9]) that:

$$G = \frac{K_I^2}{E'} \tag{2.12}$$

where $E' = E$ (Young's modulus) for plane stress or $E' = E/(1 - \nu^2)$ for plane strain.

Gross and Srawley [10] have analysed the three point bend specimen for linear elastic loading using a boundary collocation technique. Using Williams stress function they developed an expression for the stress intensity factor at the crack tip which is dependent only on the load and specimen geometry. Their results have since been incorporated in ASTM standard E399-83 for the plane strain fracture toughness testing of metals [3]. By this technique:

$$K_I = \frac{PS}{BW^{1.5}} F\left(\frac{a}{W}\right) \tag{2.13}$$

where F(a/W) is a dimensionless function of the crack length, a, normalised by the specimen width, W. In [10] the function F(a/W) was given as:

$$F(\tfrac{a}{W}) = 2.9(\tfrac{a}{W})^{\frac{1}{2}} - 4.6(\tfrac{a}{W})^{\frac{3}{2}} + 21.8(\tfrac{a}{W})^{\frac{5}{2}} - 37.6(\tfrac{a}{W})^{\frac{7}{2}} + 38.7(\tfrac{a}{W})^{\frac{9}{2}} \qquad (2.14)$$

for the range $0.45 < a/W < 0.55$, but this has since been extended [11] to cover the full range of crack lengths, $0 < a/W < 1$, by using:

$$F(\tfrac{a}{W}) = \frac{3(\tfrac{a}{W})^{\frac{1}{2}}[1.99 - \tfrac{a}{W}(1 - \tfrac{a}{W})(2.15 - 3.93\tfrac{a}{W} + 2.7(\tfrac{a}{W})^2]}{2(1 + 2\tfrac{a}{W})(1 - \tfrac{a}{W})^{\frac{3}{2}}} \qquad (2.15)$$

At fracture, $K_I = K_Q$, which is only a valid measure of the plane strain fracture toughness, K_{Ic}, if the constraint at the crack tip is sufficient to maintain plane strain conditions. This is generally held to be the case if the smallest specimen dimension satisfies the condition [3]:

$$a,(W-a),B > 2.5\left[\frac{K_Q}{\sigma_Y}\right]^2 \qquad (2.16)$$

This condition effectively states that the smallest specimen dimension should be at least 50x the size of the plastic zone as defined by equation (2.7).

Similar expressions to equations (2.13) - (2.15) for the three point bend specimen have been developed and tabulated for other specimen geometries [12,13,14]. Tada et al [14] also give compliance formulae for the three point bend specimen which have proved useful in the development of the present analysis (see section 4.4).

2.2. Elasto-plastic fracture mechanics.

The size restriction (2.16) for a valid plane strain fracture toughness measurement requires impractically large test specimens to characterise the fracture behaviour of high toughness, low strength materials. In the 1960s and 1970s much work was carried out to develop test methods with less severe size requirements. In their review paper on the subject, Shih et al [15] note that any characterising parameter should be representative of the stress and deformation state around the crack tip, but, at the same time, capable of evaluation from global measurements remote from the crack. The parameter should also be independent of initial crack length and specimen geometry.

The foremost parameter for characterising non-linear fracture is the J-integral [16]. This parameter is defined using the deformation theory of plasticity and so only strictly applies for monotonic, proportional loading. The latter is not the case when part of a body has yielded (eg for steel, $\nu = 0.3$ in the elastic zone, $\nu = 0.5$ in the plastic zone). History effects are also ignored and so the theory requires that there is no significant unloading during a test. Nonetheless the J-integral has proved popular because it can be shown to be representative of the magnitude of a certain type of elasto-plastic stress

singularity (see below) and is relatively easy to measure in the laboratory (by contrast with certain microstructural parameters).

The J-integral was originally defined by Rice [16] for a two-dimensional stress field about a crack tip (figure 2.3). He defined the strain energy density, U, for such a body by:

$$U = \int_0^{\epsilon} \sigma_{ij} d\epsilon_{ij} \qquad (2.17)$$

from which the J-integral is defined as:

$$J = \int_{\Gamma} (U\, dy - \underset{\sim}{T}.\frac{\partial \underset{\sim}{u}}{\partial x}\, ds) \qquad (2.18)$$

where $\underset{\sim}{T}$ is the traction vector defined along an outward normal $\underset{\sim}{n}$ from the contour Γ, defined in figure 2.3, $\underset{\sim}{u}$ is the displacement vector, and ds is an element of arc length along Γ. Of critical importance is the path-independence of the integral defined in equation (2.18). As Rice recognised, this implies that the contour defining the integral can be shrunk on to the crack tip, at which point the J-integral must become representative of the crack tip stress field. Rice and Rosengren [17] pointed out that this further implied that the product of stress and strain must obey the relationship:

$$\sigma_{ij}\epsilon_{ij} \rightarrow f(\theta)/r \quad \text{as } r \rightarrow 0 \qquad (2.19)$$

In fact, by assuming the widely used Ramberg-Osgood uniaxial stress-strain relationship [18]:

$$\frac{\epsilon}{\epsilon_Y} = \left[\frac{\sigma}{\sigma_Y}\right] + \alpha \left[\frac{\sigma}{\sigma_Y}\right]^n \tag{2.20}$$

where σ_Y is the yield stress, $\epsilon_Y = \sigma_Y/E$ is the associated elastic strain, and α and n are parameters chosen to fit the data for a given material, Hutchinson [19] and Rice and Rosengren [17] developed the so-called HRR singularity for a non-linear material. It is assumed that the linear term in equation (2.20) becomes negligible compared to the power law term as the crack tip is approached. Equation (2.20) then simplifies to:

$$\frac{\epsilon}{\epsilon_Y} = \alpha \left[\frac{\sigma}{\sigma_Y}\right]^n \tag{2.21}$$

J_2 deformation theory is then applied to generalise (2.21) to multiaxial stress states:

$$\frac{\epsilon_{ij}}{\epsilon_Y} = \frac{3}{2} \alpha \left[\frac{\sigma_e}{\sigma_Y}\right]^{n-1} \frac{S_{ij}}{\sigma_Y} \tag{2.22}$$

where S_{ij} is the stress deviator and:

$$\sigma_e = \left(\frac{3}{2} S_{ij} S_{ij}\right)^{\frac{1}{2}} \tag{2.23}$$

For power law materials, therefore, the r^{-1} singularity in U implies a $r^{-1/n+1}$ singularity in the stresses and a $r^{-n/n+1}$ singularity in the strains. The HRR singularity fields can therefore be written:

$$\sigma_{ij} = \sigma_Y \left[\frac{J}{\alpha \sigma_Y \epsilon_Y I_n r}\right]^{\frac{1}{n+1}} \hat{\sigma}_{ij}(\theta, n) \tag{2.24a}$$

$$\epsilon_{ij} = \alpha\epsilon_Y \left[\frac{J}{\alpha\sigma_Y\epsilon_Y I_n r}\right]^{\frac{n}{n+1}} \hat{\epsilon}_{ij}(\theta,n) \qquad (2.24b)$$

$$u_i = \frac{J}{I_n\sigma_Y}\left[\frac{\alpha\sigma_Y\epsilon_Y I_n r}{J}\right]^{\frac{1}{n+1}} \hat{u}_i(\theta,n) \qquad (2.24c)$$

The dimensionless functions of θ and the normalising constant I_n depend on the loading mode, n, and whether plane strain or plane stress conditions prevail. For high hardening materials n is in the range from 3 to 5, while for low hardening $n > 20$ is possible. Significantly, as n increases so the strength of the stress singularity weakens relative to the strength of the strain singularity.

From equations (2.24) J can be regarded as a measure of the intensity of the strain-hardening crack tip singularity fields in the same way that K is a measure of the intensity of the elastic crack tip singularity. Thus, equal values of J imply identical conditions at the crack tip region regardless of specimen geometry or the extent of plasticity. There are two conditions:

(i) that equation (2.21) is an adequate model of the small strain behaviour of the material,

(ii) that regions of finite strain which inevitably exist very close to the crack tip are well contained within the region over which the HRR singularity fields act.

Hutchinson [20] gives an excellent review of the conditions for such a 'J-dominant' field. They are, perhaps, best understood in terms of a second widely used crack tip characterisation parameter, δ_t, the crack tip opening displacement (CTOD). This has been variously defined in the literature but Shih [21] conveniently suggested that it should be measured at the point where a pair of 45^o lines drawn from the crack tip intercept the crack faces (figure 2.4). (Figure 2.4 also shows the crack opening displacement (COD) which can be defined as the separation of parallel faces of the crack remote from the tip.) Shih then derived a relationship between J and δ_t of the form:

$$\delta_t = d(\alpha, \epsilon_Y, n) \frac{J}{\sigma_Y} \qquad (2.25)$$

where d ranges from 0.8 for large n to about 0.3 for n=3. The CTOD is useful since it can be used as a size scale for the zone in which finite strains are important. McMeeking [22] has shown by finite element studies of crack tip blunting (ie studies which include the effect of finite strains close to the crack tip) that the position of maximum tensile stress ahead of the crack tip lies at a distance of approximately $2\delta_t$. The distance is less for strong hardening materials and the maximum stress elevation varies in magnitude from approximately $2.4\sigma_Y$ for perfect plasticity to $4.1\sigma_Y$ at n=5. At distances closer to

the crack tip than this maximum, the tensile stress reduces due to diminishing constraint. The plastic strains only become large within a distance of $1\delta_t$ from the crack tip. One condition for J-dominance must then be that the size scale R over which the HRR field is significant obeys a relation of the kind [20]:

$$R > 3\delta_t \tag{2.26}$$

Microstructurally, ductile fracture is predominantly a process of void growth, itself a finite strain process, and so equation (2.26) is satisfactory.

The extent of J-dominance is dependent on geometry and hardening. Under small scale yielding conditions numerical solutions [20] suggest that:

$$R < \frac{r_Y}{8} \tag{2.27}$$

Under fully plastic conditions for the bend configuration Shih and German [23] find from numerical studies that:

$$R < 0.07\ b \tag{2.28a}$$

for moderate to low hardening materials, where $b = (W-a)$ is the size of the remaining uncracked ligament. For the centre-cracked tensile geometry the equivalent size is:

$$R < 0.01\ b \tag{2.28b}$$

for moderate hardening and vanishingly small for low hardening as $n \to \infty$.

Combining (2.25), where $d = 0.6$ for low to moderate strain hardening, with (2.28a) and (2.26) the condition

for J-dominance under fully plastic conditions is:

$$b > 25 \frac{J}{\sigma_Y} \tag{2.29}$$

for the bend specimen, compared with:

$$b > 175 \frac{J}{\sigma_Y} \tag{2.30}$$

for the centre-cracked specimen. Shih and German [23] then assert that plane strain conditions will be satisfied if:

$$B > b \tag{2.31}$$

The use of the J-integral as a fracture criterion was pioneered by Begley and Landes [24,25]. They exploited an alternative formulation of the J-integral, proposed by Rice [16], as the potential energy difference between two identically loaded bodies with neighbouring crack sizes:

$$J = - \frac{1}{B} \frac{d\Pi}{da} = \frac{1}{B} \frac{d\Pi}{d(W-a)} \tag{2.32}$$

where Π is the potential energy. It can be shown (see, for example, [26]) that, for non-linear elastic deformation, for crack extension under constant displacement the change in potential energy $d\Pi$ is the same as the change in elastic strain energy dU, while for crack extension under constant load the change in potential energy $d\Pi$ is equal to minus the change in complementary energy dU^*. Thus equation (2.32) can be rewritten:

$$J = - \frac{1}{B}\left[\frac{\partial U}{\partial a}\right]_u = \frac{1}{B}\left[\frac{\partial U^*}{\partial a}\right]_P \tag{2.33}$$

From this definition it is easy to see that, by comparison with equation (2.11), the J-integral is equivalent to G in the limit of small scale yielding:

$$J = G = \frac{K^2}{E'} \qquad \text{for small scale yielding} \qquad (2.34)$$

Equation (2.34) supplies the link between linear elastic and elasto-plastic fracture mechanics. In general, however, since the assumption of a monotonic stress-strain characteristic is not true for most materials, this equation cannot be used to interpret J in terms of the energy available for crack extension.

Begley and Landes [24] derived J-integral values using equation (2.32) from multi-specimen tests on A533B pressure vessel steel and Ni-Cr-Mo-V steel alloy. The specimens used in these tests were much smaller than allowed for valid K_{Ic} measurement, but the values of toughness derived using equation (2.34) compared favourably with K_{Ic} measurements obtained from correctly sized specimens. As a result of Begley and Landes' work, Paris [27] suggested an empirical size relationship for valid J_{Ic} measurements of the form:

$$B, b > \lambda \frac{J_{Ic}}{\sigma_Y} \qquad (2.35)$$

where $\lambda = 25 - 50$ for the Begley and Landes data. Equation (2.35) agrees very well with the condition later determined for J-dominance (2.29).

Rice et al [28] determined that for bend specimens with deep cracks equation (2.32) can be rewritten in the form:

$$J = \frac{2\ U_{crack}}{B\ (W - a)} \tag{2.36}$$

where U_{crack} is the component of energy absorption due to the crack. Some authors [29,30] have questioned the use of U_{crack} in equation (2.36) and have proposed the simpler form:

$$J = \frac{2\ U}{B\ (W - a)} \tag{2.37}$$

where U is the total area under the load-displacement curve:

$$U = \int_0^u P\ du = \int_0^\theta M\ d\theta \tag{2.38}$$

Atkins and Mai [26] identified the omission of the rotation of the beam outside of the plastic ligament in the derivation of equation (2.36) and so (2.37) will be preferred in this thesis.

Sumpter and Turner [29] further proposed the more general expression:

$$J = \eta_e \frac{U_e}{B\ (W - a)} + \eta_p \frac{U_p}{B\ (W - a)} \tag{2.39}$$

where η_e and η_p are geometry dependent functions and the total energy is divided into elastic (including uncracked body energy) and plastic components, U_e and U_p. That this

is a more appropriate form was clearly demonstrated by Srawley [30] who looked at the ratio of J_I, as defined by equation (2.33), to the total work done per unit area of net cross-section:

$$\frac{J_I}{U/[B(W-a)]} = \frac{(W-a)}{U}\frac{\partial U}{\partial(W-a)} = \left[\frac{\partial \ln U}{\partial \ln(W-a)}\right]_u \qquad (2.40)$$

Comparing (2.39) and (2.40) shows that:

$$\eta_e = \frac{\partial \ln U_e}{\partial \ln(W-a)} \qquad (2.41a)$$

$$\eta_p = \frac{\partial \ln U_p}{\partial \ln(W-a)} \qquad (2.41b)$$

Equations (2.41) indicate the validity of using (2.37) to estimate the J-integral. Srawley found that for linear elastic behaviour $\eta_e = 2$ for $a/W > 0.5$ (in fact, $\eta_e = 2.02 \pm 0.02$ over the range $0.475 < a/W < 1.0$) and for perfect plasticity $\eta_p = 2$ based on Green and Hundy's limit load solution [31]. For work hardening materials Kanninen and Popelar [6] have looked at the values of η_p applied to an approximate elasto-plastic solution developed by the US Electric Power Research Institute [32]. They found that:

$$\eta_p = f(a/W,n) \qquad (2.42)$$

This relationship will be discussed in more depth in section 5.5.

The use of the J-integral to characterise elasto-plastic crack initiation depends on the extent to which it is truly representative of the crack tip stress

field under general yielding conditions. For it to be a useful parameter the J-integral for a small specimen undergoing general yield must be the same as that for a large specimen with small scale yielding. Slip line fields for different geometries can vary considerably [33], but if crack tip blunting occurs then, given certain geometric conditions - such as equations (2.29) to (2.31) - these variations may not be important [34,35] (see figure 2.5). As already noted, the effect of blunting is to elevate the stress level some distance ahead of the crack tip. Hancock and Cowling [33] measured a range of δ_t for several standard specimens varying by a factor of 10 from the double-edge-cracked tensile panel to the single-edge-notched tensile panel. Using finite element analyses, Liu and Zhuang [35] calculated that even allowing for the different geometric restrictions on each geometry - equations (2.29) and (2.30) - there are still considerable differences in the crack-tip fields for small scale and general yielding. They suggested that in many cases of general yield loss of constraint results in relaxation of the stress ahead of the crack tip, increased ductility, and hence fracture at higher values of δ_t (and J). They proposed a dual parameter fracture criterion for such cases involving the CTOD and a measure of triaxiality, σ_{yy}/σ_e - the ratio of local tensile to effective stress - at a distance $x = 2\delta_t$ from the crack tip. A major drawback

of this approach is that the local tensile stress cannot be directly measured and must be calculated from a finite element program. However, in cases where there is loss of constraint it seems that such an approach is inevitable.

The discussion above has been limited to power law hardening materials since the stress-strain behaviour of materials presented in this study can reasonably be characterised by such a relationship. For other material constitutive laws the theory is less well developed and similar formulations must be sought.

2.3. Microstructural aspects of crack initiation.

As well as the global fracture parameters discussed above, fracture may be categorised on a microstructural scale. Typically the fracture mode is described as cleavage (brittle) or fibrous (ductile rupture). Knott [36] identified a nucleus, usually a second phase particle (eg carbide), as initiating the process in each case. In cleavage the nucleus is formed by a pile-up of dislocations causing a local stress increase until the particle or interface cracks. Propagation of such a nucleus in a fast, uncontrolled manner results in a crystalline, often shiny fracture surface due to cleavage. In a more ductile material, once a nucleus has been formed

by cracking a particle or debonding a particle/matrix interface, the resulting flaw is too blunt a stress concentrator to propagate as a sharp crack. Fracture proceeds by expansion of such nuclei as voids until they finally coalesce by either internal necking or fast shear. The fracture surface is characteristically dimpled (the size of the dimples being related to the distribution of second phase particles).

Cleavage fracture is characteristic of lower shelf behaviour[1] and dominates in BCC crystallographic structures. Fibrous fracture occurs in FCC crystallographic structures, such as aluminium alloys, and in steels above the cleavage/fibrous transition temperature (ie on the upper shelf) [36].

It is generally assumed [2,36,37,38] that cleavage fracture is controlled by a critical value of the local stress, σ_f, and fibrous fracture by a critical value of the local strain, ϵ_c.

Ritchie et al [37] proposed that for cleavage initiation of sharp cracks the local stress, σ_{yy}, exceeded the critical fracture stress, σ_f, over a microstructurally significant length scale, l_f, (the RKR model). Ritchie et al [38] developed this theory using the HRR singularity applied in the limit of small scale yielding to produce a general expression relating the plane strain fracture toughness, K_{Ic}, to the critical fracture stress:

1 as defined in figure 2.7.

$$K_{Ic} = \beta^{-\frac{(n+1)}{2}} l_f^{\frac{1}{2}} \left[\frac{\sigma_f^{\frac{n+1}{2}}}{\sigma_Y^{\frac{n-1}{2}}} \right] \tag{2.43}$$

where:

$$\beta = f(n) \left[\frac{(1 - \nu^2)}{\epsilon_Y I_n} \right]^{1/n+1} \tag{2.44}$$

Since equation (2.43) relies on the existence of the HRR singularity and small scale yielding its range of validity must be tested by experiment. l_f is typically found to be a small multiple of the grain size, probably the distance from the crack tip where the first grain boundary carbide initiates fracture [37].

Similarly, the ductile fracture criterion can be expressed as the requirement that the critical fracture strain, ϵ_c, be exceeded over a minimum distance within the body, l_c [38,39]. Again the relationship between K_{Ic} and this critical strain has been developed:

$$K_{Ic} = \text{constant } (\epsilon_c l_c \sigma_Y E)^{\frac{1}{2}} \tag{2.45}$$

although in this case the interpretation of K_{Ic} as the limiting stress intensity factor at an elastic singularity may no longer be valid. The length l_c seems to represent not only the distance between individual particles which nucleate voids but also the critical number of such voids required to initiate crack growth [38].

Thus the fracture properties of a metal with a given chemical composition can be expected to vary with

parameters such as grain size, which, in turn, vary with heat treatment. In the case of AISI 4340 steel (the US equivalent of the En24 steel studied here) the grain size has been observed to increase with austenitisation temperature giving rise to improved toughness measurements [40].

The problem of constraint in ductile crack problems is also significant. McClintock [41] has shown that the existence of a triaxial stress state greatly increases the rate of growth of voids at inclusion sites. However, as discussed at the end of section 2.2, there is an opposite tendency for the crack tip to blunt, a process which reduces the stress elevation [22]. If the blunting process dominates then the difference between specimens with triaxial and planar stress states will be reduced. However, if triaxiality is the more important effect derived parameters such as J_{Ic} will be geometry dependent unless plasticity is fully contained. This dependence on geometry is observed and discussed further by Hancock and Cowling [33]. Kalthoff et al [42] and Ritchie et al [40] have discussed the consequent effect of notch bluntness in the Charpy test on measured fracture toughness values.

2.4. Dynamic fracture mechanics.

In the analysis of a dynamic fracture experiment it is necessary to distinguish between three possible effects of the dynamic loading:

(i) stress intensification at the crack tip due to local inertia (ie wave) effects,

(ii) macroscopic inertial effects in the specimen and loading system,

(iii) strain rate dependence of material properties (such as yield stress, fracture toughness, critical cleavage stress) and fracture mode.

Furthermore, as noted by Nilsson [43], the major difficulty is to determine the instant of crack initiation "for which no truly reliable method exists".

Over very short time intervals the loading of the crack tip is by means of stress waves: a complex interaction between the initial impact wave and reflections from the specimen surfaces [44]. Over longer time scales a more quasi-static stress field may be considered to exist and the applied bending or tensile loads become the most significant.

Theoretical reviews of dynamic fracture include excellent studies by Kanninen [45], Nilsson [43,46], and Klepaczko [47].

Assuming linear elastic conditions, the most widely

used dynamic crack initiation condition can be stated as:

$$K_I(t) > K_{Id}(\dot{K}_I) \qquad (2.46)$$

where K_{Id} is assumed to be a material function which may be determined by experiment, and $\dot{K}_I$ is the rate of change of the stress intensity factor. Equation (2.46) is only strictly valid when the non-linear zone, which must inevitably exist very close to the crack tip, is well contained within the K_I stress field. By analogy with the static case, this condition is usually expressed in terms of the characteristic length:

$$b,B > w \left[\frac{K_I}{\sigma_Y}\right]^2 \qquad (2.47)$$

For quasi-static conditions w = 2.5, the well-known ASTM condition (cf equation 2.16). It is assumed that this relation holds for dynamic cases, too, but there is no theoretical justification for this [43].

When the linear theory no longer applies the body must be modelled using elasto-plastic constitutive laws which may then be strain rate dependent. Many conservation integrals similar in form to Rice's J-integral (equation 2.18) have been proposed to characterise dynamic, elasto-plastic problems. In reviewing these, Moran and Shih [48] concluded that some are meaningless since they do not relate to the crack tip stress fields (in the way that the J-integral does through the HRR singularity) while most of the rest are generalisations of the dynamic energy release

rate, G_d, defined by:

$$G_d = \lim_{\Gamma \to 0} \int_\Gamma \left[(U + T)n_1 - \sigma_{ij} n_j \frac{\partial u_i}{\partial x_1} \right] d\Gamma \qquad (2.48)$$

where σ_{ij} and u_i are the Cartesian components of stress and displacement, and n_i are the components of a unit vector normal to Γ and pointing away from the crack tip. U and T are the strain and kinetic energy densities defined by:

$$T = \frac{1}{2} \rho \left[\frac{\partial u_i}{\partial t} \right] \left[\frac{\partial u_i}{\partial t} \right] \qquad (2.49a)$$

$$U = \int_0^t \sigma_{ij} \left[\frac{\partial \epsilon_{ij}}{\partial t} \right] dt \qquad (2.49b)$$

The kinetic energy density term is included for a propagating crack since the contour Γ then moves through the confining medium. For the case of a stationary crack tip it is bounded at the crack tip and makes no contribution to (2.48). The energy release rate for this case is:

$$G_d = J_d = \lim_{\Gamma \to 0} \int_\Gamma \left[U n_1 - \sigma_{ij} n_j \frac{\partial u_i}{\partial x_1} \right] d\Gamma \qquad (2.50)$$

Comparing (2.50) with (2.18), it is seen that the J-integral in the dynamic case is determined only as the contour is shrunk onto the crack tip. In other words it is no longer path independent since local inertia effects result in the stress field no longer being proportional at each material point.

Thus, if J is to be used to characterise dynamic elasto-plastic crack initiation, it is necessary to demonstrate that the crack tip field is indeed J-dominant. Further, since the J-integral is no longer path independent in the dynamic case, the use of deep crack estimation formulae such as equations (2.37) and (2.39) must be justified.

Both these problems have been addressed by Nakamura et al [49] using a finite element model of the three point bend fracture specimen. They argued that a reasonable measure of the time required to establish a J-dominant field at the crack tip could be found by considering the ratio of kinetic energy to strain energy in the specimen. At first this ratio is substantially greater than 1.0, but after a certain transition time it falls rapidly through 1.0 and settles to a value less than 0.1. After this transition time Nakamura et al hypothesise that a J-dominant field is established. This concept is discussed further in section 5.6 together with an examination of the contribution of specimen inertia in evaluating the deep crack formulation of the J-integral (equation 2.37).

The general problem of accounting for inertia effects without recourse to expensive and time-consuming finite element computations can be approached using 1-dimensonal lumped mass-spring models [4,5,50]. This is the technique adopted here and it is discussed in depth in chapters 4

and 5. Some more empirical methods will be presented in section 2.5.

The strain rate dependency of yield stress has been addressed by many authors. For mild steel Jones [51] recommended the Cowper-Symonds relationship:

$$\frac{\sigma_{Yd}}{\sigma_Y} = 1 + \left[\frac{\dot{\epsilon}}{C}\right]^{1/p} \tag{2.51}$$

where C and p are material constants. For mild steel (where C = 40.4 s^{-1} and p = 5) this implies a doubling of the yield stress for an increase in strain rate, $\dot{\epsilon}$, of approximately 5 orders of magnitude. The same relationship (2.51) has been fitted to data for aluminium alloy, alpha-titanium, and 304 stainless steel [51].

For AISI 4340 VAR (vacuum arc remelted) steel Tanimura and Duffy [52] fitted the results of incremental strain rate tests in shear to relationships of the form:

$$m = \frac{\ln(\tau_d/\tau_s)}{\ln(\dot{\gamma}_d/\dot{\gamma}_s)} \tag{2.52}$$

or:

$$\frac{1}{\beta} = \frac{\tau_d - \tau_s}{\ln(\dot{\gamma}_d/\dot{\gamma}_s)} \tag{2.53}$$

where τ_d and τ_s are the values of shear stress in the dynamic and static cases and $\dot{\gamma}_d$ and $\dot{\gamma}_s$ are the appropriate shear strain rates. They noted that for FCC and HCP metals the strain rate parameters derived from incremental tests (ie tests with a step change in strain rate) could be

different from those obtained in constant strain rate tests between the same limits due to history effects. However, for BCC metals such as 4340 steel, these history effects are considered to be small. For three tempers of the 4340 steel Tanimura and Duffy found that the elevation of yield stress for a variation in the applied strain rate of over 5 orders of magnitude was between 6% and 12%. (These torsional test results can be converted to approximate axial equivalents by assuming the von Mises yield criterion and an incompressible material, whence $\sigma_Y = \tau_Y 3^{\frac{1}{2}}$, $\epsilon_Y = \gamma_Y / 3^{\frac{1}{2}}$.)

In dynamic fracture tests it is the stress intensity factor that is commonly measured with time rather than the strain rate. Moreover, the strain rate will be different in different parts of the specimen. Klepaczko [2] attempted to relate the change of stress intensity factor with time, $\dot{K}_I$, to the strain rate developed at the edge of Irwin's plastic zone, assuming the von Mises yield criterion. He obtained a function of the form:

$$\dot{\epsilon} = \frac{\sigma_Y}{E K_I} \dot{K}_I f(\nu) \qquad (2.54)$$

where $f(\nu) = 1$ was claimed in Klepaczko's derivation, but, strictly speaking, $f(\nu) = (1 + \nu)$ for plane strain and $f(\nu) = (1 - \nu)$ for plane stress (see Appendix 1).

Hoff et al [53] developed a similar expression to equation (2.54) for a strain-hardening material with the

HRR singularity stress-strain field (equations 2.24):

$$\dot{\epsilon}_{ij} = \alpha\epsilon_Y \left[\frac{EJ}{\alpha\sigma_Y{}^2 I_n r}\right]^{\frac{n}{n+1}} \left[\frac{n}{n+1}\right] J^{\frac{-1}{n+1}} \dot{J}\, \hat{\epsilon}_{ij} \qquad (2.55)$$

Comparing equations (2.24b) and (2.55) gives:

$$\dot{\epsilon}_{ij} = \frac{n}{n+1} \frac{\dot{J}}{J} \epsilon_{ij} \qquad (2.56)$$

and if ϵ_{ij} is estimated by the Ramberg-Osgood pure power law (equation 2.21), where $\epsilon_Y = \sigma_Y/E$, then:

$$\dot{\epsilon}_{ij} = \alpha \frac{\sigma_Y}{E} \left[\frac{\sigma}{\sigma_Y}\right]^n \left[\frac{n}{n+1}\right] \frac{\dot{J}}{J} \qquad (2.57)$$

and, for small scale yielding, differentiating equation (2.34) gives:

$$\dot{\epsilon}_{ij} = 2\alpha \frac{\sigma_Y}{E} \left[\frac{\sigma}{\sigma_Y}\right]^n \left[\frac{n}{n+1}\right] \frac{\dot{K}_I}{K_I} \qquad (2.58)$$

For $\sigma = \sigma_Y$ (ie at the edge of the plastic zone) equation (2.58) gives a strain rate of similar magnitude to (2.54). However, Hoff et al [54] calculated that the strain rate in the process zone close to the crack tip could be several orders of magnitude greater than in the plastic zone.

The rate of change of the stress intensity factor, $\dot{K}_I$, is generally approximated by the mean value:

$$\dot{K}_I = \frac{K_{Ic}}{t_f} \qquad (2.59)$$

where K_{Ic} is the critical stress intensity factor (fracture toughness) attained after a loading time $t = t_f$.

On the basis of equation (2.54) Klepaczko [2] has described the loading rate spectrum (figure 2.6) from an assumed quasi-static level ($\dot{K}_I$ = 1 MPam$^{\frac{1}{2}}$/s), through standard test pieces in conventional machines ($\dot{K}_I$ < 1x10^3 MPam$^{\frac{1}{2}}$/s), to stress wave loading using machines such as the Hopkinson pressure bar ($\dot{K}_I$ < 1x10^6 MPam$^{\frac{1}{2}}$/s), and finally shock wave loading ($\dot{K}_I \sim$ 1x10^9 MPam$^{\frac{1}{2}}$/s).

One implication of increased strain rate is to alter the restriction on minimum specimen size required to maintain plane strain constraint for elastic specimens (equation 2.16) and to give J-dominance in elasto-plastic specimens (equations 2.29 - 2.30). At a given temperature the typical variation of yield stress with strain rate is given by equation (2.51), and, if the loading rate sensitivity of fracture toughness is defined by [2]:

$$\eta = \left[\frac{\partial K_{Ic}}{\partial \log \dot{K}_I}\right]_T \qquad (2.60)$$

then equation (2.16), for example, can be rewritten as:

$$a,(W-a),B > 2.5 \; \frac{K_{Ics} + \eta \log(\dot{K}_I/\dot{K}_{Is})}{\sigma_{Ys}\left[1 + (\dot{\varepsilon}/C)^{1/P}\right]} \qquad (2.61)$$

The loading rate sensitivity of fracture toughness η is often negative, particularly on the lower shelf, so the tendency is for both the raised yield stress and lower fracture toughness to combine to permit valid K_{Ic} tests with smaller (less expensive) specimens (with the slight

reservation expressed in the discussion of equation 2.47).

Hoff et al [53] postulated that if the critical CTOD is rate insensitive then equation (2.25), together with equation (2.34) for small scale yielding, implies that:

$$\frac{J_{Icb}}{J_{Ica}} = \left[\frac{K_{Icb}}{K_{Ica}}\right]^2 = \frac{\sigma_{Yb}}{\sigma_{Ya}} \qquad (2.62)$$

where subscripts a and b refer to two different loading rates. Thus J_{Ic} would increase with loading rate. Besides neglecting the rate dependency of the coefficient d in equation (2.25) - which from [21] is likely to be important for small n - the assumption of a rate insensitive CTOD in the derivation of equation (2.62) may not be compatible with the enhancement of void nucleation and growth processes by a higher mean stress level (which, in turn, scales with yield stress).

2.5. Instrumented impact testing.

The Charpy pendulum test was one of the earliest techniques used to characterise the fracture behaviour of steel with temperature. Although it proved possible to define lower shelf (cleavage) and upper shelf (ductile) fracture zones (figure 2.7) in terms of the energy lost by the pendulum these values were not readily translated into parameters such as the plane strain fracture toughness.

In the 1970s considerable effort was put into developing an instrumented version of the test in which the forces generated in the hammer during impact were measured using strain gauges (see, for example, [55,56,57]). The approach sought to combine the standard method of static fracture toughness testing [3] with the standard for notched bar impact testing [58]. Server [59,60] proposed a number of guidelines for the conduct of such an "instrumented impact test". In particular, he pointed out that the impact loading of a specimen created inertial oscillations in the measured load which tended to reduce in magnitude with time (figure 2.8). Server proposed that a reliable load measurement at fracture could only be obtained if the time to fracture, t_f, satisfied the condition:

$$t_f > 3\tau \tag{2.63}$$

where τ is the period of oscillations in the load-time record. The time period τ could be predicted empirically for the Charpy specimen (S/W = 4) by:

$$\tau = 3.36\left[\frac{W}{c}\right](EBc_s)^{\frac{1}{2}} \tag{2.64}$$

where c is the speed of a stress wave through the specimen and c_s is the specimen compliance. A further requirement when evaluating the total fracture energy W_m was to ensure that the the total available energy $E_o = \frac{1}{2}mV_o^2$ (where m and V_o are the mass and initial velocity of the hammer)

should be sufficient to ensure that the specimen was completely fractured. This condition was expressed in the form:

$$E_o > 3W_m \qquad (2.65)$$

and claimed to represent a reduction in striker velocity of no more than 20% up to maximum load. Initiation was assumed to take place at maximum load for purely elastic fracture, from which equation (2.13) gives the dynamic plane strain fracture toughness. For ductile fracture the criterion of initiation at maximum load was held to be non-conservative though no alternative approach was suggested. The deep-crack formulation of the J-integral (2.37) was proposed for characterising the fracture.

The problem of inertial oscillations was discussed in more depth by Ireland [61] for the case of pendulum impact. A typical force-time measurement from strain gauges mounted on the tup is shown in figure 2.8. The first peak is attributed to the force induced by rigid body acceleration of the specimen from rest to a velocity near that of the impacting hammer. This force is a maximum at the moment of impact and then rapidly decreases. The limited frequency response of the electronic measuring system results in a sinusoidal force measurement. The magnitude of the oscillation is related to the impact velocity. Subsequent oscillations occur due to stress wave effects and the periodic release of stored strain energy.

The vibration mode of the specimen is expected to be a combination of modes 1 and 3 (see figure 2.9). The frequency of stress wave reflections in the Charpy specimen is approximately 100 kHz (ie the ratio of dilatational wave speed to path length between the supports) and the tup will have a similar characteristic frequency dependent on its dimensions. The net effect is to produce a signal oscillating at about 30 kHz. Changes of impact velocity have little effect on the frequency but a large effect on the magnitude of the oscillations. Changes in specimen compliance have apparently no effect on either the frequency or the amplitude of oscillation, a phenomenon examined by the analysis in section 4.3.

Ireland [61] also noted that investigators who placed additional strain gauges on the specimen found that the loads there had a smaller amplitude of oscillation and were approximately 180^{o} out of phase with the tup force.

Ireland [61] further identified five energy absorbing processes which take place during the impact event:

(i) acceleration of the specimen from rest to the velocity of the hammer,

(ii) bending of the specimen,

(iii) deformation at the specimen load points,

(iv) vibrations within the impact machine after initial contact with the specimen,

(v) elastic energy stored within the machine.

To these must be added the energy required to fracture the specimen. Thus, while the total energy absorbed in a test might be easy to measure, the derivation of an energy value suitable for calculating the J-integral from equation (2.37) is complex. Again the analysis of chapters 4 and 5 will prove useful in this context.

Kobayashi et al [62] presented data on large three point bend specimens which suggested that Server's criterion for the time to fracture (equation 2.63) is a special case limited to certain (small) geometries. They recommended the development of dynamic analyses which allow directly for inertial effects.

Iyer and Miclot [63] considered the determination of the J-integral (equation 2.37) in the instrumented Charpy test using specimens with varying crack length. To evaluate the energy absorbed by the specimen they performed two operations on each measured force-time trace. Firstly they calculated the energy lost by the pendulum in successive time increments by relating the area under the force-time curve to the initial velocity and so derived a force-displacement curve. The second operation was to correct this curve for the compliance of the test machine. This was evaluated (as a function of load) in a separate test. The first correction was found to be only about 2.5% of the overall energy, but the second amounted to 30% in some cases.

Kobayashi [64] reported a similar analysis procedure for the instrumented Charpy test in which the inertial oscillations in the measured load were numerically smoothed. Load point deflection was determined from the rotation at the hammer axis and hence the apparent energy, E', stored in the specimen and test machine calculated. Kobayashi assumed that this could be related to the real energy absorbed by the specimen, E, by:

$$E \approx E'\left[\frac{c_s}{c_s + c_m}\right] \qquad (2.66)$$

where c_s and c_m are the compliance of the specimen and test machine respectively. Kobayashi evaluated c_m in an elastic low blow (ie low strain rate) test on an unnotched specimen as c_m = 12.2 nm/N and assumed that it would remain constant across a range of temperature and strain rate. This assumption will be discussed in chapter 5. It was found that approximately 20% of the energy at maximum load was absorbed in the test machine. From other low blow tests Kobayashi concluded that crack initiation took place prior to the attainment of maximum load and that the energy absorbed up to crack initiation could be calculated from:

$$E_i \approx 0.8\ E_{max} \qquad (2.67)$$

No attempt was made to justify the application of this expression to a wide range of impact velocities and crack tip strain rates.

The problem of reliably determining the load point displacement is largely solved if a Hopkinson pressure bar is used to load the specimen. Such a test has been described by Nicholas [65] and is the basis of the approach developed here (see chapter 3).

The second problem of machine compliance is examined more deeply in chapters 4 and 5.

Finally, the third major problem in the instrumented impact test has been the detection of crack initiation. Many authors, for example Iyer and Miclot [63], Tsukada et al [66], and Nguyen-Duy et al [67], have assumed this occurs at the maximum load. While Iyer and Miclot at least verified this assumption for slow bend tests, it is very difficult to test during high speed impact. By contrast, Kobayashi [64] found that in low blow tests crack initiation actually occurred prior to maximum load. Kalthoff et al [42] compared the load-time signals from strain gauges mounted on a drop-weight tup to measurements of the dynamic stress intensity factor made using the method of shadow caustics. They noted that the dynamic stress intensity factor only started increasing some time after the initial rise in tup load and that initiation occurred some time after the peak load was obtained. Thus there is no consensus on the relationship of remote load measurements to crack initiation and it seems likely that this will vary with material, temperature, and impact

velocity.

A possible alternative approach is to instrument the specimen itself with one or more strain gauges close to the crack tip [68], an approach that will be discussed further in section 3.6.

Kalthoff and co-workers [42,69,70] have highlighted further problems with the instrumented Charpy test, including that of loss of contact between the specimen and tup and between the specimen and anvil. Such effects only underline the necessity for a fully dynamic analysis.

2.6. Finite element analysis in dynamic fracture.

Gallagher [71] has reviewed the application of finite element modelling techniques to fracture mechanics problems. The discussion here will be limited to representations of the crack tip singularity using suitably modified isoparametric elements (ie elements in which the elastic interpolation functions are the same as the shape interpolation functions). Alternative techniques exist [71] in which special crack tip elements are created with the classical fracture mechanics solutions incorporated directly in the finite element formulation.

Henshell and Shaw [72] and Barsoum [73] independently observed that if the mid-side node of a quadratic

isoparametric line element is moved to the quarter-point (see figure 2.10a) then the derivative of the shape function is singular at one end (point 1 in figure 2.10a). It can further be shown that if the displacement field is expressed in terms of the same shape functions then the strain singularity at that point has the required order $(1/r)^{\frac{1}{2}}$. Thus a crack tip can be modelled at the corner node of a quadrilateral 8-noded element (figure 2.10b). It was later realised that the singularity condition did not exist inside the element, but Barsoum [74] corrected this by collapsing one side of the element to form the triangular element shown in figure 2.10c.

Gallagher [71] and Owen and Fawkes [75] have also reviewed various techniques for deriving the stress intensity factor (K_I) and the strain energy release rate (G). Plasticity effects can be incorporated through suitable constitutive relationships (eg Ramberg-Osgood [18]) or in a piece-wise manner from measured stress-strain curves. Moran and Shih [48] discussed an alternative formulation of the J-integral as a domain integral which is more suited to incorporation in finite element calculations than the line integral form.

Dynamic fracture analyses using finite elements can largely be placed in three categories:

(i) representation of the effect of local material inertia and strain rate on initiation fracture properties

[49,53,54,75,76],

(ii) modelling of the complex interactions between specimen and loading system [77],

(iii) crack propagation studies [78].

The third category is beyond the scope of this thesis; the other two are discussed in more depth below.

Hoff et al [53,54] developed an "inertialess" loading technique by specifying constant nodal velocities scaled appropriately from the static deflection. Having thereby isolated strain rate effects they then derived effective dynamic Ramberg-Osgood coefficients, α_d and n_d, by combining equations (2.21), (2.51) and (2.56) to give a dynamic stress-strain characterisation defined by:

$$\sigma_{Yd} = \sigma_Y \left[\frac{\epsilon}{\alpha_d \epsilon_Y}\right]^{1/n_d} \qquad (2.68)$$

With this approach they demonstrated that if, as discussed in section 2.4, critical CTOD is taken as a rate-insensitive fracture criterion, then a dynamically loaded rate-sensitive material will withstand a higher J-integral before this δ_c is reached, compatible with the change of yield stress given in equation (2.62).

Nakamura et al [49,75] have analysed two specimen geometries - notched round bar and three point bend - with a view to examining the effect of local material inertia on the establishment of a J-dominant stress field and the subsequent use of far-field measurements to characterise

the stress state at the crack tip. Their findings have been discussed in section 2.4 and will be developed further in chapter 5.

Tvergaard and Needleman [76] employed more elaborate constitutive relationships which included the effect of void coalescence through a void volume fraction which could increase due to nucleation and/or growth. Nucleation could be stress- or strain-controlled. Failure was deemed to occur either by cleavage when the stress over an element scale length exceeded the critical cleavage stress or by void nucleation and coalescence once a certain critical stress or strain had been achieved. Because the degree of stress elevation due to triaxiality at the crack tip increases with strain rate it was demonstrated that high strain rate can promote the cleavage failure mode ahead of the ductile failure mode. Due to stress relaxation with void growth the energy absorbed in the transition temperature range increased sharply as the fracture mode changed from cleavage to ductile.

Norris and Marston [77] modelled both the striker and the specimen in a Charpy impact test. By studying the early wave effects they identified specimen-striker separation as reported by Bohme and Kalthoff [69]. Their model also permitted slip of the specimen at its supports.

Further development of finite element modelling is likely to prove important in the areas of predicting

specimen/test machine interaction and studying 3-dimensional effects [79] which become important when determining the effect of crack tip constraint.

2.7. Dynamic crack initiation: experimental results.

Extensive fracture toughness measurements for different metals across a wide range of temperature and strain rate are not common. Individual authors have tended to concentrate on one or at most two strain rates. Klepaczko [2,80,81] has been one of the few to attempt a review of the available data and its synthesis with the microstructural relationships described in section 2.3. Figure 2.11 reproduces fracture toughness measurements on a carbon steel (0.45% C) at room temperature [82]. The fracture toughness is seen to fall at intermediate loading rates and to rise again at very high rates. The existence of a minimum fracture toughness which is less than the static value clearly has important design implications. Klepaczko [2] suggested that the fracture behaviour can be described in terms of the surface:

$$K_{Ic} = f(\dot{K}_I, T) \qquad (2.69)$$

from which safe design levels can be established.

Krabiell and Dahl [83] have presented data for three structural steels in terms of such a fracture surface.

Figure 2.12 shows a selection of their results for Fe E 460 steel (German standard). At very low temperatures dynamic and static values of the fracture toughness coincide, but as temperature increases a negative loading rate sensitivity is observed and the transition temperature range is shifted to higher temperatures. At very high temperatures the loading rate sensitivity becomes slightly positive (although by this stage the K_{Ic} evaluation is no longer strictly valid due to loss of constraint).

Similar results have been found by Marandet et al [84] for SA 508 Cl. 3 steel at two loading rates (figure 2.13) and by Costin and Duffy [85] for 1018 cold-rolled steel (figure 2.14).

From basic thermodynamic considerations Klepaczko [2] has developed a constitutive relationship for the yield stress as a function of temperature and strain rate. This expression, combined with the microstructural criteria for lower shelf fracture (equation 2.43) and upper shelf fracture (equation 2.45), has been used to model the Fe E 460 data of Krabiell and Dahl. The negative loading rate sensitivity in the transition zone is shown to be due to the effect of increasing yield stress. The positive loading rate sensitivity of the upper shelf is again predicted to be a function of yield stress by the simplistic approach of Hoff et al [53] - equation (2.62) -

and the microstructural model (equation 2.45). However, none of these models predicts the minimum in fracture toughness shown for the 0.45% C steel in figure 2.11. The rise in fracture toughness at very high loading rates may be due to the effect of adiabatic heating at the crack tip causing a local rise in the yield stress [86] or, perhaps, to a change in critical cleavage stress induced at very high loading rate [80].

Results for AISI 4340 (the US equivalent of the En24 steel reported here) have been contradictory. Costin et al [87] found that for samples tempered to Rockwell C 48 no rate sensitivity was evident between the static value of K_{Ic} = 61.6 MPam$^{\frac{1}{2}}$ and the dynamic value of K_{Id} = 62.7 MPam$^{\frac{1}{2}}$. However, later tests on the same material [88] gave a mean value K_{Id} = 58.3 MPam$^{\frac{1}{2}}$ for the instrumented Charpy test ($\dot{K}_I$ = 2.2 x 10^5 MPam$^{\frac{1}{2}}$/s) and K_{Id} = 56.3 MPam$^{\frac{1}{2}}$ for a test at slightly higher strain rate ($\dot{K}_I$ = 2.2 x 10^6 MPam$^{\frac{1}{2}}$/s).

By contrast, Homma et al [89] in tests on a temper to Rockwell C 51 measured a large fall in fracture toughness from K_{Ic} = 50 MPam$^{\frac{1}{2}}$ to K_{Id} = 31.7 MPam$^{\frac{1}{2}}$ ($\dot{K}_I$ = 5 x 10^5 MPam$^{\frac{1}{2}}$/s) accompanied by a change in the appearance of the fracture surface from dimpled rupture in the static test to a mixture of dimples and cleavage facets in the dynamic test.

Giovanola [90] with a similar temper to Rockwell C

50, determining stress intensity factors by Loss's static calibration method [68], reported a static fracture toughness K_{Ic} = 63.7 MPam$^{\frac{1}{2}}$ against a dynamic K_{Id} = 58.5 MPam$^{\frac{1}{2}}$ ($\dot{K}_I$ = 3 x 10^5 MPam$^{\frac{1}{2}}$/s) with no significant change in the fracture surface of dimples with both intergranular and cleavage fractures.

Two possibilities for the contradictory nature of these results arise from the specimen composition and geometry. Ritchie et al [40] have noted that comparing different heat treatments of AISI 4340 the trend in fracture toughness obtained with fatigue pre-cracked specimens could be the opposite to that obtained with notched specimens. This phenomenon was explained in terms of the effect of notch bluntness on the constraint ahead of the crack tip. Furthermore, Cox and Low [91] have shown that a small rise in the amount of sulphur in AISI 4340 steel can cause a marked fall in the fracture toughness (from 106.9 MPam$^{\frac{1}{2}}$ for 0.004% S to 74.7 MPam$^{\frac{1}{2}}$ for 0.013% S at a tempering temperature of 430^{o}C). They describe the fracture process as occurring in a brittle manner by dimpled rupture due to highly localised plastic deformation at voids initiated at inclusions of manganese sulphide (and hence the reduction in toughness with increasing sulphur impurity).

Bilek [92] attempted to examine the effect of crack velocity on fracture toughness. He found that for the

385°C temper the dynamic fracture toughness ranged from a minimum of K_{Id} = 37 MPam$^{\frac{1}{2}}$ (at $\dot{a}$ = 60 m/s) to K_{Id} = 90 MPam$^{\frac{1}{2}}$ (at $\dot{a}$ = 1000 m/s) compared with a static value of K_{Ic} = 62 MPam$^{\frac{1}{2}}$. However, since he achieved the range of crack velocities by varying the notch root radius (from 0.2 mm - low velocity - to 1.0 mm - high velocity) it must be questioned whether his results were not merely a function of constraint, as discussed above.

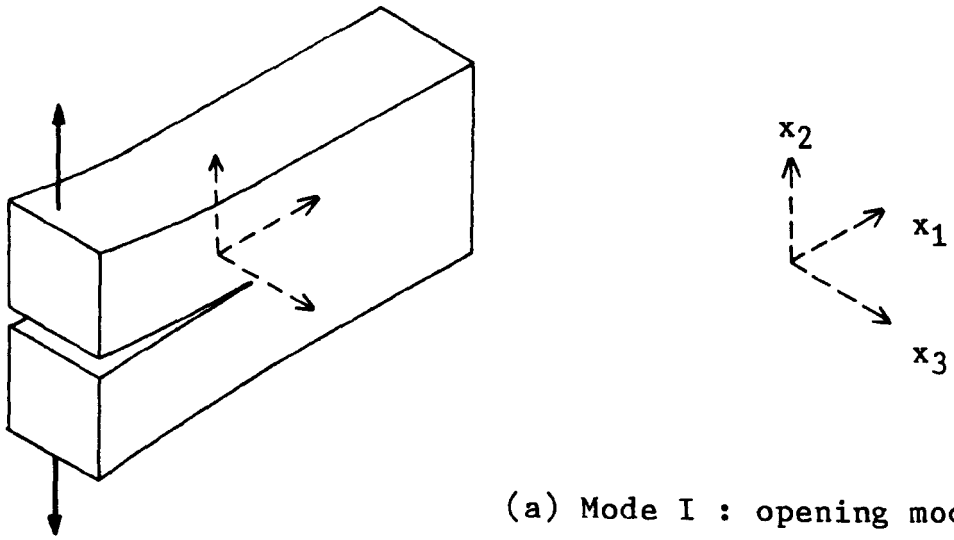

(a) Mode I : opening mode.

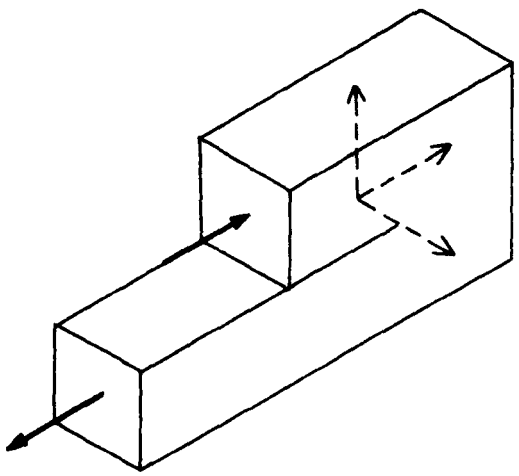

(b) Mode II : sliding mode.

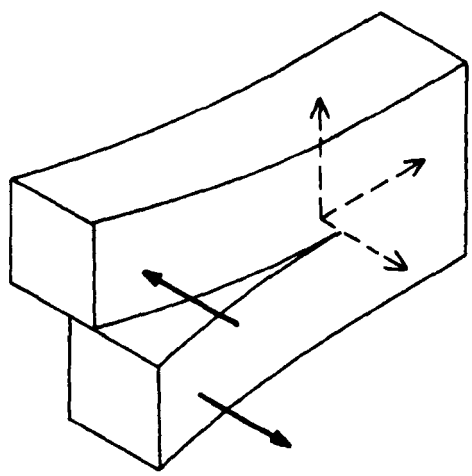

(c) Mode III : tearing mode.

FIG. 2.1. The three loading modes for a cracked body.

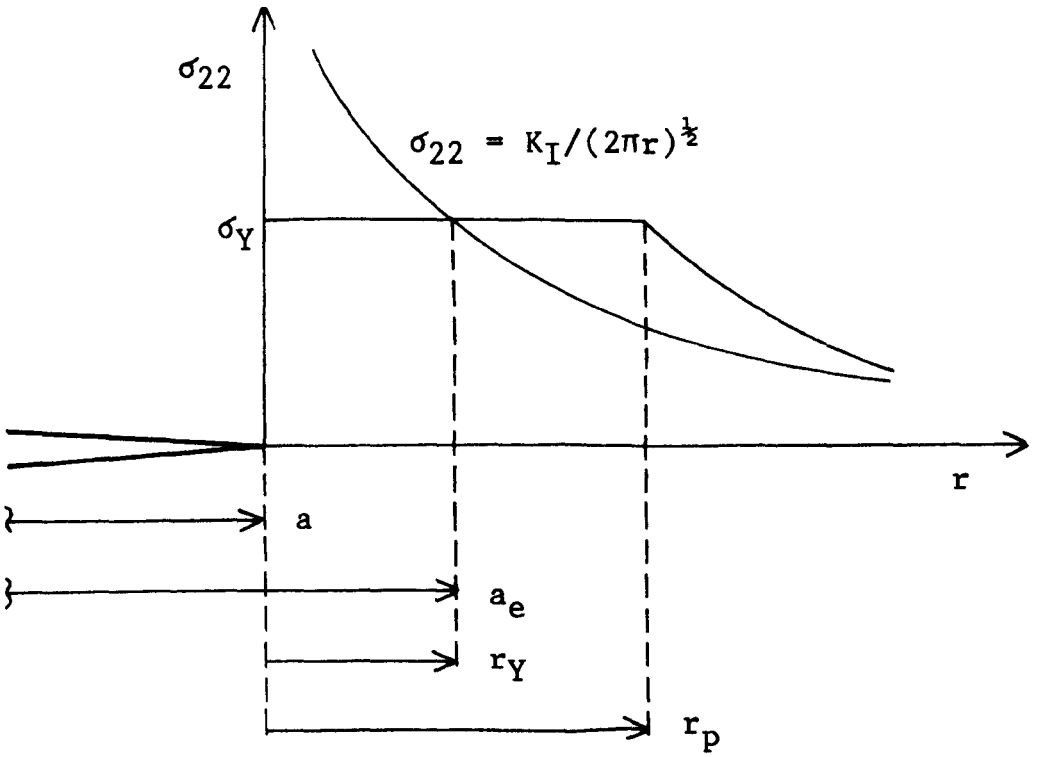

(a)

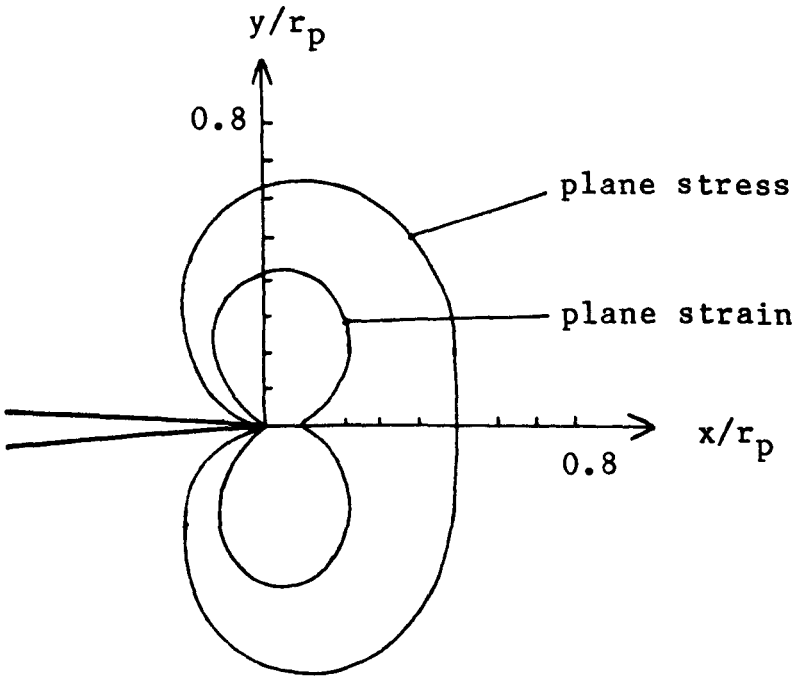

(b)

FIG. 2.2. Crack tip stress distributions showing:
(a) elastic/inelastic stress distribution,
(b) plastic zone boundaries.

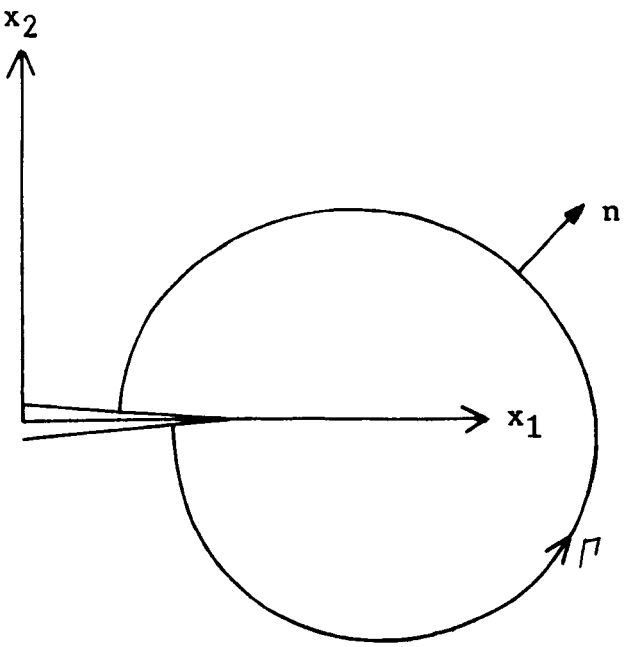

FIG. 2.3. Contour for definition of the J-integral in a plane, cracked body.

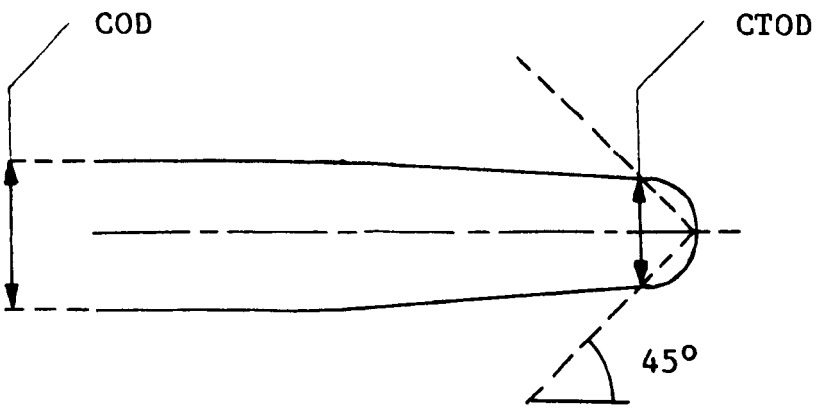

FIG. 2.4. Crack opening displacement (COD) and crack tip opening displacement (CTOD).

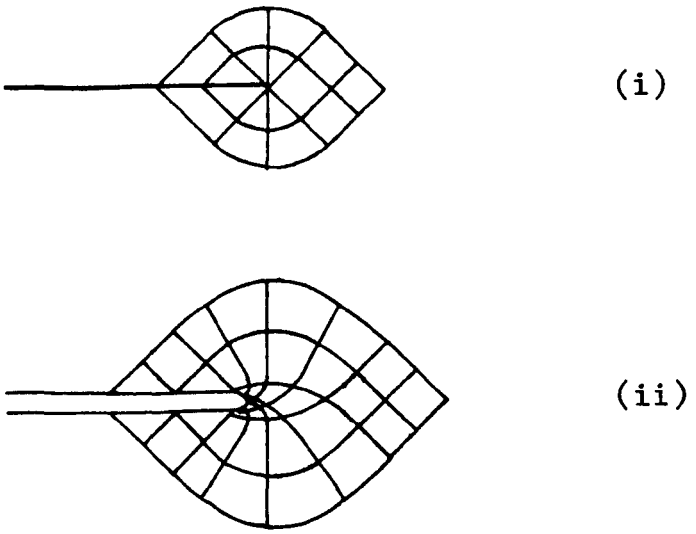

FIG. 2.5a. Comparison of Prandtl slip line fields for:
(i) a sharp crack,
(ii) a circularly blunted crack tip [33].

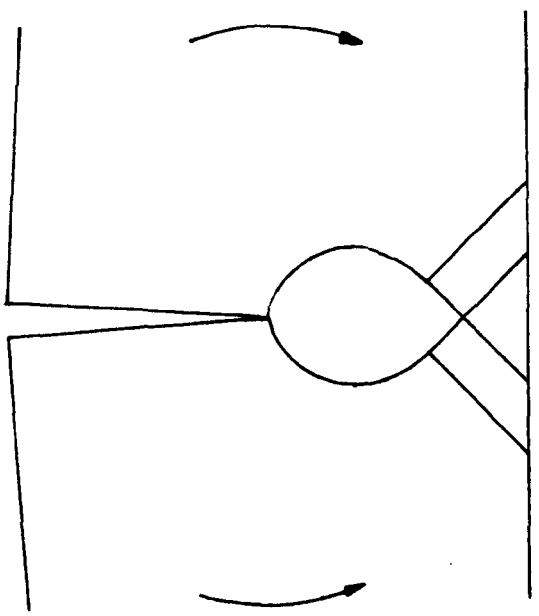

FIG. 2.5b. Slip line field in the three point bend specimen [33].

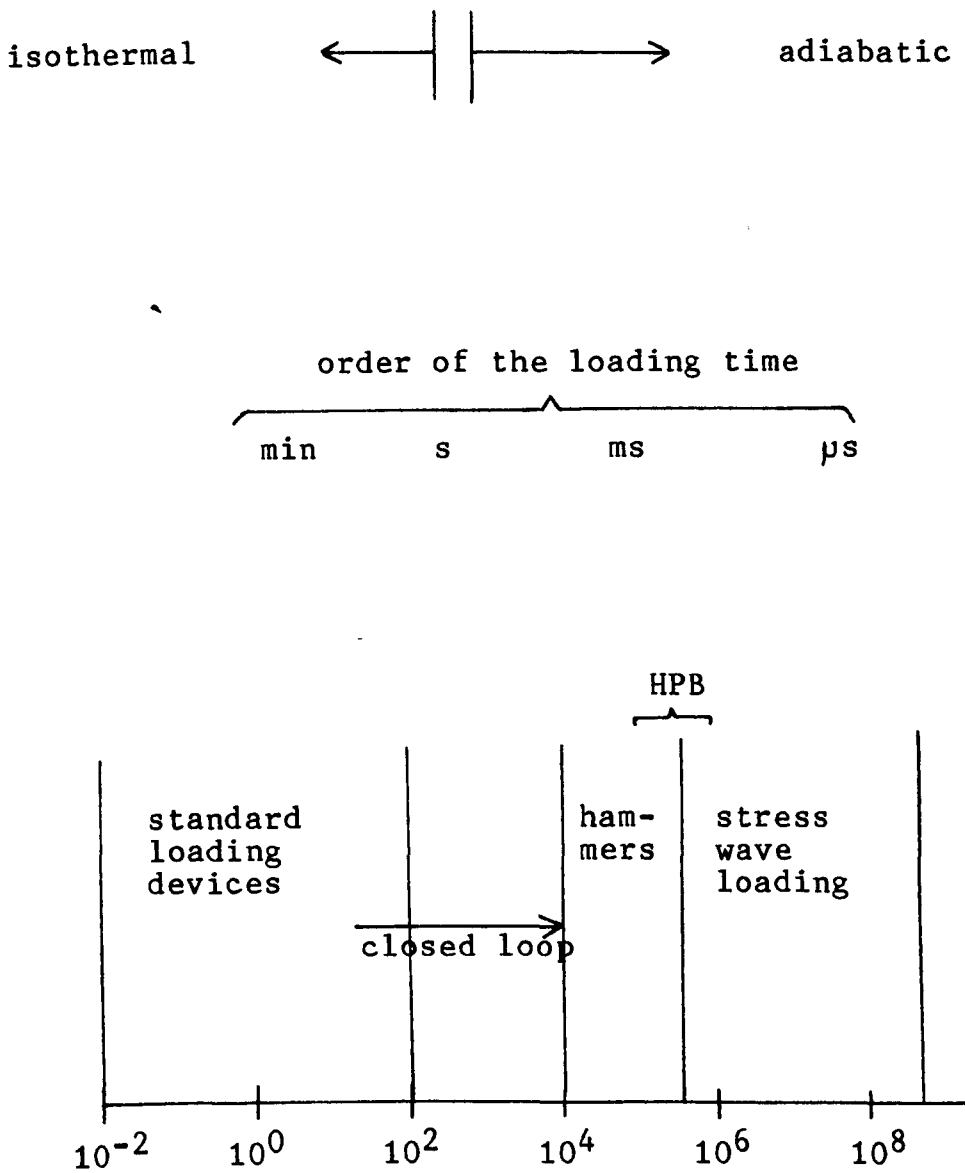

FIG. 2.6. Loading rate spectrum after Klepaczko [2].

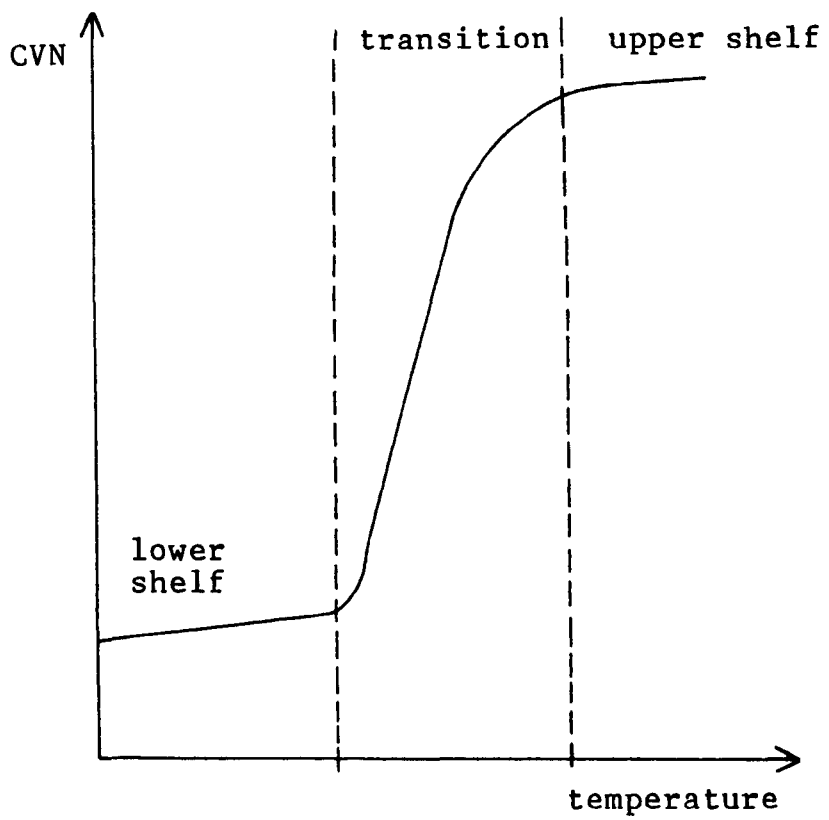

FIG. 2.7. Schematic diagram of Charpy V-notch energy (CVN) v temperature for steel [6].

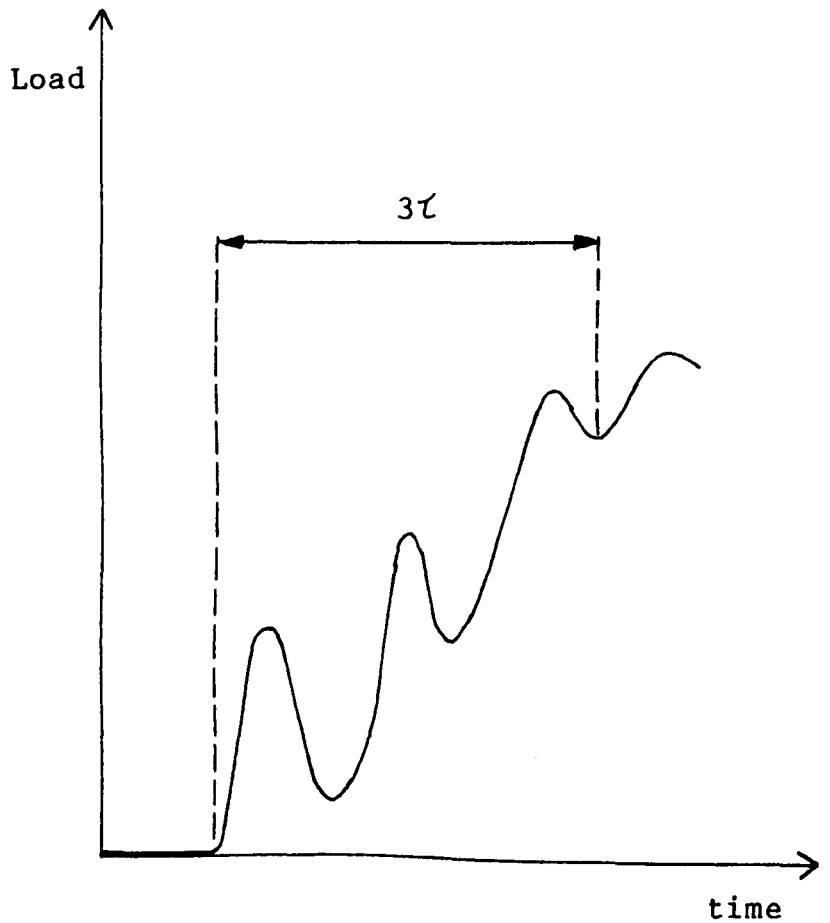

FIG. 2.8. Inertial oscillations in the load-time record for an instrumented Charpy impact test [61].

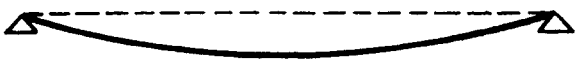

Mode 1

Mode 2

Mode 3

FIG. 2.9. Vibration modes of a simply-supported beam.

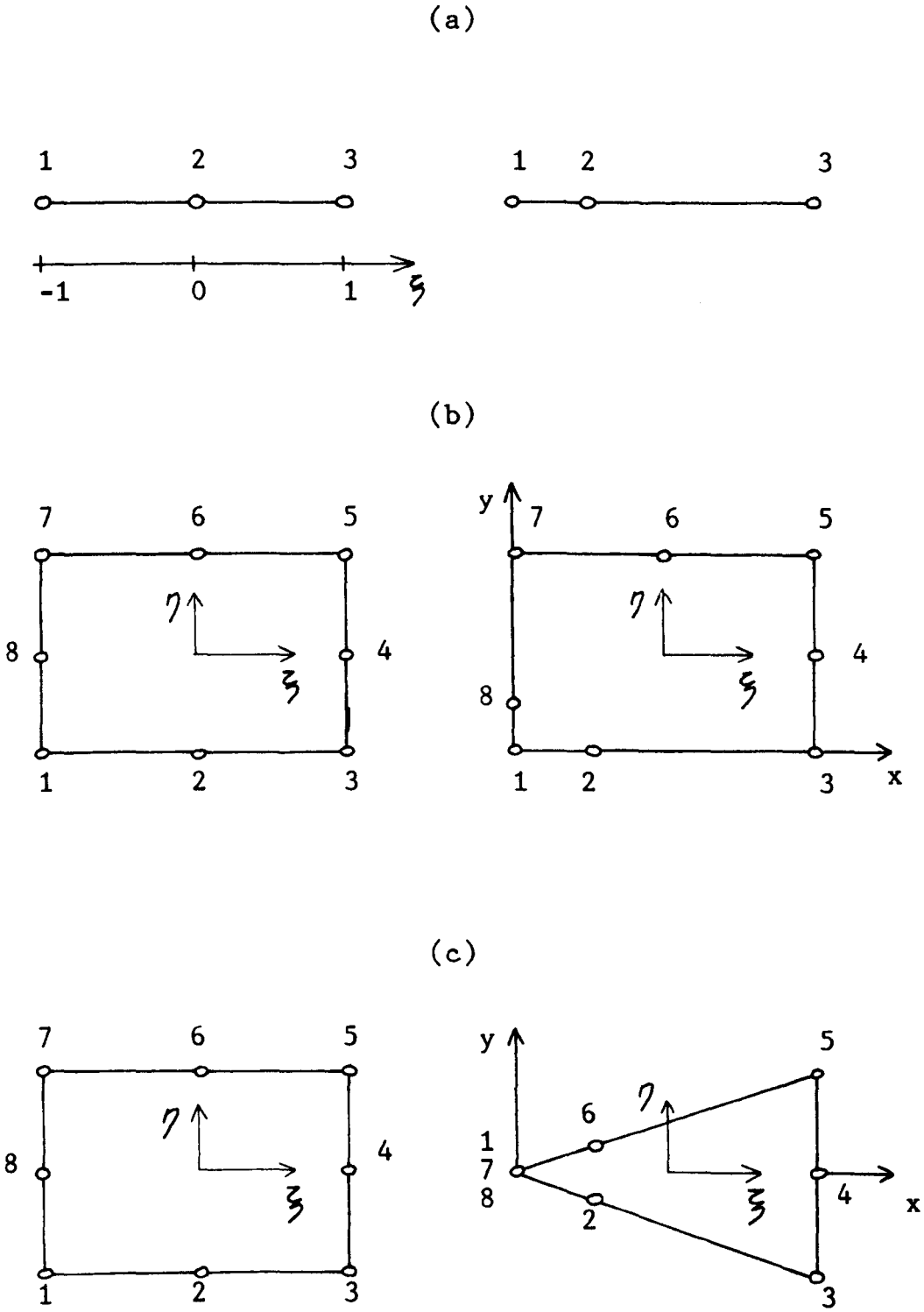

FIG. 2.10. Isoparametric finite element representations showing the ¼-point crack tip singularity:
(a) line element,
(b) quadrilateral element,
(c) quadrilateral element collapsed to triangle.

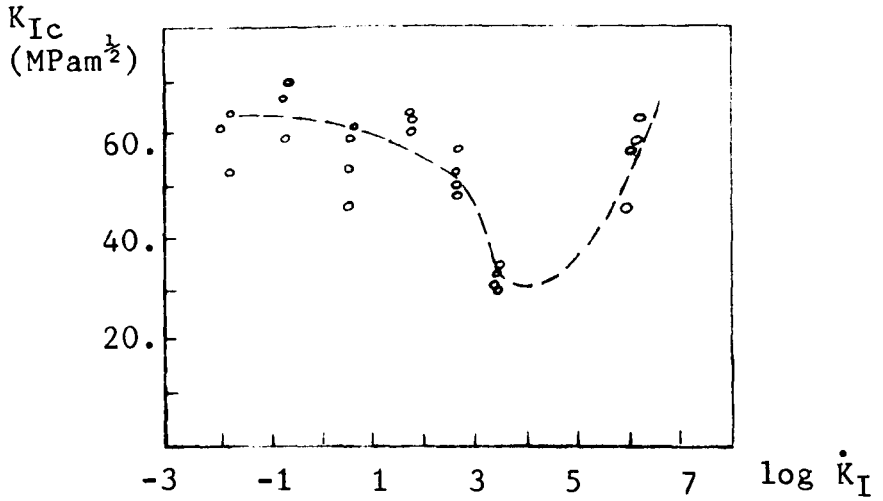

FIG. 2.11. Effect of loading rate on the fracture toughness of 0.45% C steel at room temperature [82].

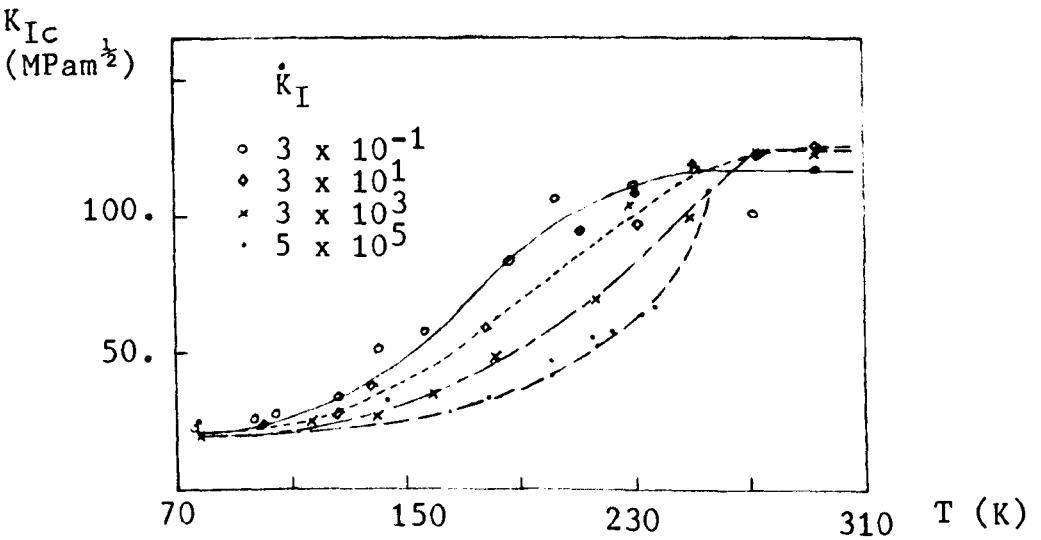

FIG. 2.12. Fracture toughness as a function of temperature and loading rate for Fe E 460 steel [83].

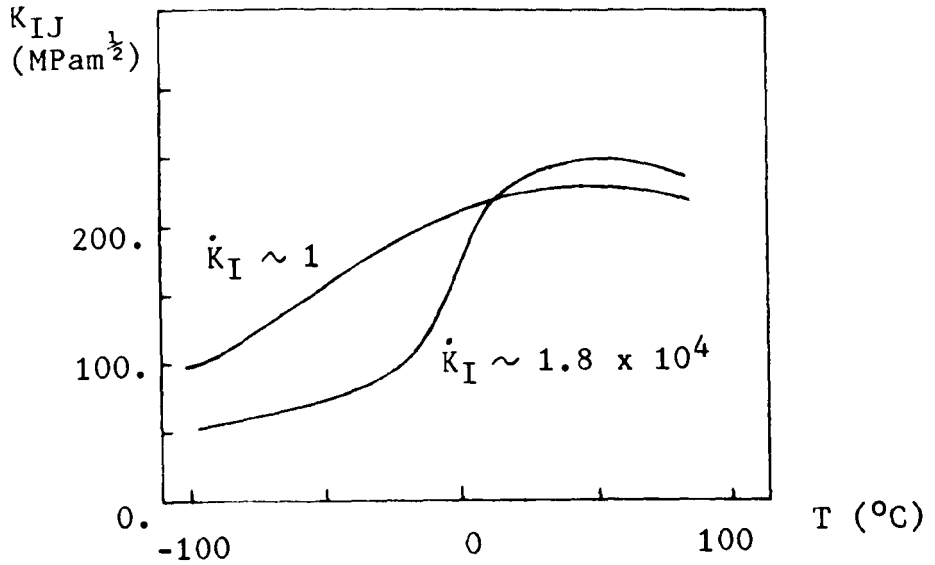

FIG. 2.13. Fracture toughness as a function of temperature and loading rate for SA 508 Cl 3 steel [84].

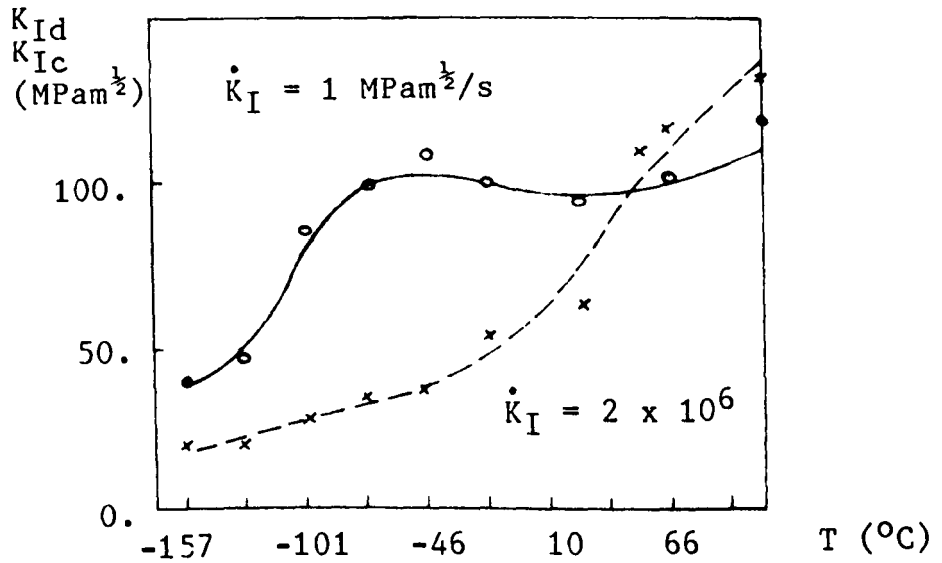

FIG. 2.14. Static and dynamic fracture toughness of 1018 CRS as a function of temperature [85].

3. THE THREE POINT BEND IMPACT TEST LOADED WITH THE HOPKINSON PRESSURE BAR.

3.1. Introduction: the Hopkinson pressure bar.

In 1913 Hopkinson [93] used a ballistically suspended steel bar to transmit short pressure pulses from the detonation of gun-cotton at one end of the bar to a series of different length short bars attached lightly to its opposite end by magnetic attraction. By measuring the momentum imparted to the shorter bars Hopkinson was able to approximate the shape and time history of the pressure pulse generated by the detonation of the gun-cotton.

Kolsky [94] adapted this technique to measure the stress-strain characteristics of materials at high strain rates by wedging a sample of the material between two bars instrumented with microphones and detonating a charge at the opposite end of one of the bars. This is the so-called split Hopkinson bar arrangement.

Further development included the introduction of strain gauges to measure the longitudinal stress waves generated in the bars and a second striker or travelling bar to replace the need for an explosive charge.

Nicholas [65] employed this arrangement of one bar impacting another to perform instrumented impact tests on several grades of beryllium using Charpy specimens loaded

in three point bend configuration. He demonstrated that the force-time and displacement-time behaviour of the specimens could be easily deduced from measurements at a single strain gauge mounted approximately halfway along the incident bar and that inertial oscillations were considerably reduced by comparison with results from instrumented Charpy tests at similar loading rates. However, the energy measured to failure was similar for both types of test.

Tanaka and Kagatsume [95] performed similar tests on 0.45% C steel except that they replaced the anvil support used by Nicholas with a cylindrical, instrumented output tube in a split Hopkinson bar arrangement. They deduced the load on the specimen from the stress wave in the support bar and the deflection of the specimen from the relative displacement of the ends of the incident bar and output bar.

Yokoyama and Kishida [96] used a similar technique to study aluminium alloy and titanium alloy, except that they replaced the single transmitter tube with two instrumented bars. The rise in transmitted load occurred 50×10^{-6} s after the initial impact load reached the specimen, suggesting a loss of contact between the specimen and its supports.

Ruiz and Mines [97,98] derived force-time and displacement-time characteristics for a pressure vessel

steel using two measurement points on the incident bar alone. This was the fundamental approach adopted for work in this thesis. It is described below together with some improvements to the test technique.

3.2. General arrangement of apparatus.

The apparatus basically consisted of two coaxial, cylindrical steel bars used to generate and transmit a pressure pulse to a standard Charpy specimen supported by an anvil (figures 3.1 - 3.3). The first, or "travelling" bar was accelerated by means of a catapult powered by bungees. Its velocity could be controlled by moving the saddle shown in figure 3.1 backwards and forwards along the supporting bars. The travelling bar then impacted the second - "incident" - bar which in turn was in direct contact with the specimen under test. Good contact with the specimen was ensured by attaching the incident bar to the anvil with another, lightly tensioned bungee.

The stress wave generated by the impact between the two bars was measured using strain gauges positioned at points S1 and S2 in figure 3.1. There were two strain gauges at each measurement point, positioned on opposite sides of the bar, so that, by means of a Wheatstone bridge network, it was possible to separate out the normal stress

from any bending stress which might have been induced by the impact (see section 3.3). The resulting strain gauge signals were amplified by a gain of 2 - 10 x 10^3 and stored on a DL1080 transient recorder (figure 3.4). Recording was triggered by the leading edge of the S1 signal attaining a certain voltage. A fifth strain gauge (S3) was attached to the specimen itself to determine the instant of crack initiation (see section 3.5). All strain gauge records were subject to high frequency cut-off (-3dB) at 1 MHz and low frequency cut-off (-3dB) at d.c. conditions, giving an excellent range of frequency sensitivity. A sampling rate of 0.2 x 10^{-6} s was selected, thereby giving good resolution to all events with a period greater than 1 - 2 x 10^{-6} s.

The velocity of the travelling bar could be determined from the strain gauges at S1 and S2 using 1-dimensional wave mechanics. It was also measured independently by a photocell placed close to the impact point which then gave a basis for proving the calibration of the rig.

3.3. Calibration of the Hopkinson pressure bar.

A general Wheatstone bridge network is shown in figure 3.5a. For a balanced bridge voltage e_{bc} = 0 and

hence:

$$\frac{R_1}{R_4} = \frac{R_2}{R_3} \tag{3.1}$$

If R_1 is made an "active" gauge (ie the strain gauge) then it will undergo a change of resistance δR_1 on loading with a strain ϵ_1 such that:

$$\epsilon_1 = \frac{1}{k_g} \frac{\delta R_1}{R_1} \tag{3.2}$$

where k_g is the strain gauge sensitivity. Measurements may be taken either by:

(i) using a calibrated variable resistor at R_2 or R_4 to balance the bridge, or,

(ii) measuring the unbalanced voltage across e_{bc} after the bridge has been first balanced for the no-load condition.

The first technique is impractical for high speed dynamic tests. Using the second approach, it was assumed that equation (3.1) still applies under the out-of-balance condition although this is not strictly true. It can then be shown [99] that for maximum voltage sensitivity $R_1 = R_2 = R_3 = R_4$, under which conditions the voltage sensitivity for a single active gauge at R_1 is given by:

$$S_v = \frac{e_{bc}}{\epsilon} = \frac{E_m k_g}{4} \tag{3.3}$$

where E_m is the driving emf for the bridge.

In order to eliminate bending effects two strain

gauges were used on opposite sides of the incident bar (figure 3.5b). If these gauges have the no-load resistances R_1 and R_1' then under load their resistance will change by the increments δR_1 and $\delta R_1'$ such that:

$$\delta R_1 = \delta R_n + \delta R_b \tag{3.4a}$$

$$\delta R_1' = \delta R_n - \delta R_b \tag{3.4b}$$

where subscript n refers to normal stress load and subscript b to bending stress load.

The two possible circuits for eliminating the bending component δR_b are shown in figures 3.5c and 3.5d. It can be shown that the circuit in figure 3.5d has twice the voltage sensitivity of the circuit in figure 3.5c and that this voltage sensitivity is given by:

$$S_v = \frac{e_{bc}}{\epsilon_n} = \frac{E_m k_g}{2} \tag{3.5}$$

provided that $\delta R_1/R_1 \ll 1$. (For a nominal impact velocity of 2.5 m/s, $\delta R_1/R_1 \approx 5 \times 10^{-4}$, so this condition is well satisfied.) Thus the circuit in figure 3.5d was selected with $k_g = 2.03$, $R_1 = R_2 = R_3 = R_4 = 120\Omega$, and $E_m = 5V$.

To ensure that equation (3.5) gives a correct measure of the level of strain in the incident bar, it was used to deduce the velocity of the impact bar in each test and the result compared with the photocell measurement. From 1-dimensional stress wave analysis (see, for example, [100]) the strain induced in a bar by the passage of an elastic stress wave with velocity c is:

$$\epsilon = \frac{\sigma}{E} = \frac{\rho c V}{E} \tag{3.6}$$

where V is the local particle velocity and E is Young's modulus. The elastic wave velocity can be expressed as:

$$c = \left[\frac{E}{\rho}\right]^{\frac{1}{2}} \tag{3.7}$$

and so, from equations (3.6) and (3.7):

$$V = c\epsilon \tag{3.8}$$

which is the particle velocity generated in the incident bar by the collision of the travelling bar at one end. Again from 1-dimensional stress wave analysis [100] applied to the collision of two bars of different cross-sectional area (figure 3.6), equilibrium requires that:

$$A_1\sigma_1 = A_2\sigma_2 \tag{3.9}$$

Substituting from equation (3.6), for bars of identical material, equation (3.9) can be rewritten:

$$V_1 = \frac{A_2}{A_1} V_2 \tag{3.10}$$

where V_1 and V_2 are the particle velocities after collision of the travelling and incident bars respectively. If V_0 is the initial velocity of the travelling bar, then, by continuity:

$$V_0 - V_1 = V_2 \tag{3.11}$$

Combining equations (3.8), (3.10), and (3.11), the travelling bar velocity immediately prior to impact is:

$$V_0 = \left[1 + \frac{A_2}{A_1}\right] V_2 = \left[1 + \frac{A_2}{A_1}\right] c\epsilon \qquad (3.12)$$

The strain magnitude ϵ in equation (3.12) was determined directly from the mean voltage measured at the S1 strain gauge using equation (3.5). The resulting evaluations of velocity are compared with the equivalent photocell measurements in figure 3.7 for a range of impact velocities. Agreement is within 2% for $V_0 < 2.5$ m/s but as high as 6% for one of the high speed tests. However, for the higher speed tests the photocell measurements were comparatively erratic (due to short measurement times) while the V_0 calculation (equation 3.12) for back to back tests (ie those for which the saddle position had not been altered) proved far more consistent.

The electronic measuring system was in turn calibrated using reference voltages applied to the terminals of the differential amplifiers.

3.4. Derivation of force-time and velocity-time traces.

The analysis procedure for the strain gauge readings at S1 and S2 has been described by Ruiz and Mines [97]. The principle is that the stress wave generated by the impact of the travelling bar propagates down the incident bar to the specimen where part of it is reflected and part

of it transmitted through the specimen. Assuming that the pulses generated in the bar are purely elastic and travel in a non-dispersive manner at the elastic wave velocity, c, it is possible by appropriate manipulation of the S1 and S2 traces to determine the force and velocity at the tip of the incident bar. A limiting time for useful measurements is imposed by the fact that these values can no longer be accurately determined once the reflected unloading wave has reached S1. This limit is achieved provided that the travelling bar is long enough to give a continuous stress pulse at S1 (ie it must be at least as long as the incident bar). The assumptions of 1-dimensional wave mechanics as stated above are no longer strictly valid at the tip of the incident bar which is profiled to form a wedge and the implications of this will be discussed later.

The basic data reduction technique is depicted schematically in figure 3.8. The strain gauges at S1 measure the incident wave, ϵ_I, while those at S2 register initially the incident wave and subsequently the difference between the incident wave and the reflected wave, $\epsilon_I - \epsilon_R$. ϵ_R can be determined by aligning the two traces and subtracting appropriately. Further shifting of the reflected wave to coincide with the rise of the incident wave is equivalent to studying the stress wave history at the point of reflection (which, to a first

approximation, can be assumed to be at the tip of the incident bar). The force on the specimen is then given by:

$$F = A\ E\ (\epsilon_I - \epsilon_R)_{tip} \qquad (3.13)$$

where E is Young's modulus and A is the cross-sectional area of the incident bar. The particle velocity at the tip of the bar is:

$$V = c\ (\epsilon_I + \epsilon_R)_{tip} \qquad (3.14)$$

3.5. Specimen specifications and preparation.

The specimens were standard Charpy three point bend notched impact specimens (55 x 10 x 10 mm), as described by ASTM standard E23 [58] and illustrated in figure 3.9. The materials used and their heat treatments are specified in section 3.7. After their appropriate heat treatment the specimens were fatigue pre-cracked to approximately half their width using an Amsler vibrophone in the three point bend configuration and following the recommendations of Ireland [101] with respect to maximum load and loading range. These recommendations require the fatigue crack to extend at least 2.5 mm beyond the notch tip and during the last 0.5 mm of fatigue crack growth the maximum stress intensity factor for the fatigue cycle must lie within the range [101]:

$$0.00013\ E < (K_f)_{max} < 0.00029\ E \qquad (3.15)$$

The maximum load for each specimen material was evaluated to lie at the lower end of this range (since the upper limit was found to be comparable to the static fracture toughness values for all the materials used in the study), although higher values were sometimes needed to initiate the fatigue crack. The further stipulation that the stress intensity range should not be less than 0.9 $(K_f)_{max}$ was not achieved. In practice a range of only about 0.6 - 0.8 $(K_f)_{max}$ was found possible before chattering began at the supports.

Figure 3.9 also shows the position of the specimen crack tip strain gauge which was used to monitor crack initiation (see section 3.6). The strain gauges used were of constantan on a polyimide backing with larger than usual copper tabs to facilitate soldering of leads. Their specification was CEA-06-062UW-120. Installation was carried out using M-Bond 610 adhesive, following the surface preparation and curing cycle specified by the manufacturers [102].

3.6. The detection of dynamic crack initiation.

The problem of detecting the instant of dynamic crack initiation has been discussed in section 2.5. The importance of inertial effects means that the assumption

of initiation occurring when the impactor load achieves a maximum value is too simplistic. It is necessary therefore to have a technique for determining the moment of crack initiation which is independent of the load-time trace. In the current study two possible techniques were considered, namely:

(i) an alternating current potential difference (ACPD) commercial crack detector manufactured by Matelect Ltd (Crack Growth Monitor CGM5), and,

(ii) a strain gauge mounted on the surface of the specimen close to the crack tip.

The ACPD technique was developed by Marandet et al [84] and Venkatasubramanian and Unvala [103]. An alternating current is passed through the specimen and the potential difference measured across the crack. When the crack initiates the impedance rises. The method has several advantages over the corresponding direct current technique which requires large currents and great care that temperature variations do not generate thermoelectric and drift voltages which can be mistaken for crack growth. The ACPD approach relies on the skin effect where currents are restricted close to the surface and, since the AC impedance is much larger than the DC resistance, smaller currents can be used. AC coupled amplifiers are used to remove the DC voltage errors described above. Venkatasubramanian and Unvala have used the technique to

monitor slow crack growth and Marandet et al to measure the dynamic fracture toughness of SA 508 Cl 3 steel at an intermediate loading rate ($\dot{K}_I$ = 1.8 x 10^4 MPam$^{\frac{1}{2}}$/s). The latter used a current of 3A at frequency 10 kHz. Application of the ACPD technique in high speed dynamic tests is undocumented. The maximum frequency offered by the CGM5 was 100 kHz which suggested a resolution of the order of 10 x 10^{-6} s which would have been barely satisfactory. Unfortunately at this frequency the skin depth in steel is very shallow and the resulting signal too weak to interpret. Unvala [104] recommended an optimum operating frequency of 10 kHz for steel which would not achieve the required resolution, but even at a compromise of 30 kHz the signal was too weak and erratic. It was therefore concluded that the equipment was unsuitable for high rate tests on steel. It is also worth noting in this context that Okumura et al [105] have found that for very tough materials the AC impedance also increases with significant crack tip blunting, thus making initiation in elasto-plastic materials very difficult to determine. This point does not seem to have been appreciated by Marandet et al [84] who assumed that initiation took place at the minimum potential difference for a wide range of specimen temperature.

The use of a strain gauge mounted on the specimen itself to determine the instant of crack initiation in

linear elastic specimens is widely known. Mall et al [68] have even calibrated the strain gauge under static loading conditions to enable them to determine the midspan load during a dynamic test without the confusing presence of the inertial loads sensed by a transducer mounted on the impactor itself. Their technique is limited, however, to purely elastic tests (since the calibration cannot be carried out beyond the yield point of the metal) and is also time consuming in that each individual specimen must be calibrated. In this study it was decided to use the strain gauge as a purely qualitative assessment of the stress state of the specimen, anticipating that elastic cleavage initiation would be registered by a sharp drop in the reading and seeking to determine whether the technique would also work into the elasto-plastic transition range.

MacGillivray and Cannon [106] have conducted a survey of suitable strain gauge types, adhesives, and locations on the specimen. Following their recommendations the strain gauge type CEA-06-062UW-120 was selected. These strain gauges were known to have good characteristics within the required temperature range (-100°C to +125°C). The strain gauges were mounted on the specimen centre-line approximately 5 mm from the crack tip (see figure 3.9).

Another promising technique for monitoring crack initiation has been developed more recently by Kalthoff and co-workers and reported in English by Spies [107]. In

this technique the specimen is slightly magnetised so that when the crack initiates the resulting change in the field can be picked up by an electro-magnetic sensor. Again, the technique does not yet appear to have been used in the elasto-plastic range of material behaviour. Unfortunately awareness of this technique came too late to permit its incorporation in the test programme.

3.7. Material specification.

The material specification for the various heats of En24 steel employed in the study is given in table 3.1. The En24 steel was selected because of its high strength and relatively low toughness which make it an ideal candidate for testing with the Charpy specimen size (see discussion of equation 2.16). Unfortunately insufficient material was ordered initially and the two batches ultimately used had different compositions - the second batch containing a larger proportion of manganese than allowed for in the En24 specification (see table 3.1). In addition, En24 is very sensitive to heat treatment. The effect of these small differences in composition, and, perhaps, also some small variation in the heat treatment, resulted in grossly different fracture characteristics for the specimen batches HC1 and HC2 which were nominally

equivalent. Six specimens from the HC2 batch were manufactured to a length of only 45 mm to examine the effect of reduced specimen inertia. Specimen batch HC3 was tempered at a higher temperature than HC2 in order to promote more ductile behaviour. In all there were 25 HC1 specimens, 26 HC2 specimens (including the 6 shorter specimens), and 10 HC3 specimens. Table 3.1 also shows the specification for AISI 4340, the nearest US equivalent to En24.

The HC1 specimen batch was supplied in the as-quenched condition in the form of 16 mm diameter circular-section bar, the HC2 and HC3 specimens to the same heat treatment in 20 mm diameter circular-section bar. The specimens were then rough machined oversize, tempered as specified in table 3.1, and then finish machined.

As examples of a non-steel, specimens of two different magnesium alloys were provided by Magnesium Elektron Ltd. These were a heavy rare earth alloy, Elektron WE54, and a zinc-copper-manganese alloy, Elektron ZCM 630-T6 (see table 3.2). 21 specimens were supplied of each alloy.

The magnesium alloy specimens were cast into 8" x 8" x 1" sand cast plates, heat-treated, radiographed, cut, and finally machined [108].

Sections were cut of each of the main specimen types.

These were polished and then etched to reveal the finer details of the structure. The steel specimens revealed a structure typical of tempered martensite. The magnesium alloy WE54 showed a fine equiaxed grain structure with occasional particles at the grain boundaries, while the ZCM 630-T6 alloy possessed a more refined grain size of the characteristic lamellar form of eutectic magnesium with intermetallics at the grain boundaries.

3.8. Development of the test apparatus.

The mechanical parts of the apparatus remained unchanged throughout the test programme, with the exception of two early alterations made towards the end of the HC1 specimen batch (prior to tests 028 and 032-035). These alterations comprised replacing the incident bar due to some irregularities which had been noted in the shape of the tip profile and a redesign of the anvil.

The geometry of the wedge-shaped profile of the tip of the incident bar is shown in figure 3.10. It differs from the shape of the profile recommended for the standard Charpy test machine in ASTM standard E-23 [58] by having an included angle of 60^{o} rather than 30^{o}, a modification which was made to reduce the measurement error incurred at the change of section in the HPB analysis. It was also

hoped that it would serve to improve the stiffness of the test machine. Any small irregularities in the profile result in poor contact with the specimen.

The anvil originally comprised two adjustable jaws mounted on a large block (figure 3.11a). This was apparently intended to facilitate alignment of the rig and specimen, but in practice the jaws had too great a freedom of movement and they were replaced with a single, more rigid block (figure 3.11b).

The net effect of these two alterations was to improve the squareness with which the specimen was presented to the incident bar and resulted in a much improved test repeatability. A bungee was used to lightly clamp the incident bar to the specimen prior to each test since preliminary results showed a tendency for some slack to appear in the system prior to impact.

3.9. The test programme.

It was originally hoped to study the test materials across a wide range of temperature and strain rate. The strain rate was to be varied by adjusting the impact velocity of the travelling bar, but unfortunately the range of strain rates achievable in this fashion proved to be very limited. A lower velocity limit is imposed by the

requirement of obtaining crack initiation before the reflected wave reaches the S1 measurement point (see section 3.4), while if the velocity is too high inertia effects predominate and both the identification of crack initiation and the subsequent determination of fracture toughness become very difficult (see chapter 4).

A temperature range of about 200°C was achieved, however. Sub-ambient temperatures were obtained by immersing the test specimen in liquid nitrogen for a period of about ten minutes, then inserting it in the rig and allowing it to heat up to the required test temperature. In the case of the En24 steel specimens the temperature was measured using a thermocouple spot-welded to the surface. Tests at Imperial College [106] have shown that temperatures measured in this way differ by only about 1°C from those measured at the specimen centre-line by thermocouples inserted through drilled holes. In the case of the magnesium alloy specimens the thermocouple was inserted in a small hole drilled in the specimen since spot-welding proved impossible. Temperatures above ambient were obtained using a hot air blower to heat the specimen in situ to approximately 10°C above the required temperature and then allowing it to cool. Heating the specimen in situ in this fashion will inevitably have given rise to uneven temperature distributions and, although it is hoped that these will have evened out

somewhat during the cooling process, it is felt that these temperature measurements will not have been as accurate as those from the very cold tests. Furthermore, some heat conducted back along the incident bar necessitating a rezeroing of the bridge balance immediately prior to the test.

The complete temperature and strain rate (in terms of travelling bar velocity at impact) conditions for the dynamic fracture tests are presented in table 3.3 for the En24 steel specimens and in table 3.4 for the magnesium alloy specimens.

In addition two specimens of the En24 HC2 batch and one specimen of the En24 HC3 batch were tested on a DARTEC machine at room temperature in order to obtain measurements of the static fracture toughness. The room temperature static fracture toughness for the magnesium alloy specimens was supplied by the manufacturers (see table 3.2).

3.10. Static fracture toughness measurements of En24.

The DARTEC machine was operated in three point bend configuration using an anvil and impactor of similar design to those used with the Hopkinson pressure bar rig (HPB). The crosshead speed was set to its lowest value and

the load applied incrementally in steps of about 200 N. Graphs of load v crosshead displacement are presented in figure 3.12 for the two HC2 specimens and in figure 3.13 for the HC3 specimen.

In the case of the HC2 specimens the applied load dropped abruptly as the crack initiated but since the tests were displacement-controlled the cracks were able to arrest. The specimens were heat-tinted (by heating for 1 hour at 200°C), then chilled in liquid nitrogen and broken open in the HPB rig to discover the fracture characteristics. In both cases the cracks had run for about 1 mm across a broad front in the middle of the specimen which reduced rapidly at the extreme edges where little growth had occurred. Fracture toughness values of 37.9 $MPam^{\frac{1}{2}}$ (specimen 068) and 38.2 $MPam^{\frac{1}{2}}$ (specimen 069) were obtained using maximum load and equations (2.13) and (2.15). For a nominal yield stress, σ_Y = 1458 MPa (figure 5.6b), the minimum ligament size (equation 2.16) for a valid fracture toughness measurement from these tests is 1.7 mm which was easily satisfied.

The HC3 specimen proved to be far more ductile and the load did not drop off rapidly once maximum load had been achieved, nor was it evident from the surface that cracking had started. The specimen was again heat-tinted and broken open to reveal a short central crack which tapered at the edges. The accurate determination of crack

initiation in this case would require the testing of many specimens to different loads. Furthermore, due to the considerable plasticity developed, a valid K_{Ic} measurement could not be made and an accurate assessment of the machine compliance would be needed in order to accurately determine the characteristic J-integral. For these reasons no attempt was made to estimate the static fracture toughness of the HC3 specimen. Figure 3.13 is included to show only the level of force obtained in the static test which varies considerably from that obtained in the dynamic tests reported later.

3.11. Discussion of characteristic features of the Hopkinson Pressure Bar instrumented impact test.

The HPB data reduction technique is shown for a typical test (En24 HC2 test 059 - T = 20°C, V_0 = 1.7 m/s) in figure 3.14 with the derived force-time and velocity-time relationships given in figure 3.15.

Since the derivation of force and velocity from the S1 and S2 strain gauge measurements involves relative time shifts of the data, confidence in the accuracy of the derived values depends on the repeatability of the time shifts from test to test and their relationship to the physical features of the test apparatus. This will be

particularly true over short time periods. For longer times the even, flat-topped nature of the incident (S1) wave (see, for example, figure 3.14a) will tend to compensate for such errors in the force and velocity calculations. However, the matching of the specimen strain gauge measurement of crack initiation to the force-time trace is again intimately dependent on the accuracy of the time shifts. For these reasons the determination of all these parameters will now be discussed in detail.

It can be seen from the raw S1 and S2 data traces (figures 3.14a and 3.14b) that electronic noise makes the definition of a precise zero measurement impossible. A nominal value (Zero) was chosen by sampling the first 60 data bits for both the S1 and S2 signals. A search was then made backwards from the maximum reading to find the time on the rising portion of the S1 signal when this value (Zero1) was last registered. This time, t_{01}, was then assumed to mark the rise of the incident strain wave and was used as the datum for subsequent time shifts. A similar search backwards from the maximum reading was made to find the time at which the uncalibrated stress level (Zero + 10) was last achieved for both S1 (Merge1) and S2 (Merge2). The first time shift parameter, t_{12}, was then defined as:

$$t_{12} = \text{Merge2} - \text{Merge1} \qquad (3.16)$$

(Zero + 10) was chosen to define t_{12} since, being on the

steeply rising part of the stress wave, it is more sharply defined than (Zero). t_{12} is the time taken for the incident wave to travel from the S1 measurement position to the S2 measurement position. Its value can be predicted from the longitudinal wavespeed, c (equation 3.7), in steel and the separation L_{12} of the strain gauges S1 and S2 (figure 3.8):

$$t_{12} = \frac{L_{12}}{c} \tag{3.17}$$

The result of the time shift of S2 by $-t_{12}$ relative to S1 is shown in figure 3.14d where the signals have also been calibrated above the previously defined (Zero) levels using equation (3.5). Any misalignment of the rising portion of the traces can be attributed to a combination of discretisation errors in the resolution of the DL1080 recorder, zero error, and attenuation of the stress wave between S1 and S2. However, in general, the coincidence of the two curves is very good.

Subtraction of the time-shifted S2 trace from the S1 trace results in the reflected unloading (tensile) wave (figure 3.14e). The rise point of this wave was estimated from the time-shifted, uncalibrated S2 signal by finding the time relative to t_{01} at which the stress level (Max - 2) first occurs after the peak value (Max). This time shift, t_{232}, is the time taken for the incident wave to travel from S2 to the reflection point in the tip

region of the incident bar and then for the reflected wave to travel back to S2. The location of this reflection plane relative to the S2 strain gauge, L_{232}, can be determined from:

$$t_{232} = \frac{2L_{232}}{c} \tag{3.18}$$

and should be somewhere within the wedge-shaped profile of the tip of the incident bar.

The reflected wave (ϵ_R) was then time-shifted by $-t_{232}$ relative to the S1 trace (ϵ_I) and the force and velocity calculated from equations (3.13) and (3.14). Thus the force-time and velocity-time relationships presented in figure 3.15 pertain to the particular measurement plane defined by equation (3.18) and not the actual tip of the incident bar itself.

The rise time of the specimen strain gauge (S3) signal relative to the datum of the derived force-time relationship was then calculated as:

$$t_{03} = t_{01} + t_{12} + \frac{t_{232}}{2} \tag{3.19}$$

It will be noted from figure 3.15c that this results in an initial period of some 15 - 20 x 10^{-6} s during which no load is registered by the specimen strain gauge. A small portion of this is due to the short distance between the reflection plane and the tip of the incident bar; the rest is consistent with observations by Ireland [61] and will

be seen in chapter 4 to result from the domination of inertial behaviour in the specimen during the initial loading phase.

The S1 and S2 strain gauge separation, L_{12} = 753 mm and c = 5169 m/s, so, from equation (3.17), $t_{12} = 145.7 \times 10^{-6}$ s. The second column of table 3.5 gives the t_{12} time shifts for En24 HC2 and HC3 specimens. The mean value is 729 data bits (145.8×10^{-6} s) and 75% of the tests lie within the range 727 to 731 (total range 721 to 734). This agreement is very good and the size of variation entirely attributable to zeroing and discretisation errors.

The value of the second time shift parameter, t_{232}, is more problematic. As the loading, compressive stress wave encounters the profiled change of section of the incident bar part of it will be reflected and part transmitted. This process will continue all along the end section of the incident bar and so represents a source of error that is not accounted for in the analysis. The error will be less for a shorter profiled tip and this was the reason for selecting an included tip angle of 60° rather than the 30° recommended for the instrumented Charpy test in ASTM standard E-23 [58]. The start of the change of section was therefore located only 15 mm from the specimen. The S2 strain gauge was 166.5 mm from the specimen so the range of values of L_{232} to give part and

total reflection is:

$$151.5 \text{ mm} < L_{232} < 166.5 \text{ mm} \qquad (3.20)$$

and hence, from equation (3.18):

$$58.6 \times 10^{-6} (293) < t_{232} < 64.4 \times 10^{-6} (322) \qquad (3.21)$$

From the third column of table 3.5 the mean value of t_{232} registered in the En24 HC2 and HC3 tests was $t_{232} = 303$ samples (60.6×10^{-6} s) with 67% of tests lying within the range 298 to 308 (total range 287 to 317). $t_{232}/2$ represents the time from the first passage of ϵ_I past S2 to the instant when some of that wave is reflected. The specimen is only loaded when the remaining portion of ϵ_I reaches the tip of the profiled section. Thus, on average, the specimen is not yet loaded for the first 4×10^{-6} s of the derived force-time and velocity-time traces. The implications of this will be discussed further in chapter 4.

Having determined the relative shift of the specimen strain gauge trace (equation 3.19), it remains to define the moment of crack initiation. For the abrupt initiation of a cleavage crack in a mining steel at low temperature this has been observed to be accompanied by a large drop in the S3 reading [109]. In general there is no such large drop in the measurements for either En24 steel or the magnesium alloys presented here. The assumption that the crack initiates at the maximum specimen strain gauge reading is also suspect since this can occur a

disproportionately long time after the maximum impactor load has been realised. However, in many cases there is a sharp drop or similar feature some time before the maximum reading which coincides approximately with the maximum impactor load (at least for specimens showing reasonably elastic behaviour). The signal after this "first drop" is often noisier and less regular than prior to it, giving rise to the hypothesis that it denotes the initiation of a crack inside the specimen which later, perhaps, arrests or propagates slowly, the load being carried by the outer ligaments (and hence S3 remains partially loaded). The increased level of noise on the signal could then be due to stress waves generated by the movement of the crack. Two examples of this behaviour are shown in figures 3.16 and 3.17. These show results for En24 HC2 tests 052 and 053 at the same nominal test condition of T = 100°C and V_0 = 2.5 m/s. In both cases the "first drop" in the S3 signal (excepting some uncharacteristic noise in the case of test 052) coincides approximately with the maximum impactor load. In the case of test 053 (figure 3.17) in particular the S3 signal immediately shows a higher level of noise.

3.12. Force-time characteristics in the HPB test.

Representative force-time traces summarising the major trends in the experimental data are presented in figures 3.18 to 3.31. Only one trace is shown for each loading condition since those from repeat tests were very similar (compare, for example, figures 3.16 and 3.17 and figures 4.13a and 4.13b).

Figures 3.18 and 3.20 show the effect of test temperature on the response of En24 HC1 specimens at two different impact velocities (2.5 m/s and 3.2 m/s); figure 3.19 shows the effect of impact velocity at constant temperature (-20°C). Figure 3.21 shows the effect of test temperature on the response of En24 HC2 specimens at an impact velocity of 2.5 m/s. Comparing figures 3.18b and 3.21a demonstrates the very different response of these nominally identical materials. Figures 3.22 and 3.23 compare the behaviour of the standard Charpy specimens (L = 55 mm) with the truncated specimens (L = 45 mm) for a range of impact velocity at room temperature. Figure 3.24 shows the behaviour of the standard specimen at lower impact velocities. Figure 3.25 shows the response of the more ductile En24 HC3 specimens for a range of impact velocity at room temperature.

The temperature response of the magnesium alloys is presented at two impact velocities (figures 3.26 and 3.27

for Elektron ZCM 630-T6 and figures 3.29 and 3.30 for Elektron WE54) and their response to impact velocity at room temperature (figure 3.28 for ZCM 630-T6 and figure 3.31 for WE54).

Typically the force-time traces are oscillatory with a disproportionately large first peak. The height of this initial peak scales approximately with impact velocity independent of temperature, but is also somewhat sensitive to small changes in the time shift parameters. The peak to peak height of the subsequent oscillations is also dependent on the impact velocity (figures 3.19, 3.24, 3.25, 3.28, 3.31) and for the steel specimens some damping is observed as the test temperature increases (figures 3.18 and 3.20). Figures 3.18, 3.20, and 3.21 show the development of an extra peak as temperature increases, implying the presence of temperature-related plasticity in the steel specimens. The time period of the initial peak is longer than for the subsequent oscillations. The frequency of these later oscillations is generally similar for both the steel and the magnesium alloy specimens. The only exception is the truncated specimens which exhibit a substantially higher frequency of oscillation (figure 3.23) which is compatible with the findings of Bohme and Kalthoff [69,70]. It should also be noted that the S3 strain gauge signals from these specimens are much more oscillatory than in the equivalent measurements on

standard specimens (figure 3.22).

The assumption of crack initiation at the first sharp drop in the S3 strain gauge signal for the results from En24 HC1 and HC2 specimens (figures 3.18 to 3.24) indicates that initiation takes place at a time either just before or just after maximum impactor load. In some cases (for example, figures 3.18c and 3.19c) the maximum S3 strain gauge reading is substantially later than the maximum impactor load and the selection of the "first drop" criterion seems well justified. In test 063 (figure 3.24a) fracture occurs after a time longer than that for which a measurement of the impactor force can be made. This is possible because measurements are limited by the position of S1 and the loading pulse length is determined by the length of the travelling bar.

For the more ductile En24 HC3 specimens no such clear features are obvious on the S3 strain gauge traces (figure 3.25) and the instant of crack initiation is not clear. Note that the specimens 070 and 071 (figure 3.25a) did not fracture completely during the test, but were permanently bent. On heat tinting (for 1 hour at 200°C) and then breaking open specimen 070 at very cold temperature it was found that a 1mm long crack had been initiated and then arrested inside the specimen. The measured impactor force-time traces indicate considerable plastic deformation for all the tests on this batch of specimens.

By contrast with the steel specimens, there is no clear effect of temperature on the impactor force-time characteristics derived for the magnesium alloy Elektron ZCM 630-T6 (figures 3.26 and 3.27). This observation is reflected in the similarity of the S3 strain gauge signals. A slight raising of the impactor force-time curve with increasing temperature is observed for the magnesium alloy Elektron WE54 at low impact velocity (figure 3.29), but this effect is hardly discernible at higher velocity (figure 3.30). Again these trends are also seen in the S3 strain gauge measurements where the peak shifts to a later time as temperature increases and the reading then falls off less rapidly. However, for both alloys it is difficult to interpret the S3 strain gauge data in terms of fracture initiation. The behaviour of the magnesium alloy specimens with increasing impact velocity (figures 3.28 and 3.31) is similar to that for the steel specimens except that the size of the initial peak is proportionately much greater than the rest of the signal.

3.13. Description of the fracture surfaces.

The magnesium alloy specimens all broke cleanly with no shear lips leaving a rough, granular-looking fracture surface. The En24 HC1 and HC2 steel specimens all had much

smoother, more finely structured fracture surfaces with small shear lips at the edges which increased slightly in size with temperature. The En24 HC3 steel specimens produced distorted and pitted fracture surfaces with large shear lips (with the exception of the two specimens tested at low impact velocity which did not fracture completely).

A more detailed examination of selected fracture surfaces was carried out on the scanning electron microscope. Comparing room temperature examples of the two batches of En24 steel - HC1 and HC2 - revealed that the HC1 fracture surface (figure 3.32) was composed of 80 - 90% ductile failure with just the occasional cleavage facet, whereas the HC2 fracture surface (figure 3.33) exhibited a mixture of predominantly intergranular and cleavage fracture with only about 10% ductile voids. The effect of increasing temperature producing an increase in the proportion of ductile voids is clearly seen by comparing En24 HC2 steel fracture surfaces for test temperatures of -80°C (figure 3.34), +20°C (figure 3.33), and +100°C (figure 3.35). The distorted specimen shape for the En24 HC3 steel tested at high impact velocity is shown in figure 3.36a and a close-up of the totally ductile fracture surface in figure 3.36b.

No change in the appearance of the fracture surface with temperature was noted for the magnesium alloys. Figure 3.37 shows the characteristic intergranular

fracture surface of Elektron WE54 tested at room temperature. Figure 3.38 shows the fracture surface of Elektron ZCM 630-T6 which is obscured by the formation of (presumably) oxide on the surface, but is probably also intergranular.

TABLE 3.1. Compositional analysis and heat treatment of En24 steel specimens

En24 (AISI 4340)	Chemical composition %			
	C Carbon	Si Silicon	Mn Manganese	S Sulphur
Min.	0.35(0.38)	0.10(0.15)	0.45(0.60)	-
Max.	0.45(0.43)	0.35(0.30)	0.70(0.80)	0.05(0.04)
HC1 *	0.44	0.20	0.63	0.025
HC2 HC3 *	0.37	0.34	0.75	0.030

P Phosphorus	Ni Nickel	Cr Chromium	Mo Molybdenum
-	1.30(1.65)	0.90(0.70)	0.20(0.20)
0.05(0.035)	1.80(2.00)	1.40(0.90)	0.35(0.30)
0.005	1.52	1.14	0.24
0.026	1.42	1.40	0.20

Heat treatment according to BS 970 Part 1:

(1) Heat at 835°C for 1 hour and quench in oil bath

(2) Temper for 1 hour at the following temperature and then air cool:

(i) HC1/HC2 : 375°C (Rockwell C hardness 48)

(ii) HC3 : 560°C (Rockwell C hardness 36.5)

* Specimen compositional analysis performed by Amtac Laboratories Ltd, Altrincham.

TABLE 3.2. Compositional analysis, heat treatment, and physical properties of Mg alloy specimens.

Elektron WE54 *		Elektron ZCM 630-T6 *	
Composition		**Composition**	
Yttrium	5.0 - 5.5 %	Zinc	5.5 - 6.5 %
Heavy rare earths	1.5 - 2.0 %	Copper	2.4 - 3.0 %
Neodymium	1.5 - 2.0 %	Manganese	0.25 - 0.75 %
Zirconium	0.4 % min.	Iron	0.05 % max.
Magnesium base		Magnesium balance	
Heat treatment		**Heat treatment**	
Solution heat treat for 8 hours at 525°C. Hot water or polymer quench. Age for 16 hours at 250°C.		8 hours at 440°C. Hot water quench. 16-24 hours at 180-200°C. Air cool.	
Physical properties (20°C)		**Physical properties** (20°C)	
Density	1850 kg/m^3	Density	1840 kg/m^3
Proof stress 0.1% / 0.2%	177 MN/m^2 200 MN/m^2	Proof stress 0.1% / 0.2%	125 MN/m^2 143 MN/m^2
Tensile strength	250-255 MN/m^2	Tensile strength	210-225 MN/m^2
Fracture toughness	11.4 MNm$^{-1.5}$	Fracture toughness	16.5 MNm$^{-1.5}$

* Data provided by Magnesium Elektron Ltd.

TABLE 3.3. En24 test conditions.

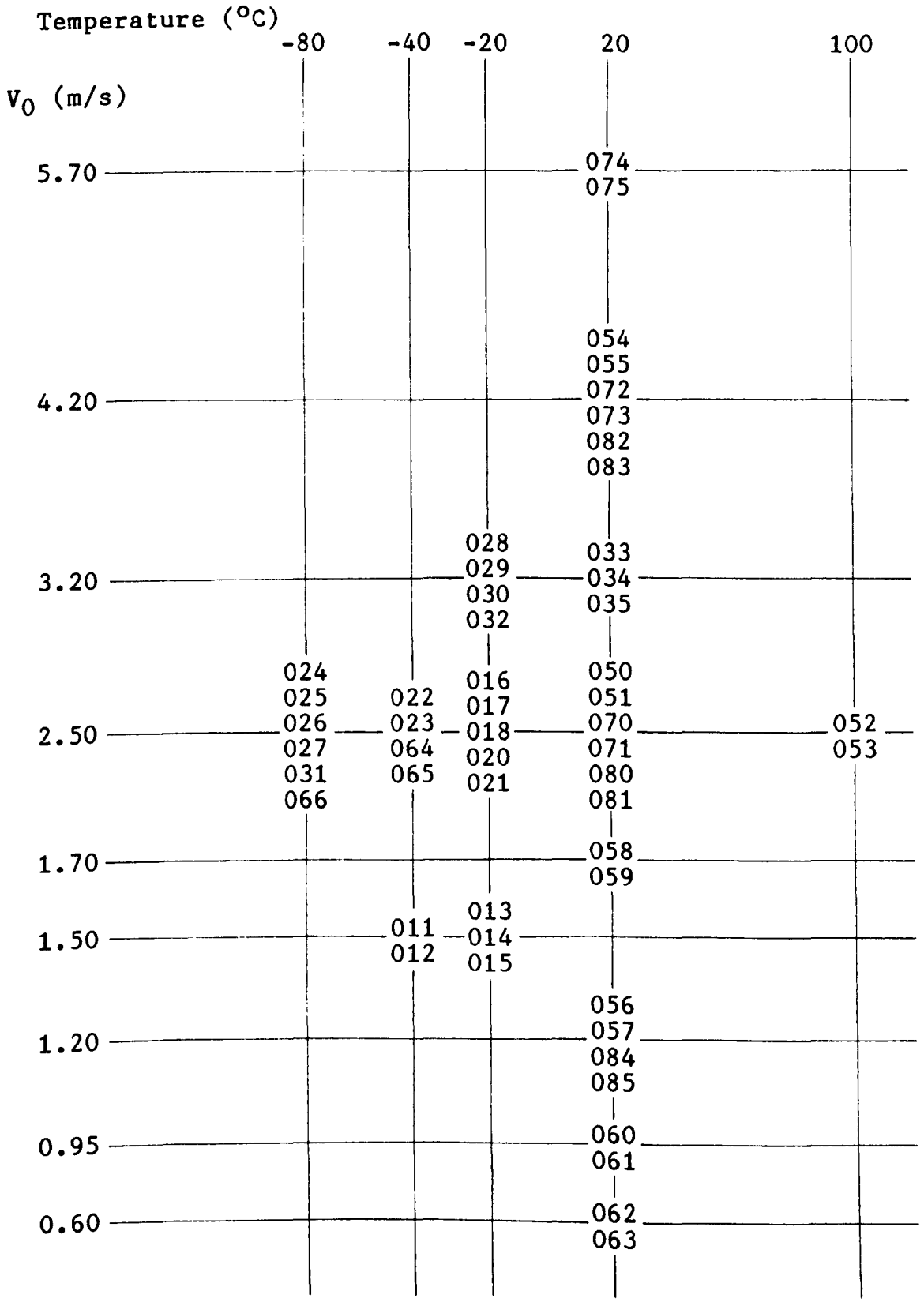

(table 3.3 continued)

Key :

01-, 02-, 03-	En24 HC1 (375°C temper - first batch)
05-, 06-	En24 HC2 (375°C temper - second batch)
08-	En24 HC2 (375°C temper - second batch) (truncated specimens)
07-	En24 HC3 (560°C temper - second batch)

TABLE 3.4. Magnesium alloy test conditions.

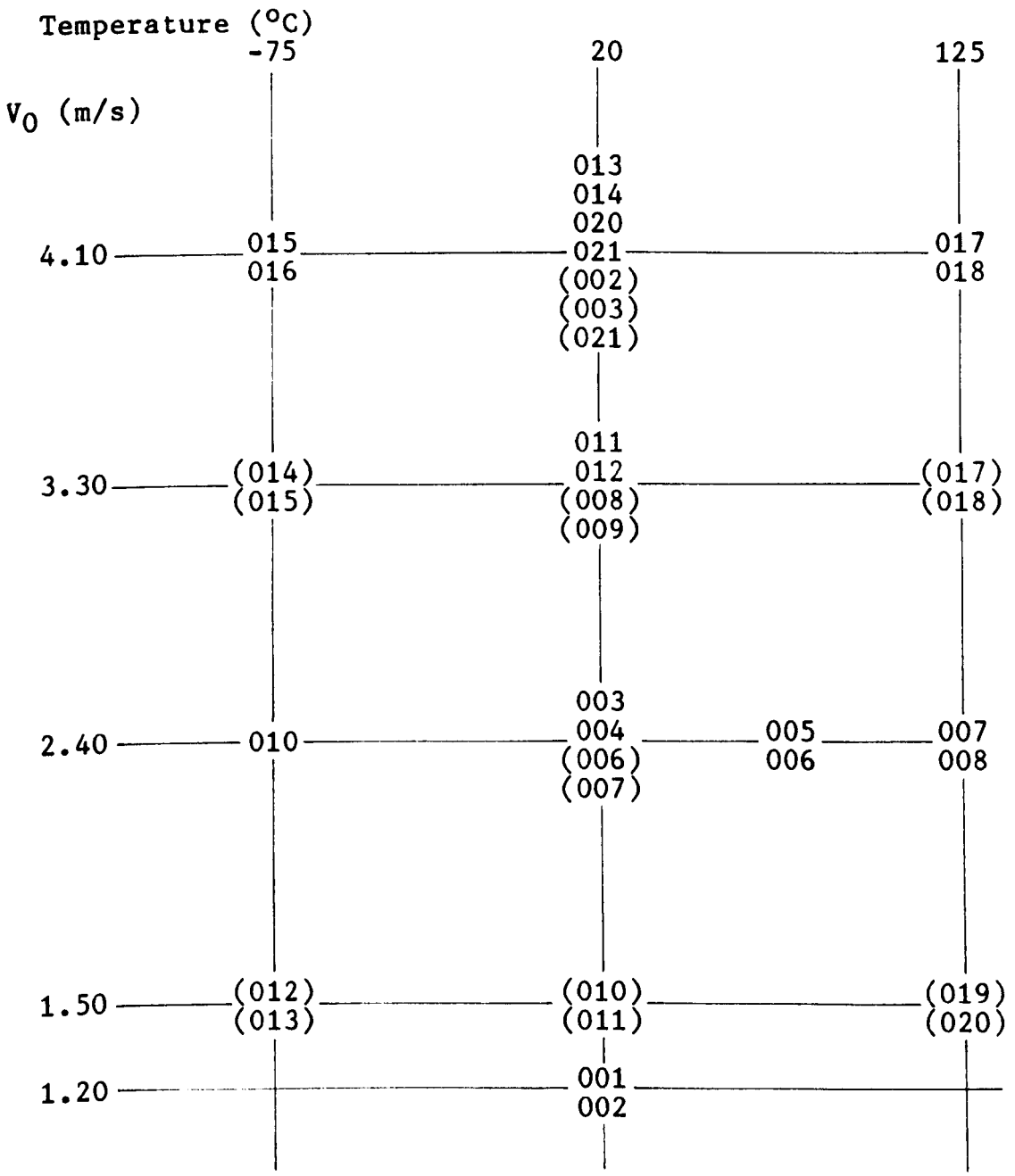

Key : ZCM 630-T6
(WE54)

TABLE 3.5. t_{12} and t_{232} time shift data for En24 HC2/HC3.

Test No.	t_{12} (bits)	t_{232} (bits)
050	728	305
051	732	296
052	728	311
053	728	300
054	730	302
055	729	307
056	733	308
057	734	301
058	724	302
059	729	317
060	729	287
061	730	289
062	722	300
063	721	300
064	727	306
065	730	298
066	727	305
070	727	303
071	728	308
072	729	306
073	728	311
074	729	301
075	730	309
080	729	307
081	728	304
082	728	298
083	730	313
084	728	292
085	734	308

N.B. 1 data bit = 0.2×10^{-6} s

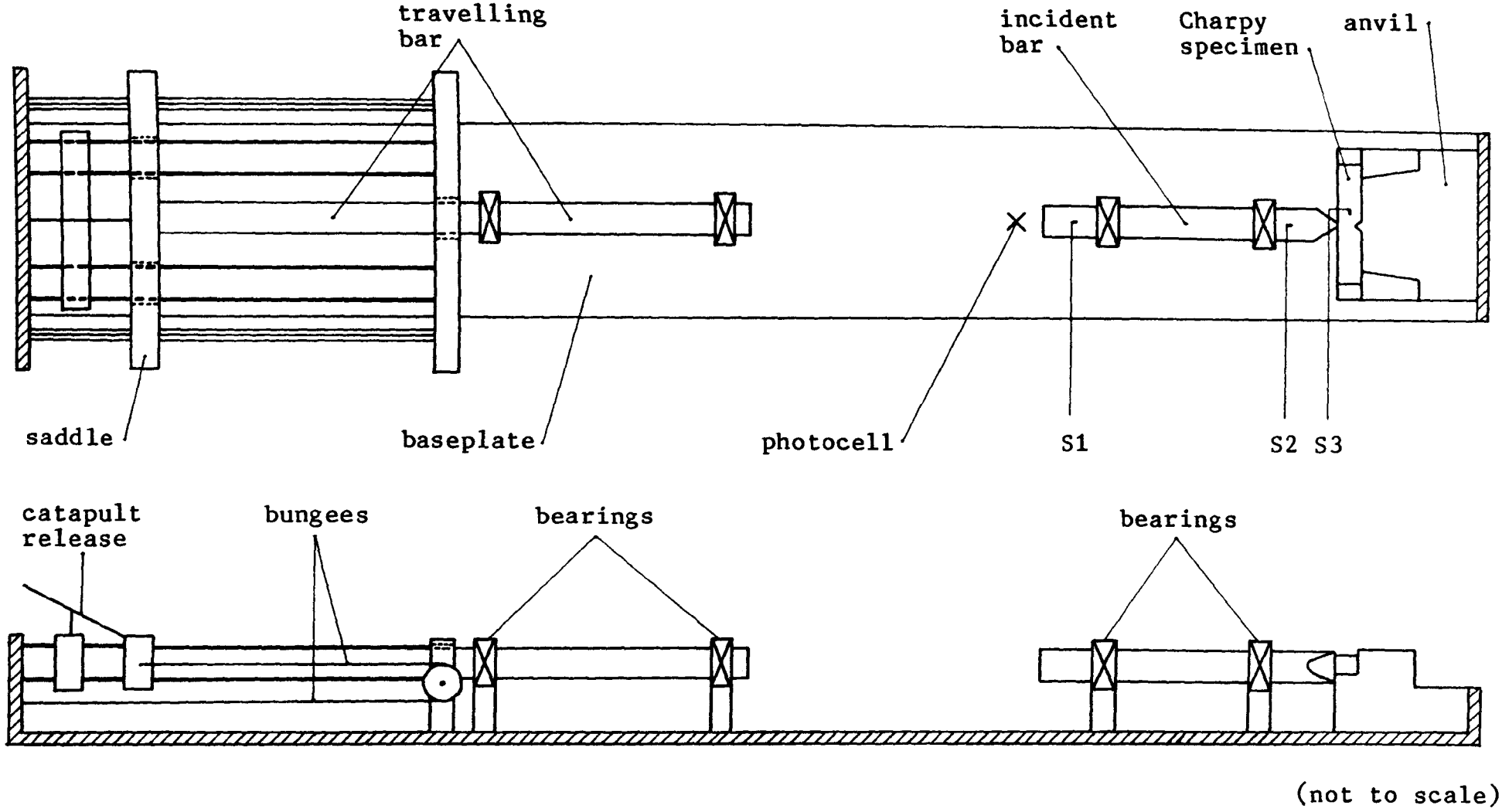

FIG. 3.1. General arrangement of apparatus: the Hopkinson pressure bar instrumented impact rig.

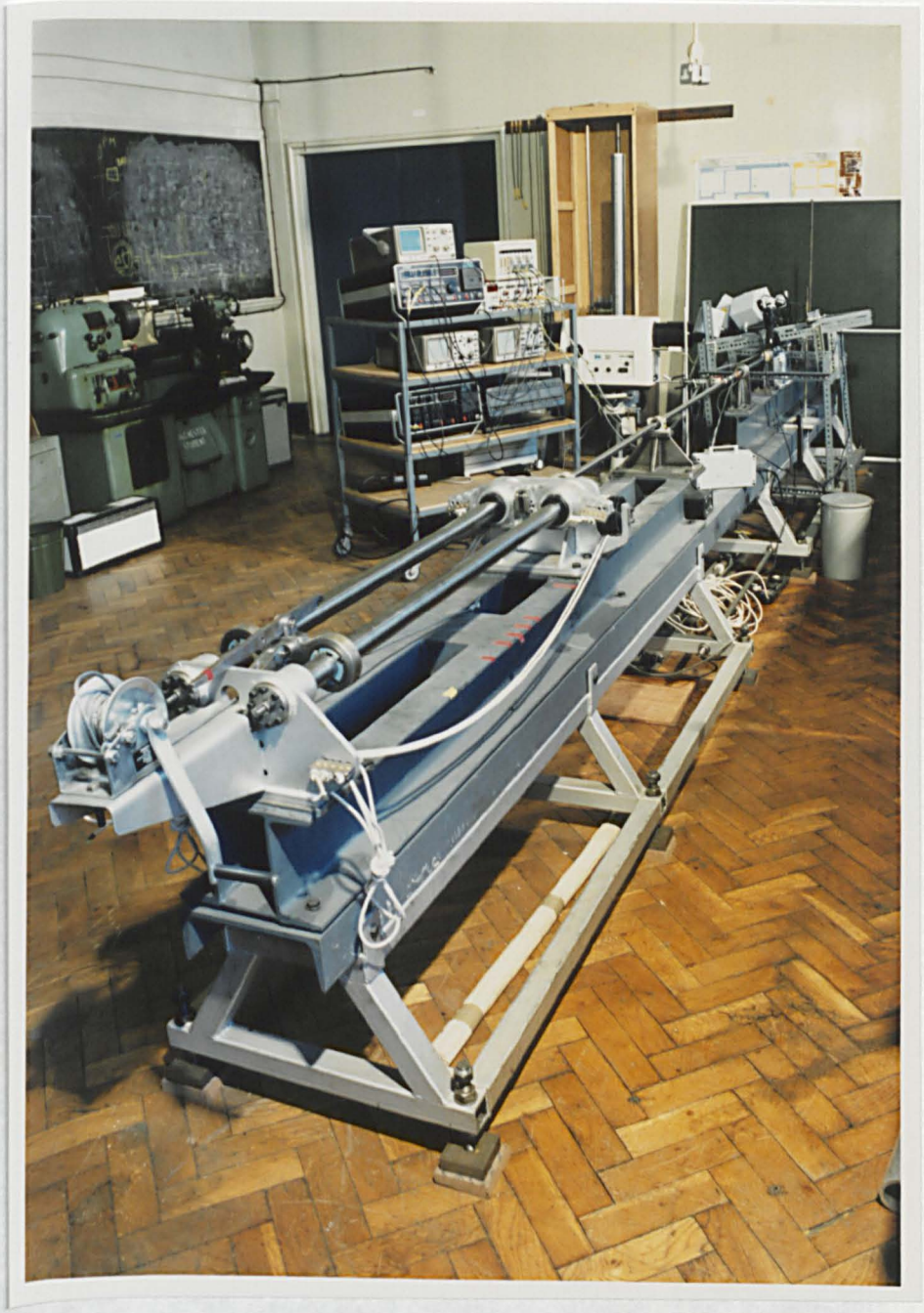

FIG. 3.2. The Hopkinson pressure bar instrumented impact rig: general view of catapult system, travelling bar, incident bar, and instrumentation.

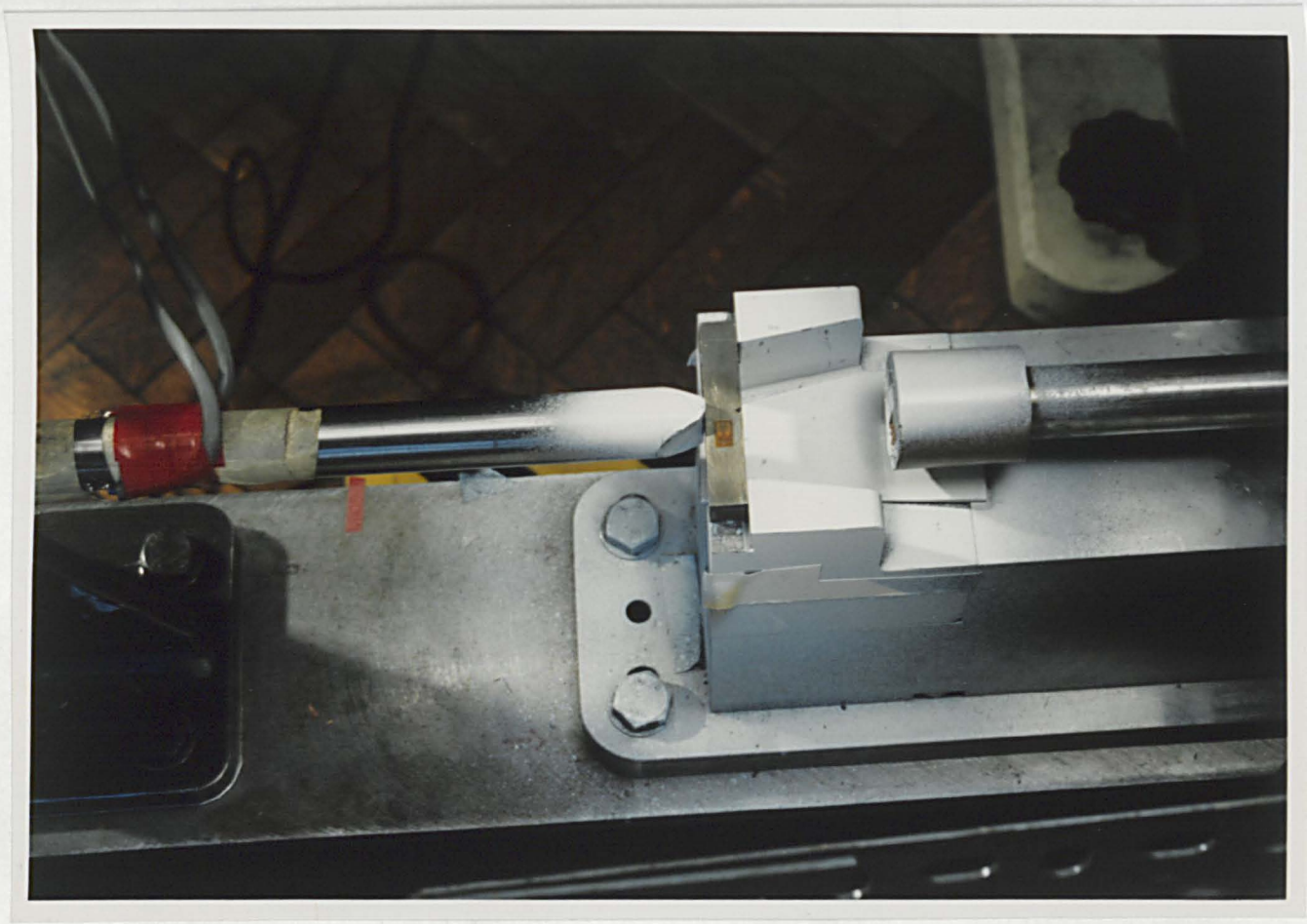

FIG. 3.3. The Hopkinson pressure bar instrumented impact rig: close-up of Charpy specimen, incident bar, and anvil.

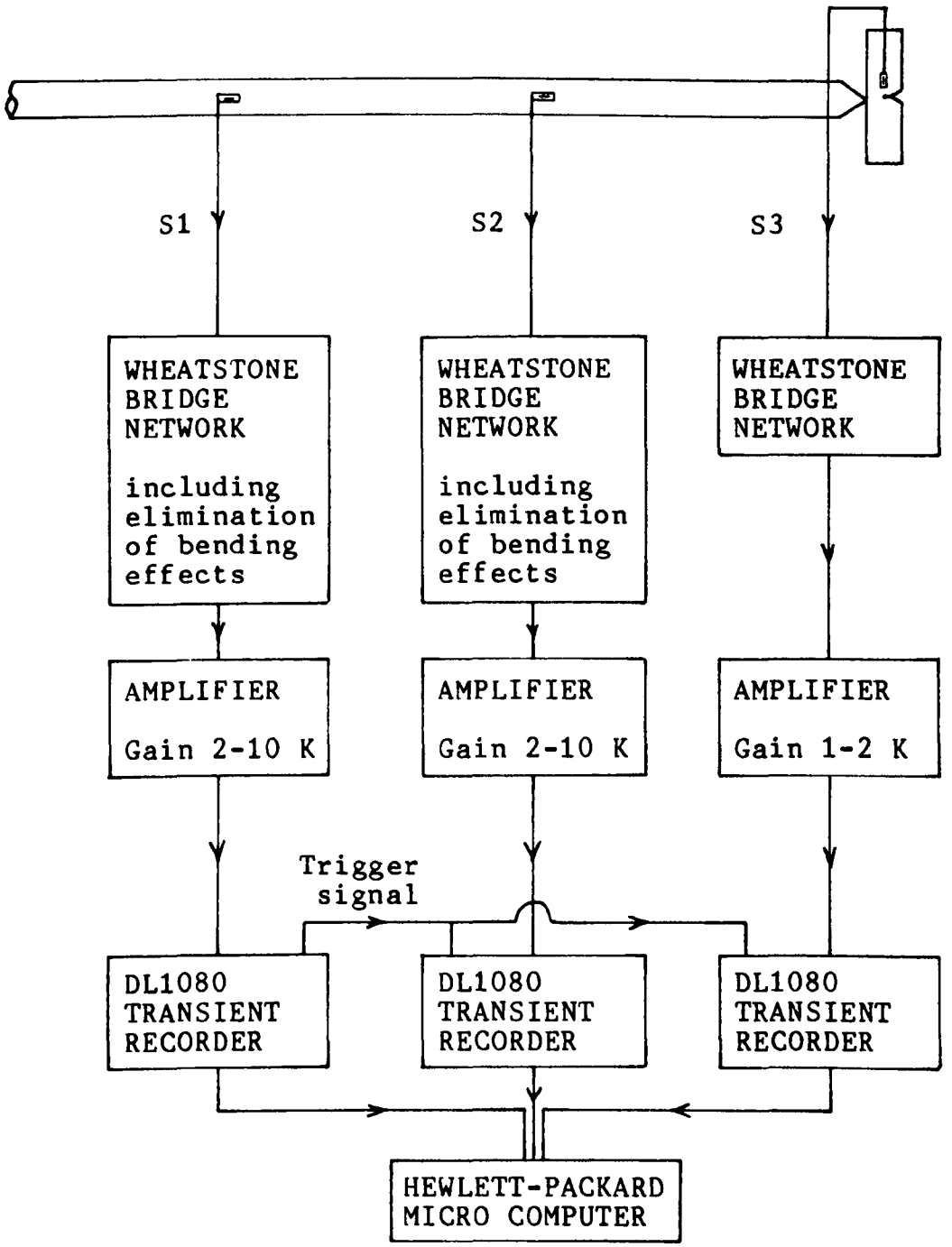

FIG. 3.4. Flow diagram of instrumentation and data recording/analysis system.

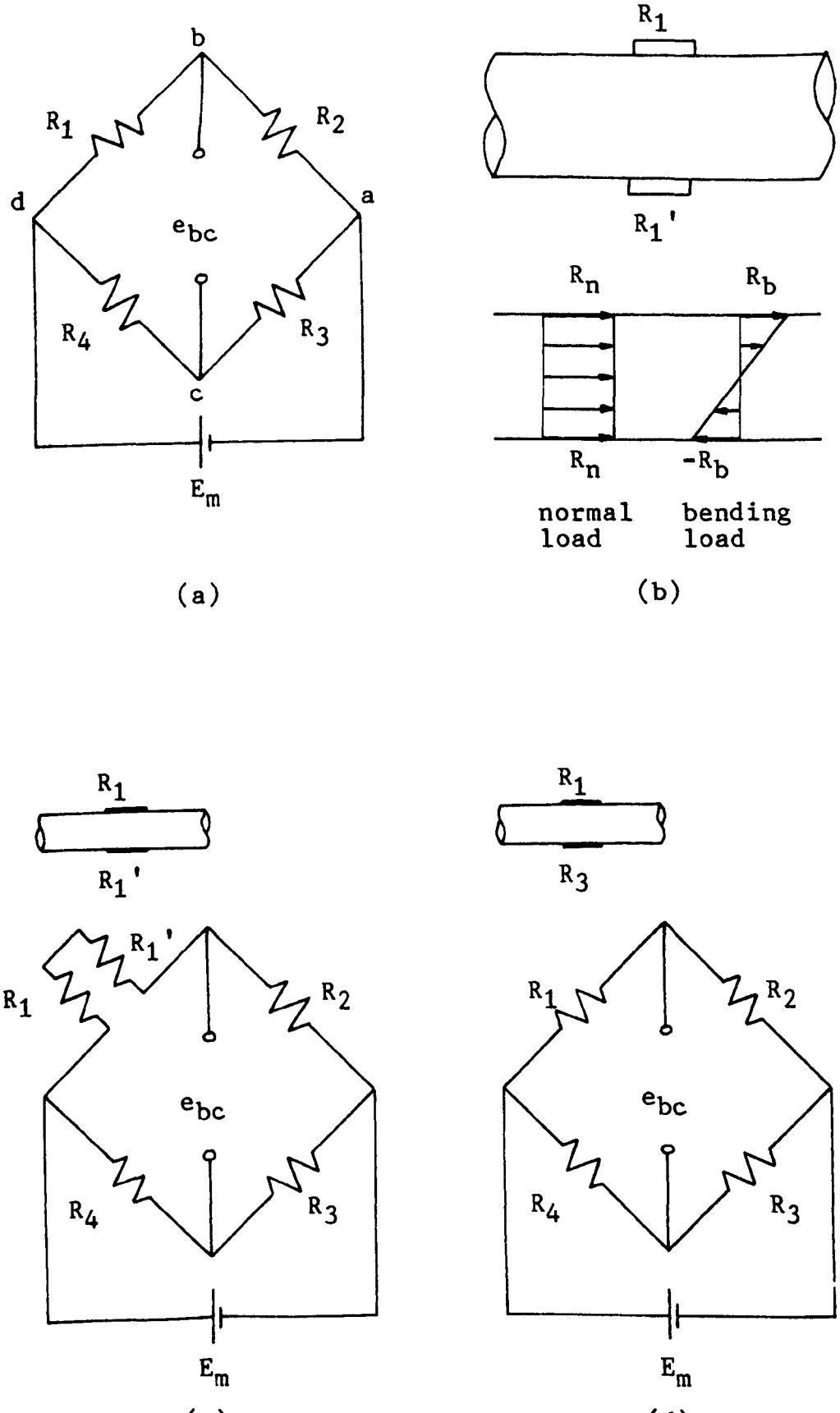

FIG. 3.5. Wheatstone bridge networks for elimination of bending stresses in the incident bar [99].

initial velocity	V_0	0
final velocity	V_1	V_2
area of cross-section	A_1	A_2

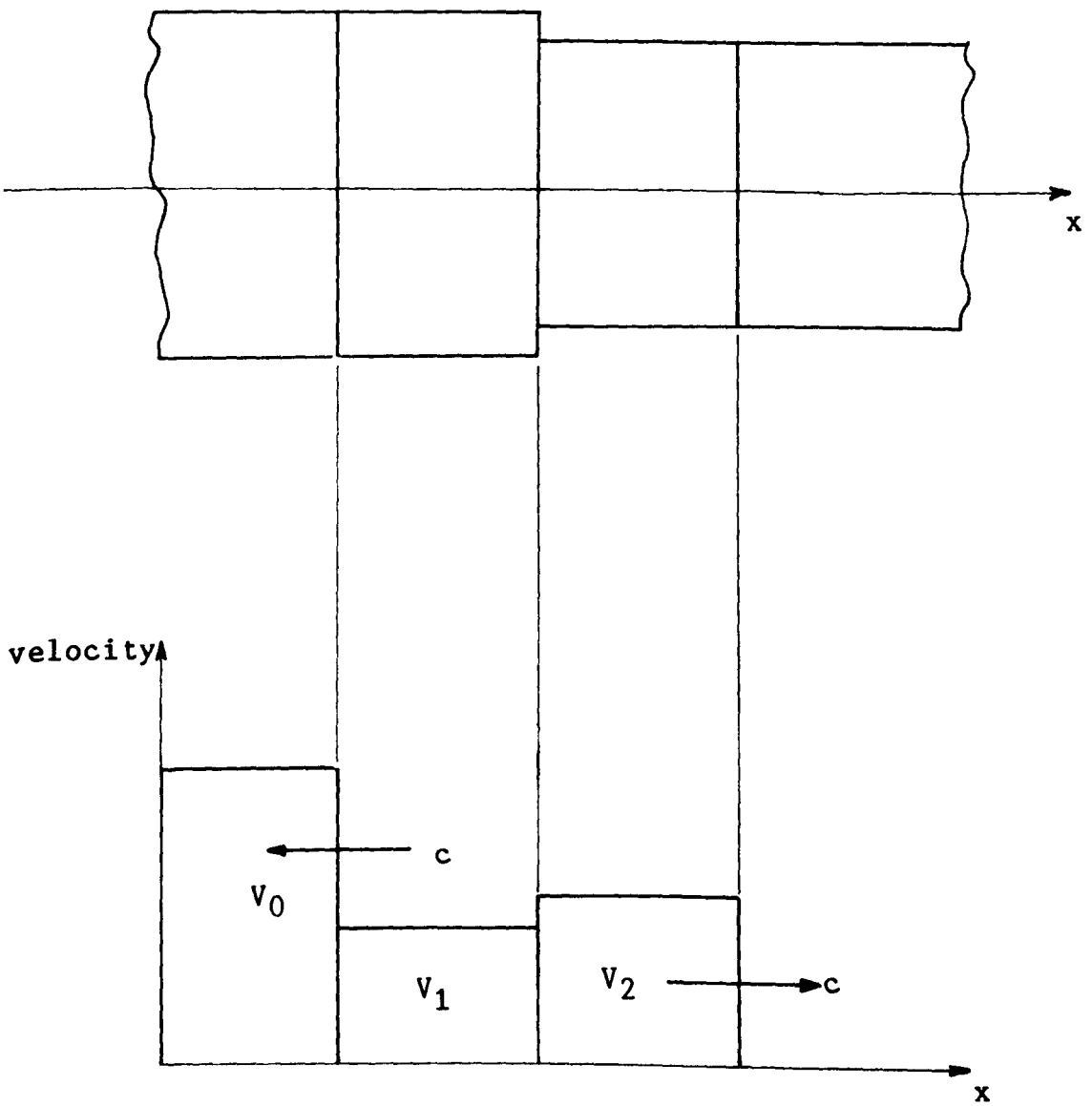

FIG. 3.6. The collision of two bars of different cross-sectional area.

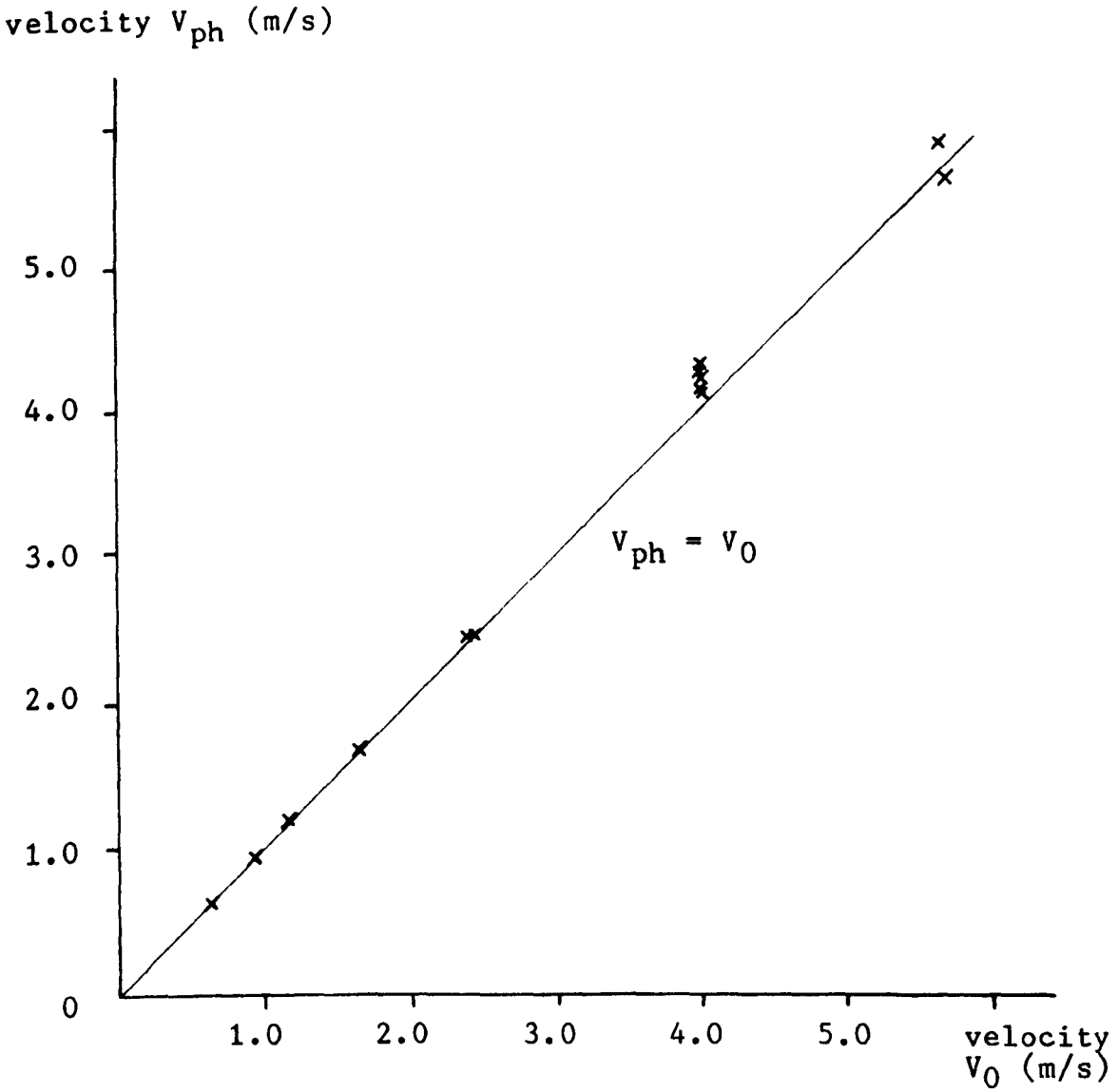

FIG. 3.7. Velocity of impact bar calculated from strain gauge measurement S1 (V_0) calibrated against photocell (V_{ph}).

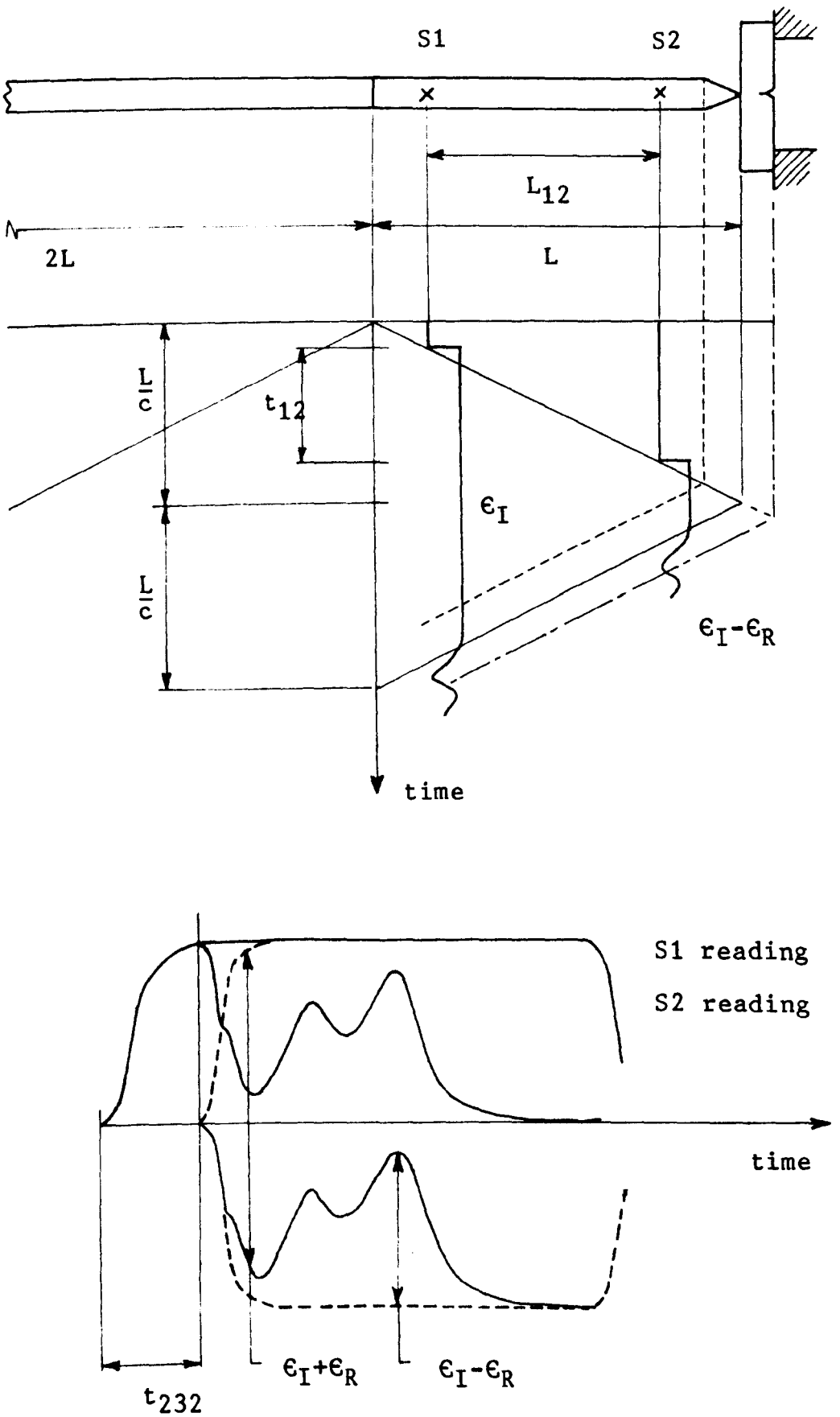

FIG. 3.8. Stress wave mechanics of the Hopkinson pressure bar rig (adapted from [97]).

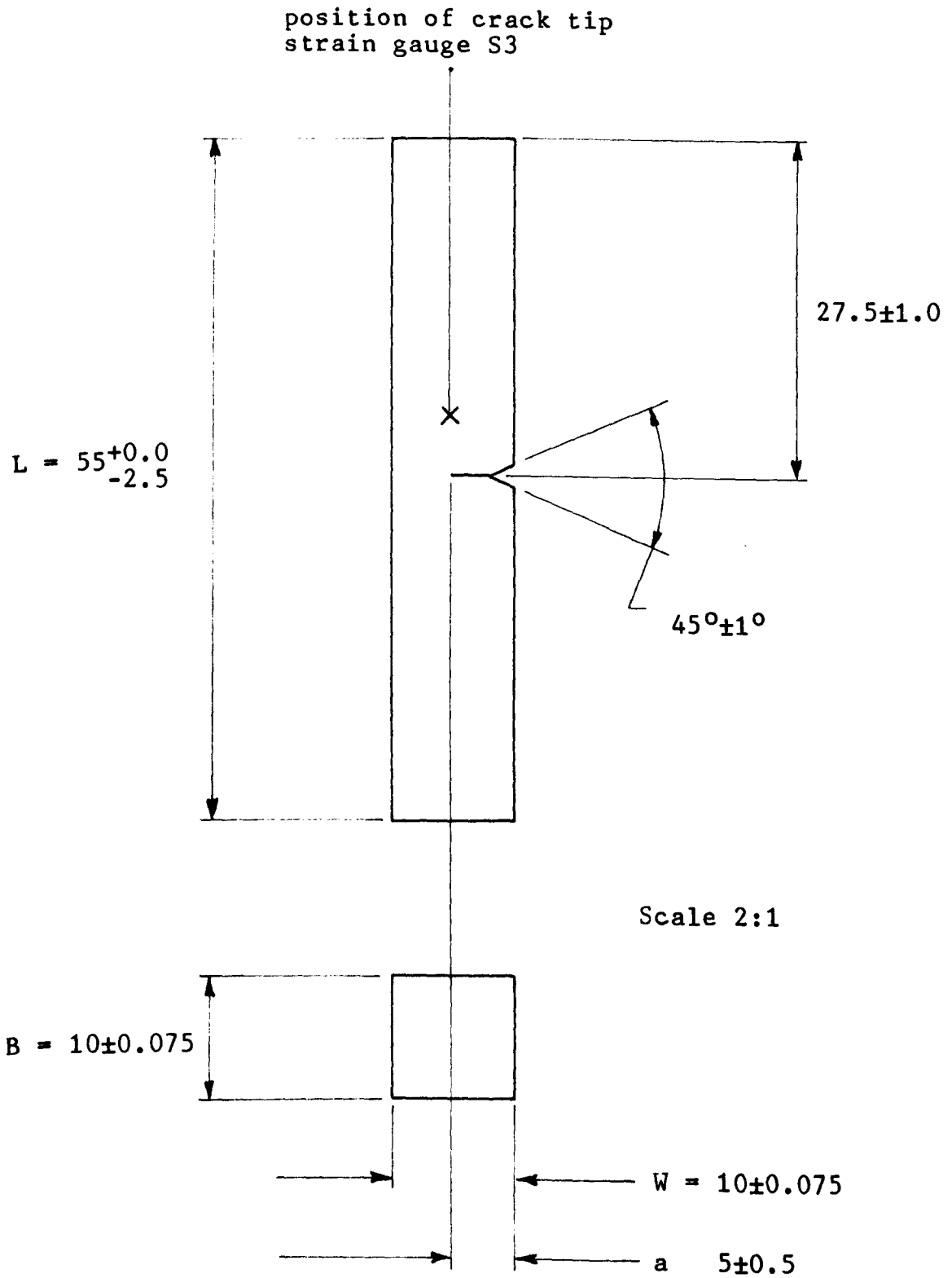

FIG. 3.9. Charpy test specimen showing position of the crack tip strain gauge S3.

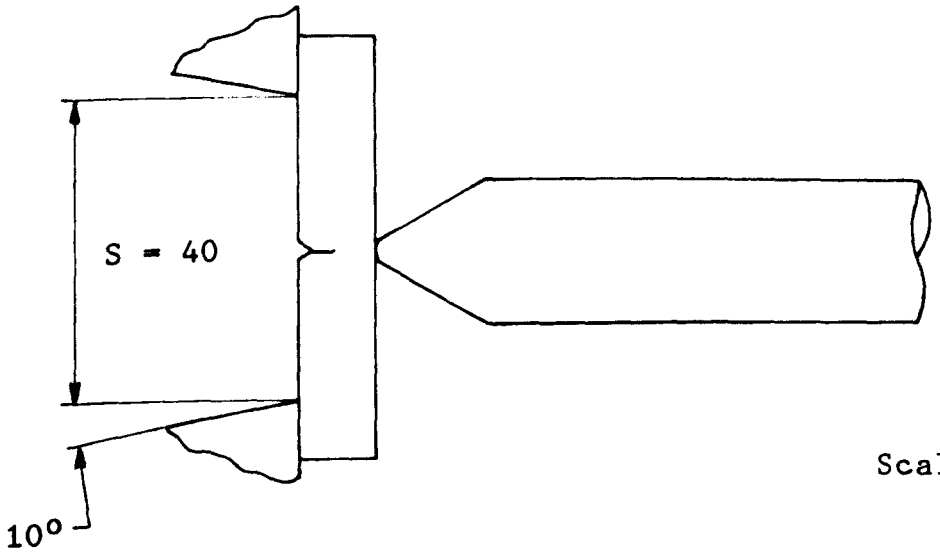

(a)

Scale 1:1

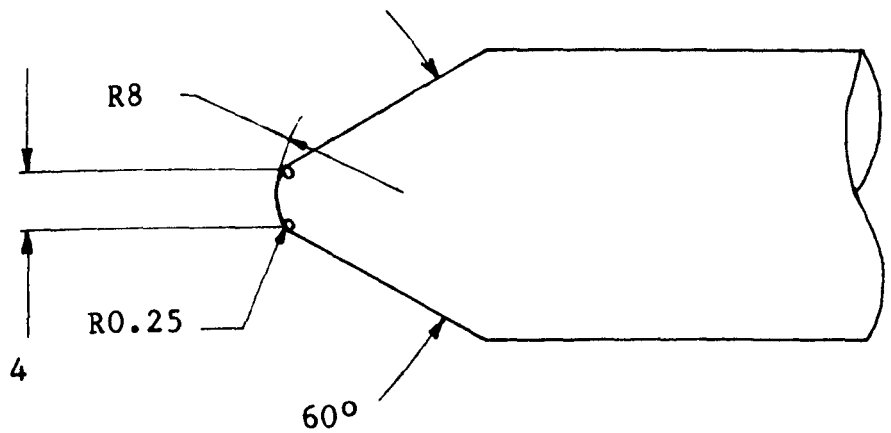

(b)

Scale 2:1

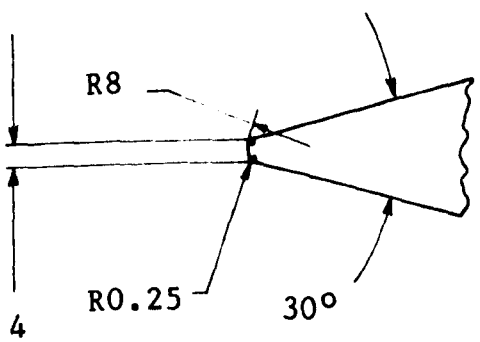

(c)

Scale 1:1

FIG. 3.10. Detail of specimen support (a) and the profiled end of the incident bar (b) compared with the standard Charpy hammer (c).

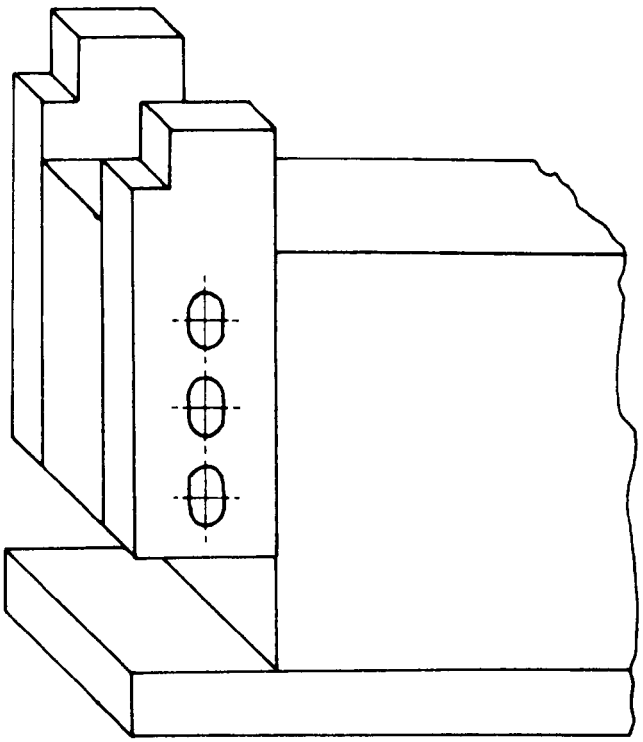

FIG. 3.11a. Original anvil with two adjustable jaws.

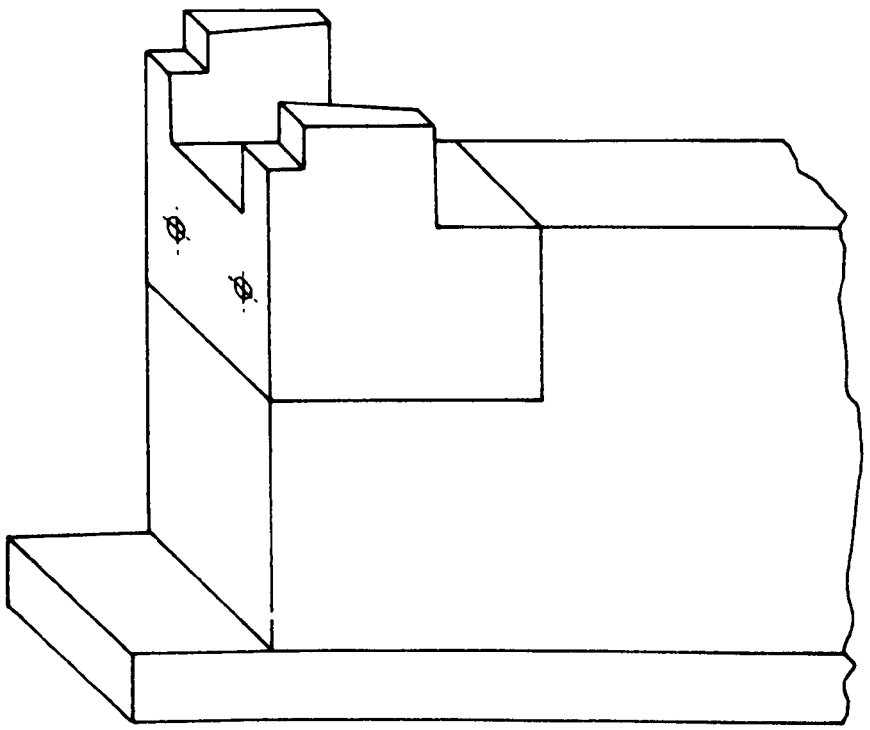

FIG. 3.11b. Second anvil with a single rigid block bolted to the base anvil.

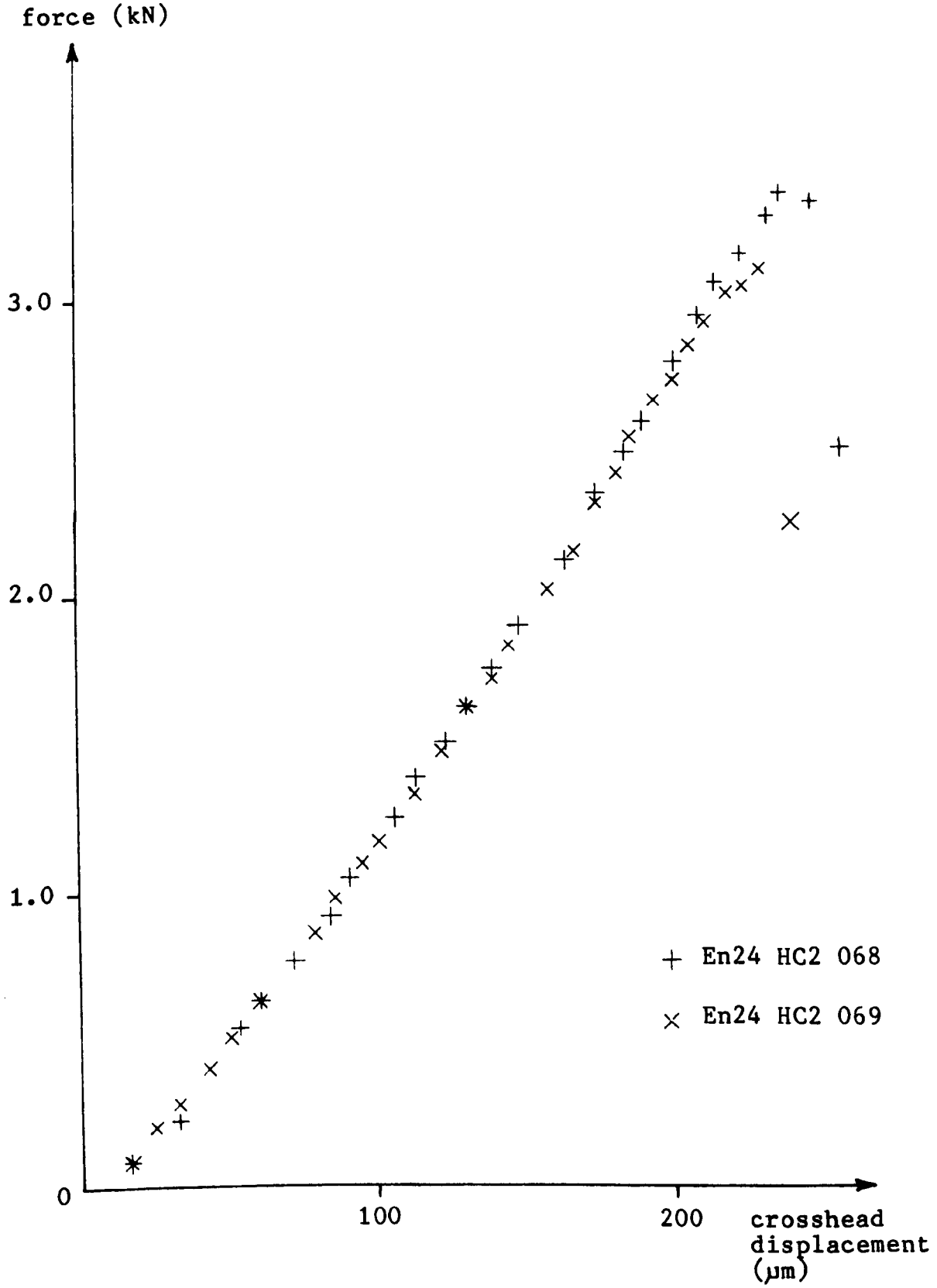

FIG. 3.12. Incremental load-displacement tests (En24 HC2).

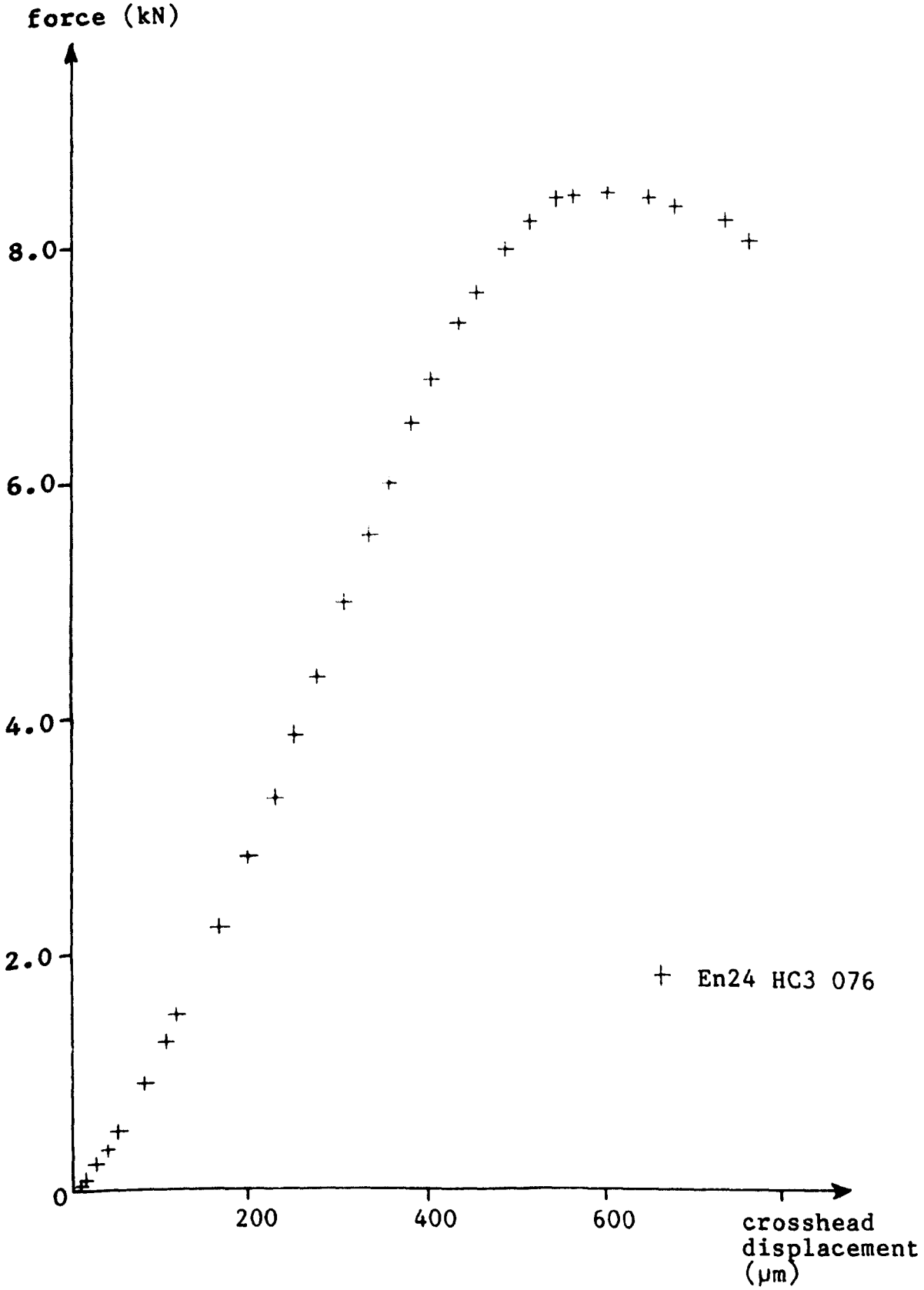

FIG. 3.13. Incremental load-displacement test (En24 HC3).

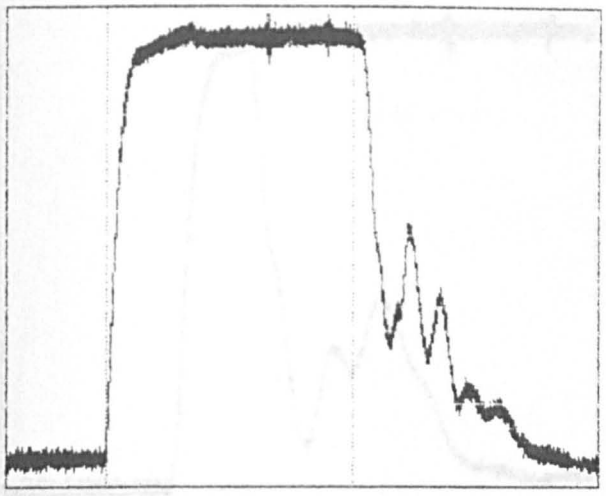

FIG. 3.14a.

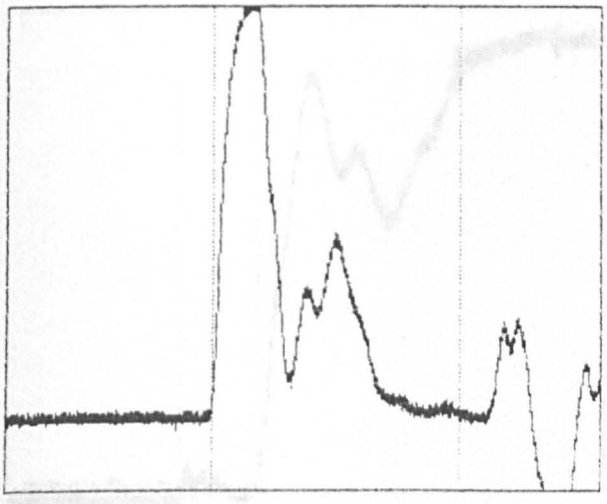

FIG. 3.14b.

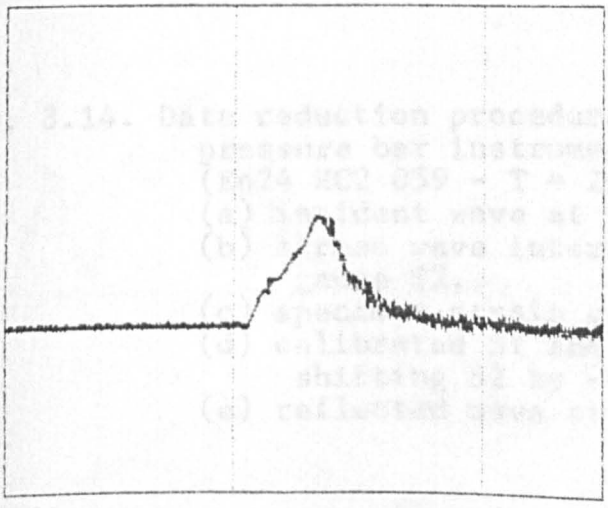

FIG. 3.14c.

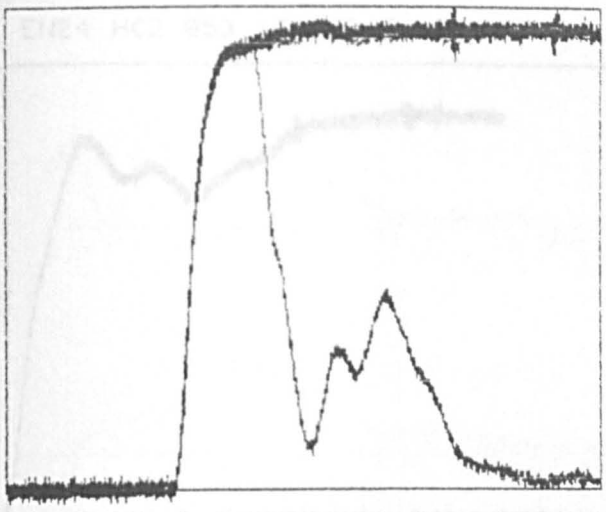

FIG. 3.14d.

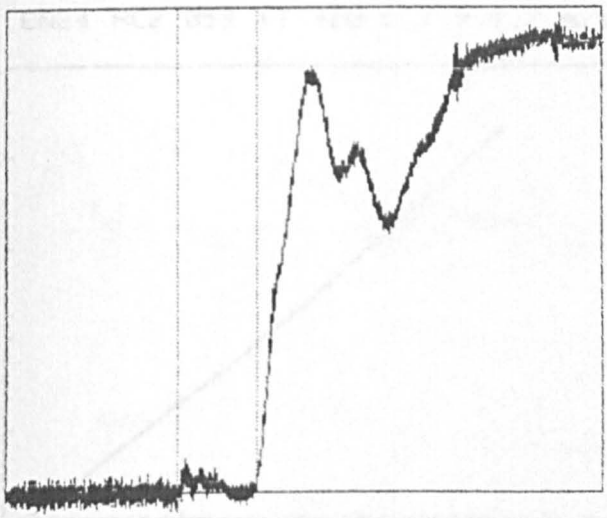

FIG. 3.14e.

FIG. 3.14. Data reduction procedure for the Hopkinson pressure bar instrumented impact test (En24 HC2 059 - T = 20°C : V_0 = 1.7 m/s):
(a) incident wave at strain gauge S1,
(b) stress wave interaction at strain gauge S2,
(c) specimen strain gauge measurement S3,
(d) calibrated S1 and S2 signals aligned by shifting S2 by $-t_{12}$ relative to S1,
(e) reflected wave at tip of incident bar.

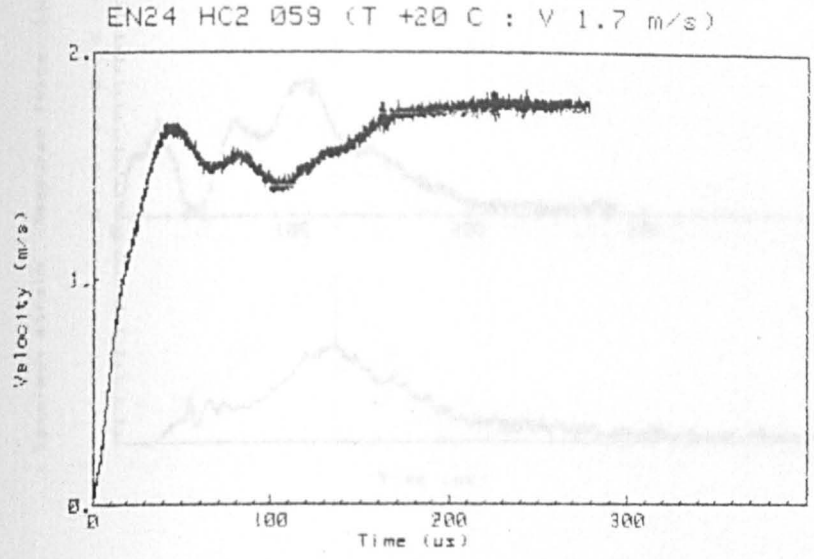

FIG. 3.15a.

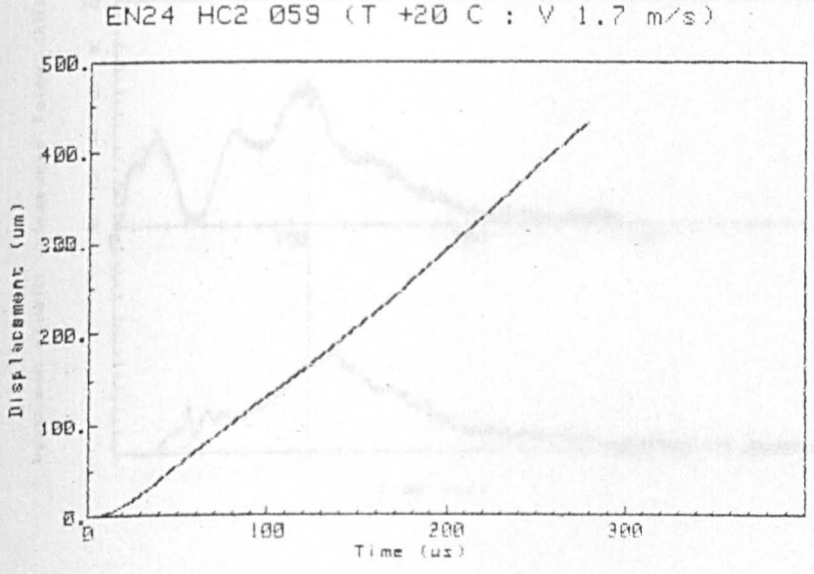

FIG. 3.15b.

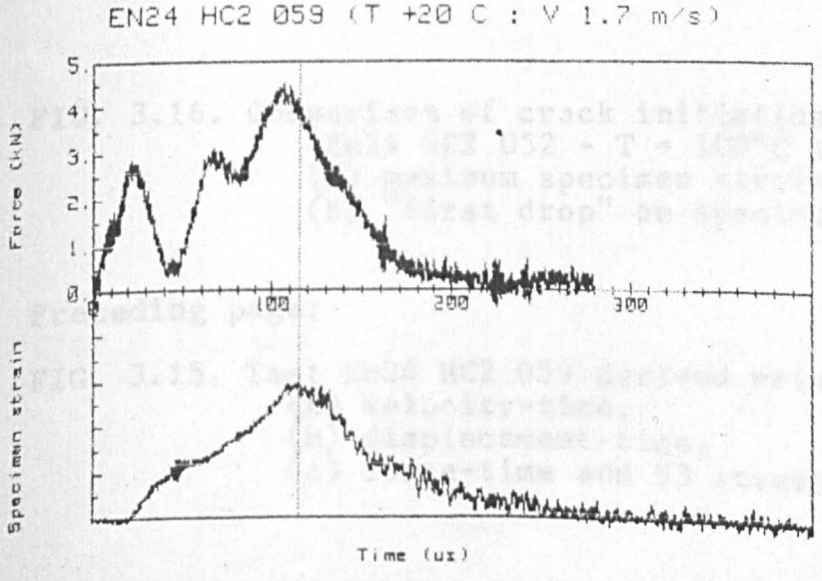

FIG. 3.15c.

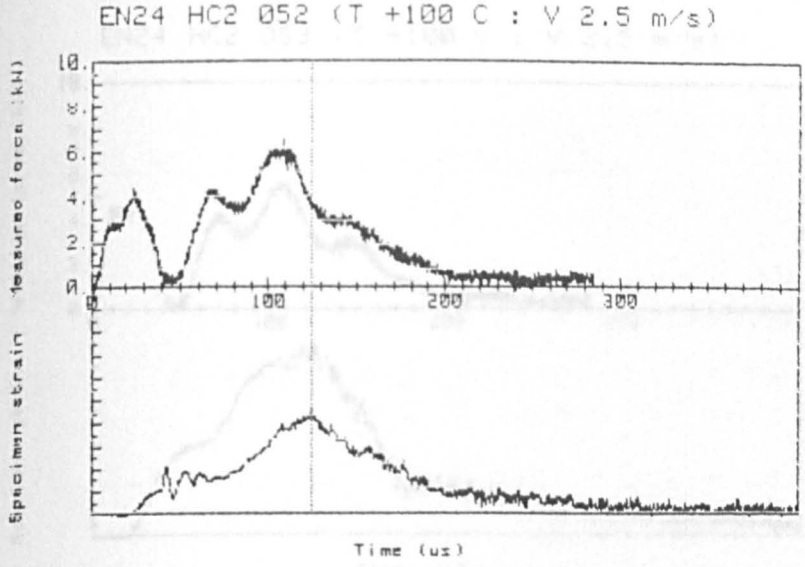

FIG. 3.16a.

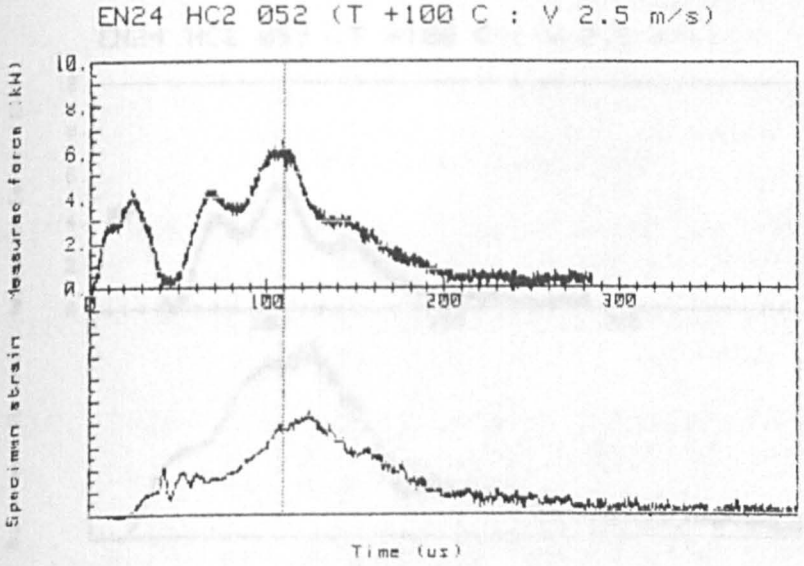

FIG. 3.16b.

FIG. 3.16. Comparison of crack initiation criteria (En24 HC2 052 - T = 100°C : V_0 = 2.5 m/s): (a) maximum specimen strain gauge reading, (b) "first drop" on specimen strain gauge.

Preceding page:

FIG. 3.15. Test En24 HC2 059 derived relationships: (a) velocity-time, (b) displacement-time, (c) force-time and S3 strain-time.

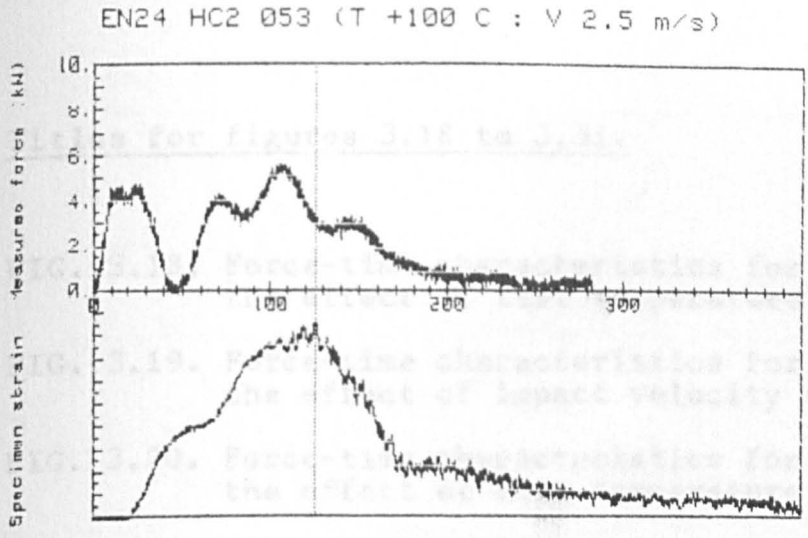

FIG. 3.17a.

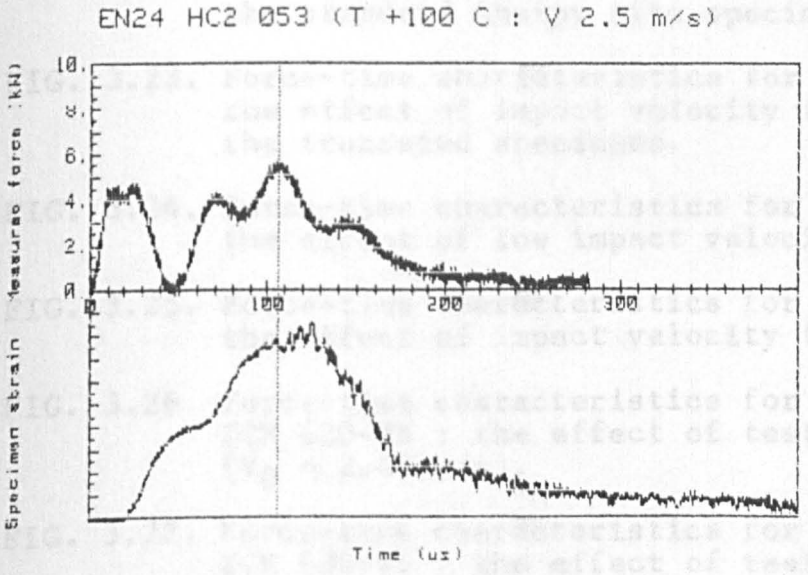

FIG. 3.17b.

FIG. 3.17. Comparison of crack initiation criteria (En24 HC2 053 - T = 100°C : V_0 = 2.5 m/s): (a) maximum specimen strain gauge reading, (b) "first drop" on specimen strain gauge.

Titles for figures 3.18 to 3.31.

FIG. 3.18. Force-time characteristics for En24 HC1 : the effect of test temperature (V_0 = 2.50 m/s).

FIG. 3.19. Force-time characteristics for En24 HC1 : the effect of impact velocity (T = -20°C).

FIG. 3.20. Force-time characteristics for En24 HC1 : the effect of test temperature (V_0 = 3.20 m/s).

FIG. 3.21. Force-time characteristics for En24 HC2 : the effect of test temperature (V_0 = 2.50 m/s).

FIG. 3.22. Force-time characteristics for En24 HC2 : the effect of impact velocity (T = 20°C) in the standard Charpy size specimens.

FIG. 3.23. Force-time characteristics for En24 HC2 : the effect of impact velocity (T = 20°C) in the truncated specimens.

FIG. 3.24. Force-time characteristics for En24 HC2 : the effect of low impact velocities (T = 20°C).

FIG. 3.25. Force-time characteristics for En24 HC3 : the effect of impact velocity (T = 20°C).

FIG. 3.26. Force-time characteristics for magnesium alloy ZCM 630-T6 : the effect of test temperature (V_0 = 2.40 m/s).

FIG. 3.27. Force-time characteristics for magnesium alloy ZCM 630-T6 : the effect of test temperature (V_0 = 4.10 m/s).

FIG. 3.28. Force-time characteristics for magnesium alloy ZCM 630-T6 : the effect of impact velocity (T = 20°C).

FIG. 3.29. Force-time characteristics for magnesium alloy WE54 : the effect of test temperature (V_0 = 1.50 m/s).

FIG. 3.30. Force-time characteristics for magnesium alloy WE54 : the effect of test temperature (V_0 = 3.30 m/s).

FIG. 3.31. Force-time characteristics for magnesium alloy WE54 : the effect of impact velocity (T = 20°C).

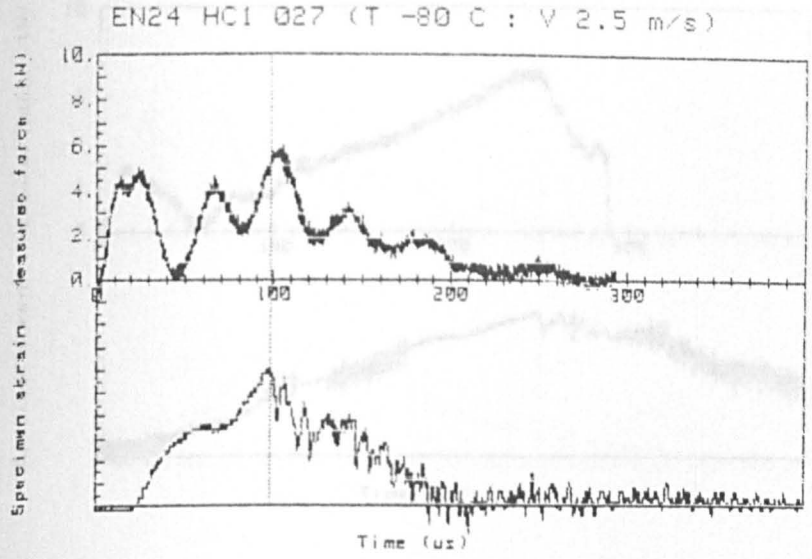

FIG. 3.18a.

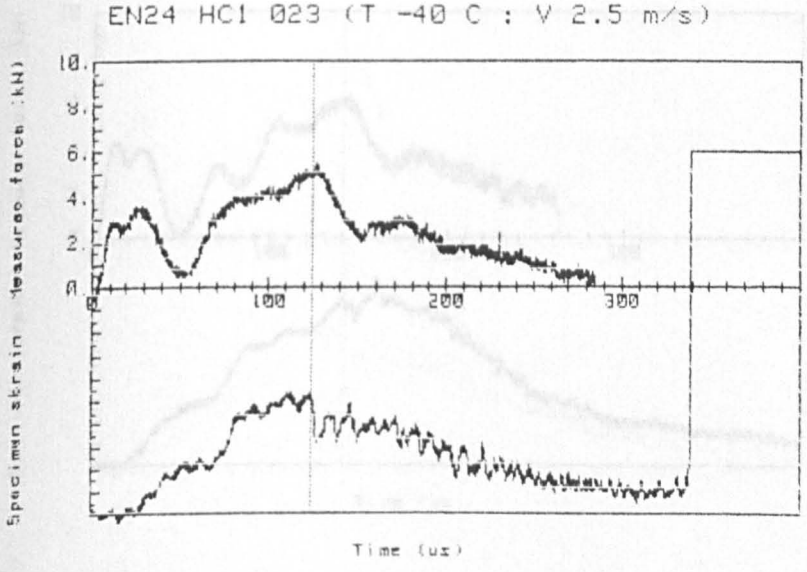

FIG. 3.18b.

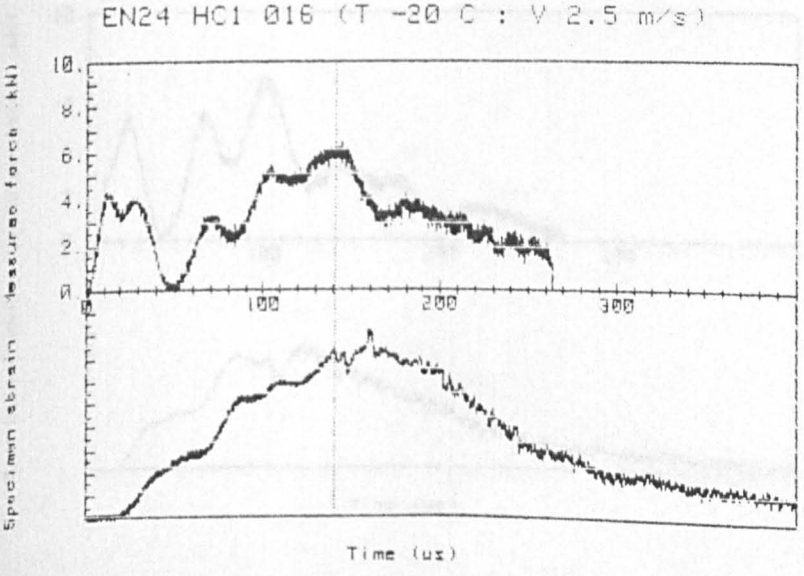

FIG. 3.18c.

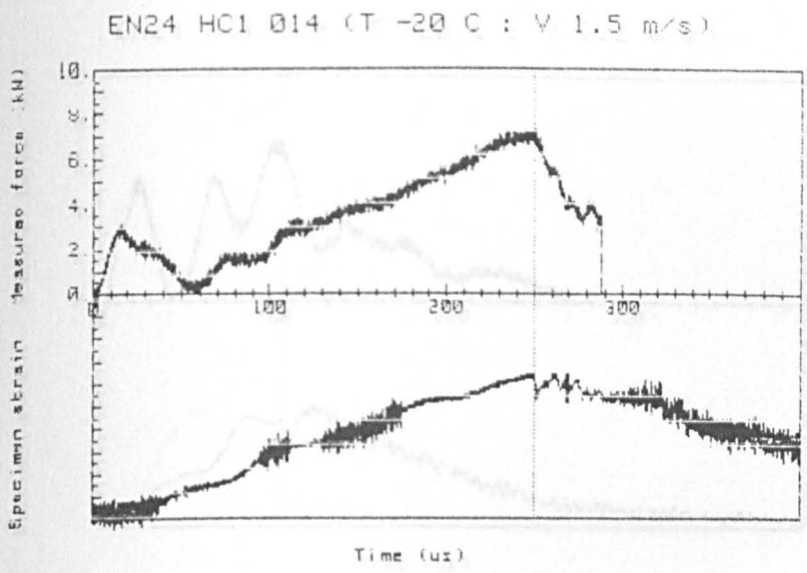

FIG. 3.19a.

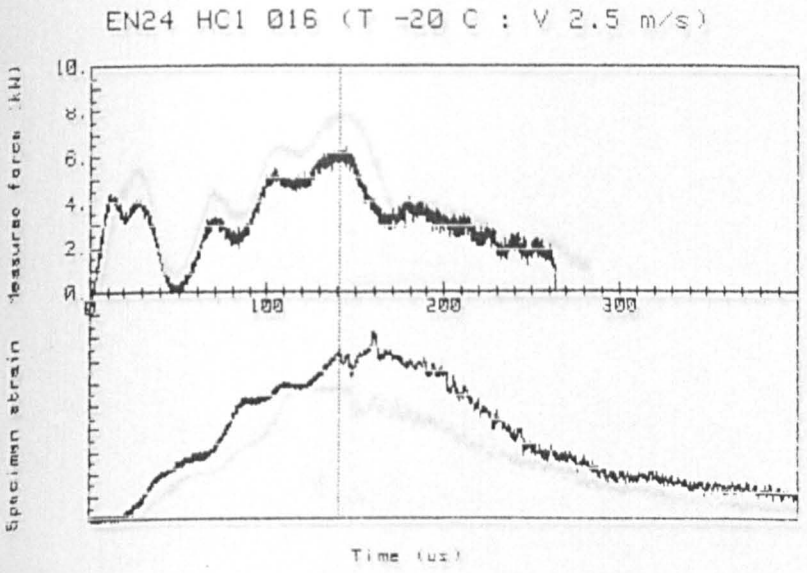

FIG. 3.19b.

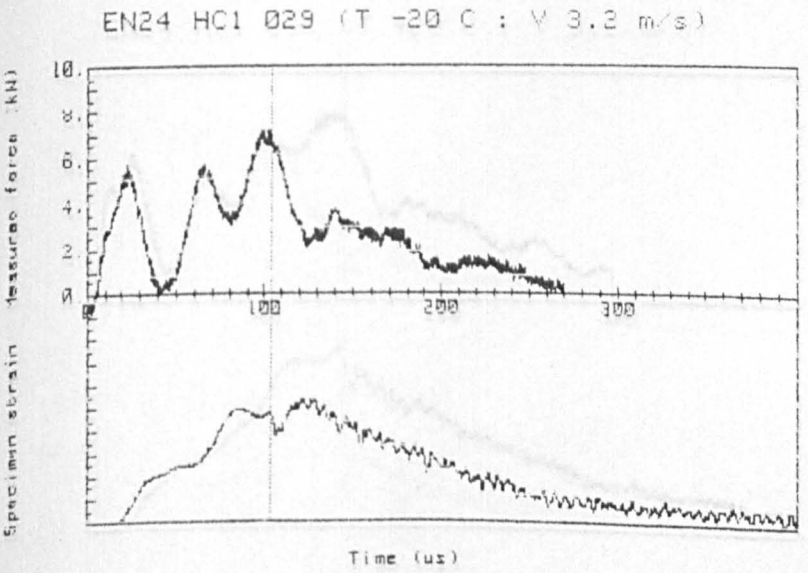

FIG. 3.19c.

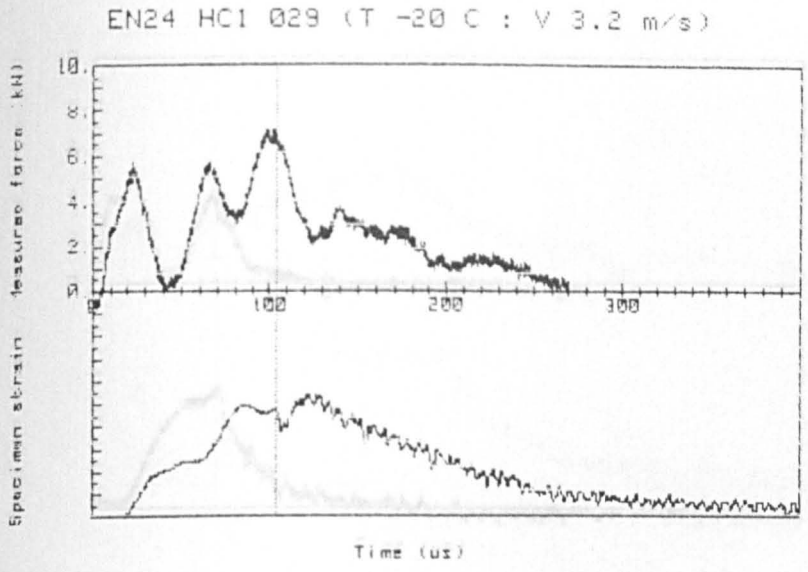

FIG. 3.20a.

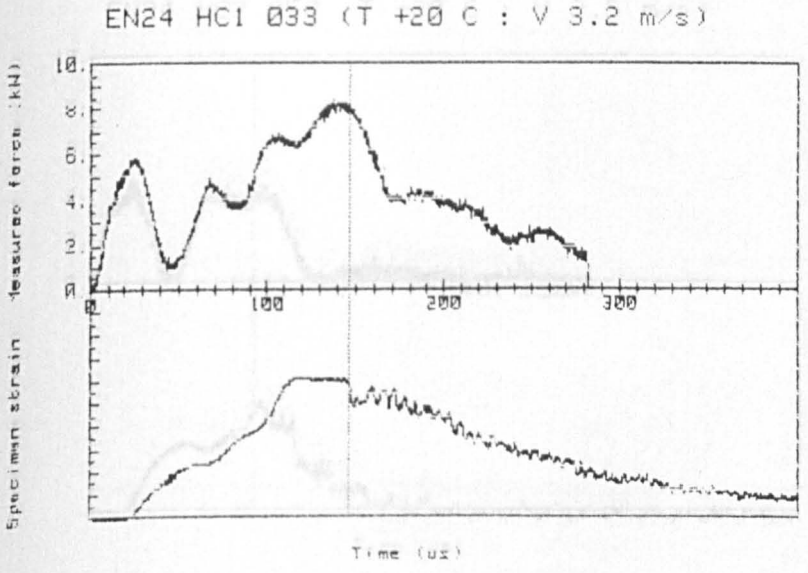

FIG. 3.20b.

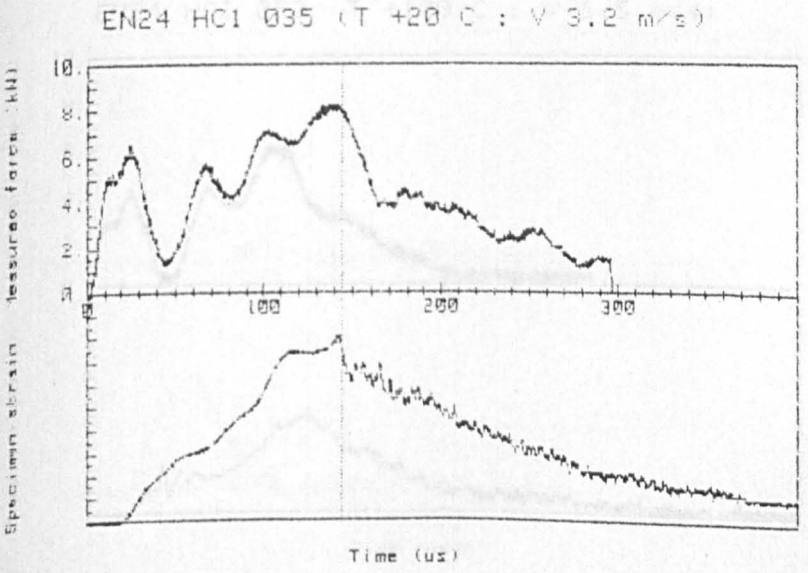

FIG. 3.20c.

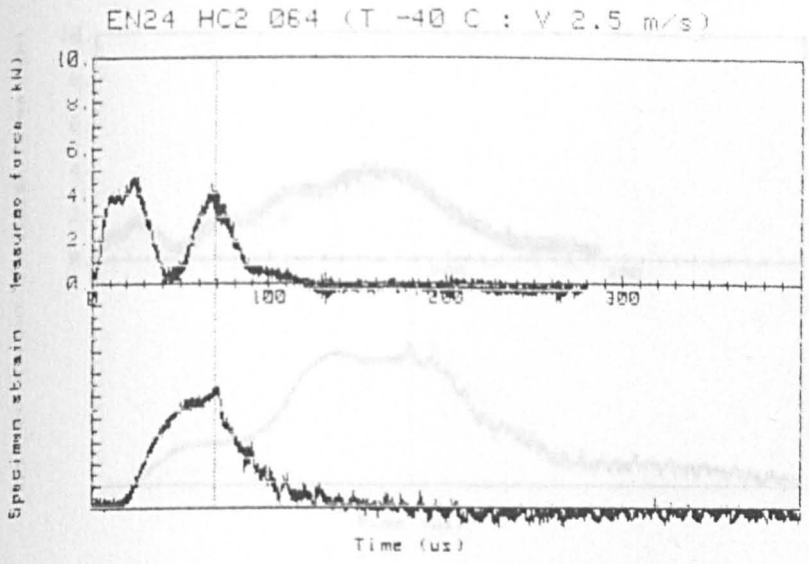

FIG. 3.21a.

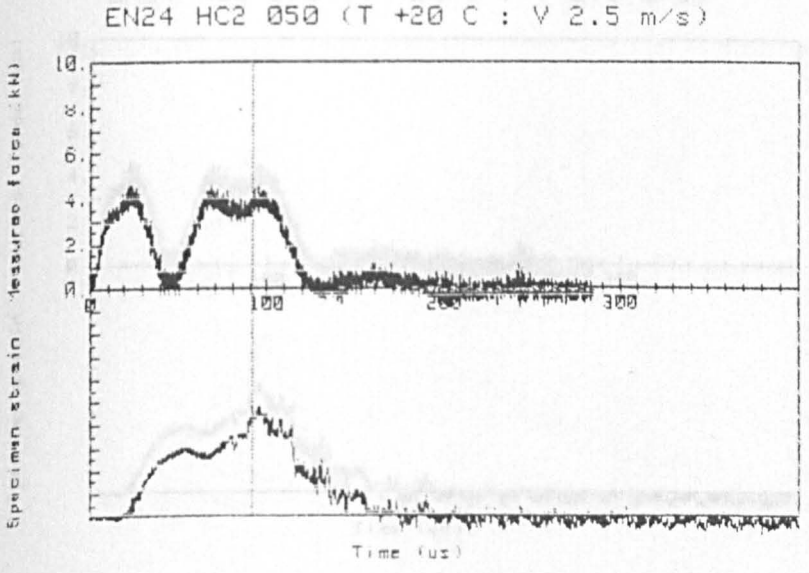

FIG. 3.21b.

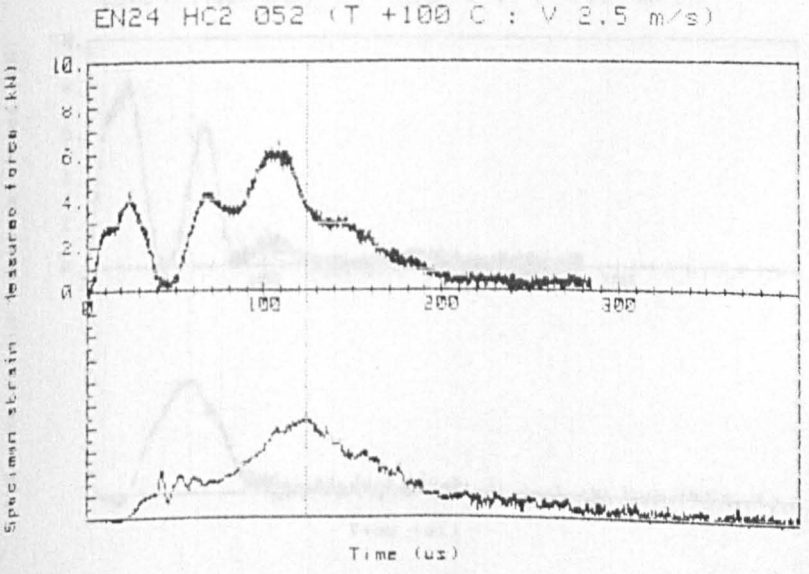

FIG. 3.21c.

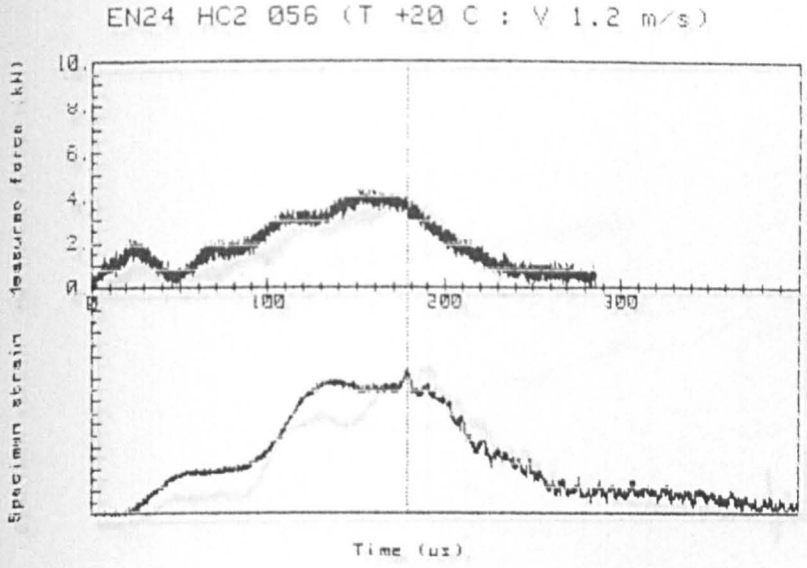

FIG. 3.22a.

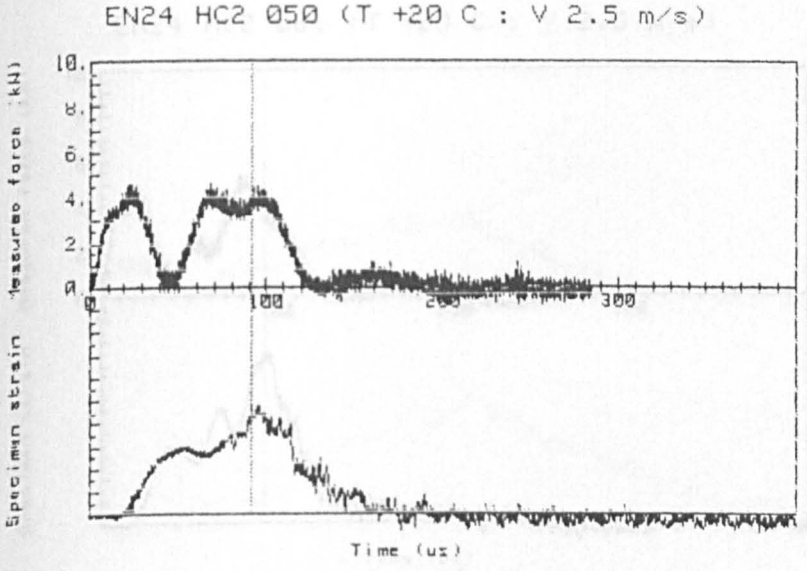

FIG. 3.22b.

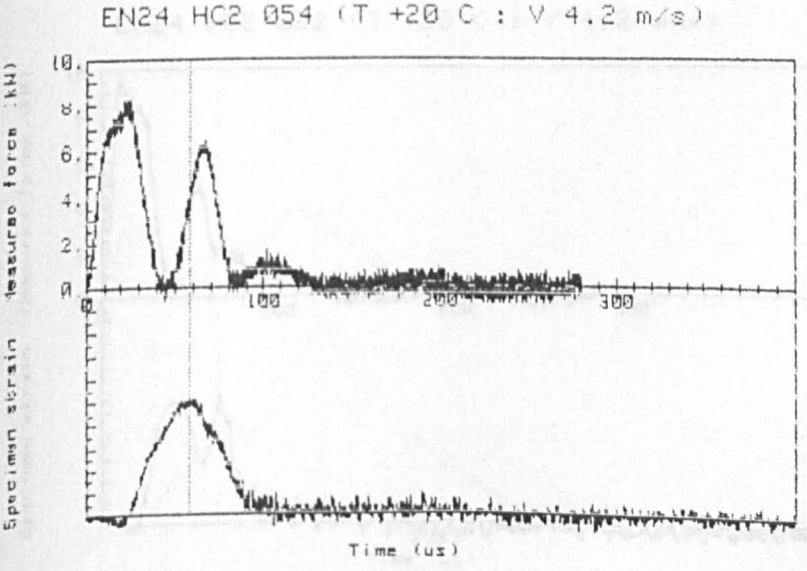

FIG. 3.22c.

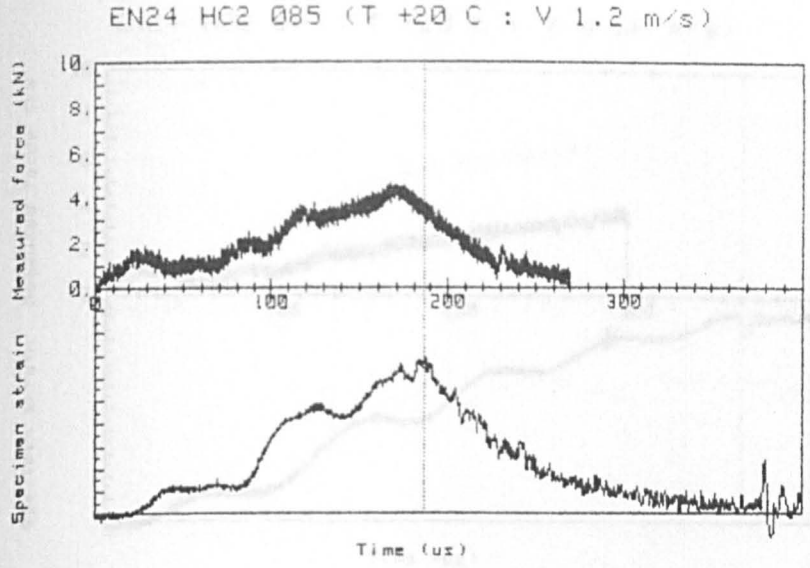

FIG. 3.23a.

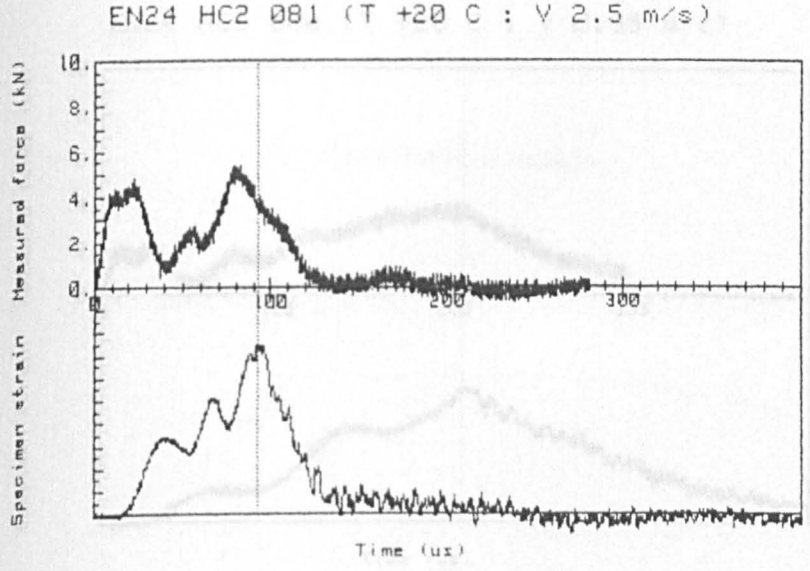

FIG. 3.23b.

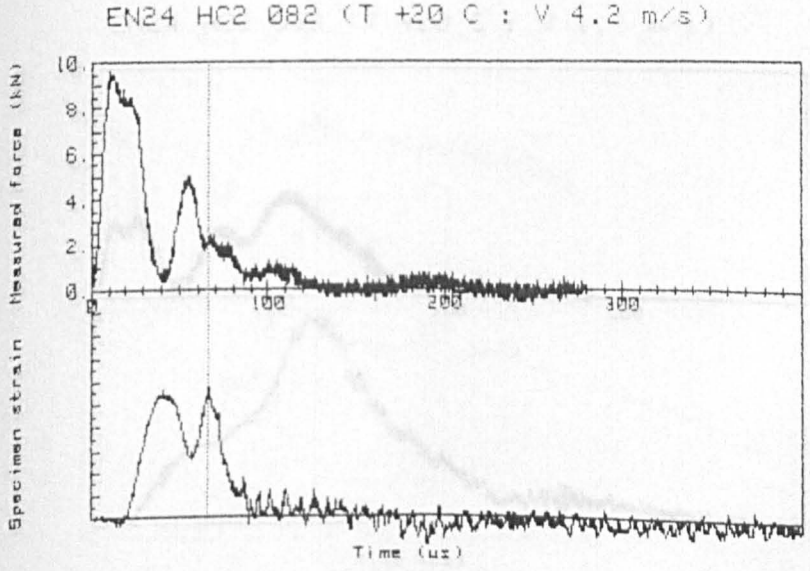

FIG. 3.23c.

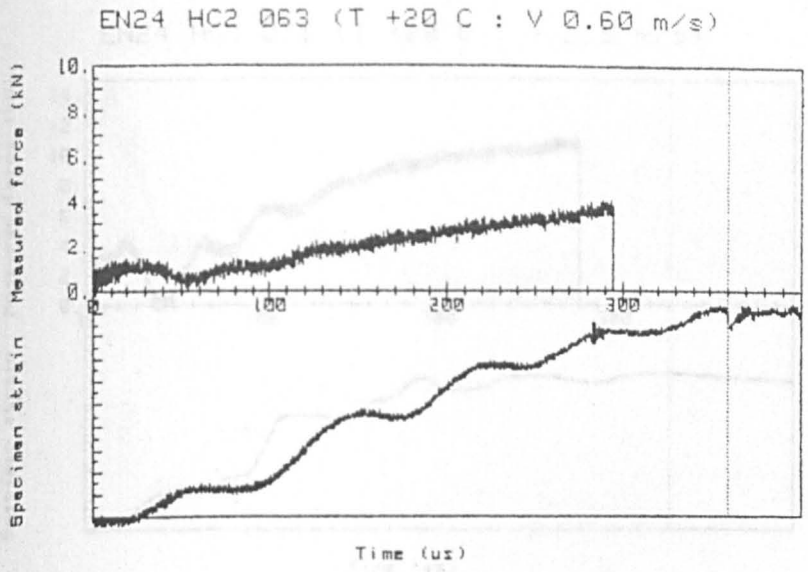

FIG. 3.24a.

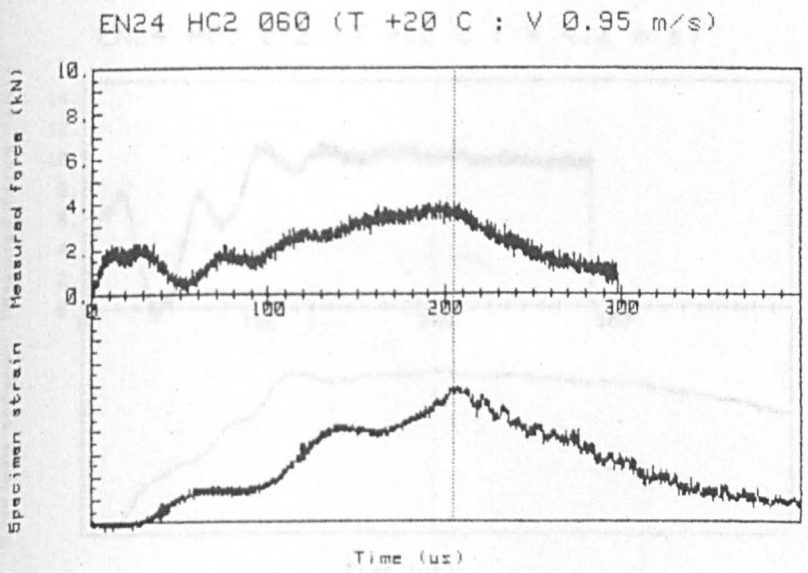

FIG. 3.24b.

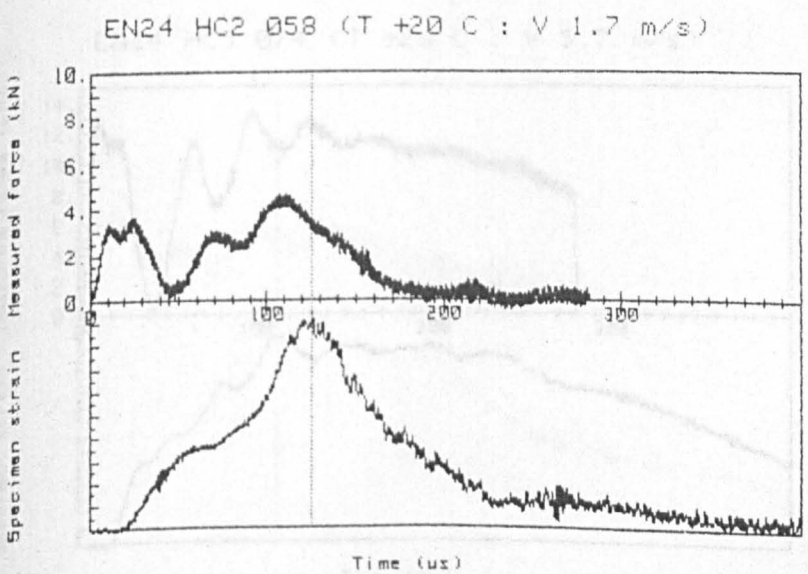

FIG. 3.24c.

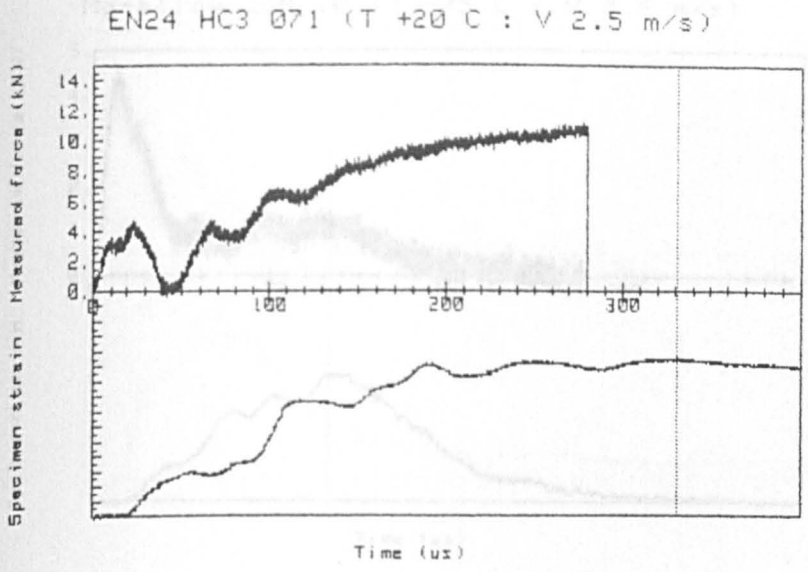

FIG. 3.25a.

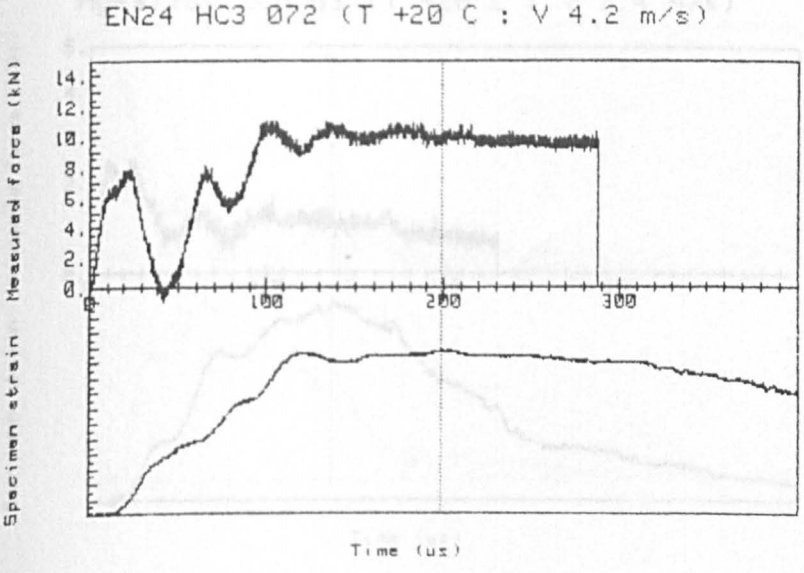

FIG. 3.25b.

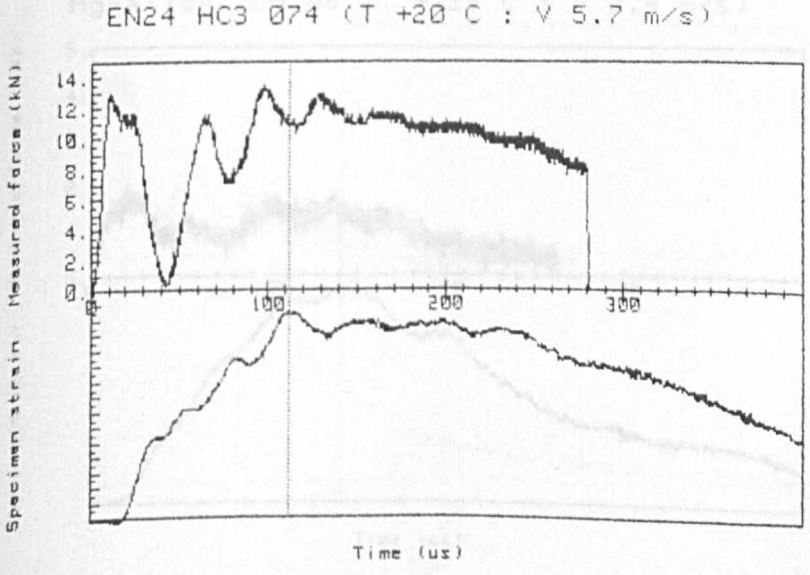

FIG. 3.25c.

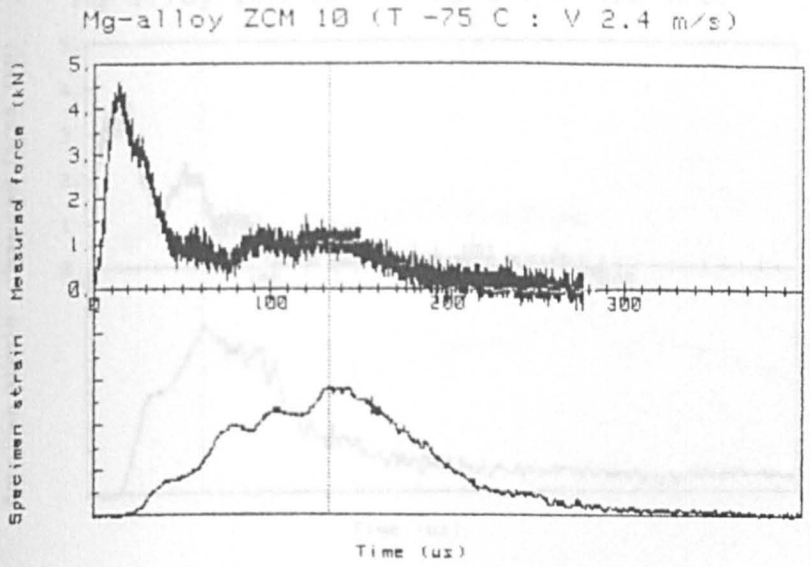

FIG. 3.26a.

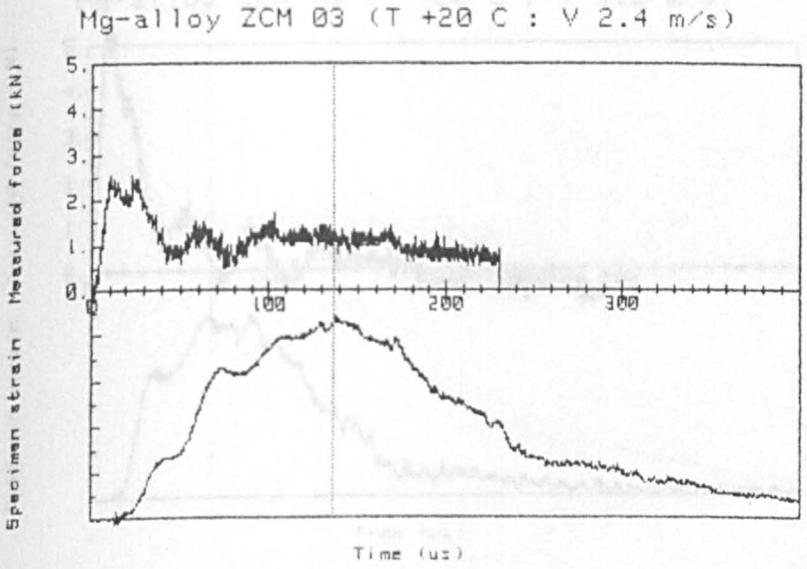

FIG. 3.26b.

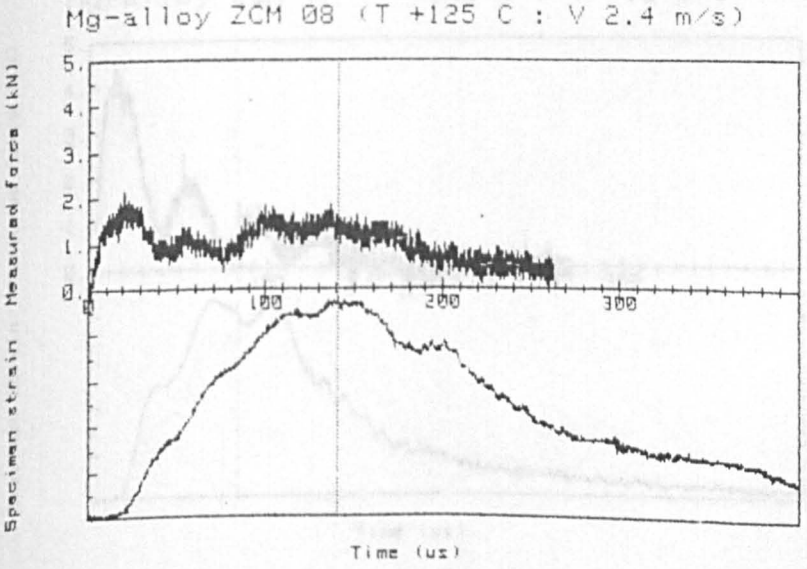

FIG. 3.26c.

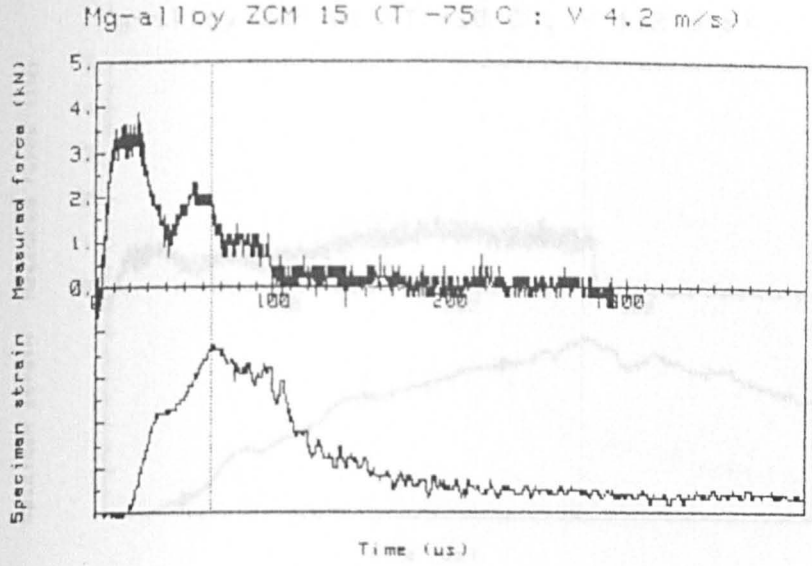

FIG. 3.27a.

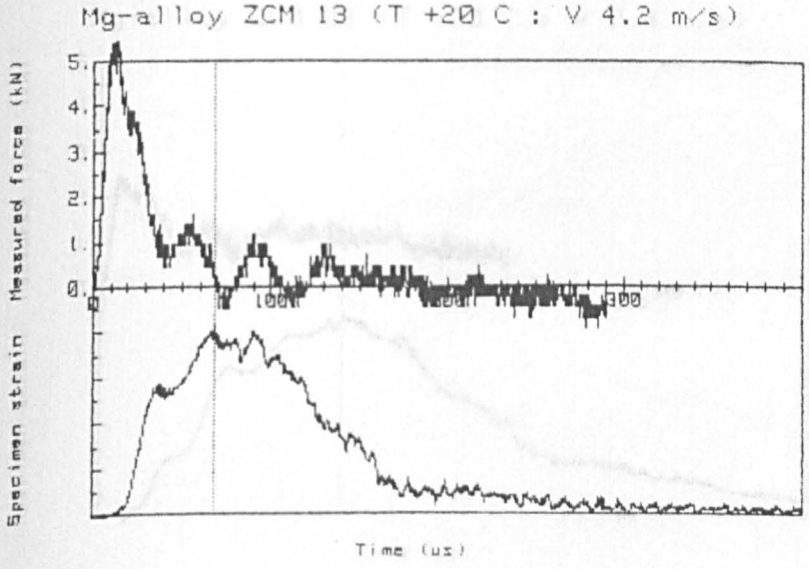

FIG. 3.27b.

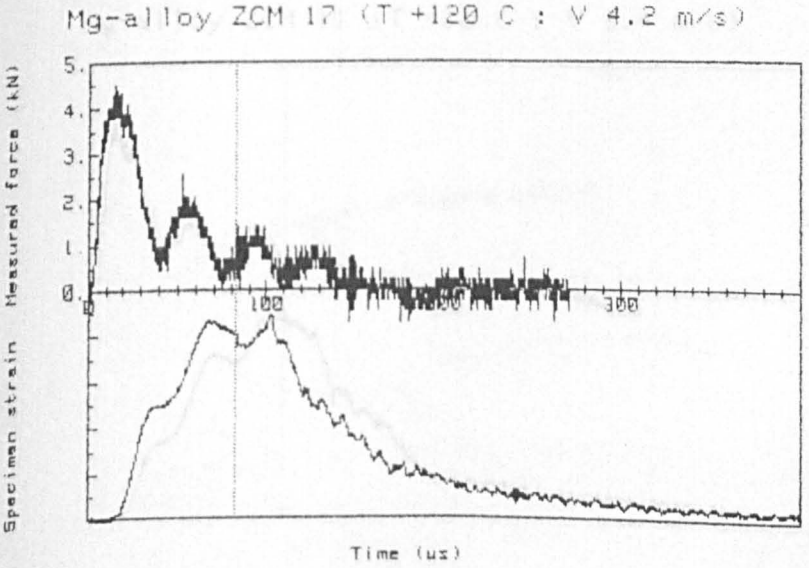

FIG. 3.27c.

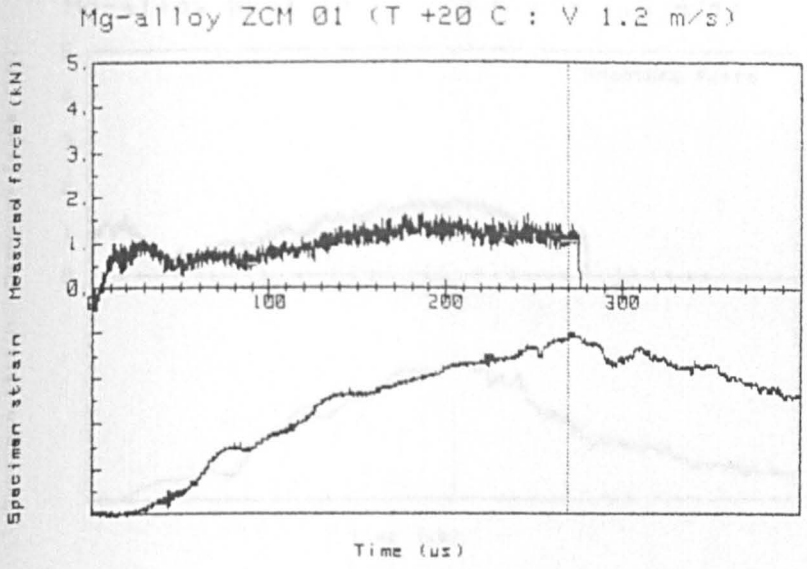

FIG. 3.28a.

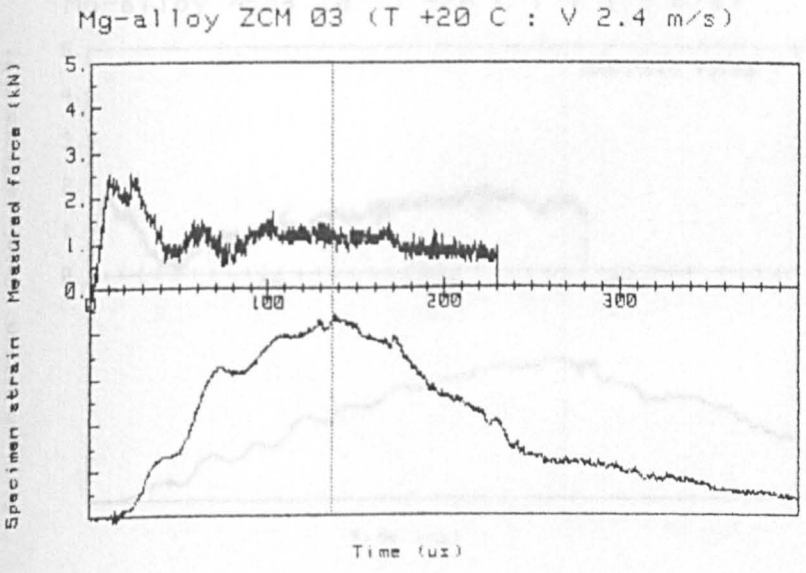

FIG. 3.28b.

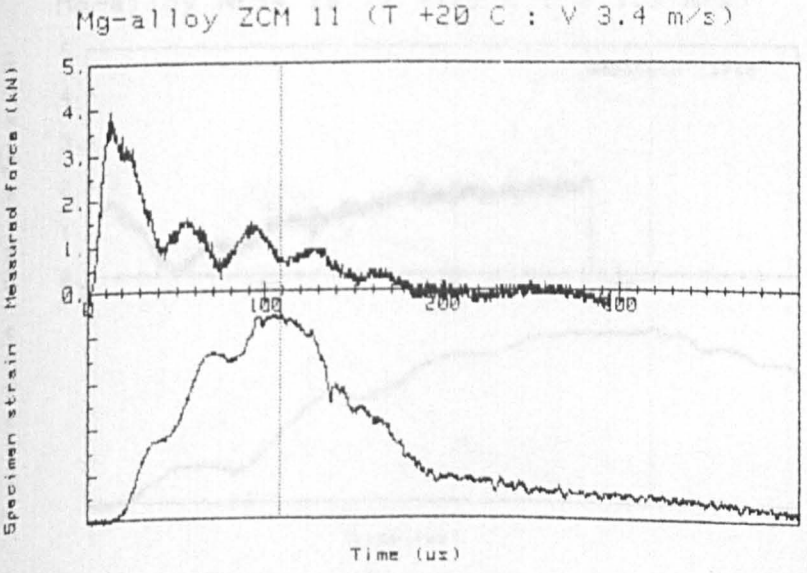

FIG. 3.28c.

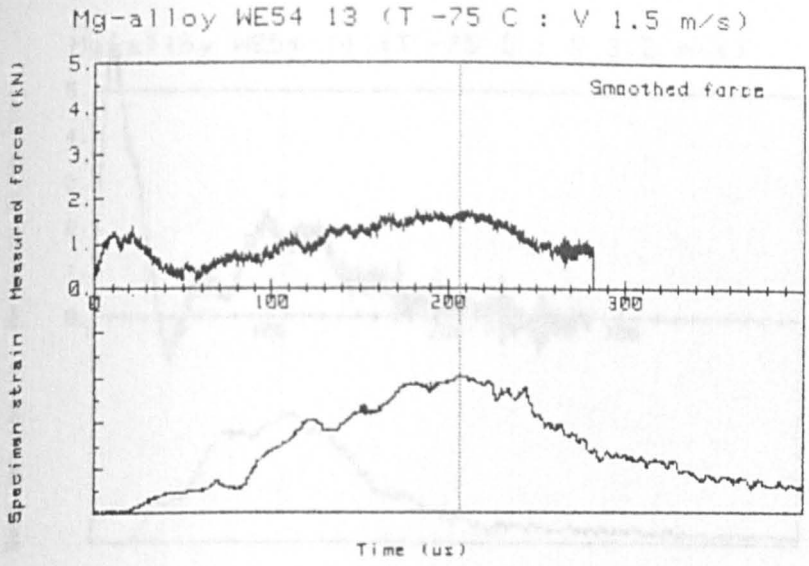

FIG. 3.29a.

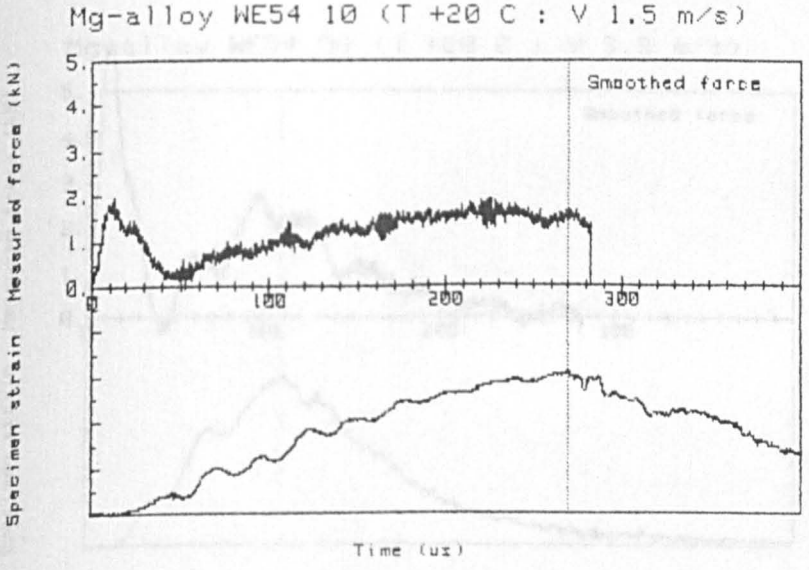

FIG. 3.29b.

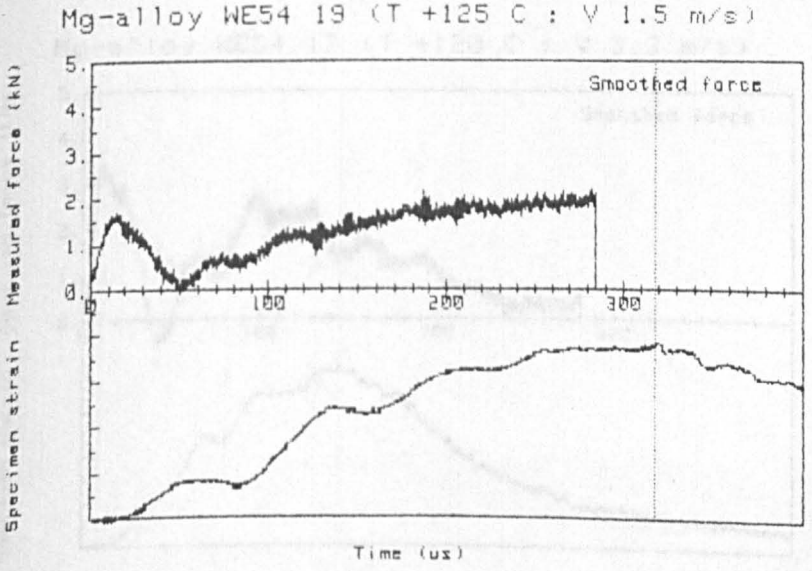

FIG. 3.29c.

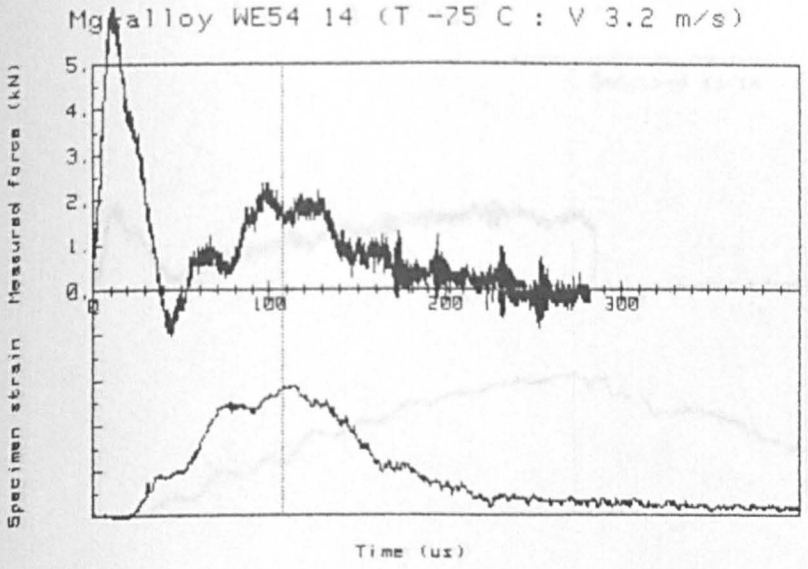

FIG. 3.30a.

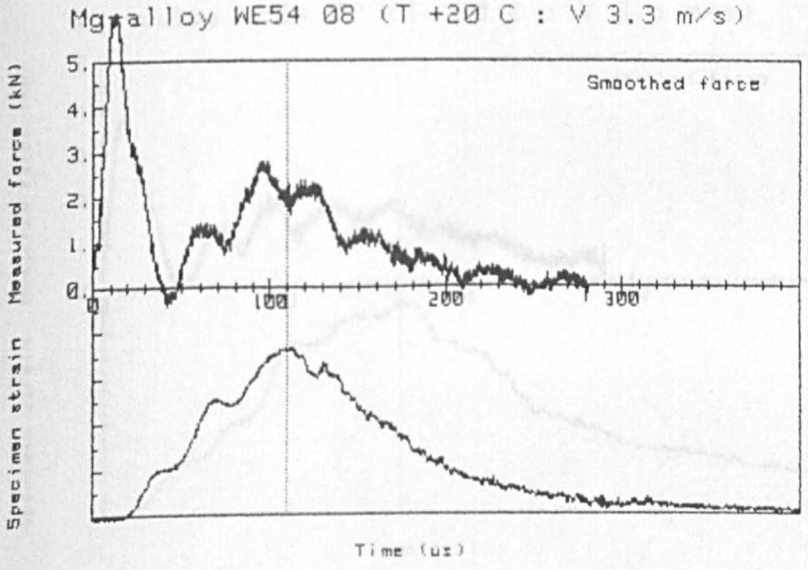

FIG. 3.30b.

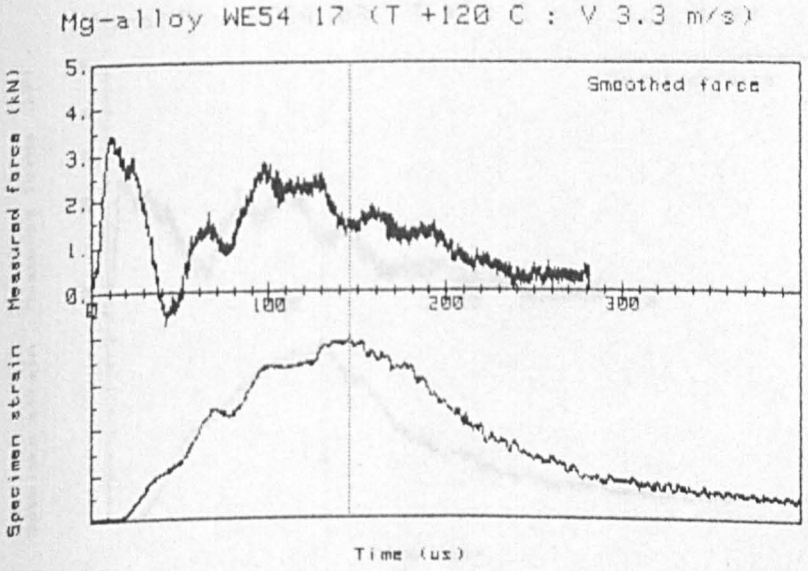

FIG. 3.30c.

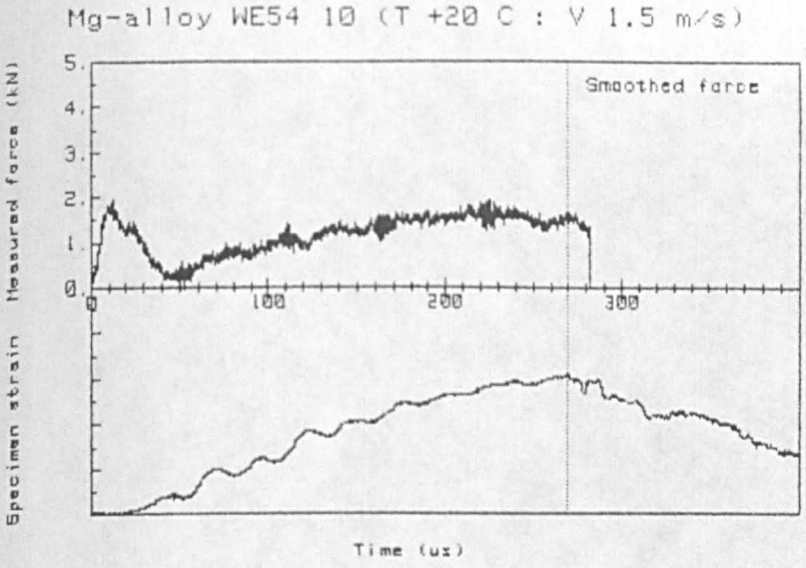

FIG. 3.31a.

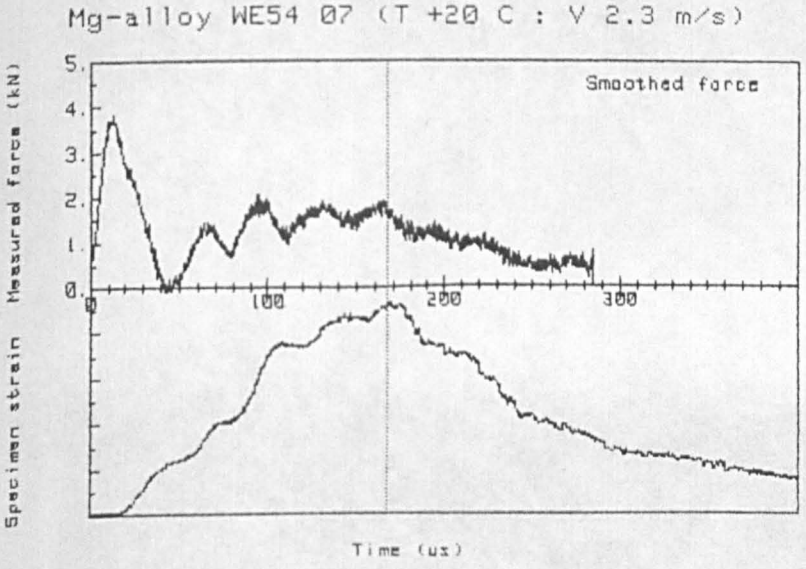

FIG. 3.31b.

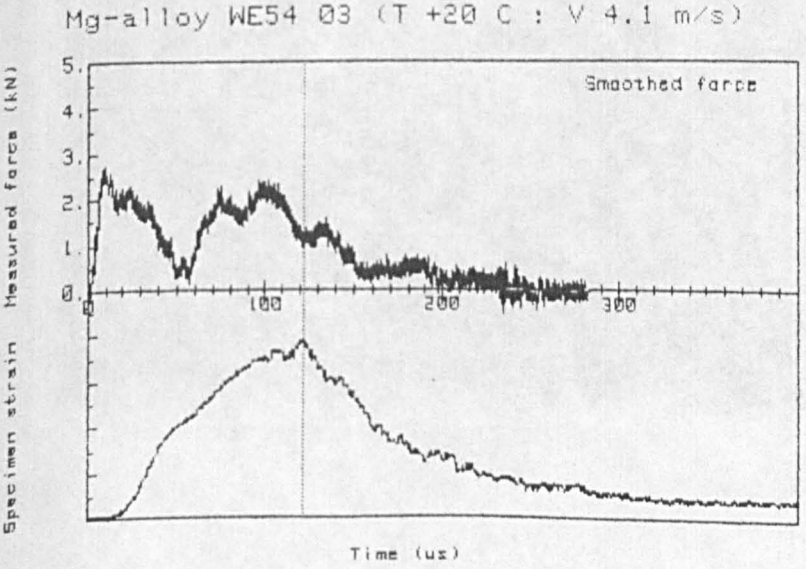

FIG. 3.31c.

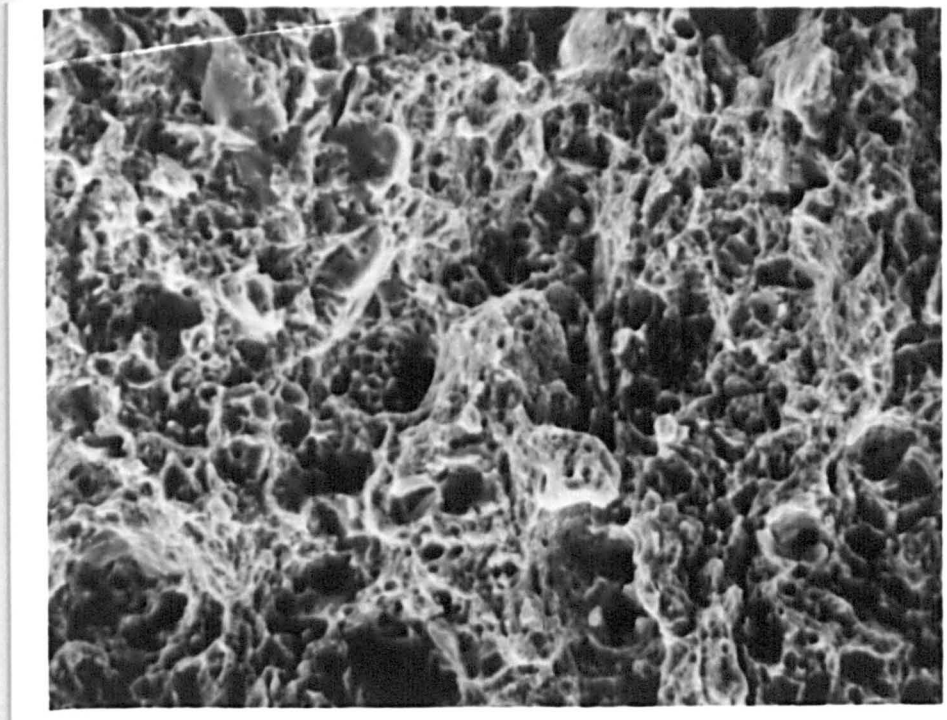

FIG. 3.32. SEM photograph of En24 HC1 033 (T = 20°C) fracture surface (x 600).

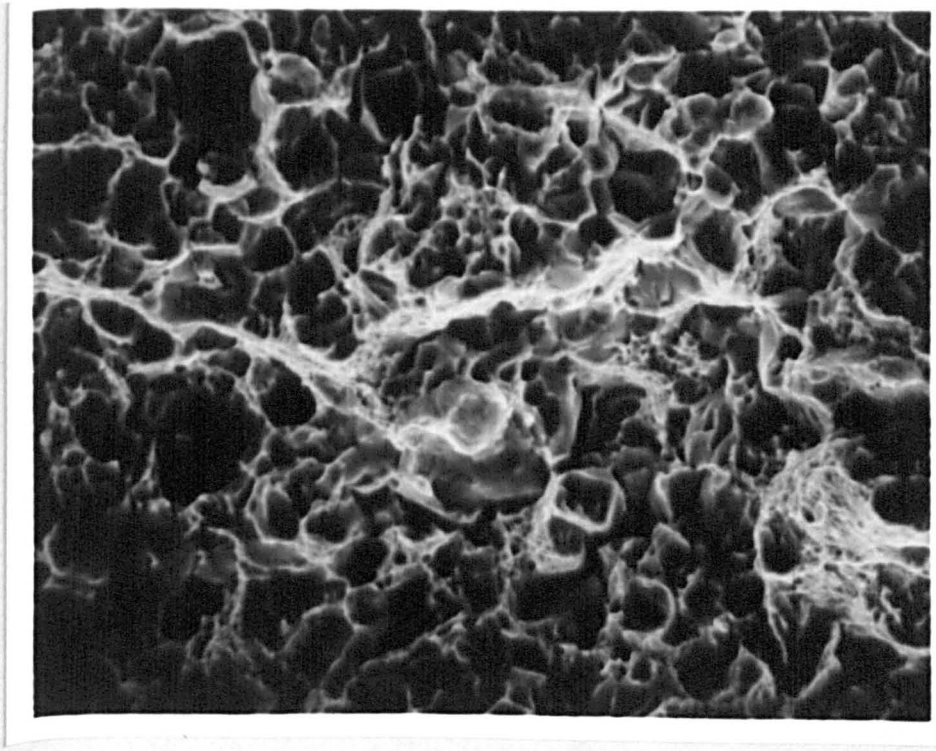

FIG. 3.33. SEM photograph of En24 HC2 050 (T = 20°C) fracture surface (x 580).

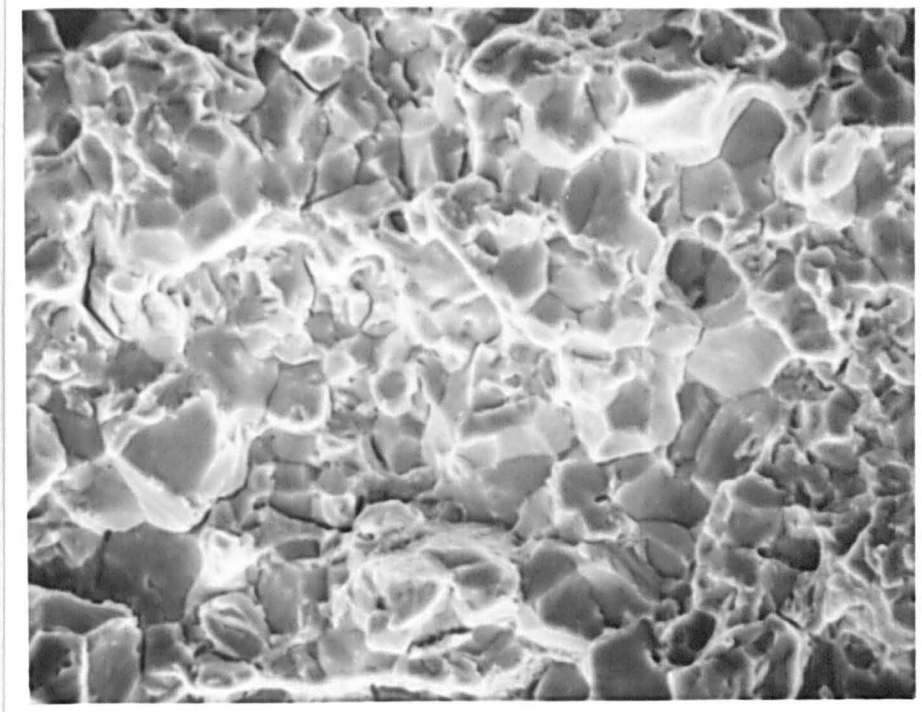

FIG. 3.34. SEM photograph of En24 HC2 066 (T = -80°C) fracture surface (x 600).

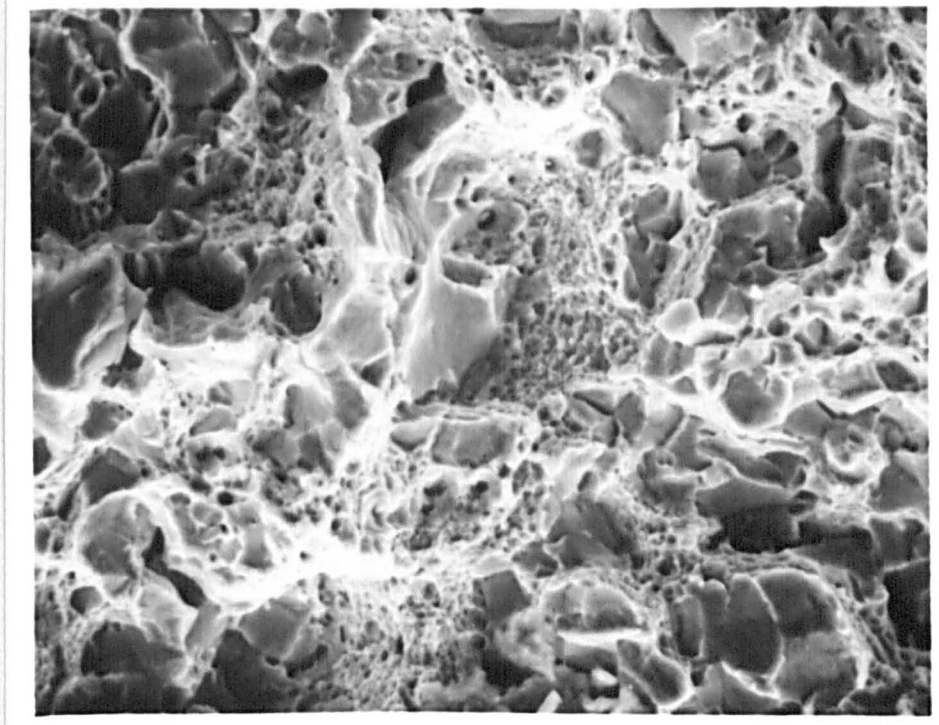

FIG. 3.35. SEM photograph of En24 HC2 052 (T = 100°C) fracture surface (x 670).

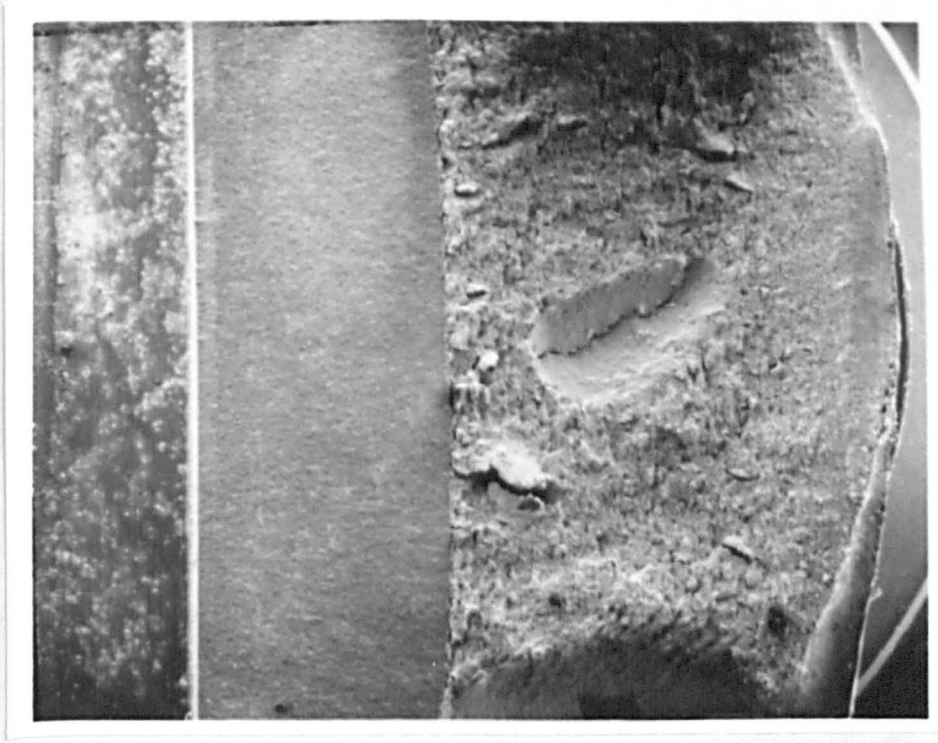

FIG. 3.36a. SEM photograph of En24 HC3 075 (T = 20°C) fracture surface: general view (x 9.5).

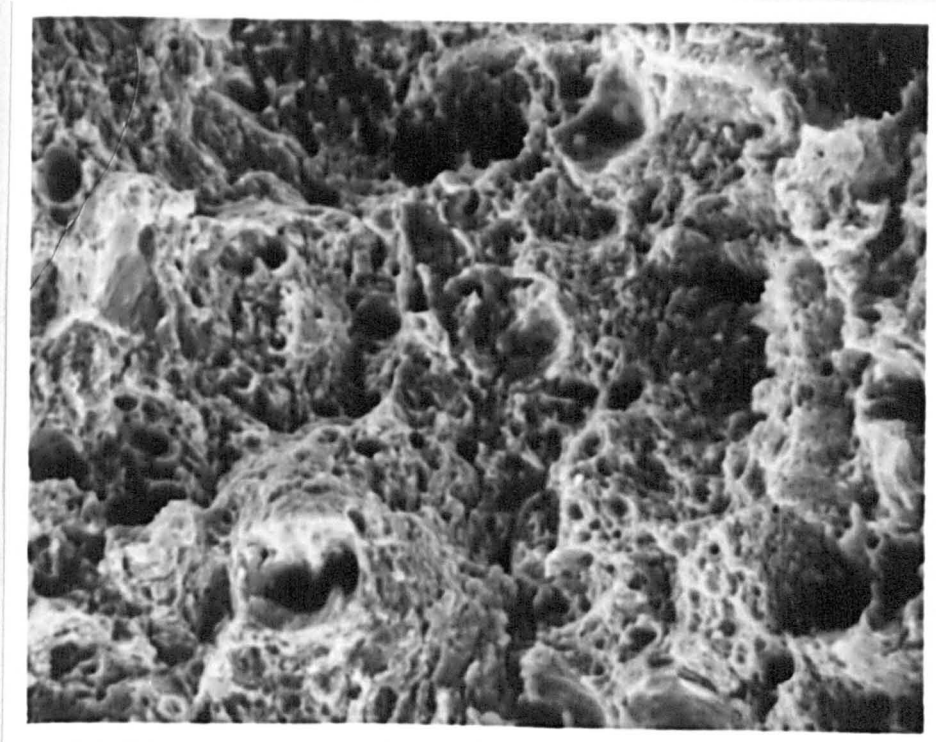

FIG. 3.36b. SEM photograph of En24 HC3 075 (T = 20°C) fracture surface: detail (x 600).

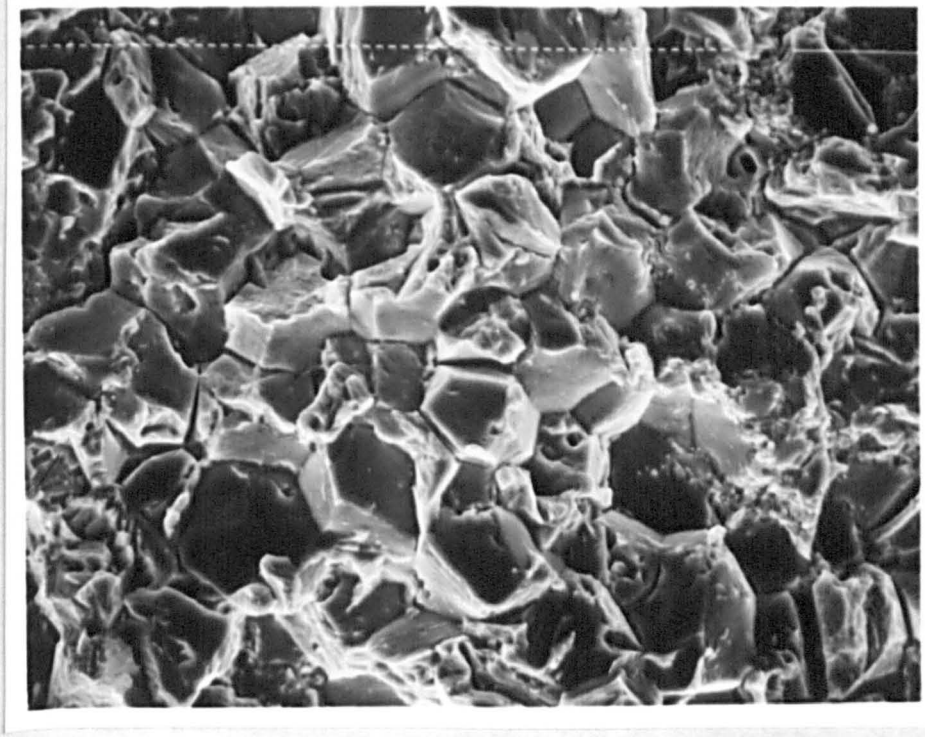

FIG. 3.37. SEM photograph of Mg alloy WE54 (T = 20°C) fracture surface (x 170).

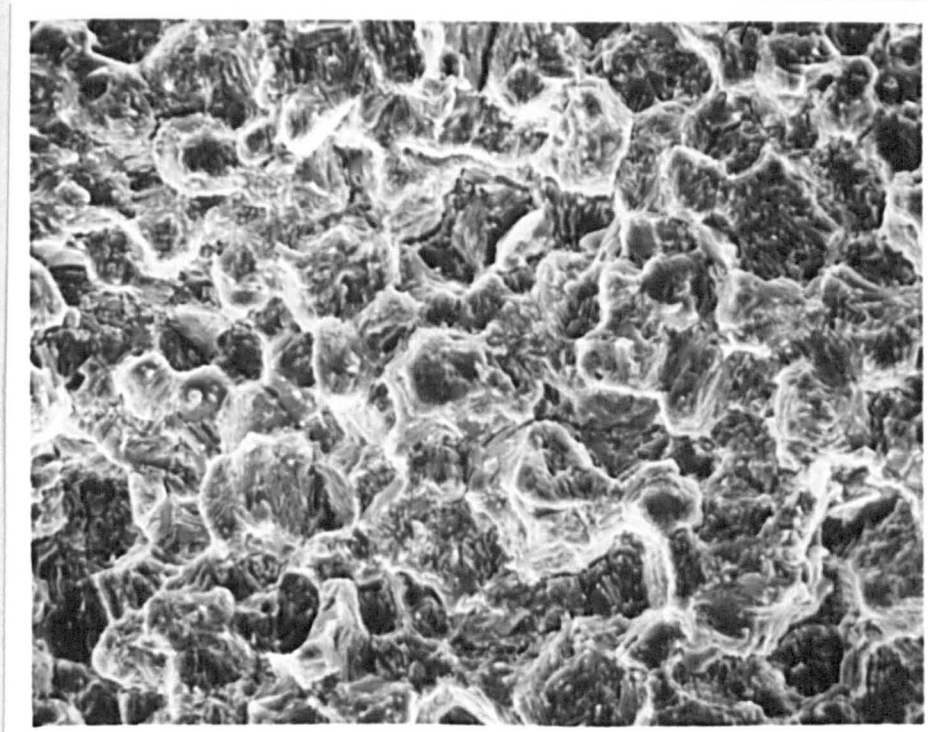

FIG. 3.38. SEM photograph of Mg alloy ZCM-630-T6 (T = -75°C) fracture surface (x 170).

4. THE LINEAR INERTIAL MODEL OF THE HOPKINSON PRESSURE BAR TEST.

4.1. Introduction.

It was noted in the discussion of the instrumented impact test in section 2.5 that the impactor force-time measurement is dominated by inertial effects which must be allowed for when calculating the dynamic fracture toughness or dynamic J-integral for any given test. Since it is the current intention in using the Hopkinson pressure bar test to study high loading rates it is obvious from a simple inspection of the force-time characteristics in figures 3.18 to 3.31 that the analysis here must allow for these inertial effects. (It would, of course, be possible to adapt the design of the HPB rig to operate at lower impact velocities where the inertial oscillations would be practically negligible by comparison with the standard Charpy test at the same loading rates.)

The most ambitious approach would be to use a 3-dimensional finite element model of the specimen, the anvil, and the Hopkinson pressure bars. However, a study of this kind, reducing the requirements to a 3-dimensional model of the specimen alone with simplified support and loading conditions [79], resulted in an analysis which took approximately 100 hours on a Cray supercomputer. Such

computer-loading would be useless for a projected standard test technique and can at best be used to validate simpler models. Even 2-dimensional finite element models are bulky and difficult to use with realistic boundary conditions due to the complex geometry of the wedge-shaped profile of the incident bar and the anvil. Because of these difficulties it was felt that a 1-dimensional model of the system - providing it could account for parameters such as the initial crack length and the total specimen length - would be almost as accurate in representing the load-time history, while at the same time allowing a considerable saving of computer time. If successful, such a model would be suitable to form the basis of a standard test technique.

Nash [110,111] has described an approximate technique to predict the hammer force and specimen bending moment in a dynamic three point bend test using a refined 1-dimensional bending theory. This approach has been developed by Kishimoto et al [112] to produce a simple expression relating the dynamic and quasi-static fracture toughness values. Although mathematically complex, this method enables dynamic fracture toughness values to be easily calculated once the natural frequency of the cracked specimen is known. However, it is currently restricted to linear elastic material behaviour.

A still simpler approach has been suggested by Glover

et al [4] and Williams and co-workers [5,50,113] in which the specimen is represented by a point mass supported on a spring. The method has the advantage that the loading and support system can be represented by further springs (and masses, if required) and insight gained into the specimen/loading system interaction. The approach was developed for the standard Charpy test assuming a constant rate of displacement at the load point. It will be shown in the following section that the accurate determination of load point displacement in the HPB test makes the method especially applicable in this case, although a numerical rather than analytic solution of the governing equation is required. In subsequent sections the various components of the model are examined in detail and consideration made of their effect on the final derivation of fracture toughness. A further advantage of the lumped mass-spring, or "inertial", model is that elasto-plastic effects can be introduced by changing the specimen stiffness and this will be discussed further in chapter 5.

4.2. The numerical lumped mass-spring model.

The essential features of the lumped mass-spring model are shown in figure 4.1. The specimen is represented by an effective mass m' supported on a spring of stiffness

k_2. The contact between the loading system and the specimen is represented by a second spring of stiffness k_1. It is then possible to break down the stiffnesses k_1 and k_2 into series components which can be identified physically in the Hopkinson pressure bar test system (figure 4.1) as:

$$k_1 = \left[\frac{1}{k_w} + \frac{1}{k_{c1}}\right]^{-1} \tag{4.1}$$

and:

$$k_2 = \left[\frac{1}{k_s} + \frac{1}{k_{sup}}\right]^{-1} \tag{4.2}$$

where k_w is the stiffness of the impactor (in this case the wedge-shaped profile at the end of the incident bar), k_{c1} is the so-called "contact", or indentation, stiffness (calculated from the Hertzian contact problem in the elastic case), k_s is the stiffness of the specimen itself, and k_{sup} is a combination of the stiffness of the abutments k_a and the support "contact" stiffness k_{c2}.

The equation of motion for the model is then simply:

$$m'\ddot{u} + (k_1 + k_2)u = k_1 v(t) \tag{4.3}$$

where u(t) is the displacement of the specimen at the load point and v(t) is the displacement imposed on the loading system at surface A in figure 4.1. From the analysis in chapter 3 it is obvious that surface A should be the point of reflection of the incident stress wave. In section 3.11 it was shown that this plane cannot be precisely located,

although it is closer to the beginning of the change in section than to the tip of the bar. For this reason it is assumed hereafter that surface A is located at the beginning of the change of section of the incident bar.

The force generated at the tip of the incident bar is then given by:

$$P_1 = k_1[v(t) - u(t)] \tag{4.4}$$

while the force experienced by the specimen is:

$$P_2 = k_2u(t) = P_1 - m'\ddot{u} \tag{4.5}$$

Williams and Adams [5] and Glover et al [4] then assumed a constant impact velocity V and hence a ramp displacement function:

$$v(t) = Vt \tag{4.6}$$

In effect, this assumes that the pendulum in the Charpy test moves at a constant velocity throughout the test (an assumption that inevitably introduces a small error - see, for example, [63] reported in section 2.5). Analysis of the Hopkinson pressure bar stress waves, however, gives the real particle velocity V(t) (equation 3.14) and hence, by integration, the real displacement. It is then possible to solve equation (4.3) numerically using the Runge-Kutta-Nystrom technique for second order differential equations (see, for example, [114]). At the same time it is a simple matter to include a viscous damping term $c\dot{u}$ on the left hand side of equation (4.3) should this be considered desirable. The numerical algorithm to solve equation (4.3)

is given in Appendix 2.

Since the Hopkinson pressure bar wave analysis also gives the force at surface A (equation 3.13), a useful check on the accuracy of the model can be obtained by comparing this measured force with the predicted force given by:

$$F_p = P_1 + m_w\ddot{v} \qquad (4.7)$$

where m_w is the mass of the incident bar between surface A and the specimen. The wedge-shaped end of the incident bar is therefore assumed to behave as a point mass with acceleration $\ddot{v}(t)$ calculated by differentiating the measured velocity V(t). In practice it was found necessary to smooth excess oscillations in the raw signal of V(t) by using a five point moving average technique both before and after the differentiation.

4.3. Evaluation of the equivalent point mass m'.

The magnitude of the equivalent point mass m' controls the strength of the oscillations in the force history of the model. Glover et al and Williams and Adams used conventional vibration theory to derive the equivalent point mass for the first mode of vibration of an uncracked beam:

$$m' = \frac{17}{35} \rho SBW = 0.49 \rho SBW \qquad (4.8)$$

where B and W are specimen dimensions, S is the supported span, and ρ is the material density. Equation (4.8) is derived in appendix 3.1.

This value of the equivalent point mass takes no account of the notch and fatigue crack length in pre-cracked Charpy specimens, nor of the overhangs of typical specimens at the supports. Thus, it is to be expected that:

$$m' = f(\rho, S, B, W, a/W, S/L) \qquad (4.9)$$

The effect of notch and fatigue crack depth can be estimated by adapting the eigenvalue analysis of Nash [110] for a cracked Euler-Bernoulli beam. In this analysis plasticity effects, shear deflection, and rotary inertia are neglected and a refined 1-dimensional bending theory used to derive a shape function $Y_i(x/S)$ for the deflected beam. Appendix 3.2 shows how an equivalent point mass can be derived from Nash's theory by equating the kinetic energy of the equivalent point mass with the distributed energy of the beam. This gives an equivalent mass:

$$m' = 0.38 \rho SBW \qquad (4.10)$$

In a specimen with such a small span to width ratio ($S/W = 4$) it may not be reasonable to neglect the effects of shear deformation and rotary inertia as in the Euler-Bernoulli beam discussed above. The Timoshenko beam

studied by Kishimoto et al [115] includes these effects but their approach was otherwise the same as Nash. They found that the time period of the force oscillation increases relative to the Euler-Bernoulli case which implies a reduction in the frequency of vibration, w, so that, for constant machine/contact stiffness k_1 the equivalent mass would be greater (by equation 4.14).

The effect of higher mode vibration has been considered by Williams [116] for the uncracked beam as a further series of equivalent masses and stiffnesses, but for the three point bend test configuration he found that less than 1% of the energy lay in the second mode. However, Tse et al [117] have noted that the effects of rotary inertia are more pronounced at higher frequencies and so the influence of the higher modes may still be greater than implied by Williams' calculation.

Further evidence of the importance of the third vibration mode can be obtained by calculating the natural frequency of vibration of a simply-supported beam constrained by a spring at its midpoint (figure 4.2a). This is a more realistic representation of the three point bend specimen than that used by Williams in deriving equation (4.8) and shows that the stiffness k_1 also influences the equivalent mass of the system. Again neglecting the effects of shear deformation and rotary inertia, the standard wave equation for the Euler-

Bernoulli beam is:

$$EI \frac{\partial^4 u}{\partial x^4} + \rho A_0 \frac{\partial^2 u}{\partial t^2} = 0 \qquad (4.11)$$

By assuming harmonic solutions of the form $u = f(x)e^{iwt}$ and applying appropriate boundary conditions, it can be shown that (see appendix 3.3) the natural frequencies are given by:

$$w^2 = \frac{EI}{\rho A_0} \left[\frac{N_m}{(S/2)}\right]^4 \qquad (4.12)$$

where N_m is a solution of the frequency equation:

$$\frac{k_1}{2} \left[\tan(N_m) - \tanh(N_m)\right] + 2EI \left[\frac{N_m}{(S/2)}\right]^3 = 0 \qquad (4.13)$$

For such a system the governing equation of the equivalent mass is found by setting equation (4.3) to zero. From the resulting expression for the natural frequency the equivalent mass is:

$$m' = \frac{(k_1 + k_2)}{w^2} \qquad (4.14)$$

Using the value of k_2 for an unnotched beam ($k_2 = 48EI/L^3$) equation (4.13) was solved for various values of k_1 and the appropriate natural frequencies and equivalent masses calculated (table 4.1). Figure 4.2b shows the effect of k_1 on the solution of equation (4.13). It can be seen that as $k_1 \rightarrow 0$, then $N_m \rightarrow n\pi/2$ (where n = 1,3,5,7,9...), and the frequency of the first mode is:

$$w_1 = \frac{\pi^2}{S^2}\left[\frac{EI}{\rho A_0}\right]^{\frac{1}{2}} \tag{4.15}$$

which is the solution for the frequency of the first mode of vibration of a pinned-pinned beam with no midpoint constraint, and hence:

$$m' \rightarrow \frac{k_2}{w^2} = 0.01546\ (kg) = 0.49\ \rho SBW \tag{4.16}$$

Also, as $k_1 \rightarrow \infty$, $N_m \rightarrow 3\pi/2$, and the frequency of the first mode is then:

$$w_1 = \frac{9\pi^2}{S^2}\left[\frac{EI}{\rho A_0}\right]^{\frac{1}{2}} \tag{4.17}$$

which is the solution for the frequency of the third mode of vibration of a pinned-pinned beam. In this case:

$$m' \rightarrow \frac{k_1}{w^2} \rightarrow \infty \tag{4.18}$$

which is to be expected since the centre of the beam has now effectively become a node. This is no longer physically accurate since the centre of the beam is free to move laterally under forced loading, but equations (4.16) and (4.18) do illustrate the important conclusion that the equivalent mass is dependent on the ratio k_1/k_2. The natural frequency of the system is bounded by the two limits imposed by equations (4.15) and (4.17).

The effect of specimen "overhang" at the supports will now be considered. Bohme and Kalthoff [69,70] have shown that this overhang has a marked influence on the

size and frequency of inertial oscillations in the measured force-time relationship. They considered the effect of varying a/W and L/W. Specimens with a/W = 0.5 and L/W = 4.1 were observed to have larger dynamic oscillations than specimens of longer length (L/W = 5.5) or shallower crack depth (a/W = 0.3).

An attempt to quantify the contribution of overhang to the equivalent specimen mass was made using a finite element model. The specimen was modelled in two dimensions using plane strain elements and loaded through springs in the same way as in the inertial model. The mesh used in the calculations is shown in figure 4.3. It incorporates the quarter point concept for modelling the elastic crack tip singularity (see section 2.6) together with similarly modified transition elements [118] to link the quarter point elements to the conventional isoparametric elements in the rest of the mesh.

The stiffness of the mesh under static loading compared favourably with the value derived by Tada et al [14] for a cracked beam - equation (4.28) below. Refinement of the mesh close to the loading and support points resulted in a decrease in the stiffness which was attributed to local effects due to the loading being concentrated at a single node. This fact prevented a proper demonstration of mesh convergence, but the satisfactory result for the static loading case is

presented as giving confidence in the suitability of the model. For the dynamic loading a time-step of 0.5×10^{-6} s was selected to satisfy the criterion that a stress wave should be able to cross the largest element at least once in any given time-step. The loading was input as the displacement history at the end of the spring k_1 (see figure 4.3) for the En24 HC1 027 test.

It was then assumed that the lumped mass-spring model presented in section 4.2 could be applied to the finite element model such that the mesh would have an equivalent mass for any given loading condition. As shown above, this mass may vary with the stiffness k_1. Analyses were carried out for several different nominal stiffness values k_1 and the resulting predictions of load compared with the measured force-time trace for test 027 to determine which had the closest frequency response (figure 4.4). Using this stiffness value the mesh was then loaded using a constant displacement rate (which effectively removed the influence of forcing frequency effects) and the natural frequency determined by measuring the peak to peak period (figure 4.5a). (In practice this period varied slightly from cycle to cycle and for consistency the second and third peaks were used to measure the period.) Equation (4.14) could then be used to evaluate the equivalent mass, or, in practice, the approximation:

$$m' = \frac{k_1}{w^2} \tag{4.19}$$

since k_1 is typically found to be at least an order of magnitude greater than k_2. The equivalent mass derived in this way should include the effects of rotary inertia and shear deformation, as well as those of k_1/k_2 and the specimen overhangs. A good fit to the experimental data was obtained with $k_1 = 5 \times 10^8$ Nm^{-1} and an equivalent mass $m' = 0.023$ kg, or:

$$m' = 0.73\rho SBW \tag{4.20}$$

For the truncated specimen (figure 4.5b) the equivalent mass by this technique was found to be $m' = 0.0155$ kg, or:

$$m' = 0.49\rho SBW \tag{4.21}$$

indicating the large role played by the overhangs in determining the behaviour of the specimen.

For the magnesium alloy (figure 4.6), for $k_1 = 1.2 \times 10^8$ Nm^{-1}, the equivalent mass came out to be $m' = 0.0056$ kg, or:

$$m' = 0.76\rho SBW \tag{4.22}$$

The difference between equations (4.20) and (4.22) is within the likely error of the method.

4.4. Evaluation of specimen stiffness in the three point bend test.

For an unnotched, uncracked, simply supported beam loaded at its midpoint Timoshenko and Goodier [119] give the deflection as:

$$u_{nc} = \frac{PS^3}{48EI} + \left[\frac{PS}{2W}\left(\frac{3}{4G} - \frac{3}{10E} - \frac{3\nu}{4E}\right) - 0.21\,\frac{P}{E}\right] \qquad (4.23)$$

where the first term is the deflection due to bending and the second a correction for local shear effects. Substituting $G = E/[2(1 + \nu)]$ and $\nu = 0.3$, equation (4.23) becomes:

$$u_{nc} = \frac{PS^3}{48EI}\left[1 + 2.85\left(\frac{W}{S}\right)^2 - 0.84\left(\frac{W}{S}\right)^3\right] \qquad (4.24)$$

In their handbook of elastic crack formulae, Tada et al [14] quote the deflection due to a crack in a three point bend specimen as:

$$u_c = \frac{PS^3}{48EI}\left[6\left(\frac{W}{S}\right) V_2\left(\frac{a}{W}\right)\right] \qquad (4.25)$$

where:

$$V_2\left(\frac{a}{W}\right) = \left[\frac{\frac{a}{W}}{\left(1 - \frac{a}{W}\right)}\right]^2 \left[5.58 - 19.57\left(\frac{a}{W}\right) + 36.82\left(\frac{a}{W}\right)^2 - 34.94\left(\frac{a}{W}\right)^3 + 12.77\left(\frac{a}{W}\right)^4\right] \qquad (4.26)$$

and thus the total deflection of a cracked beam, u, is given by the sum of equations (4.24) and (4.25):

$$u = u_{nc} + u_c$$

$$= \frac{PS^3}{48EI}\left[1 + 2.85\left(\frac{W}{S}\right)^2 - 0.84\left(\frac{W}{S}\right)^3 + 6\left(\frac{W}{S}\right)V_2\left(\frac{a}{W}\right)\right] \quad (4.27)$$

The stiffness, k_s, of the specimen:

$$k_s = \frac{P}{u} \quad (4.28)$$

is then easily determined.

4.5. Evaluation of other component stiffnesses.

The stiffness of the profiled end section of the incident bar can be calculated by dividing it firstly into a wedge and a rounded tip, then subdividing each of these into a number of elements and performing a series stiffness calculation (see figure 4.7).

In the case of the wedge the cross-sectional area A_n at a given section n is defined by:

$$A_n = 4\left[\frac{R_n h_n}{2} + \frac{R_0^2 \phi_n}{2}\right] \quad (4.29)$$

where:

$$h_n = (R_0^2 - R_n^2)^{\frac{1}{2}} \quad (4.30)$$

and:

$$\phi_n = \sin^{-1}(R_n/R_0) \quad (4.31)$$

from which the element stiffness is:

$$k_n = \frac{A_n E}{(x_n - x_{n-1})} \tag{4.32}$$

The stiffness of the rounded tip is more problematic since the load is not carried across its full width (the specimen is only 10 mm thick against a bar diameter of 19 mm). The included half angle θ_0 (see figure 4.7) is given by:

$$\theta_0 = \sin^{-1}(y_0/R_T) = \sin^{-1}(0.25) \tag{4.33}$$

The cross-sectional area of a given element is approximately:

$$A_n = W_w (y_n + y_{n-1}) \tag{4.34}$$

where W_w is a width parameter which can be adjusted to allow for the fact that the load is not carried across the full section width and y_n is the section height defined as:

$$y_n = R_T \sin\theta_n \tag{4.35}$$

at an axial distance x_n given by:

$$x_n = R_T (\cos\theta_n - \cos\theta_0) \tag{4.36}$$

The elemental stiffness again has the form of equation (4.32) and the total stiffness is:

$$k_w = \left[\sum_{n=1}^{m} \left(\frac{1}{k_n}\right)_{wedge} + \sum_{n=1}^{m} \left(\frac{1}{k_n}\right)_{tip} \right]^{-1} \tag{4.37}$$

where m is the total number of increments used in the calculation. The total mass of the profiled end section is then:

$$m_w = \rho \sum_{n=1}^{m} A_n (x_n - x_{n-1}) \tag{4.38}$$

where the summation is over both the wedge and the tip. For ease of calculation it was assumed that the load was carried over the full width of the wedge section and over the specimen thickness within the rounded tip. For the given geometry the following values were obtained:

$$m_w = 0.0144 \text{ kg} \tag{4.39}$$

$$k_w = 1.54 \times 10^9 \text{ N/m} \tag{4.40}$$

which were well converged with m = 100 increments.

The contact stiffnesses are less easily evaluated. They are generally stated to be non-linear, but then are assumed to be constant for ease of calculation [5]. Some justification for this assumption can be demonstrated by considering the linear elastic Hertzian contact problem.

Timoshenko and Goodier [119] derived the half-width b of the contact zone between a cylinder and a plane loaded with force w per unit length as:

$$b = 1.52 \left[\frac{wR}{E}\right]^{\frac{1}{2}} \tag{4.41}$$

where both the cylinder and the plane deform elastically and have similar material constants E and ν.

From the geometry of the rounded tip of the incident bar it is possible to estimate the normal deformation z caused by the Hertzian contact stress acting in this zone as:

$$z = [R_T - (R_T^2 - b^2)^{\frac{1}{2}}] \tag{4.42}$$

If the contact stiffness is then defined as the force per unit indentation at the load point, then:

$$k_c = \frac{P}{z} = \frac{wB}{z} \tag{4.43}$$

The mean stress in the contact zone is:

$$\sigma_c = \frac{P}{2Bb} \tag{4.44}$$

The radius of the rounded tip of the profiled end section of the incident bar is 8 mm, while the radius at the edges of the supports is 1 mm. The contact stiffnesses evaluated at these two interfaces are almost identical but the mean stresses are very different (see figure 4.8).

The contact stiffness at the incident bar/specimen interface was determined to be approximately constant at:

$$\begin{aligned} k_{c1} &= 18.0 \times 10^8 \text{ N/m} \quad \text{(En24 steel)} \\ k_{c1} &= 3.8 \times 10^8 \text{ N/m} \quad \text{(Mg alloy)} \end{aligned} \tag{4.45}$$

It can be seen from figure 4.1 that the contact stiffness at the supports is really made up of two identical components in parallel and so the required stiffnesses for the model were determined as:

$$\begin{aligned} k_{c2} &= 2k_c = 36.0 \times 10^8 \text{ N/m} \quad \text{(En24 steel)} \\ k_{c2} &= 2k_c = 7.8 \times 10^8 \text{ N/m} \quad \text{(Mg alloy)} \end{aligned} \tag{4.46}$$

Typical yield stress values for both materials are also shown in figure 4.8 and it is observed that the stresses generated in the contact zones exceed these

values at relatively low forces. In the present analysis it is assumed that any resulting plastic compliance will be negligible. However, in chapter 5, which discusses the effects of plasticity on specimen behaviour, a simple algorithm is introduced which allows an estimate to be made of the magnitude of this extra source of compliance.

The scale of the contact stiffness effect is such that the effective value may be significantly altered by any out-of-squareness in the rig and perhaps even surface roughness of the specimen.

The problem of evaluating the support stiffness k_{sup} is compounded by the unknown abutment stiffness k_a which cannot be estimated without a 3-dimensional finite element analysis and which is very difficult, if not impossible, to measure experimentally.

For these reasons the theoretical estimates of the stiffness components are used for comparison purposes only and the stiffness parameters k_1 and k_2 evaluated from the experimental records themselves.

4.6. Evaluation of stiffness components from the experimental record.

For the step input (equation 4.6) Glover et al [4] and Williams and Adams [5] derived the specimen

displacement u(t) as:

$$u(t) = \frac{k_1 V}{(k_1 + k_2)} \left[t - \frac{\sin wt}{w} \right] \tag{4.47}$$

The input force P_1 is then, from equation (4.4):

$$P_1 = k_1 \left[Vt - \frac{k_1 V}{(k_1 + k_2)} \left(t - \frac{\sin wt}{w} \right) \right] \tag{4.48}$$

which can be rewritten in the form:

$$P_1 = \frac{k_1}{(k_1 + k_2)} V \frac{k_2}{w} \left[wt + \frac{k_1}{k_2} \sin wt \right] \tag{4.49}$$

Differentiating equation (4.49):

$$\frac{dP_1}{dt} = \frac{k_1}{(k_1 + k_2)} V \frac{k_2}{w} \left[w + \frac{k_1}{k_2} w \cos wt \right] \tag{4.50}$$

and at time t = 0:

$$\frac{dP_1}{dt}(t=0) = k_1 V \tag{4.51}$$

Hence for a constant displacement rate test the stiffness parameter k_1 may be calculated from the initial slope of the force-time diagram.

For an initial ramp velocity input reaching velocity V_0 after time t_0:

$$v(t) = \frac{V_0}{2t_0} t^2 \tag{4.52}$$

and:

$$u(t) = \frac{k_1 V_0}{m' w^2} \left[\frac{t^2}{2t_0} - \frac{1}{w^2 t_0} + \frac{1}{w^2 t_0} \cos wt \right] \tag{4.53}$$

Hence, from equation (4.4), the input force is:

$$P_1 = k_1 V_0 \left[\frac{t^2}{2t_0} - \frac{k_1}{(k_1 + k_2)} \left(\frac{t^2}{2t_0} - \frac{1}{w^2 t_0} (1 - \cos wt) \right) \right] \tag{4.54}$$

whence, differentiating:

$$\frac{dP_1}{dt} = k_1 V_0 \left[\frac{t}{t_0} \frac{k_2}{(k_1 + k_2)} + \frac{k_1}{(k_1 + k_2)} \frac{1}{wt_0} \sin wt \right] \tag{4.55}$$

and at time t = 0:

$$\frac{dP_1}{dt}(t=0) = 0 \tag{4.56}$$

Thus for a ramp velocity input (which best models the early time history of the Hopkinson pressure bar experimental data - see figure 3.15a) the stiffness component k_1 is indeterminable by this approach. It might also be noted that for anything less than a perfect step velocity input equation (4.51) is invalid and an underestimate of the value of k_1 is likely to ensue.

However, for a given equivalent mass, it is possible to iterate the values of k_1 and k_{sup} to minimise the error between the predicted force at surface A, F_p (equation 4.7), and the force actually measured there, F_m. The root mean square error can be defined by:

$$Err = \left[\frac{1}{n} \sum_{t=0}^{t_f} [F_m(t) - F_p(t)]^2 \right]^{\frac{1}{2}} \tag{4.57}$$

where the summation is carried out over the n sample points from the numerical solution up to the time of fracture t_f predicted by the specimen strain gauge S3. k_1

and k_{sup} were varied independently to give a grid with error contours superimposed. These contours were found to indicate a clearly defined minimum which gave the best fit between the model and the experimental data. It is assumed that the variations in these iterated solutions for k_1 and k_{sup} represent and account for small changes in the configuration of the test apparatus. Such changes may arise due to changes of test condition (temperature and impact velocity) or geometry (for example, out of squareness between the specimen and the impactor/support system). In that the values were calculated up to the time of fracture indicated by the S3 strain gauge they represent mean values and may include corrections for plasticity at the loading system/specimen interfaces and the effect of any separation between the specimen and the loading system. Typical values of the stiffnesses derived by this technique are quoted in tables 4.2 to 4.4.

4.7. The derivation of dynamic crack initiation fracture toughness from the inertial model.

The characterisation of dynamic crack initiation has been discussed earlier (sections 2.4 and 2.5). Here it is assumed that stress wave effects within the specimen are negligible and that at any given instant the state of the

crack is controlled by the quasi-static stress field due to the force P_2 (equation 4.5).

For a linear elastic material the dynamic stress intensity factor K_{Id} can then be defined as the direct analogue of its static counterpart (equation 2.13) with the difference that the force $P_2(t)$ is now a function of time:

$$K_{Id} = \frac{P_2(t)S}{BW^{1.5}} F(\frac{a}{W}) \tag{4.58}$$

At time $t = t_f$ equation (4.58) gives the dynamic initiation fracture toughness of the material. As equation (4.58) explicitly excludes the inertial loading component this approach is, of course, distinct from that of authors who have used the measured load at the impactor as a direct input in calculating the dynamic stress intensity factor (see, for example, [60,88,98]). The implications of this will become apparent in the following section.

By similar reasoning, the dynamic J-integral can be determined as the dynamic analogue of the (far field) deep crack estimation formula (equation 2.37) as:

$$J_{Id} = \frac{2\ U(t)}{B\ (W - a)} \tag{4.59}$$

where the energy function:

$$U(t) = \int_0^t P_2\ d(u - u') \tag{4.60}$$

in which $(u - u')$ is the net displacement of the specimen

(see figure 4.1) and so excludes the effect of contact and support stiffnesses. As discussed in section 2.4, the use of the deep crack estimation formula to determine J must be justified in terms of the establishment of a J-dominant field which, in turn, is reasonably quasi-static (since the true dynamic J-integral is not path independent). These conditions are discussed further in section 5.6. Nonetheless, it is suggested that the form of equation (4.59) and the solution procedure leading to the evaluation of P_2 are more satisfactory and reveal more about the interaction between specimen and rig than the more piecemeal approaches of Iyer and Miclot [63] and Kobayashi [64] described in section 2.5.

4.8. Discussion of the characteristics of the three point bend impact test as revealed by the inertial model.

The working of the inertial model of the Hopkinson pressure bar impact test will now be discussed with respect to a typical test result (En24 HC2 059). The measured velocity-time and force-time traces are shown in figures 4.9a and 4.9b. The solution procedure was as follows:

(i) the velocity was integrated to give the displacement function v(t) at the measurement plane A as

input to the governing equation (4.3),

(ii) the mean crack length a was determined in accordance with the requirements of ASTM standard E-399 [3] (ie by measuring the length at midspan and quarter-span, then averaging and ensuring that all the measurements fell within the tolerances specified in [3]) and hence,

(iii) the specimen stiffness $k_s(a/W)$ was evaluated from equations (4.26) to (4.28),

(iv) the best estimate of the equivalent mass (equation 4.20) was taken from the finite element analysis described in section 4.3 ($m' = 0.023$ kg),

(v) trial values of k_1 and k_{sup} were input and the governing equation solved for the specimen displacement u(t) using the Runge-Kutta-Nystrom numerical algorithm (see appendix 2),

(vi) the predicted input force $F_p(t)$ was calculated from equations (4.4) and (4.7) and compared with the measured force $F_m(t)$, shown in figure 4.9b, to determine the error defined by equation (4.57),

(vii) steps (v) and (vi) were repeated to establish a minimum value of the error and the corresponding optimum stiffness components:

$$k_1 = 4.7 \times 10^8 \text{ N/m}$$
$$k_{sup} = 1.13 \times 10^8 \text{ N/m} \qquad (4.61)$$
$$k_s(a/W) = 4.19 \times 10^7 \text{ N/m}$$

Figure 4.10a shows the derived force $P_1(t)$ generated at the tip of the incident bar (equation 4.4) and the force $P_2(t)$ actually experienced by the specimen (equation 4.5). P_1 is seen to oscillate with time while P_2 is almost linear. In addition, the small oscillations in P_2 lag the larger oscillations in P_1 by 180^o and the loading of the specimen does not start for approximately 20×10^{-6} s after the datum. The added effect of the inertia of the profiled end of the incident bar is plotted in figure 4.10b and the resulting predicted force (equation 4.7) compared with the measured force in figure 4.10c. The agreement is seen to be very good up to the nominal time of fracture.

The time delay predicted before the rise of the P_2 force is very similar to that measured for the specimen strain gauge S3 (figure 4.10c). As discussed in section 3.11, part of this time delay ($\sim 4 \times 10^{-6}$ s) is due to the finite length of the profiled end section of the incident bar and the question arises whether the P_2 and S3 traces are correctly phased. Wave effects are specifically neglected in the inertial model analysis, but the wave passage time down the profiled end section is implicitly included in the measured input displacement function v(t) at surface A. The net effect will be to "smudge" an otherwise sharp signal and thereby damp the initial response of the specimen. It is clear, therefore, that

while the time shift defined by equation (3.19) is not strictly accurate the error introduced will be much less than 4×10^{-6} s. The nature of the two analyses in chapters 3 and 4 does not permit a more precise evaluation but the error has, at least, been reduced by the use of a 60^{o} wedge angle at the end of the incident bar rather than the standard 30^{o} in the Charpy test hammer.

The inertia of, firstly, the profiled end section of the incident bar, and, secondly, the specimen dominate the initial peak of the force-time response (figure 4.10b). Loss of contact between the incident bar and the specimen might be expected to be observed as a zero force measurement, but figure 4.10b shows the possibility that such an event could be concealed by the inertial loading of the profiled end section on the measurement plane A. Among others, Kalthoff [70] has observed separation between hammer and specimen in a three point bend drop-weight test and similar behaviour cannot be ruled out in the measurements reported here. However, if any such separation took place it was restricted to the end of the initial load oscillation and was short-lived. Kalthoff [70] has also observed loss of contact between specimen and supports but this aspect of behaviour was not studied here.

The nominal time to fracture from the S3 strain gauge is shown in figure 4.10c (assuming initiation at the

maximum strain gauge reading in the absence of any sharp "first drop" event). Obviously beyond this point the predicted solution is no longer valid since the specimen stiffness k_s is dependent on crack length and falls to zero as the crack propagates through the ligament. Section 4.12 discusses the possibility that an estimate of the crack velocity may be obtained from the rate of descent of the measured force-time trace.

The dynamic fracture toughness, evaluated by equation (4.58), for this test was $K_{Id} = 44.8$ MPam$^{\frac{1}{2}}$. The minimum size restriction for a valid plane strain measurement is given by equation (2.47). Using the static yield stress $\sigma_Y = 1458$ MPa (see figure 5.6b) this becomes:

$$b,B > 2.4 \text{ mm} \tag{4.62}$$

which is well-satisfied (see figure 3.9).

Further results from the inertial model analysis of the En24 steel specimens are presented in figures 4.11 to 4.17 and the derived values tabulated in tables 4.2 to 4.4. From section 4.5, the best theoretical estimate of k_1 for the En24 steel specimens is (equation 4.1):

$$k_1 = \left[\frac{1}{k_w} + \frac{1}{k_{c1}}\right]^{-1} = 8 \times 10^8 \text{ N/m} \tag{4.63}$$

while k_{sup} has the maximum value given by (equation 4.46):

$$k_{sup} < (k_{c2} = 36 \times 10^8 \text{ N/m})_{k_a \to \infty} \tag{4.64}$$

for a rigid anvil. These values are considerably greater than those deduced by iteration from the experimental

measurements and quoted in the tables. It has already been noted that some plastic yielding at the interfaces (particularly between specimen and support) is likely due to the magnitude of the contact stresses and this may account for some of the difference. Out of squareness may be even more significant since close examination of the specimen surfaces revealed small indentations left by the supports which tended to be deeper on one side than the other. In view of the order of magnitude disparity in the estimate of k_{sup} assuming a rigid anvil, such an assumption is clearly not justified.

Some difficulty was encountered in iterating component stiffness values at the extreme test conditions. In test En24 HC2 066 at T = -80°C the support stiffness k_{sup} was unconverged at a value $k_{sup} = 9 \times 10^9$ N/m (see table 4.3a). Similar problems were encountered with some of the magnesium alloy specimens (see section 5.9) and this seems to be a feature of tests where fracture takes place at low force levels. It probably occurs when the proportion of inertial loading is high and discretisation errors in the model are therefore more critical. Similarly, at high loading rate, for the tests on truncated specimens En24 HC2 082 and 083 ($V_0 = 4.2$ m/s) when the time to fracture $t_f < 2\ell$ the iteration technique failed to converge and mean stiffness values were used to evaluate the dynamic fracture toughness (see table 4.4b).

Model agreement for the En24 HC1 specimen batch (figures 4.11 to 4.13) is best for high impact velocity and low temperature. The model overestimates the size of the inertial oscillations at high temperature (figure 4.11c) and low velocity (figure 4.12a). Damping may be needed to improve the modelling of these conditions and, in fact, it would be easy to include a viscous damping term (see appendix 2). However, the physical justification for the inclusion of this type of damping is not clear.

Furthermore, the model agreement for the En24 HC2 specimen batch (figures 4.14 to 4.17) is excellent at all velocities and temperatures. The "first drop" initiation criterion is not always easy to apply (figures 4.14b and 4.14c), but generally gives more reasonable looking results (figures 4.15a and 4.15b). The reduced equivalent mass (equation 4.21) for the truncated specimens correctly models the higher frequency of oscillation seen in the measured force-time traces (figure 4.17) while giving iterated stiffness values k_1 and k_{sup} (table 4.4a) consistent with those derived for the full geometry. This ability to account for a significant change in specimen geometry gives confidence in the validity of the inertial modelling procedure. (For tests En24 HC2 080 and 085 the S3 strain gauge leads sheared during impact and so dynamic toughness values for these tests were evaluated using the times to fracture from tests 081 and 084 respectively.)

The effect of the introduction of the new supports (figure 3.11) and corrected tip profile of the incident bar (see section 3.8) after test HC1 029 in table 4.2 is difficult to quantify. The iterated stiffness solutions for tests at T = -20°C and V_0 = 3.2 m/s with both the old and new geometries were:

Old geometry (Fig. 3.11a) : (029) $k_1 = 5.0 \times 10^8$, $k_{sup} = 1.7 \times 10^8$ N/m
(030) $k_1 = 5.1 \times 10^8$, $k_{sup} = 1.3 \times 10^8$ N/m

New geometry (Fig. 3.11b) : (028) $k_1 = 5.1 \times 10^8$, $k_{sup} = 2.8 \times 10^8$ N/m
(032) $k_1 = 4.7 \times 10^8$, $k_{sup} = 3.3 \times 10^8$ N/m

These values do permit the tentative conclusion that the revised geometry was indeed stiffer and subsequent tests on the HC2 specimen batch (table 4.3) also showed much greater consistency of the iterated stiffness parameters.

The question arises whether the analysis is sensitive enough to detect changes in contact stiffness parameters due to the effect of temperature and strain rate on the local yield stress and, indeed, whether such changes are likely over the range of conditions covered by the tests. The iterated value of k_1 does seem to increase with impact velocity for both HC1 and HC2 specimens (tables 4.2a and 4.3a) which would be consistent with reduced plasticity due to increasing strain rate, although the range of velocity covered by the test programme might not seem to warrant the conclusion. Further work is required to clarify this point.

4.9. Summary of dynamic fracture toughness results for En24 steel.

The dynamic fracture toughness derivations are presented in tables 4.2 to 4.4 and a summary plot of dynamic fracture toughness against test temperature is presented in figure 4.18. Also shown in figure 4.18 are the static measurements reported in section 3.10 and some static measurements for AISI 4340 steel made by Lee and Kang [120]. The approximate limit for valid plane strain measurements is indicated using both the static value of yield stress and the dynamically adjusted value assuming the relationship of Tanimura and Duffy (equation 2.52) adapted to an axial stress state together with Klepaczko's loading rate relationship (equation 2.54). Again, wide disparity is observed between the En24 HC1 and HC2 specimen batches. Examining the compositional differences between HC1 and HC2 (table 3.1) shows that HC1 has a higher proportion of carbon and a lower proportion of manganese than HC2 both of which should promote more brittle behaviour [121] - the reverse of the observed trend. However, the reduced proportion of silicon [121] and the reduced level of sulphur [91] are both compatible with the observed increase in ductility. Furthermore, hardness tests on the two specimen batches showed that the HC2 specimens (Rockwell C hardness $\sim$ 49 - 50) were harder

than the HC1 specimens (Rockwell C hardness ~ 47 - 48), a variation which suggests slightly different tempering conditions leading to increased ductility of the HC1 specimens [127]. This increased ductility is very obvious in the SEM photographs of the fracture surfaces of the two materials (figures 3.32 and 3.33).

The dynamic fracture toughness values of the En24 HC2 specimens tested at very low temperatures ($T < -40^{o}C$) agree well with the static values at room temperature. However, the dynamic toughness values at room temperature are significantly larger. This positive rate sensitivity is the reverse of the embrittlement generally expected (see section 2.7) and is difficult to explain in the lower part of the transition curve. It is possible, of course, that initiation has taken place earlier than indicated by the S3 strain gauge readings. This possibility will be emphasised in the discussion of crack velocity at initiation for the magnesium alloy specimens (section 5.9) where it is observed that in a displacement-controlled test of this kind a slow crack velocity implies that significant bending loads can remain in the specimen after initiation. In the case of the En24 HC2 specimens, however, estimates of the crack velocity (section 4.12) show that this is not a likely explanation for the elevated dynamic fracture toughness levels. The increased toughness must therefore be attributed to the effect of

strain rate on the critical cleavage stress and/or a local rise in yield stress caused by adiabatic heating at the crack tip.

It is unfortunate that no static fracture toughness measurements were made with the En24 HC1 specimen batch. However, the distribution of dynamic toughness data with temperature is compatible with the static data of Lee and Kang [120] for the similar AISI 4340 steel. The En24 HC1 tests at T = -20°C and T = 20°C did not satisfy the minimum ligament requirement and so are not valid plane strain fracture toughness measurements.

Figure 4.19 shows the variation of dynamic fracture toughness of the En24 HC2 specimens with loading rate. No clear trend can be distinguished across such a limited range (2.3×10^5 MPam$^{\frac{1}{2}}$/s < $\dot{K}_I$ < 9.6×10^5 MPam$^{\frac{1}{2}}$/s), emphasising the need to take measurements on several different kinds of apparatus operating at very different loading rates. The slight positive gradient which may be discerned in figure 4.19 would be compatible with the small delay likely to exist between crack initiation and reaction to it at the S3 strain gauge. If this delay was of constant time then the error in the fracture toughness evaluation would increase with loading rate.

4.10. The constant displacement rate assumption in the inertial model.

Inspection of equations (4.49) and (4.54) shows that the oscillatory part of the P_1 solution for a ramp velocity input lags the equivalent solution for a step velocity input by 90^o, behaviour which is readily seen in figure 4.20a which compares the response to a step input with the response to a real velocity input. (In this case the step velocity input is simply the average of the real velocity input.) This has important consequences for the predicted impactor-specimen interaction and hence for the initial rise of P_2 shown in figure 4.20b from which it is evident that the assumption of constant displacement rate would result in an over-estimate of P_2 and hence of the dynamic fracture toughness (equation 4.58). Over short loading times, therefore, the Hopkinson pressure bar test cannot be considered a constant displacement rate test as is sometimes assumed.

The simple lumped mass-spring model does not allow for separation of the impactor from the specimen or the specimen from its support. Figure 4.20a shows that at this loading rate the P_1 force goes negative after about 23×10^{-6} s if a constant displacement rate is assumed. In reality the behaviour of the specimen then needs to be modelled independently of the stiffness k_1 (since there

will be a gap between specimen and impactor), whereas in the model there is a tensile force restraining the specimen. Williams and Adams [5] ignore this and apply their analytic solution beyond the separation time. A more accurate solution might be achieved by resorting to a free body model until the gap defined by u(t) - v(t) is closed.

However, with the small reservation expressed in section 4.8 with respect to the possible masking effect of the inertial load components, separation does not appear to have occurred in the Hopkinson pressure bar tests reported here, or, at worst, occurred only for very short times.

4.11. The effect of error in the value of equivalent mass.

Given the uncertainty and estimations surrounding the correct derivation of the equivalent mass it is important to establish what effect errors in this parameter might have on the iterated stiffness solutions and the final evaluation of fracture toughness. Table 4.5 gives the iterated stiffness values for a wide range of equivalent mass estimates. From figure 4.21a it can be seen that these parameters have a dramatic effect on the magnitude of oscillation of the P_1-time relationship. This is expected since Williams and Adams [5] have shown that the

size of these oscillations (for the constant displacement rate test) is strongly dependent on the ratio k_1/w. However, the effect on P_2 is not discernible on the scale of figure 4.21b. and the derived fracture toughness values given in table 4.5 are essentially constant.

Thus the value for m' used in the model will not effect the derived fracture toughness, but only the quality of matching the predicted and measured forces. Figure 4.21c shows that the value of m' = 0.023 kg derived from the finite element results (equation 4.20) gives the best fit to the experimental data for this test (HC2 059). This result, together with similar success in predicting the behaviour of the truncated specimens (figure 4.17), gives confidence in the method of determining the equivalent mass and in the integrity of the derived fracture toughness results.

4.12. Can the inertial model be used to estimate crack initiation and propagation velocities?

Examination of figures 3.22a to 3.22c shows a marked variation in the gradient of the force-time traces after crack initiation. At low impact velocity the force takes some 60 x 10^{-6} s to reduce to zero, while at high impact velocity this is achieved in some 20 x 10^{-6} s. It seems

likely that these gradients will be a function of the crack velocity $\dot{a}$ and so it should be possible to estimate the crack velocity from the traces.

For simplicity it was assumed that the crack propagated across the ligament at constant velocity. The solution was run as before until the initiation time was reached, at which point the crack length was incremented to:

$$\frac{a}{W}(I+1) = \frac{a}{W}(I) + \frac{\dot{a}\ (\Delta t)}{W} \qquad (4.65)$$

The corresponding change in the specimen stiffness was computed from equations (4.26) to (4.28) and the solution continued until the ligament was fully cracked when k_2 was set to $k_2 = 0$. The solution was run for several trial crack velocities until a reasonable match was obtained with experimental data.

Two loading conditions were examined for En24 HC2 specimens - at low and high impact velocity. For the case of low impact velocity (figure 4.22) a crack velocity of 50 m/s matches the experimental data quite successfully, while a velocity of 100 m/s is obviously too severe. In the case of high impact velocity (figure 4.23), where the S3 strain gauge suggests initiation on the rising part of the force-time trace, the situation is less clear. A crack velocity of 1000 m/s reproduces the correct behaviour immediately following initiation, but, if true, is

apparently not sustained across the ligament. A crack velocity of 100 m/s is seen to be too slow and perhaps the best value is the compromise of 250 m/s shown in figure 4.23b.

An improved technique of studying crack growth might be achieved by evaluating the stress intensity factor at each increment of growth and making appropriate adjustments to the crack velocity.

As discussed in section 2.7, Bilek [92] has suggested that the value of fracture toughness measured in dynamic tests on AISI 4340 steel is a function of crack velocity. If the estimates of crack velocity above are realistic then this finding is certainly not true of the current data, adding weight to the suspicion that Bilek's finding was a function of crack-tip constraint caused by varying the notch root radius.

4.13. En24 HC3 steel and magnesium alloy results.

It is clear from figure 3.25 that the En24 HC3 steel specimens behaved in a highly ductile manner and so the linear analysis presented here would be inadequate. Accordingly a non-linear algorithm for the specimen stiffness is developed in chapter 5.

Results from the magnesium alloy specimens, although

not necessarily appearing to be non-linear up to crack initiation, did not satisfy the plane strain requirement (equation 2.47) for valid fracture toughness measurements and so further discussion of these results is deferred until after the presentation of the non-linear model.

TABLE 4.1. Values of the equivalent mass m' for varying midspan constraint stiffness k_1.

k_1 (N/m)	k_1/k_2	N_m	w_1 (rad/s)	m' (kg)
2×10^6	.015	1.577	92771	0.01545
2×10^7	.15	1.627	98747	0.01548
2×10^8	1.5	1.97	144771	0.01579
5×10^8	3.8	2.30	197335	0.01620
1×10^9	7.7	2.62	256065	0.01725

N.B. k_2 evaluated from equation (A3.2) for an uncracked beam assuming properties for steel.

TABLE 4.2. Summary of results for En24 HC1 steel:
(a) inertial model stiffness parameters.

Temperature (°C)	-80	-40	-20	20
V_0 (m/s)				
1.5		011	014	
k_1 (x 10^8 N/m)		3.9	3.2	
k_{sup} (x 10^8 N/m)		0.48	0.63	
a/W		.529	.526	
k_s (x 10^7 N/m)		3.51	3.56	
2.5	027	023	016	
k_1	4.7	2.7	4.4	
k_{sup}	1.0	1.05	0.76	
a/W	.534	.524	.535	
k_s	3.44	3.59	3.42	
3.2			029	033
k_1			5.0	4.9
k_{sup}			1.69	1.81
a/W			.555	.559
k_s			3.13	3.07
				035
k_1				4.8
k_{sup}				2.79
a/W				.555
k_s				3.13

TABLE 4.2. (cont.) Summary of results for En24 HC1 steel:
(b) dynamic fracture toughness evaluations.

Temperature (°C)	-80	-40	-20	20
V_0 (m/s)				
1.5		011	014	
t_f (us)		217.4	250.4	
K_{Id}/K_Q ($MPam^{\frac{1}{2}}$)		62.2	76.8	
$\dot{K}_I$ ($x10^5$ $MPam^{\frac{1}{2}}/s$)		2.9	3.1	
Ligament (mm)		4.2 (3.6)	6.6 (5.7)	
2.5	027	023	016	
t_f	98.0	124.4	140.6	
K_{Id}/K_Q	56.0	69.6	76.9	
$\dot{K}_I$	5.7	5.6	5.5	
Lig.	3.1 (2.6)	5.3 (4.5)	6.6 (5.6)	
3.2			029	033
t_f			104.2	146.0
K_{Id}/K_Q			84.1	114.7
$\dot{K}_I$			8.1	7.9
Ligament			7.9 (6.7)	15.5 (13.2)
				035
t_f				144.2
K_{Id}/K_Q				118.5
$\dot{K}_I$				8.2
Ligament				16.5 (14.1)

N.B. Ligament = $2.5 \left[\frac{K_Q}{\sigma_Y}\right]^2$ based on static (dynamic) yield stress. If Ligament < 5.0 then $K_{Id} = K_Q$ (see discussion following equation 2.47).

TABLE 4.3. Summary of results for En24 HC2 steel:
(a) inertial model stiffness parameters.

Temperature (°C)	-80	-40		20		100	
V_0 (m/s)							
1.2				056	057		
k_1 (x 10^8 N/m)				4.3	4.5		
k_{sup} (x 10^8 N/m)				1.28	1.55		
a/W				.517	.510		
k_s (x 10^7 N/m)				3.70	3.81		
1.7				058	059		
k_1				4.5	4.7		
k_{sup}				1.36	1.13		
a/W				.523	.486		
k_s				3.60	4.19		
2.5	066	064	065	050	051	052	053
k_1	4.0	4.1	3.9	4.5	4.3	4.4	4.2
k_{sup}	>90.0	2.70	3.19	1.36	1.30	2.53	1.68
a/W	.505	.545	.531	.527	.522	.526	.534
k_s	3.88	3.27	3.19	3.54	3.62	3.56	3.44
4.2				054	055		
k_1				4.3	4.5		
k_{sup}				1.33	2.34		
a/W				.510	.517		
k_s				3.81	3.70		

(table continued overleaf)

(table 4.3a continued)

Temperature (°C)	-80	-40	20	100
V_0 (m/s)				
0.60			062 063	
k_1			3.5 3.1	
k_{sup}			1.59 1.82	
a/W			.518 .522	
k_s			3.68 3.62	
0.95			060 061	
k_1			3.6 4.0	
k_{sup}			1.65 1.68	
a/W			.520 .537	
k_s			3.65 3.39	

TABLE 4.3. Summary of results for En24 HC2 steel:
(b) dynamic fracture toughness evaluations.

Temperature (°C)	-80	-40		20		100	
V_0 (m/s)							
1.2				056	057		
t_f (us)				178.2	169.0		
K_{Id}/K_Q ($MPam^{\frac{1}{2}}$)				49.7	48.9		
$\dot{K}_I$ ($x10^5$ $MPam^{\frac{1}{2}}/s$)				2.8	2.9		
Ligament (mm)				2.9	2.8		
1.7				058	059		
t_f				125.2	114.8		
K_{Id}/K_Q				51.7	44.8		
$\dot{K}_I$				4.1	3.9		
Ligament				3.1	2.4		
2.5	066	064	065	050	051	052	053
t_f	63.0	69.0	70.4	91.2	94.0	109.8	105.8
K_{Id}/K_Q	39.5	39.1	40.2	52.5	52.7	68.5	63.7
$\dot{K}_I$	6.3	5.7	5.7	5.8	5.6	6.2	6.0
Lig.	1.5	1.7	1.8	3.2	3.3	5.8	5.1
4.2				054	055		
t_f				57.8	55.6		
K_{Id}/K_Q				49.4	53.4		
$\dot{K}_I$				8.5	9.6		
Ligament				2.9	3.4		

(table continued overleaf)

(table 4.3b continued)

Temperature (°C)	-80	-40	20	100
V_0 (m/s)				
0.60			062+ 063+	
t_f			365.6 359.4	
K_{Id}/K_Q			- -	
$\dot{K}_I$			- -	
Ligament			- -	
0.95			060 061	
t_f			204.0 219.2	
K_{Id}/K_Q			47.1 52.1	
$\dot{K}_I$			2.3 2.4	
Ligament			2.6 3.2	

N.B. Ligament = $2.5 \left[\frac{K_Q}{\sigma_Y}\right]^2$ based on static yield stress.

If Ligament < 5.0 then $K_{Id} = K_Q$ (see discussion following equation 2.47).

\+ S3 strain gauge indicates initiation beyond the last force-time measurement point.

TABLE 4.4. Summary of results for En24 HC2 steel (truncated specimens): (a) inertial model stiffness parameters.

Temperature (°C)	-80	-40	20	100
V_0 (m/s)				
1.2			084 085	
k_1 (x 10^8 N/m)			4.7 4.5	
k_{sup} (x 10^8 N/m)			1.23 0.99	
a/W			.507 .504	
k_s (x 10^7 N/m)			3.85 3.90	
1.7				
2.5			080 081	
k_1			4.5 5.1	
k_{sup}			1.04 0.97	
a/W			.519 .490	
k_s			3.67 4.12	
4.2			082 083	
k_1			4.75* 4.75*	
k_{sup}			1.09* 1.09*	
a/W			.501 .515	
k_s			3.95 3.73	

N.B. * Mean values for tests 080/081 and 084/085 (t_f < 2)

TABLE 4.4. Summary of results for En24 HC2 steel
(truncated specimens):
(b) dynamic fracture toughness evaluations.

Temperature (^{o}C)	-80	-40	20	100
V_0 (m/s)				
1.2			084 085	
t_f (us)			- 185.8	
K_{Id}/K_Q (MPam$^{\frac{1}{2}}$)			48.0^{+} 47.8	
$\dot{K}_I$ (x10^5 MPam$^{\frac{1}{2}}$/s)			- 2.6	
Ligament (mm)			2.7 2.7	
1.7				
2.5			080 081	
t_f			- 92.0	
K_{Id}/K_Q			50.6^{-} 48.5	
$\dot{K}_I$			- 5.3	
Ligament			3.0 2.8	
4.2			082 083	
t_f			65.4 61.4	
K_{Id}/K_Q			59.4 54.8	
$\dot{K}_I$			9.1 8.9	
Ligament			4.2 3.6	

N.B. + Based on S3 strain gauge for test 085
- Based on S3 strain gauge for test 081
Ligament as defined in table 4.3b.

TABLE 4.5. The effect of varying the equivalent mass m' on iterated values of k_1 and k_{sup} and hence on the derived fracture toughness (test En24 HC2 059).

m' (kg)	k_1 (Nm^{-1})	k_{sup} (Nm^{-1})	K_{Id} ($MPam^{\frac{1}{2}}$)
0.015	3.1×10^8	1.27×10^8	44.72
0.023	4.7×10^8	1.13×10^8	44.80
0.030	6.5×10^8	1.06×10^8	44.86

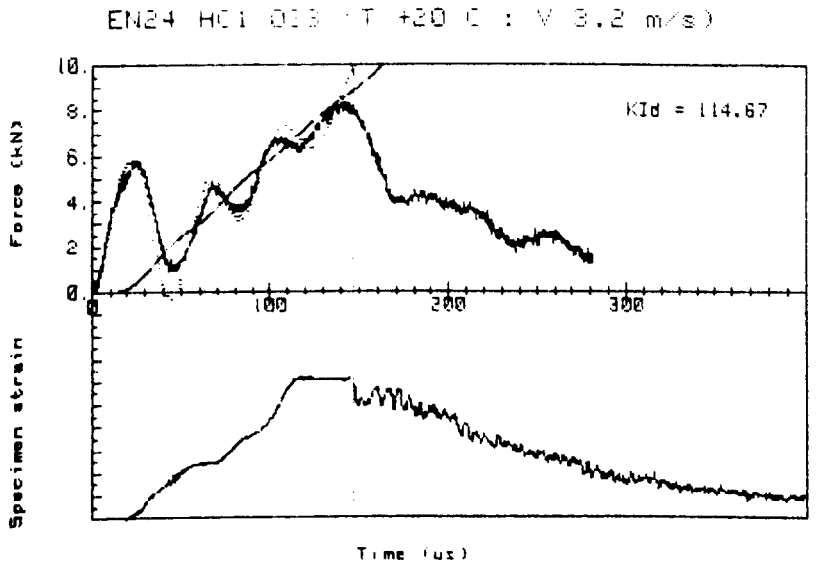

FIG. 4.13a.

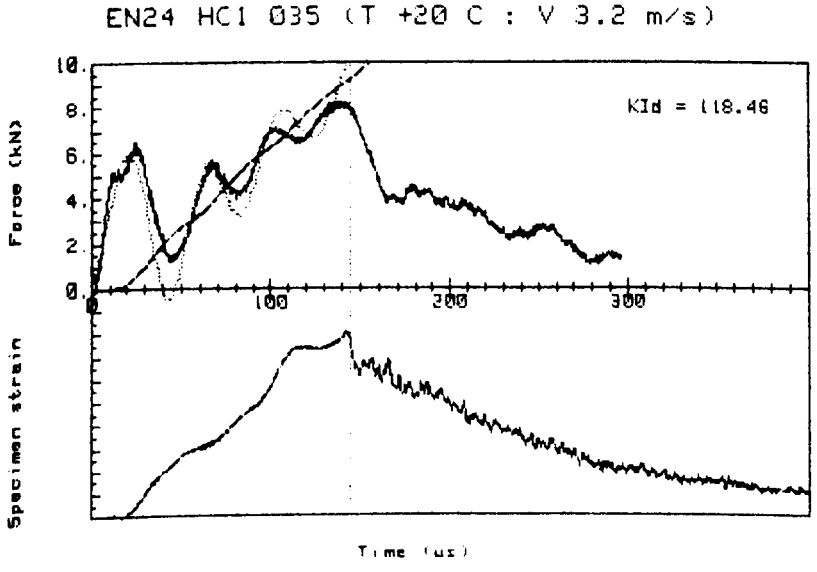

FIG. 4.13b.

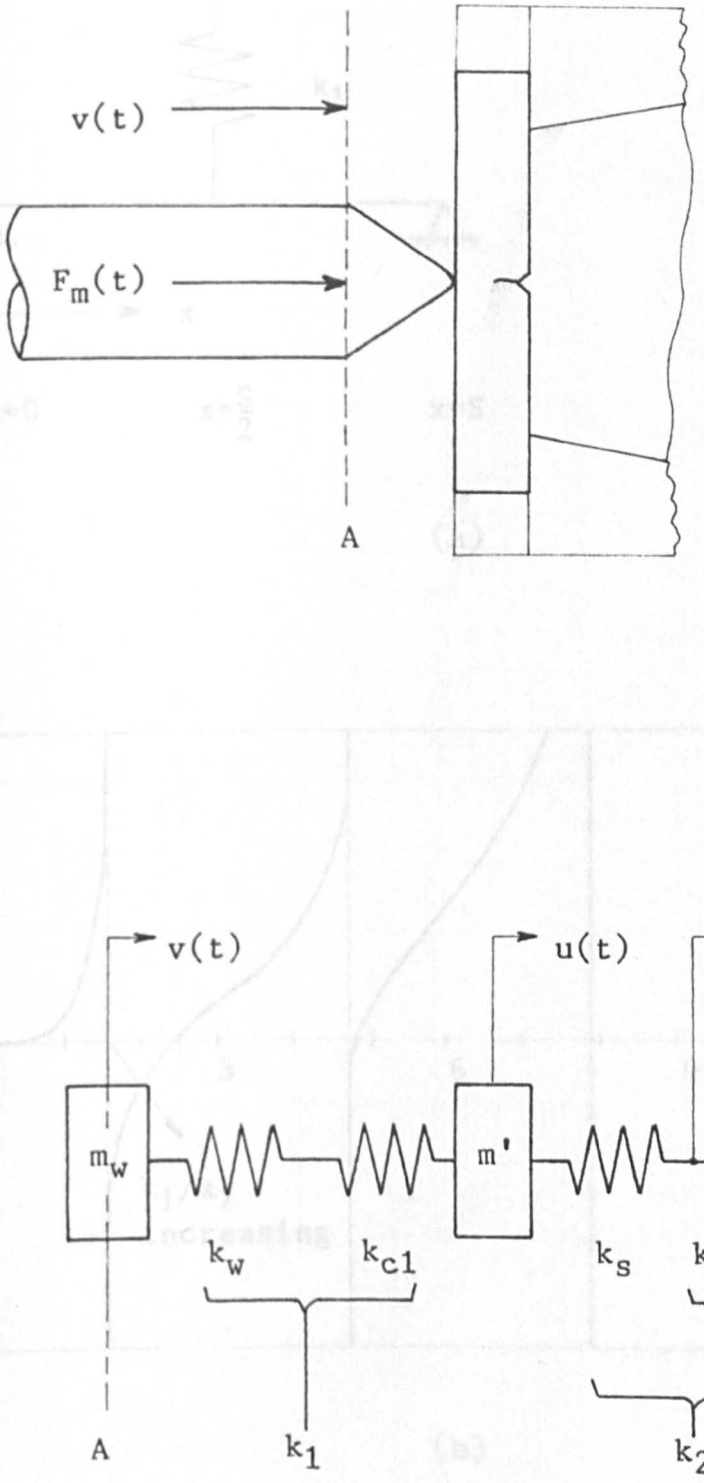

FIG. 4.1. General features of the lumped mass-spring model of the Hopkinson pressure bar test system.

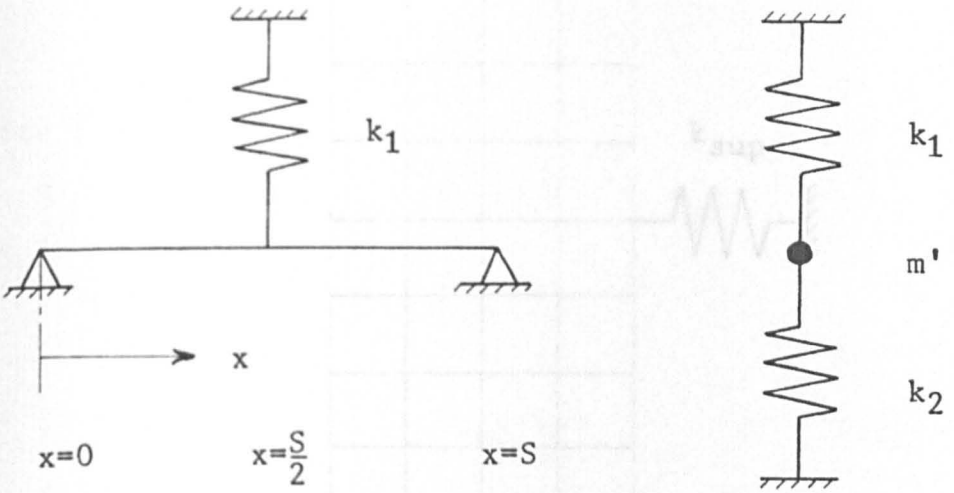

(a)

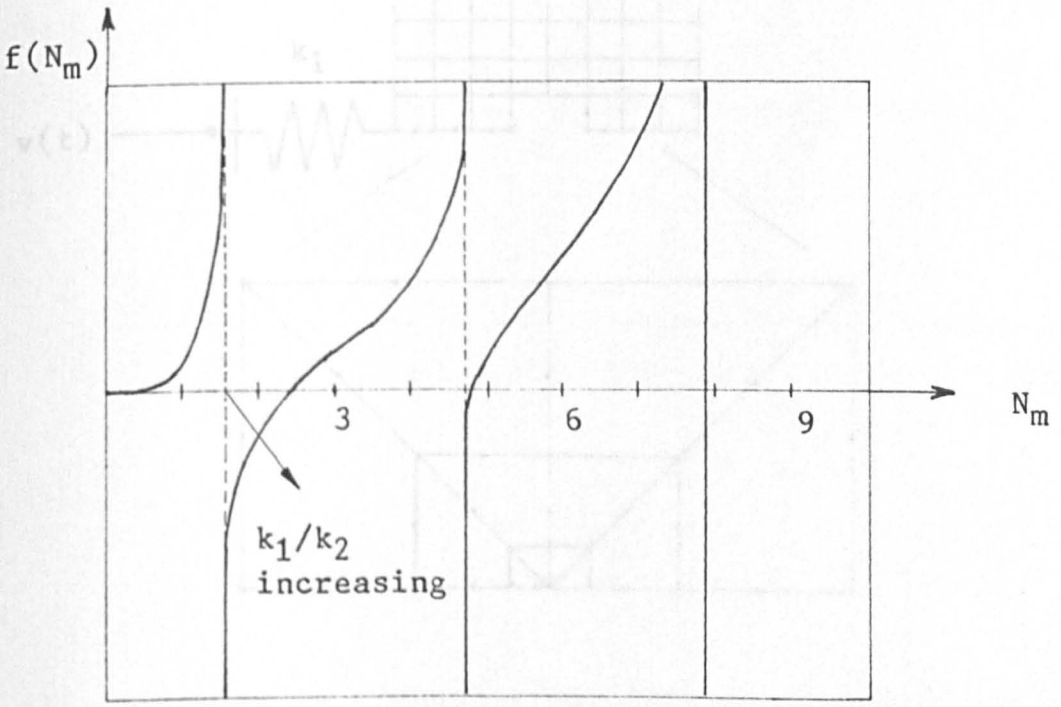

(b)

FIG. 4.2. Geometry of a beam constrained by a spring at its midpoint (a) and solutions to the frequency equation (b).

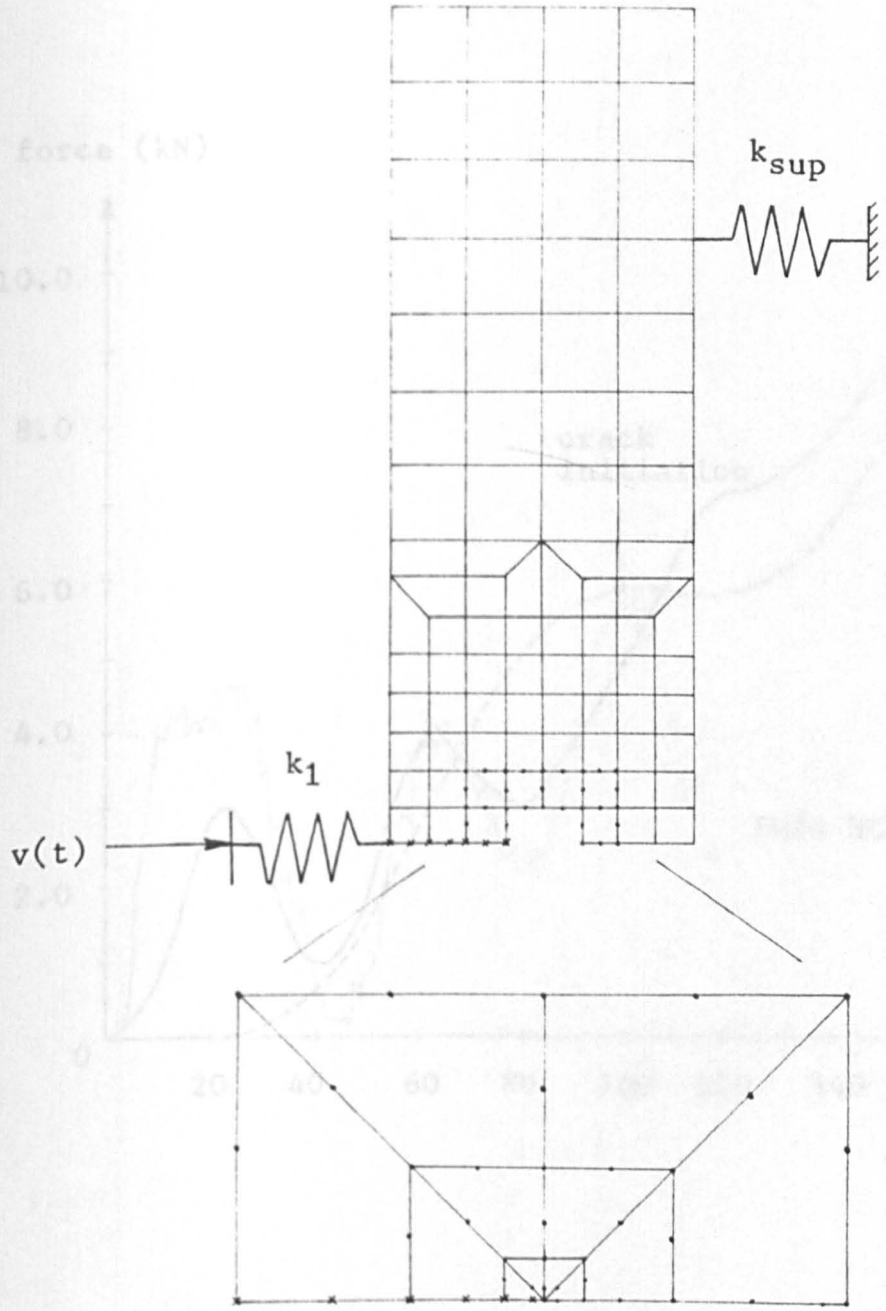

· free node (where shown)

× constrained node ($u_y = 0$)

FIG. 4.3. Finite element model of the three point bend impact specimen with detail of crack tip quarter point and transition elements.

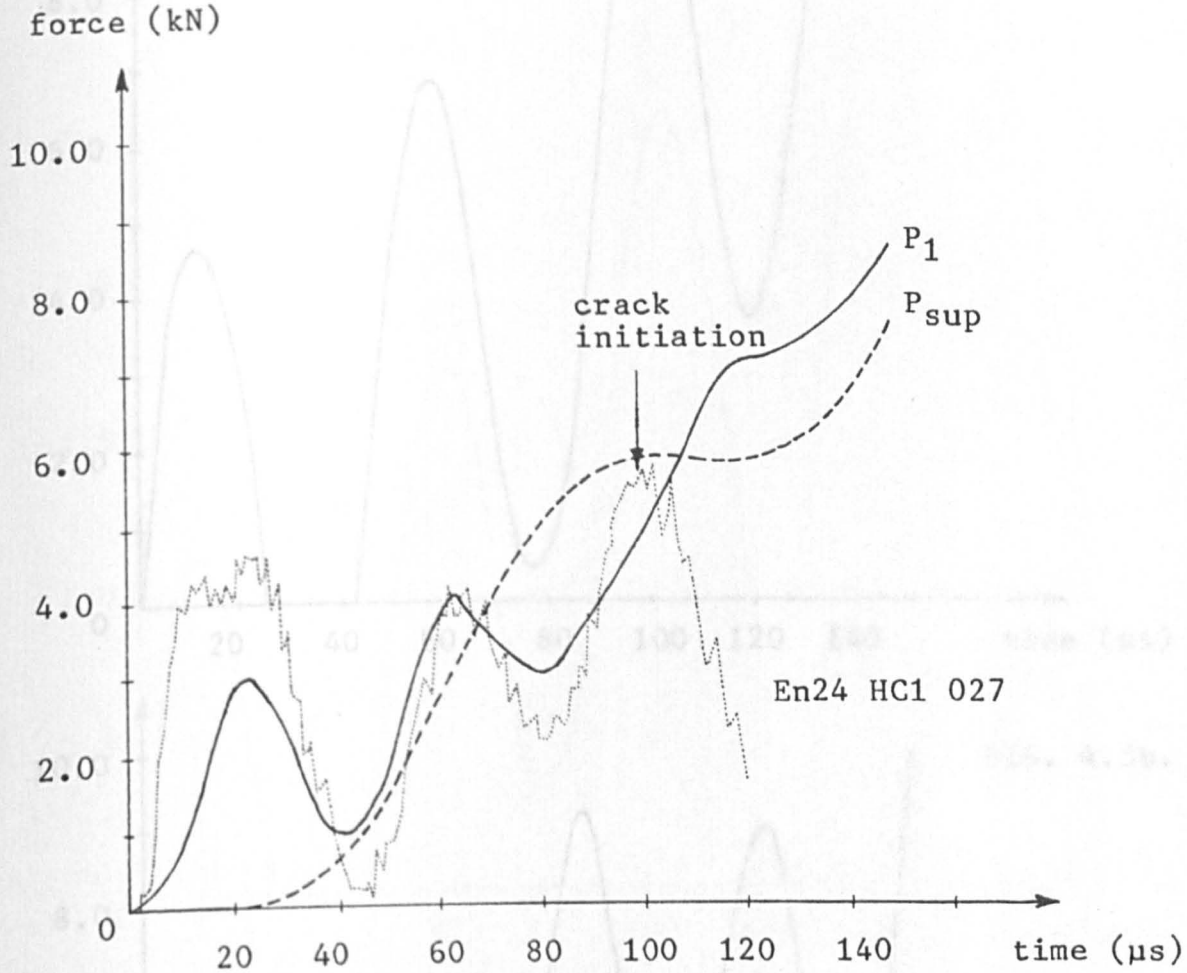

FIG. 4.4. Finite element prediction of measured load (P_1) and support load (P_{sup}) for input real displacement function from test En24 HC1 027.

Overleaf:

FIG. 4.5. Finite element prediction of measured load (P_1) for constant displacement rate in a standard steel Charpy specimen (a) and truncated specimen (b).

FIG. 4.5a.

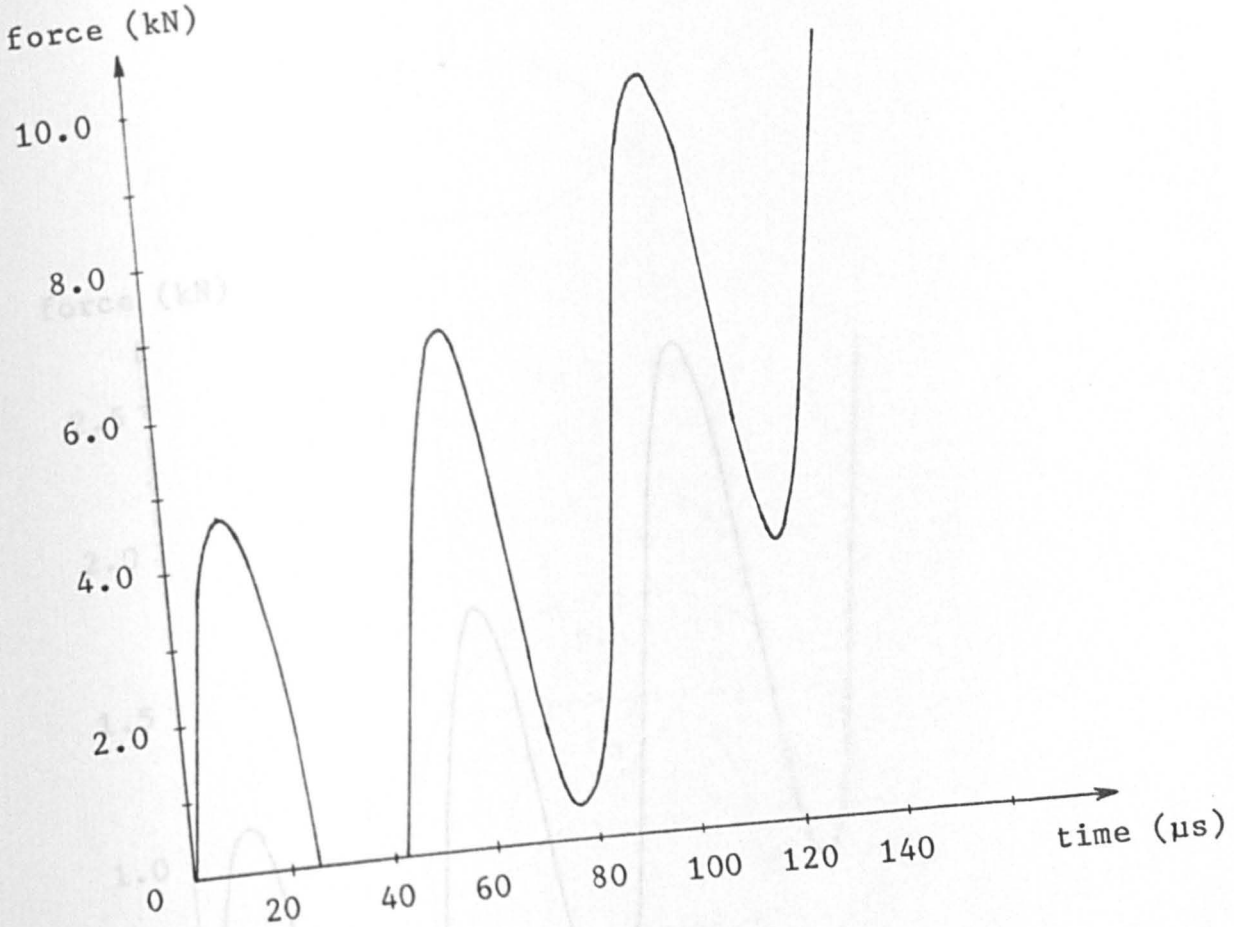

FIG. 4.5b.

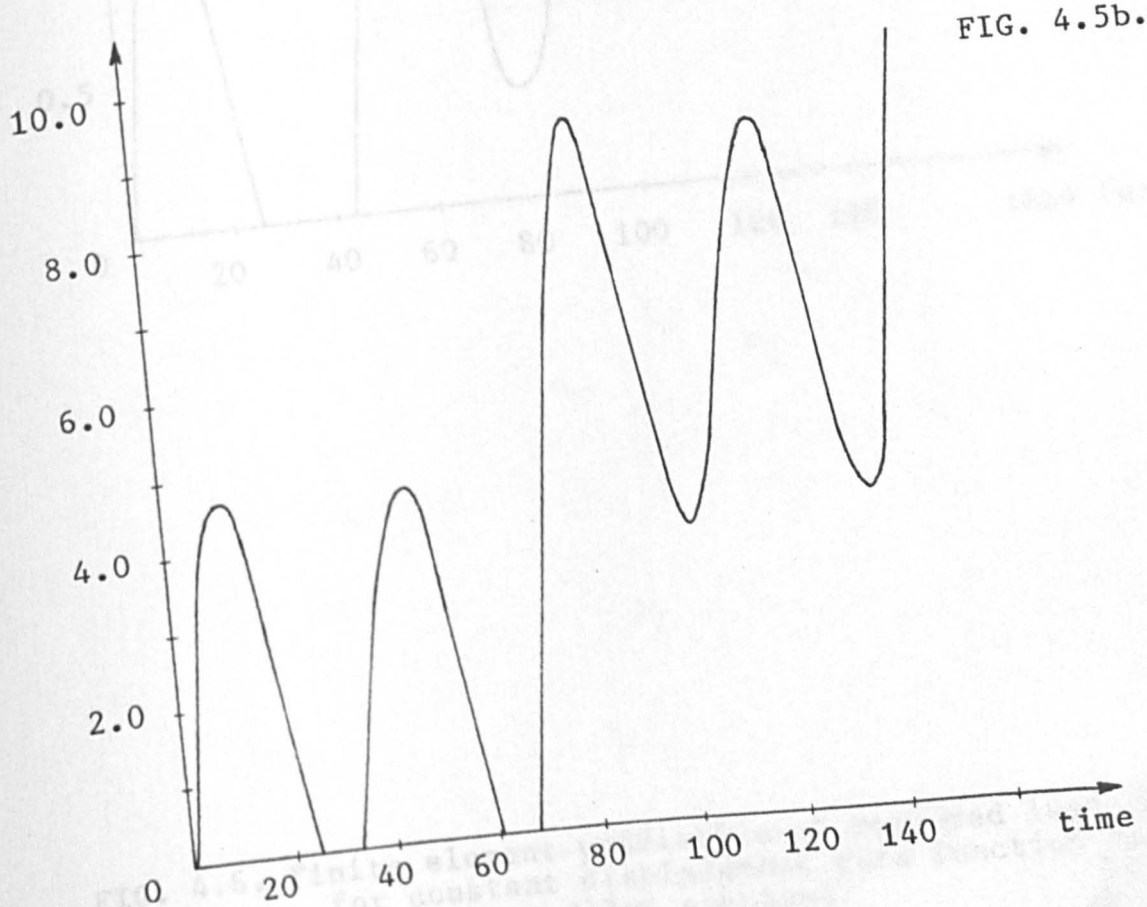

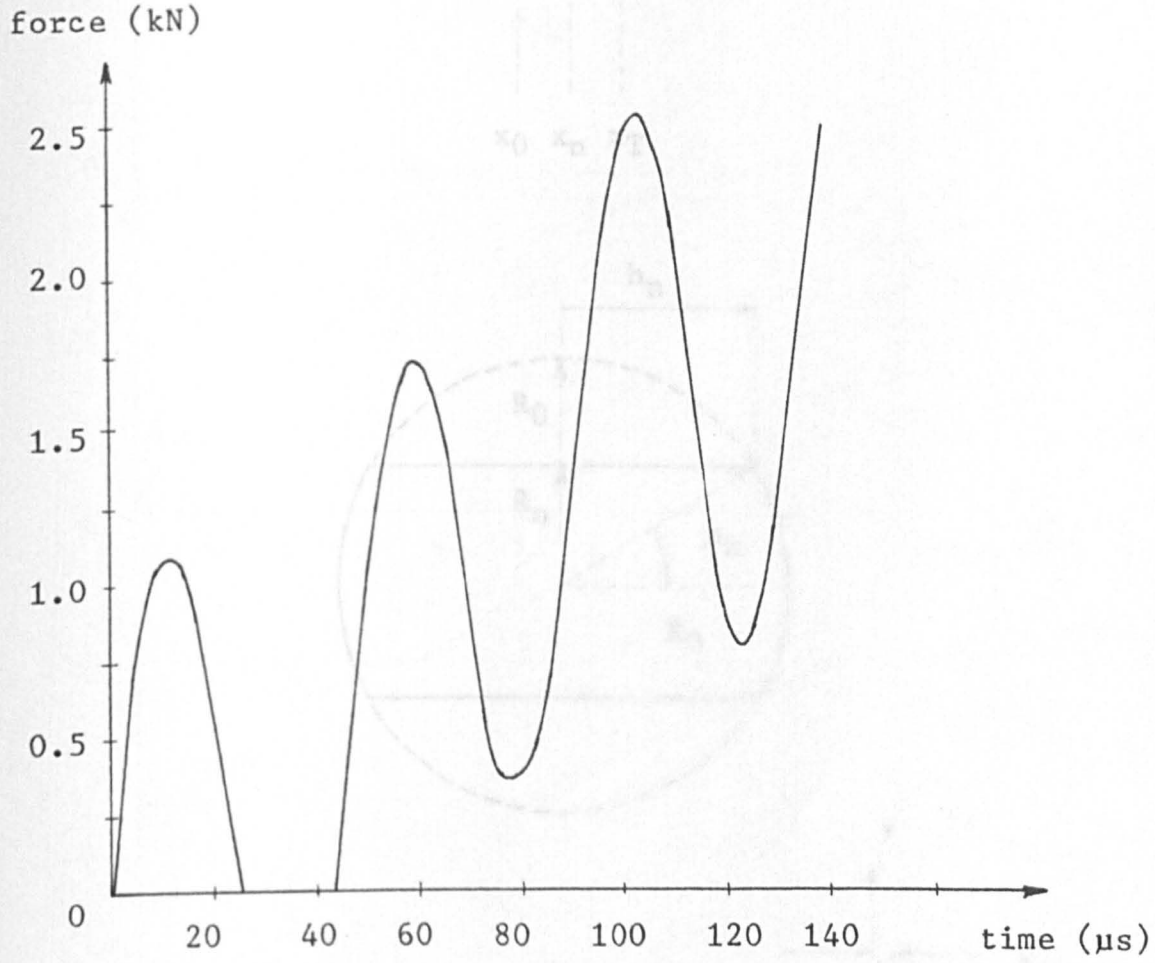

FIG. 4.6. Finite element prediction of measured load (P_1) for constant displacement rate function in a magnesium alloy specimen.

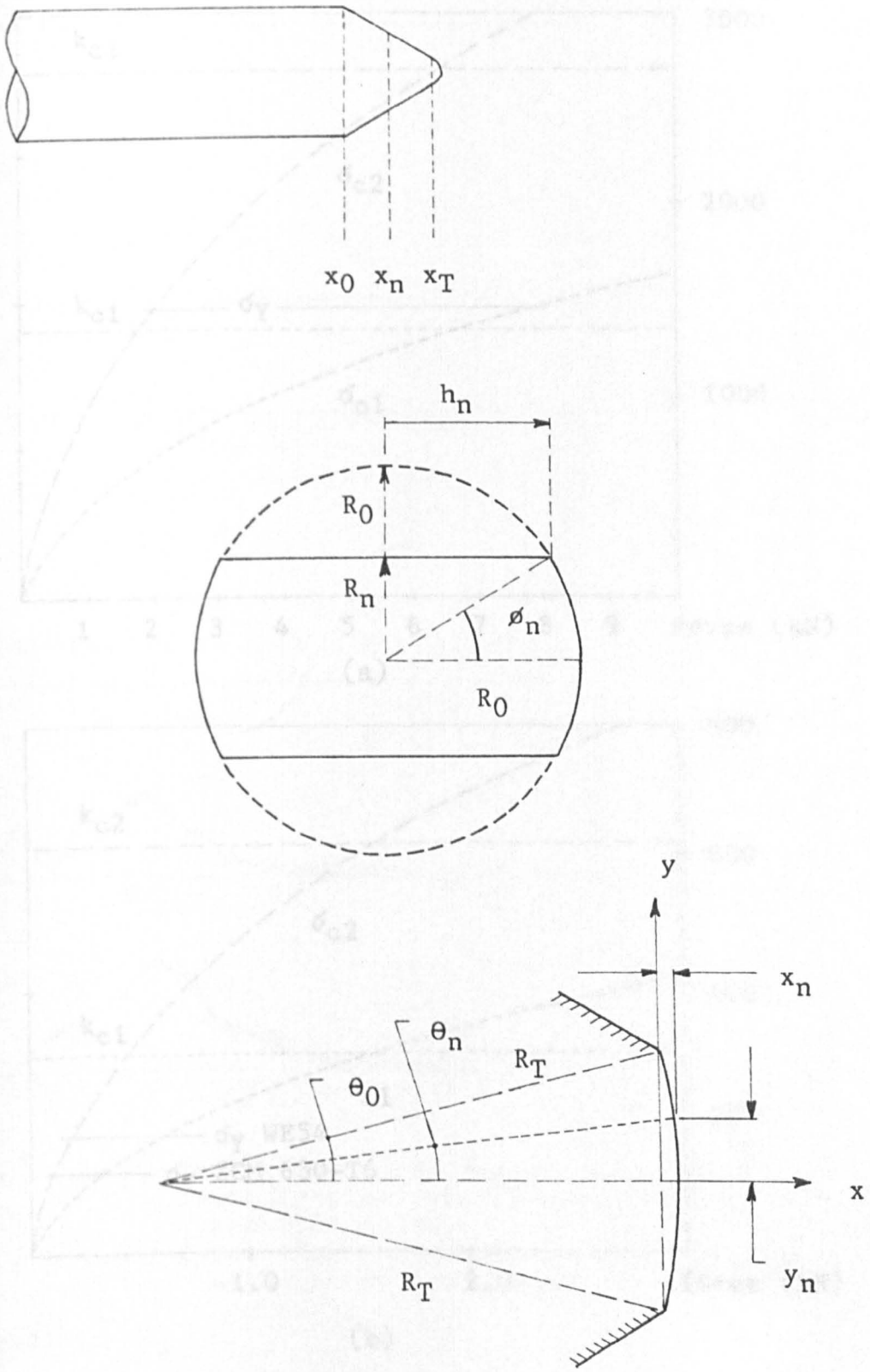

FIG. 4.7. Profiled end section of incident bar: geometry for stiffness calculation.

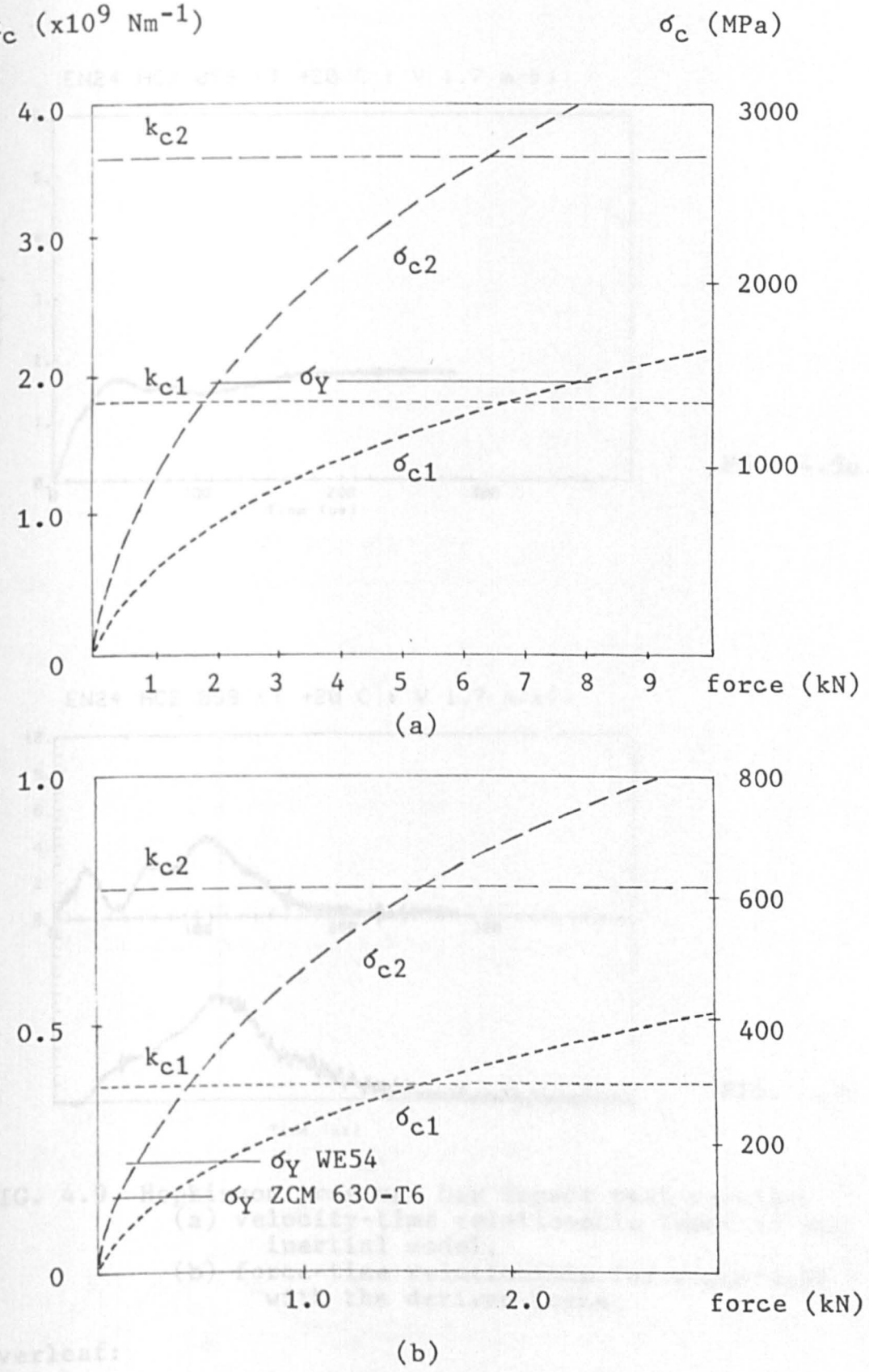

FIG. 4.8. Contact stiffness and mean stress in the contact zone for En24 HC1/HC2 steel (a) and magnesium alloy (b).

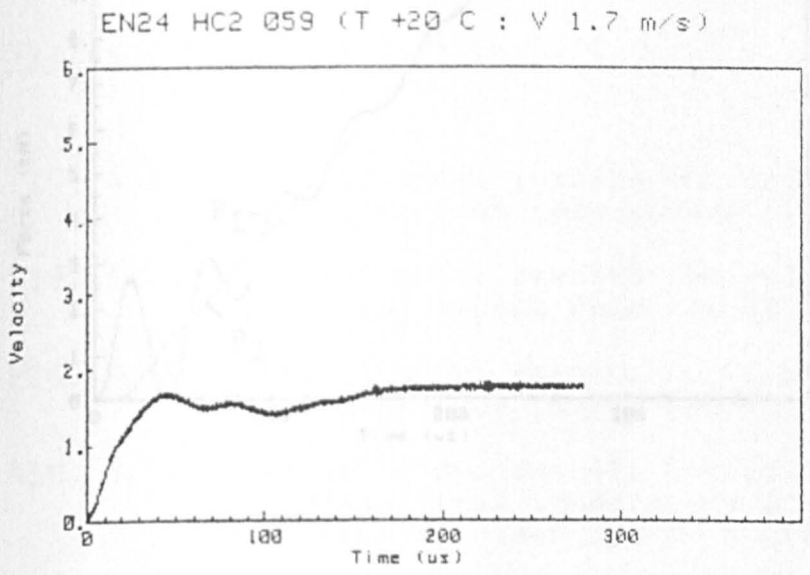

FIG. 4.9a.

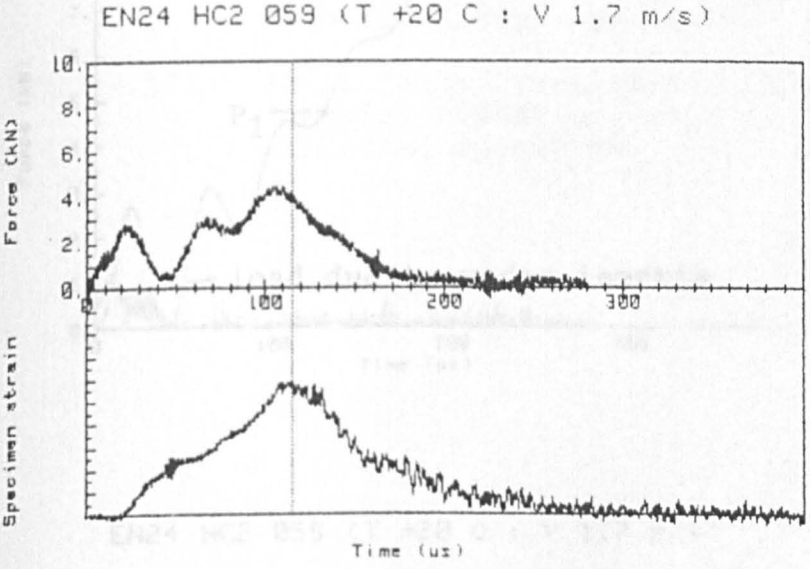

FIG. 4.9b.

FIG. 4.9. Hopkinson pressure bar impact test results:
(a) velocity-time relationship input to the inertial model,
(b) force-time relationship for comparison with the derived force.

Overleaf:

FIG. 4.10. Inertial model results:
(a) derived forces P_1 and P_2,
(b) derived forces P_1 and wedge inertia,
(c) derived force F_p compared with measured force F_m.

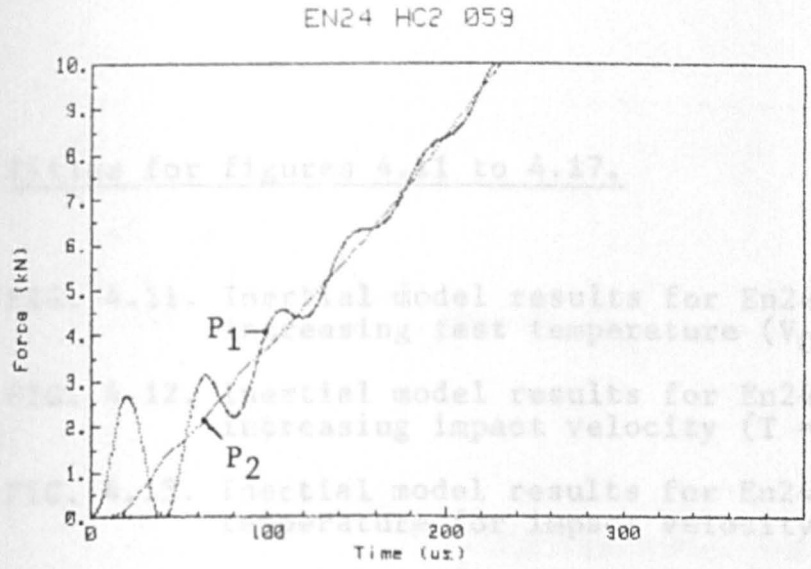

FIG. 4.10a.

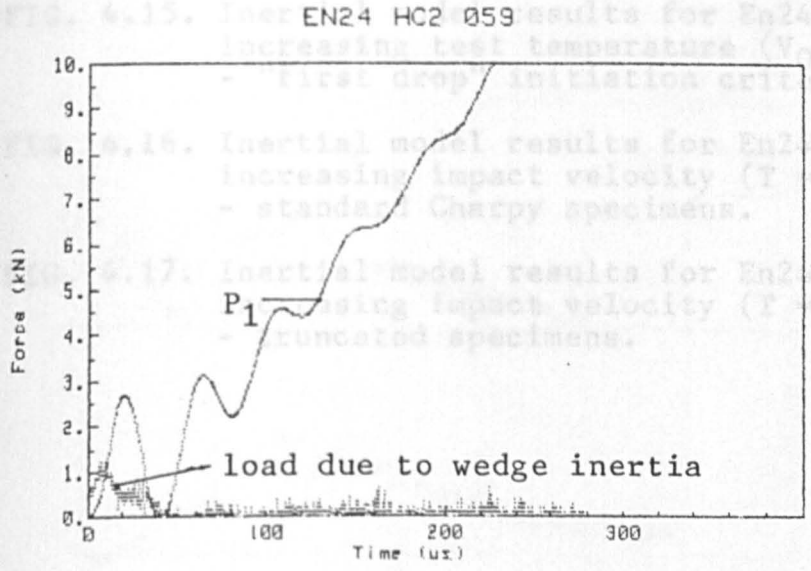

FIG. 4.10b.

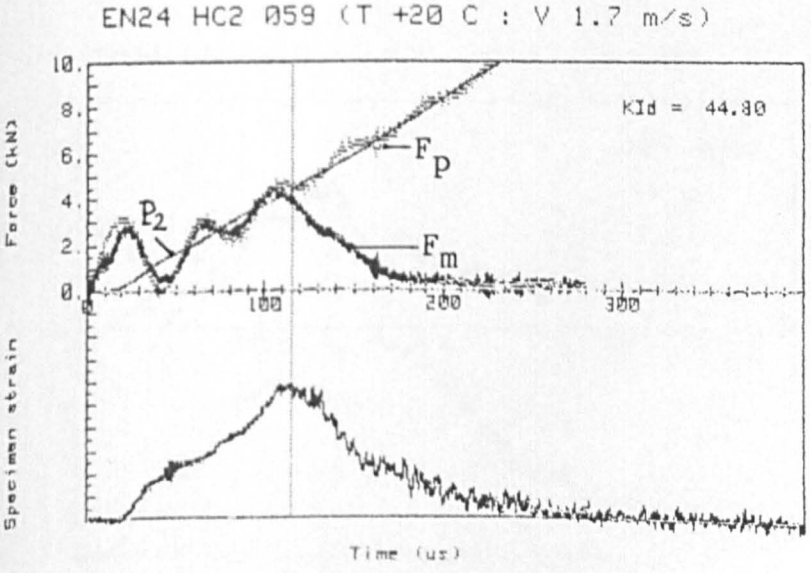

FIG. 4.10c.

Titles for figures 4.11 to 4.17.

FIG. 4.11. Inertial model results for En24 HC1 with increasing test temperature (V_0 = 2.5 m/s).

FIG. 4.12. Inertial model results for En24 HC1 with increasing impact velocity (T = -20°C).

FIG. 4.13. Inertial model results for En24 HC1 at room temperature for impact velocity V_0 = 3.2 m/s.

FIG. 4.14. Inertial model results for En24 HC2 with increasing test temperature (V_0 = 2.5 m/s) - maximum specimen strain criterion.

FIG. 4.15. Inertial model results for En24 HC2 with increasing test temperature (V_0 = 2.5 m/s) - "first drop" initiation criterion.

FIG. 4.16. Inertial model results for En24 HC2 with increasing impact velocity (T = 20°C) - standard Charpy specimens.

FIG. 4.17. Inertial model results for En24 HC2 with increasing impact velocity (T = 20°C) - truncated specimens.

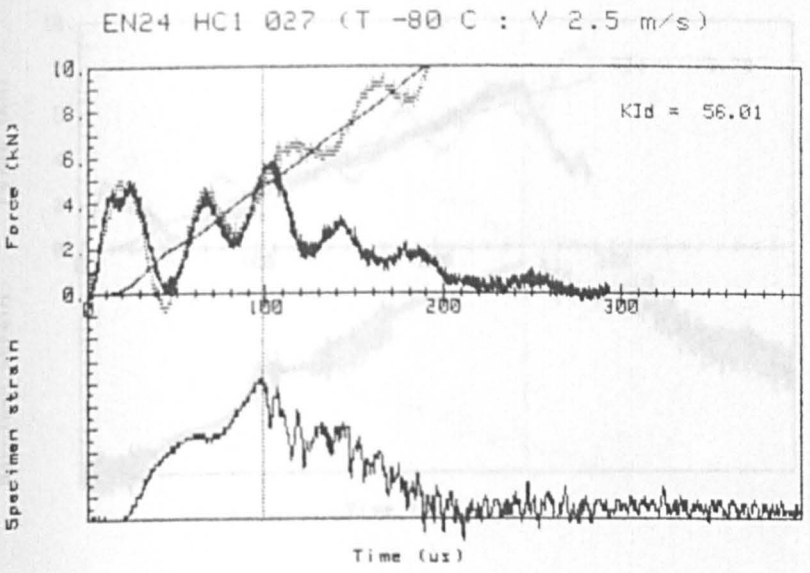

FIG. 4.11a.

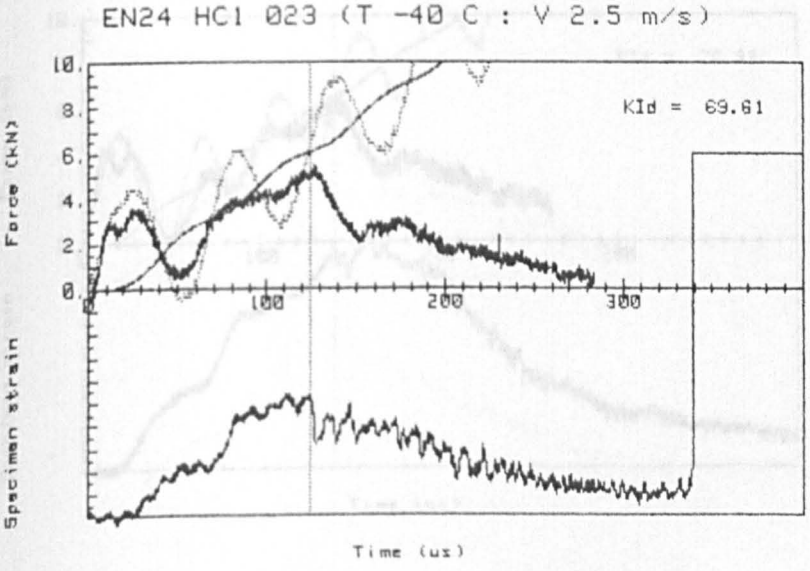

FIG. 4.11b.

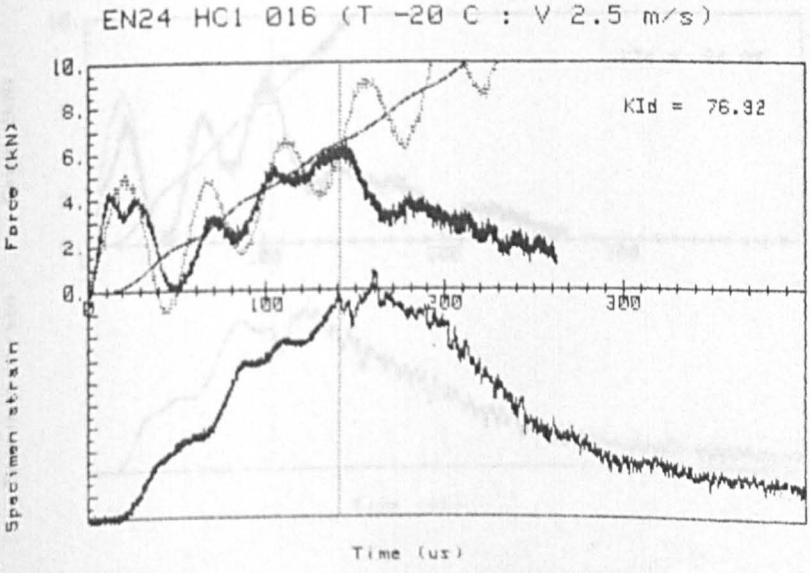

FIG. 4.11c.

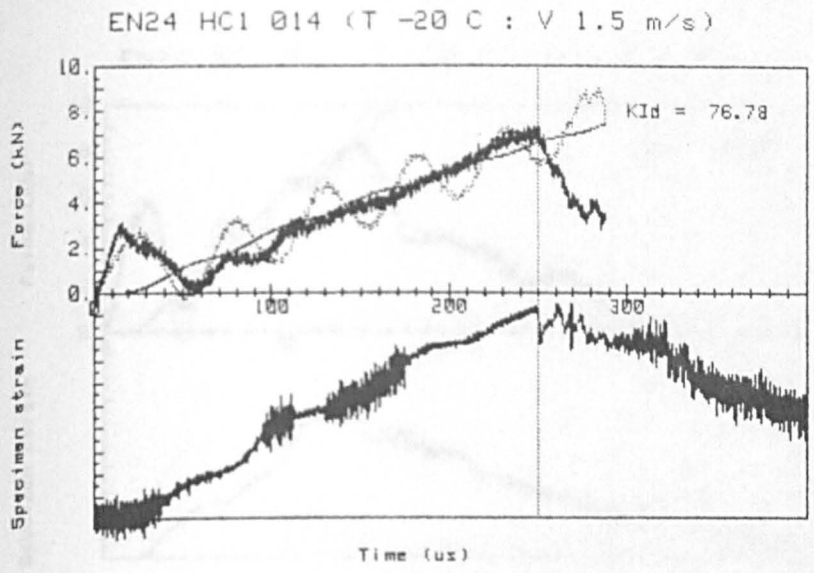

FIG. 4.12a.

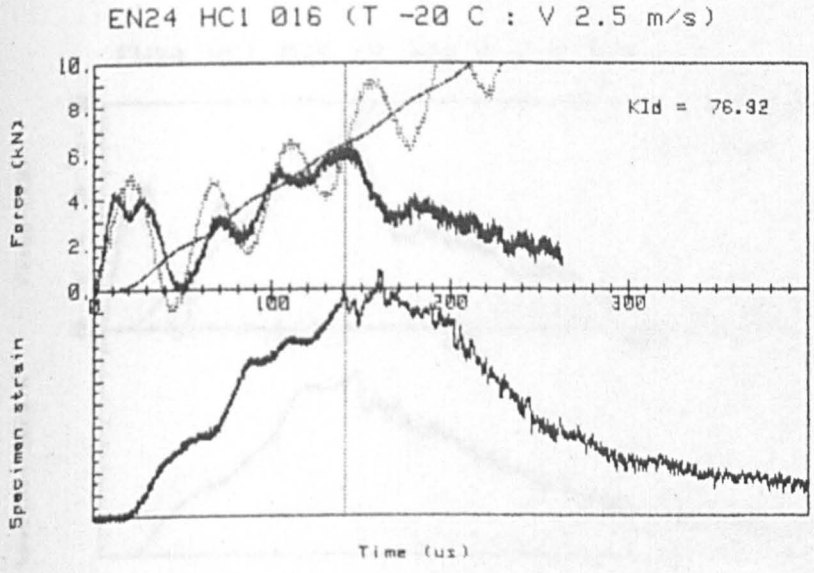

FIG. 4.12b.

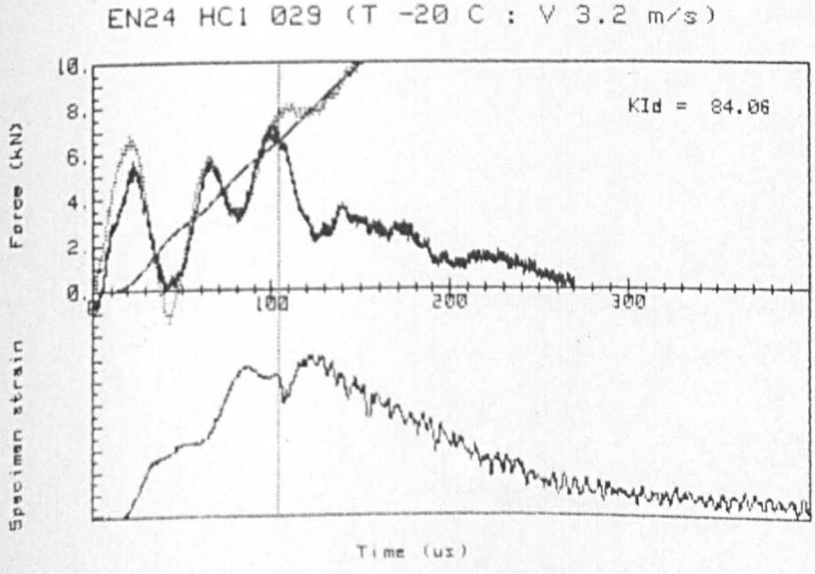

FIG. 4.12c.

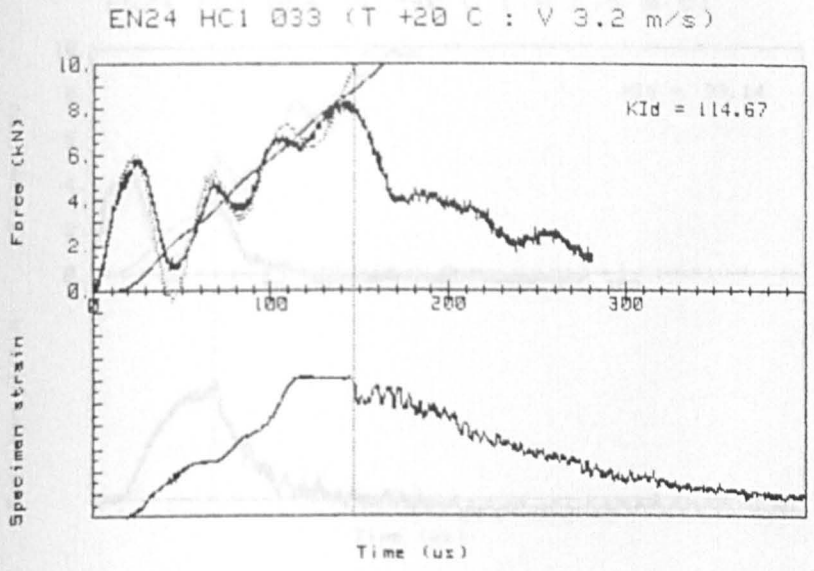

FIG. 4.13a.

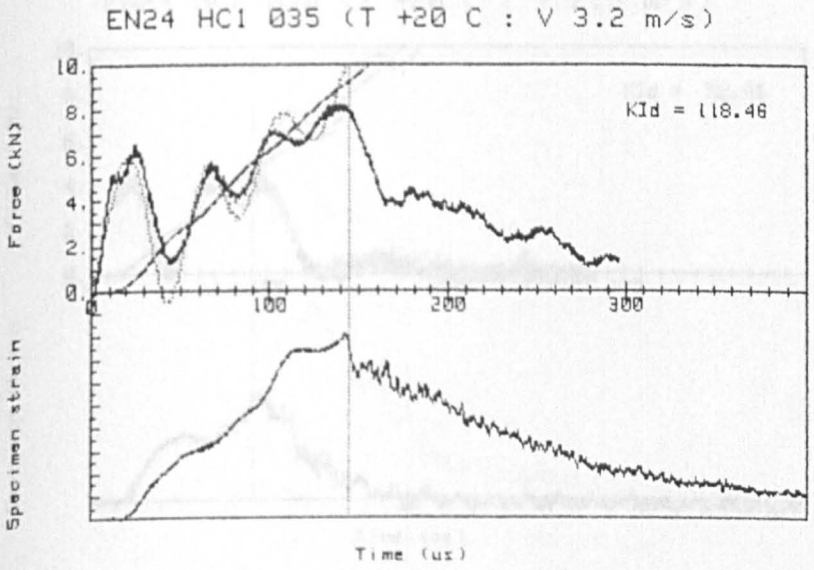

FIG. 4.13b.

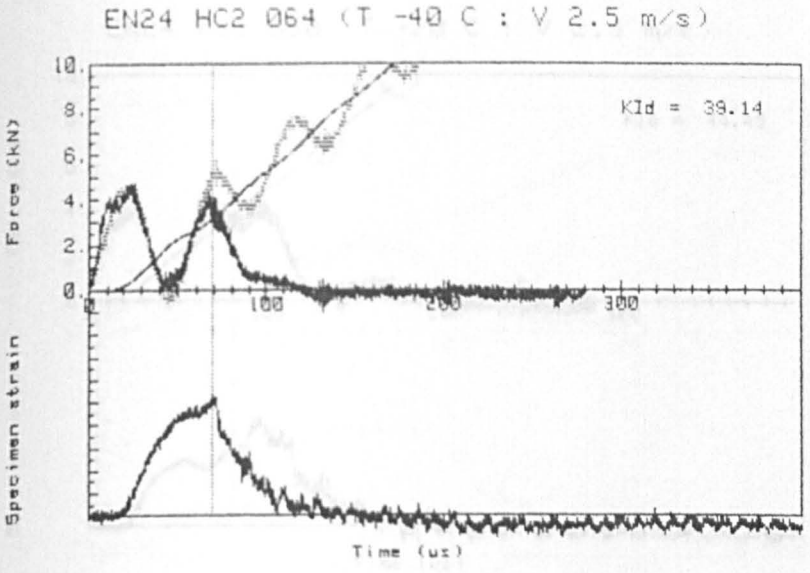

FIG. 4.14a.

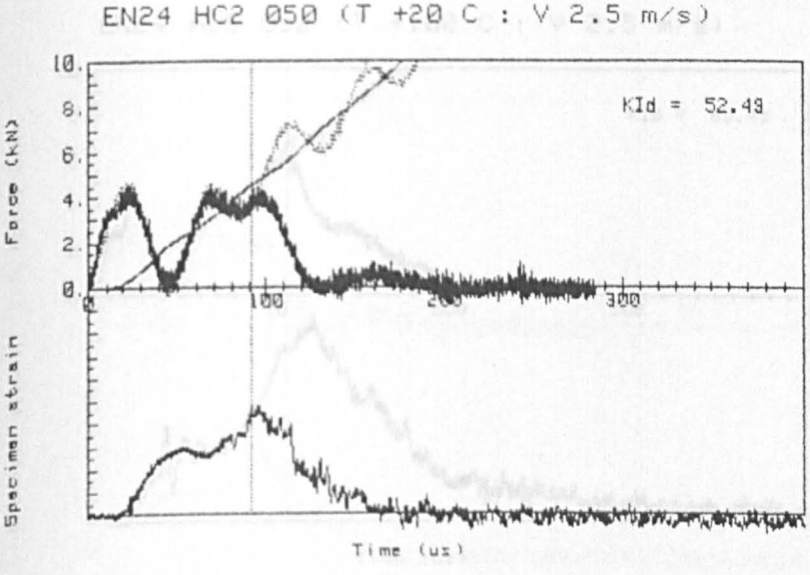

FIG. 4.14b.

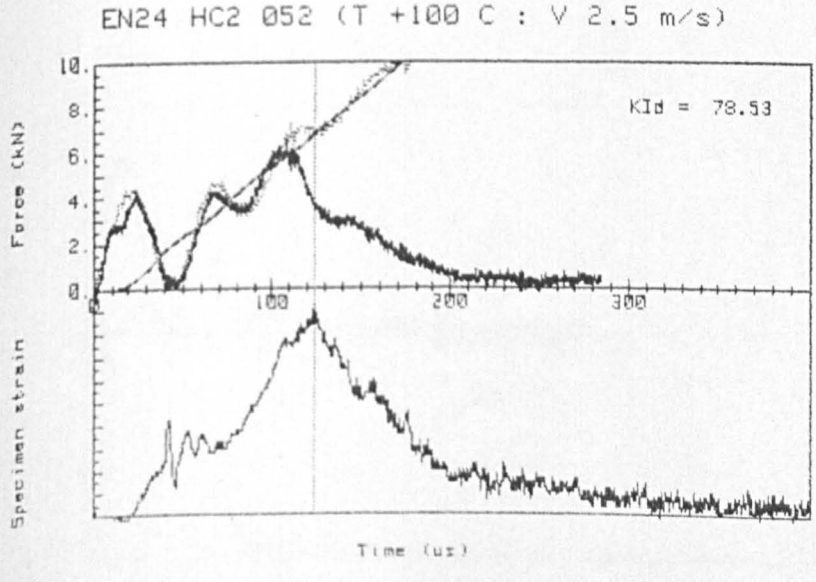

FIG. 4.14c.

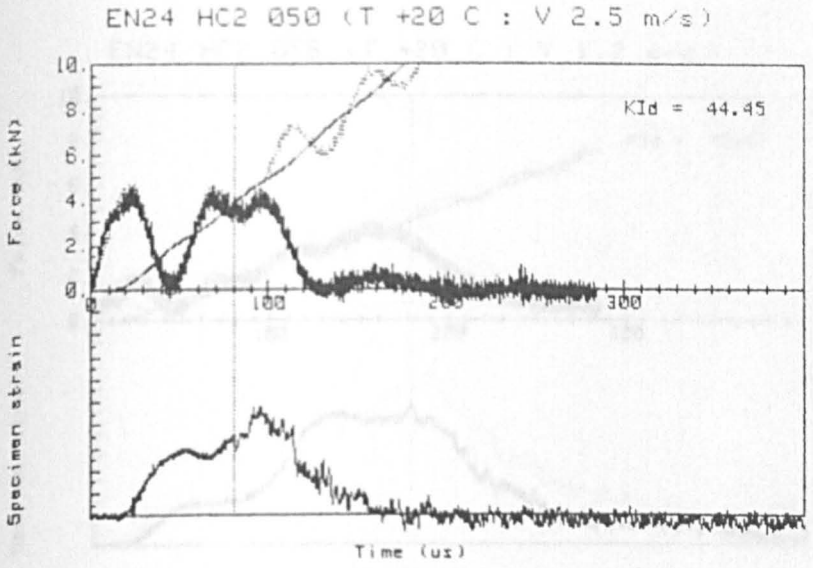

FIG. 4.15a.

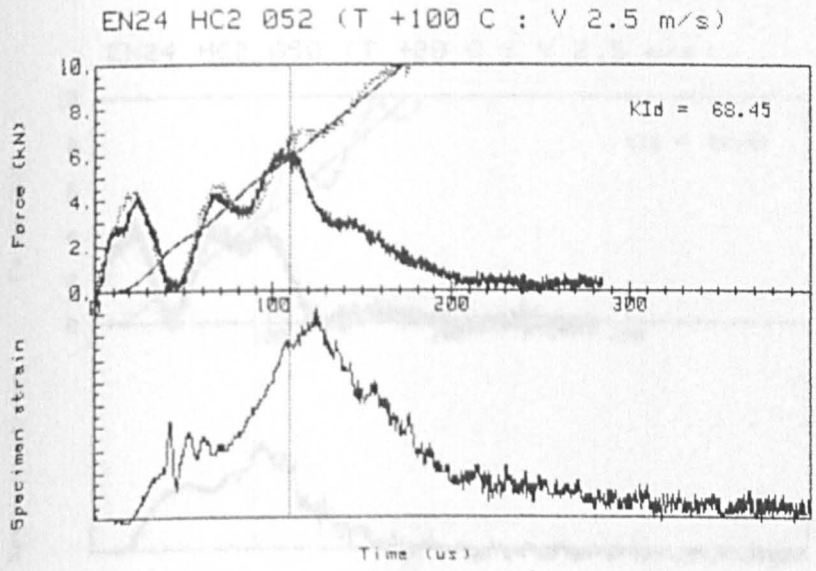

FIG. 4.15b.

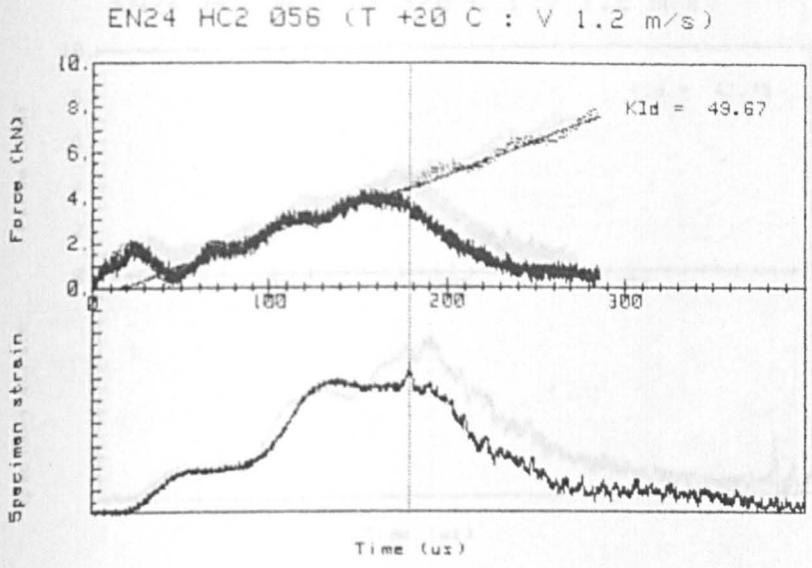

FIG. 4.16a.

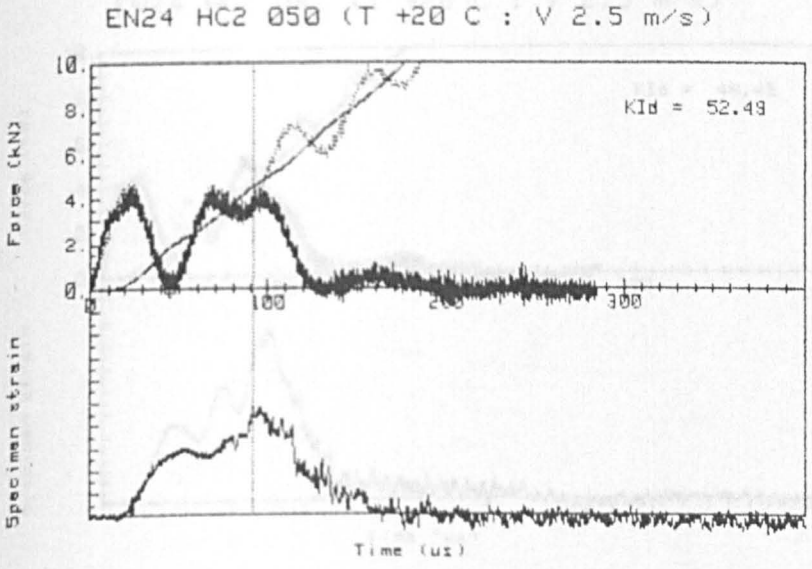

FIG. 4.16b.

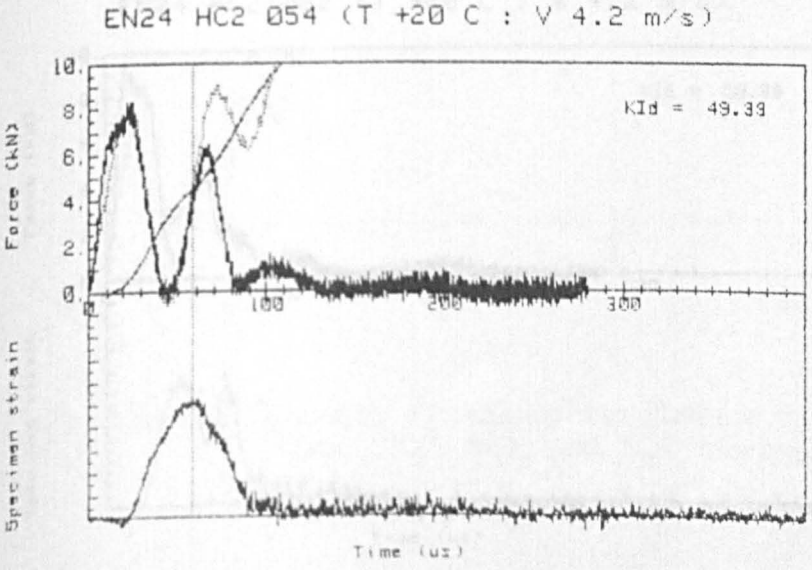

FIG. 4.16c.

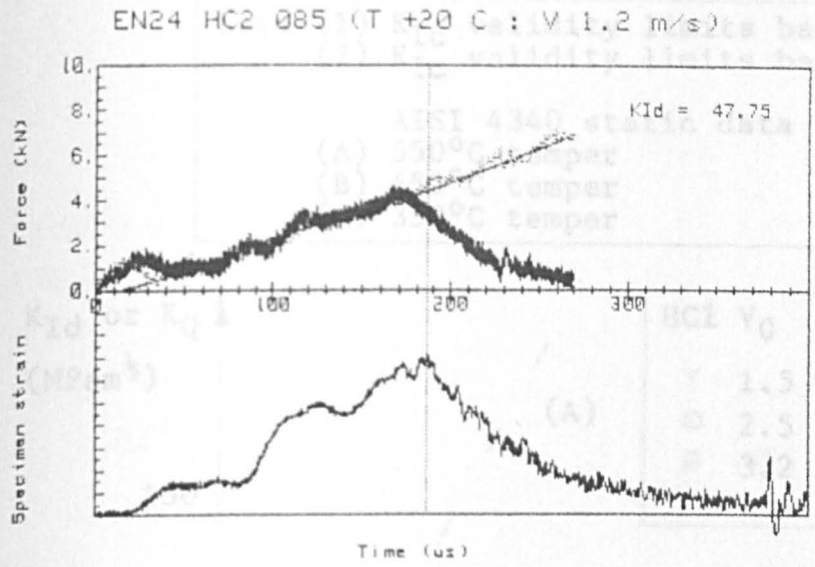

FIG. 4.17a.

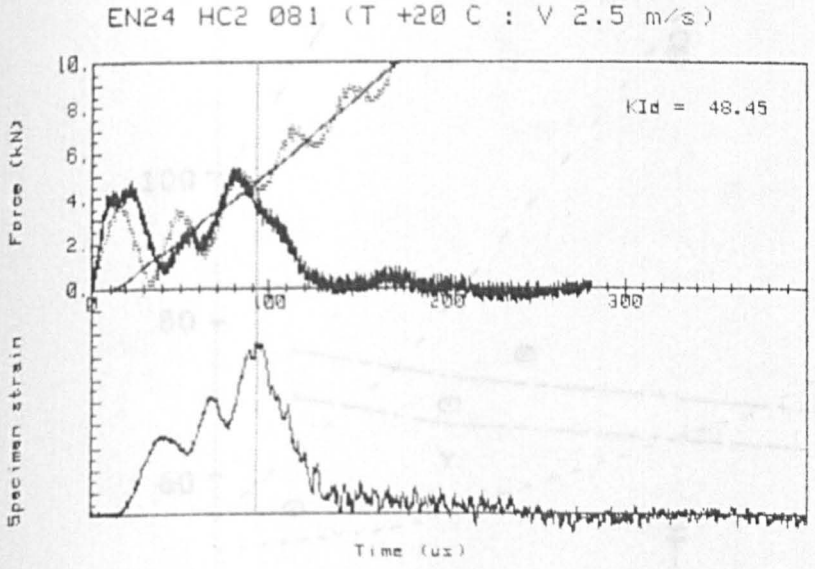

FIG. 4.17b.

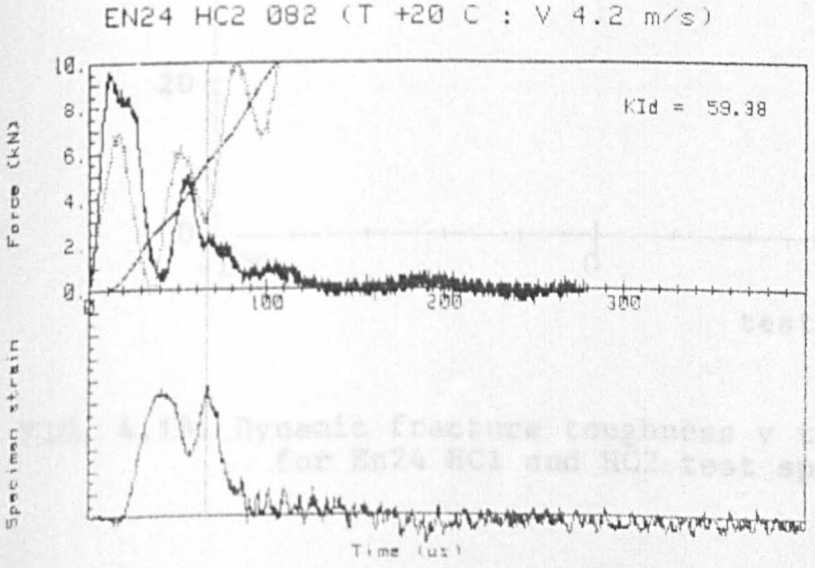

FIG. 4.17c.

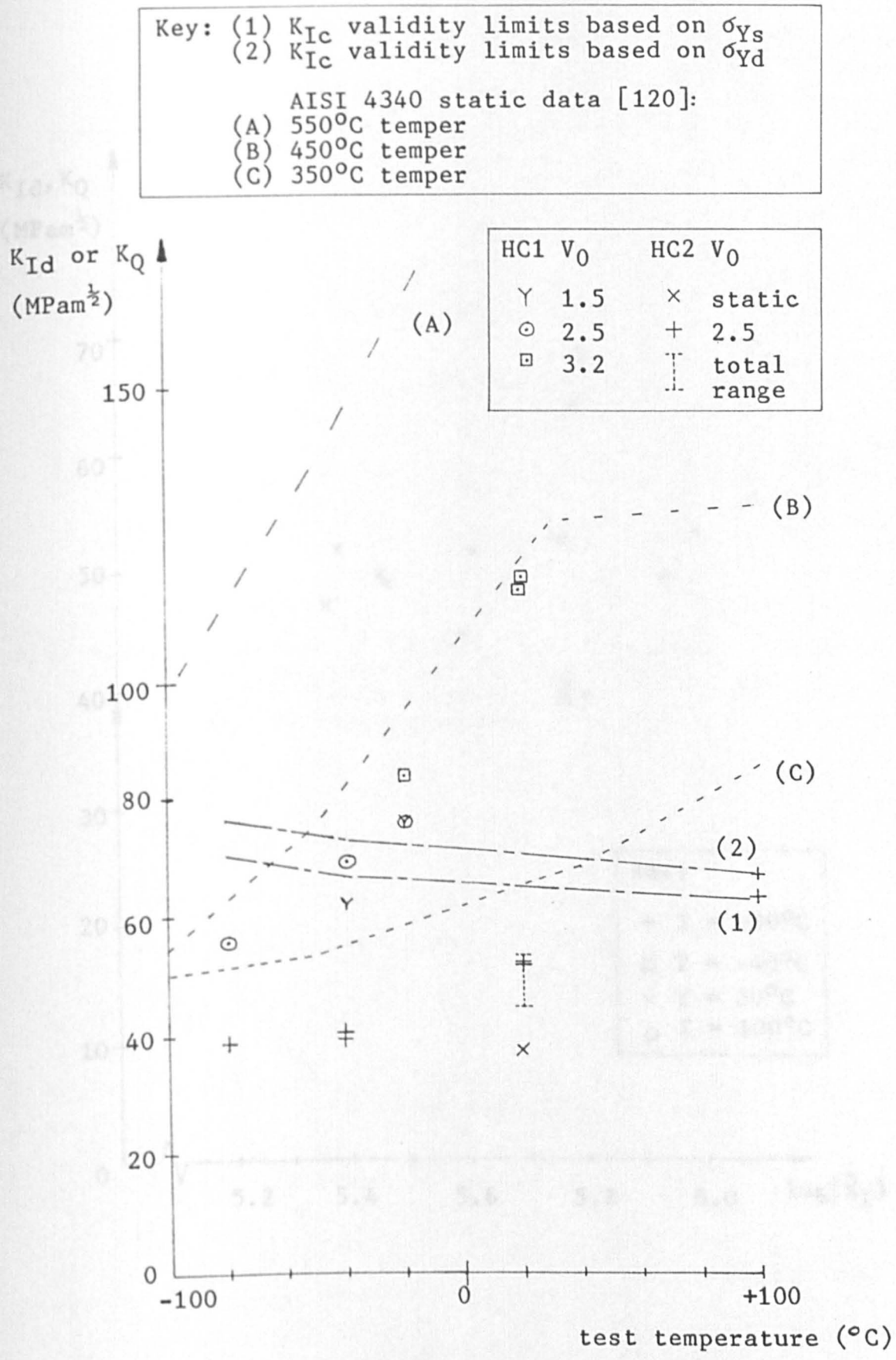

FIG. 4.18. Dynamic fracture toughness v test temperature for En24 HC1 and HC2 test specimens.

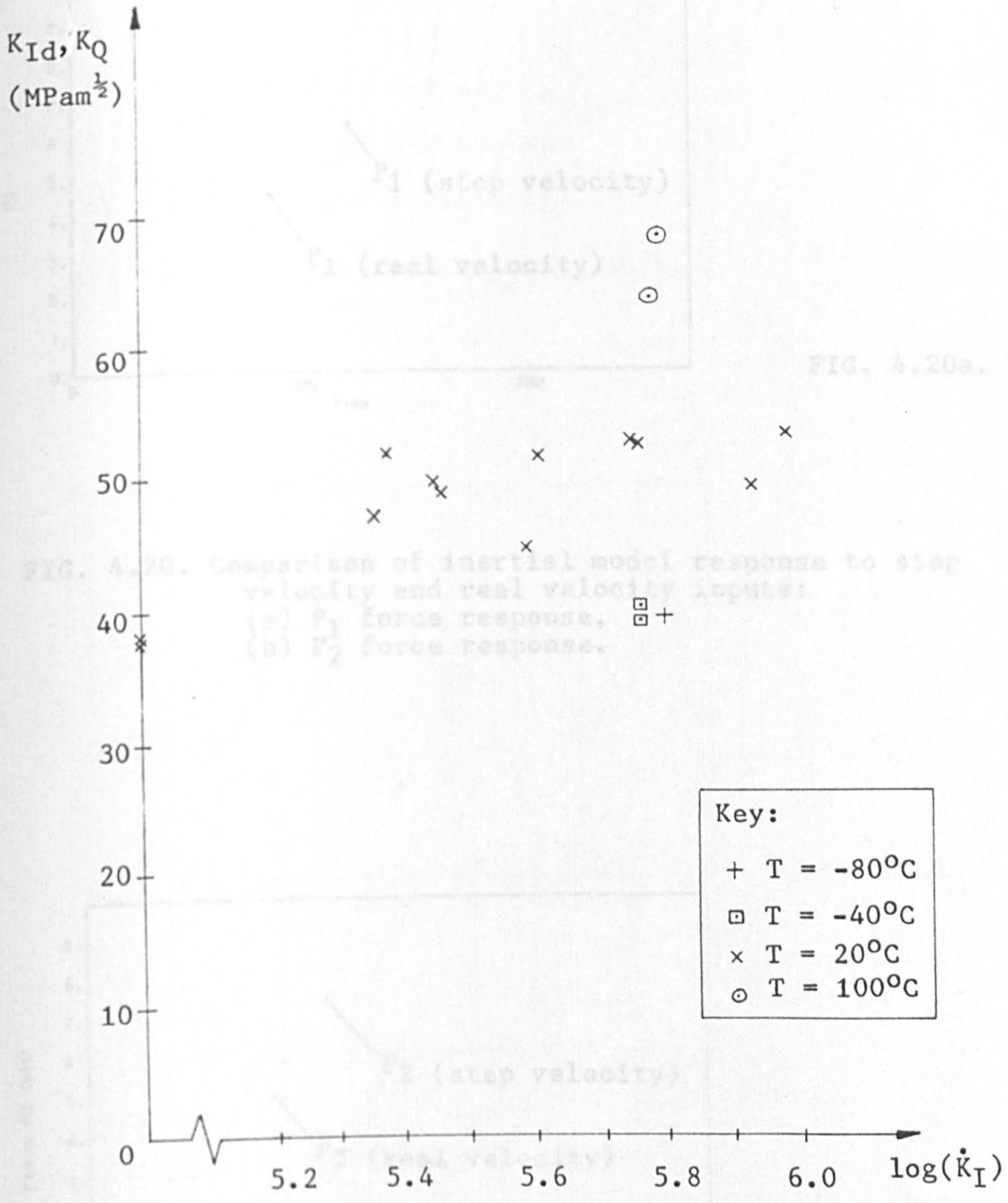

FIG. 4.19. Dynamic fracture toughness v loading rate for En24 HC2 test specimens.

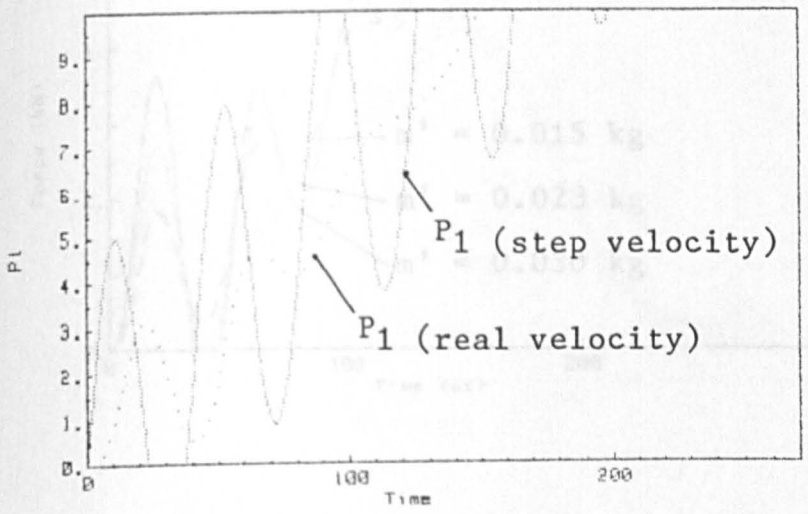

FIG. 4.20a.

FIG. 4.20. Comparison of inertial model response to step velocity and real velocity inputs:
(a) P_1 force response,
(b) P_2 force response.

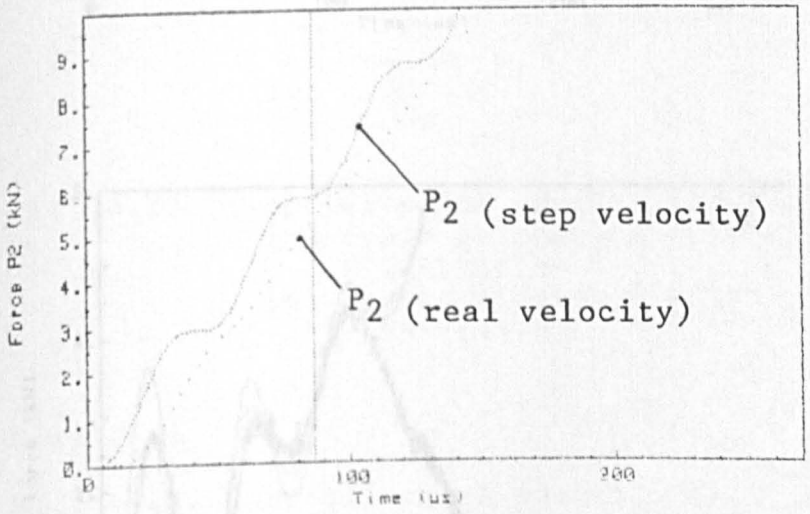

FIG. 4.20b.

Overleaf:

FIG. 4.21. Effect of varying equivalent mass on:
(a) P_1 force response, (b) P_2 force response,
(c) P_1 compared with measured force.

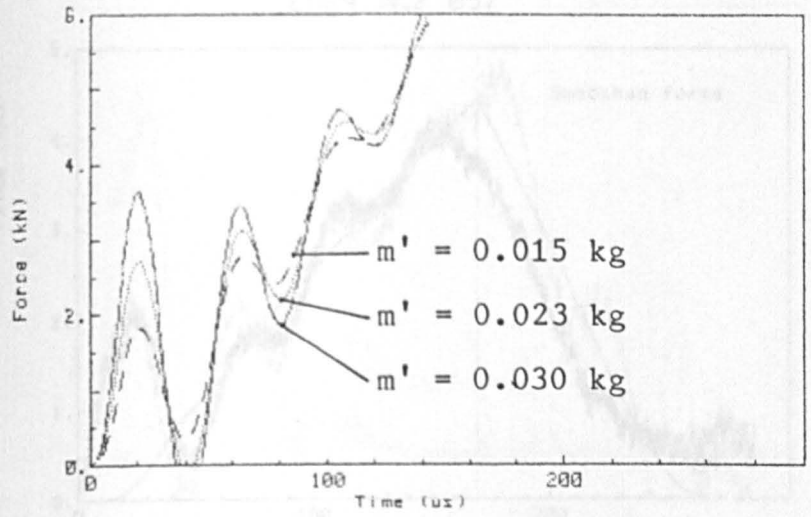

FIG. 4.21a.

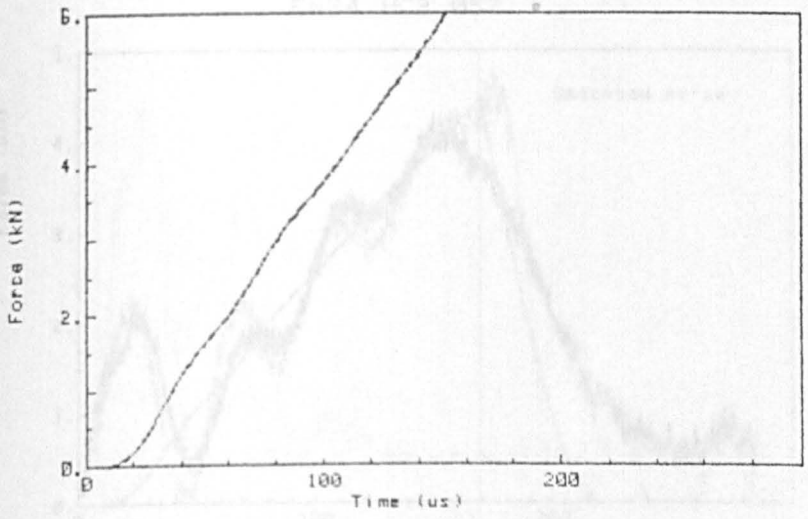

FIG. 4.21b.

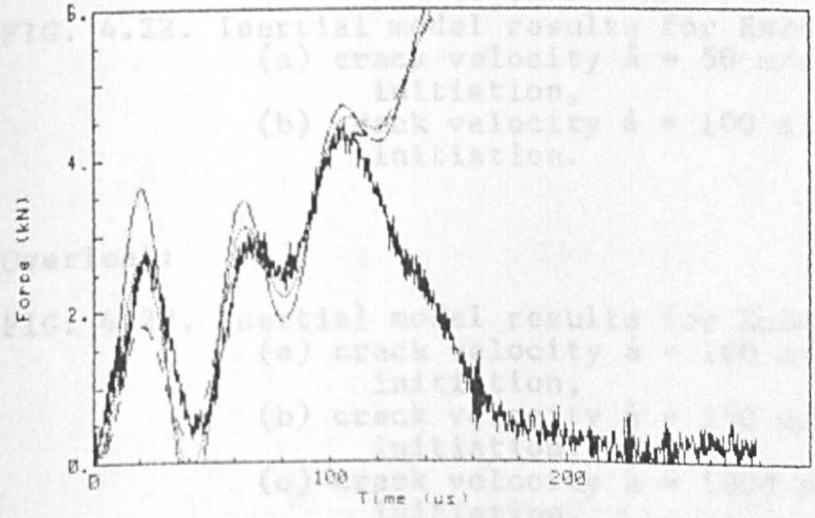

FIG. 4.21c.

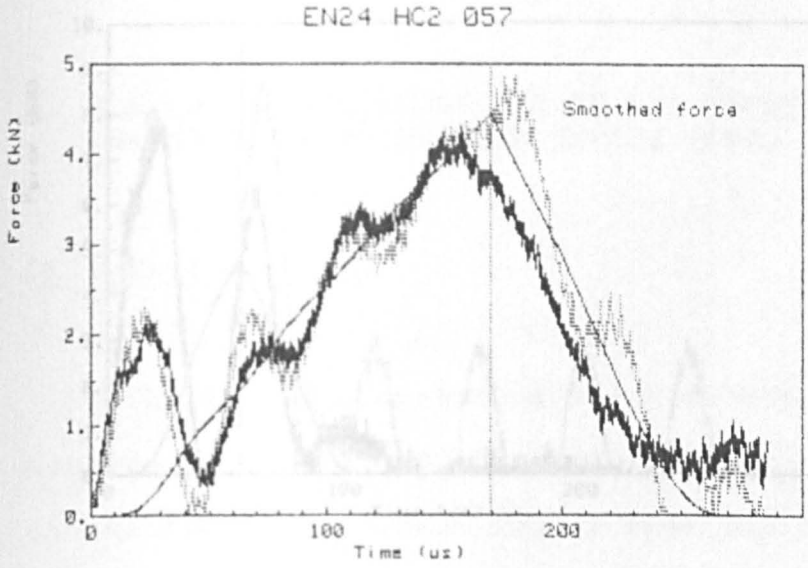

FIG. 4.22a.

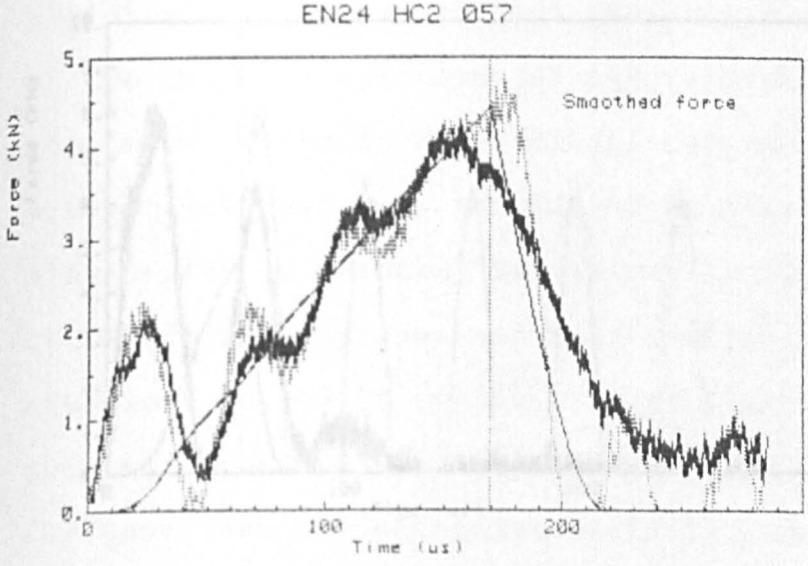

FIG. 4.22b.

FIG. 4.22. Inertial model results for En24 HC2 057 with:
(a) crack velocity $\dot{a}$ = 50 m/s after initiation,
(b) crack velocity $\dot{a}$ = 100 m/s after initiation.

Overleaf:

FIG. 4.23. Inertial model results for En24 HC2 055 with:
(a) crack velocity $\dot{a}$ = 100 m/s after initiation,
(b) crack velocity $\dot{a}$ = 250 m/s after initiation,
(c) crack velocity $\dot{a}$ = 1000 m/s after initiation.

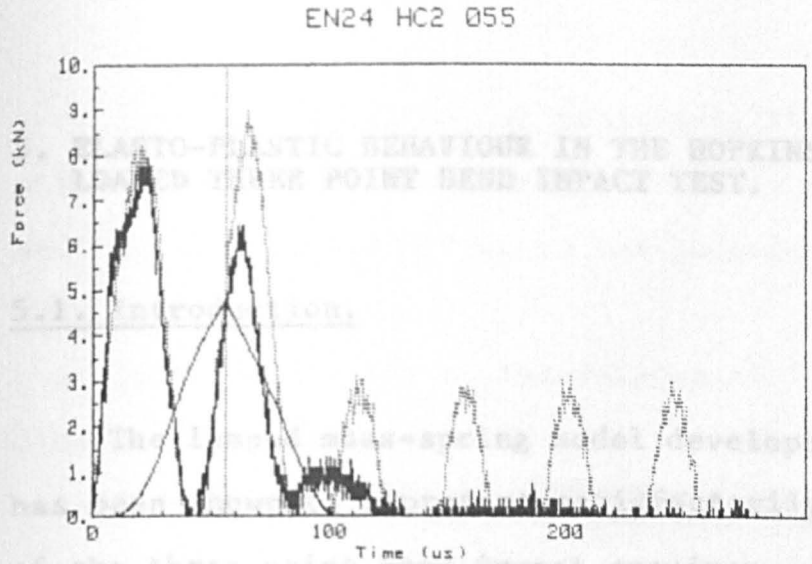

FIG. 4.23a.

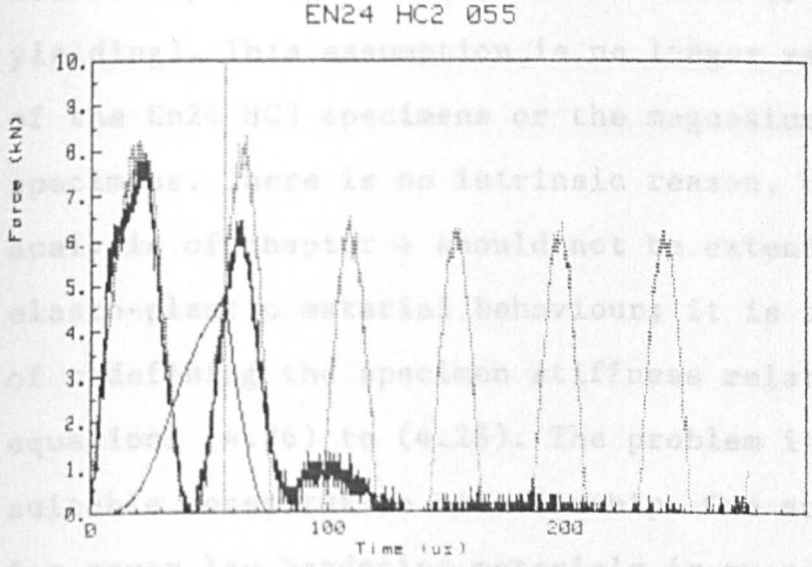

FIG. 4.23b.

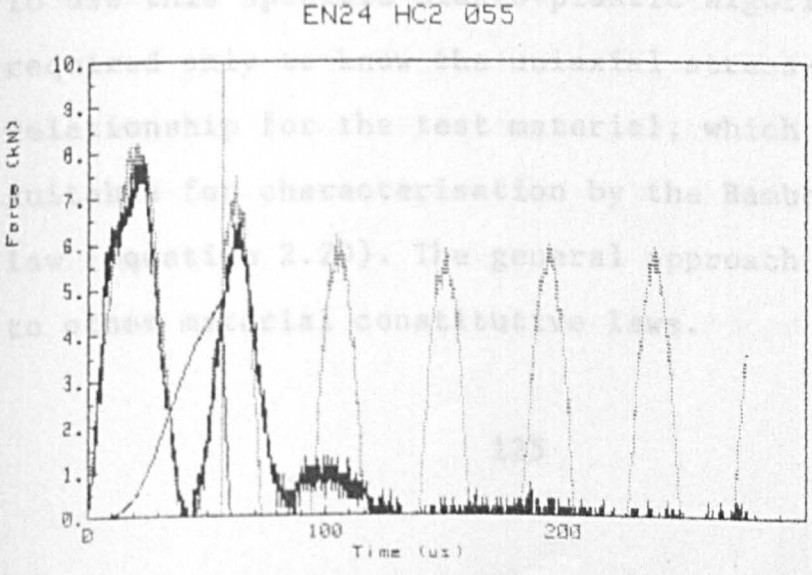

FIG. 4.23c.

5. ELASTO-PLASTIC BEHAVIOUR IN THE HOPKINSON PRESSURE BAR LOADED THREE POINT BEND IMPACT TEST.

5.1. Introduction.

The lumped mass-spring model developed in chapter 4 has been shown to represent satisfactorily the behaviour of the three point bend impact specimen up to the moment of crack initiation provided that plasticity effects can reasonably be ignored (ie in the limit of small scale yielding). This assumption is no longer valid in the case of the En24 HC3 specimens or the magnesium alloy specimens. There is no intrinsic reason, however, why the analysis of chapter 4 should not be extended to cover elasto-plastic material behaviour; it is simply a matter of redefining the specimen stiffness relationship in equations (4.26) to (4.28). The problem is to find a suitable constitutive relationship. One such relationship for power law hardening materials is presented in section 5.2 and is then included in the inertial model analysis. To use this specific elasto-plastic algorithm it is required only to know the uniaxial stress-strain relationship for the test material, which must then be suitable for characterisation by the Ramberg-Osgood power law (equation 2.20). The general approach may be adapted to other material constitutive laws.

A simple algorithm for estimating the contribution of plasticity to the contact stiffnesses is presented in section 5.4 and its effect on the behaviour of the model then explored.

Finally, the use of the J-integral to characterise dynamic crack initiation in impact loaded tests is considered and data presented for the En24 HC3 and magnesium alloy specimens.

5.2. An algorithm to include the effect of specimen plasticity in the lumped mass-spring model.

Following an approach first developed by Goldman and Hutchinson [122] to analyse a centre-cracked strip under tensile loading, Kumar et al [32] have produced expressions for the plastic deformation of the single-edge-cracked plate in three point bending. Their approach utilises the plastic component of the Ramberg-Osgood uniaxial stress-strain relationship (equation 2.21) generalised to multi-axial stress states using J_2 deformation theory (equation 2.22). Kumar et al report Ilyushin [123] as having demonstrated that the solution to the resulting boundary value problem has the following two properties:

(i) local field quantities are proportional to the

load parameter raised to the strain hardening index n, thus:

$$\frac{\sigma_{ij}}{\sigma_Y} = \left[\frac{\sigma_\infty}{\sigma_Y}\right]^n \hat{\sigma}_{ij}(\underset{\sim}{x},n) \tag{5.1}$$

where σ_∞ represents the applied stress and $\hat{\sigma}_{ij}$ is a dimensionless function of spatial position $\underset{\sim}{x}$ and n,

(ii) since the stress and strain at every point increase in exact proportion, the fully plastic solution based on the deformation theory of plasticity is the same as that given by the flow theory provided no unloading occurs.

The fully plastic crack tip parameters for the three point bend specimen are then given by:

$$J_p = \alpha\sigma_Y \epsilon_Y (W - a) h_1(\tfrac{a}{W},n) \left[\frac{P}{P_0}\right]^{n+1} \tag{5.2}$$

and:

$$u_{cp} = \alpha\epsilon_Y a h_3(\tfrac{a}{W},n) \left[\frac{P}{P_0}\right]^n \tag{5.3}$$

where P_0 is the limit load for a perfectly plastic material. This can be written in the form:

$$P_0 = \beta' \sigma_Y \frac{(W - a)^2}{S} B \tag{5.4}$$

where $\beta' = 1.456$ for plane strain conditions [31] and $\beta' = 1.072$ for plane stress conditions [124]. The dimensionless functions h_1 and h_3 have been evaluated using finite element techniques developed by Goldman and

Hutchinson [122] and tabulated in the EPRI handbook [32].

Kumar et al then propose that the behaviour of the specimen in the elasto-plastic regime (ie before complete yielding) be estimated by the superposition of the elastic solution, modified to account for the effect of the plastic zone in small scale yielding, with the plastic solution given above. Thus, the J-integral can be written as:

$$J = J_e(a_e) + J_p(a,n) \tag{5.5}$$

and the specimen displacement as:

$$u = u_e(a_e) + u_{cp}(a,n) \tag{5.6}$$

where the elastic contributions $J_e(a_e)$ and $u_e(a_e)$ are based on Irwin's effective crack length (equation 2.8) modified to account for strain hardening:

$$a_e = a + \phi r_Y \tag{5.7}$$

where:

$$r_Y = \frac{1}{\beta\pi}\left(\frac{n-1}{n+1}\right)\left[\frac{K_I}{\sigma_Y}\right]^2 \tag{5.8}$$

and:

$$\phi = \frac{1}{\left[1 + (P/P_0)^2\right]} \tag{5.9}$$

For plane strain $\beta = 6$ and for plane stress $\beta = 2$. The factor ϕ serves to reduce the plastic zone size correction under conditions of contained plasticity. The stress intensity factor K_I is evaluated from equations (2.13) and (2.15) based on the original crack length a. The elastic

component of displacement $u_e(a_e)$ is given by equation (4.27) except that the non-dimensional function $V_2(a/W)$ (equation 4.26) is evaluated in terms of the effective crack length a_e (equation 5.7).

The implementation of this plasticity correction in the analysis of chapter 4 is best seen with reference to the flow diagram in figure 5.1 and the load-deflection curve (inset to figure 5.2) defined by equation (5.6). The initial stiffness is elastic and the solution proceeds as before until the error between the numerical solution for u (and hence P_2) and the "target" solution u' defined by equation (5.11) below is larger than a given tolerance (see figure 5.2). The k_2 stiffness component is then incremented slightly (see figure 5.3) and the solution reiterated until the tolerance is satisfied. In the first instance this will mean decreasing the stiffness, but the process must allow for over-correction and hence requires increasing refinement in the incrementing procedure. The result is that the force-deflection behaviour of the specimen can be forced to follow the target solution to whatever accuracy is required.

In practice, it was found easiest to evaluate an effective "elastic" stiffness k_{2e} defined by:

$$k_{2e} = \left[\frac{1}{k_{se}} + \frac{1}{k_{sup}}\right]^{-1} \qquad (5.10)$$

where k_{se} is the specimen stiffness evaluated in terms of

the effective crack length and k_{sup} is the support stiffness as before, except that in this case it is possible to include a component to account for plastic deformation at the supports (see section 5.4). The target value of displacement u' for a given load P is then (from equation 5.6):

$$u' = \frac{P}{k_{2e}} + \alpha \epsilon_Y a h_3 \left[\frac{P}{P_0}\right]^n \qquad (5.11)$$

k_1 and (the elastic component of) k_{sup} were evaluated for each specimen by the iterative technique using equation (4.47) except that curve-fitting was restricted to the linear part of the force-time curve. This produced estimates of k_1 and k_{sup} for the En24 HC3 steel which were comparable with those computed for En24 HC2 steel in section 4.8. The estimates for the magnesium alloy specimens were more erratic due to the low magnitude of the measured forces and the difficulty of defining the truly linear part of the curves.

5.3. Stress-strain characterisation of En24 steel and magnesium alloys ZCM 630-T6 and WE54.

Use of the Kumar et al (KGS) [32] plastic solutions given in equations (5.5) and (5.6) requires fitting the Ramberg-Osgood uniaxial stress-strain relationship

(equation 2.20) to the measured stress-strain characteristic of the material under test. Ideally, this should be a dynamic stress-strain curve recorded at the identical strain rate and temperature used in the test to be analysed. In the case of a bending test the process is made difficult by the approximate nature of strain rate evaluation (see discussion following equations 2.54 and 2.58). In practice, it is often necessary to rely on statically determined stress-strain curves and to scale these using approximate relationships for the effect of strain rate - for example the Cowper-Symonds relationship (equation 2.51) discussed in section 2.4. (Again, of course, the large strain rate gradients in the bend specimen can only be accommodated very approximately.) For En24 steel the strain rate relationships developed by Tanimura and Duffy [52] for AISI 4340 VAR steel (equations 2.52 and 2.53) have already been used in determining the minimum ligament size for valid plane strain fracture toughness measurements in chapter 4. Similarly, the effect of temperature is often known only for the yield stress, but is required for the full range of stress and strain which requires further extrapolation.

Figures 5.4a to 5.4c show static stress-strain tensile data measured by Chait [125] for three tempers of AISI 4340 steel. These are fitted with Ramberg-Osgood curves using a least squares approximation. The fits are reasonable

considering the high yield stresses although, possibly, a bilinear characterisation would be more suitable. Figures 5.5a and 5.5b show tensile stress-strain data for the two magnesium alloys [126]. Although measured data was only available up to the 0.2% yield point, the analyses of the impact tests to be presented show fairly limited plasticity and so the implied extrapolation is not serious. The results of the Ramberg-Osgood characterisations are presented in table 5.1.

Yield stress data for several heats of AISI 4340 steel has been measured as a function of test temperature by Lee and Kang [120] and Tanimura and Duffy [52]. (The latter report results from torsion tests which can be used to approximate axial yield stress behaviour by assuming von Mises yield criterion and an incompressible material.) Both these sets of data are presented in figure 5.6a together with linear interpolations to the 375°C temper (nominally equivalent to the En24 HC1 and HC2 specimen batches). The very good agreement results in the mean curve of yield stress against temperature for the 375°C temper shown in figure 5.6b. The room temperature value is 1458 MPa which compares very favourably with a similar measurement for En24 [127].

By comparison, the 550°C temper (equivalent to the En24 HC3 specimen batch) has a room temperature yield stress of 1137 MPa.

Unfortunately no data is available on the variation of the stress-strain characteristic of the magnesium alloys with temperature or strain rate, although, as observed in section 3.12, the consistent shapes of the derived force-time curves for a wide range of temperature suggests that the temperature dependency of these materials is much weaker than that of the En24 steel.

5.4. The effect of plasticity on contact stiffness.

It has already been observed in figure 4.8 that the stresses generated in the contact zones between the incident bar and the specimen and between the specimen and its supports exceed the yield stress for all study materials at relatively low forces. As a first approximation of the resulting plastic component of the contact stiffness consider the contact problem of a rigid cylinder impacting a rigid-perfectly plastic plane. The cylinder will sink into the plane a distance d dependent on the magnitude of the impact force P, the yield stress of the surface σ_Y, and the area of normal contact between the cylinder and the plane. Let this area have a half-width y_0 and breadth B, then, as figure 5.7 shows:

$$2y_0B = \frac{P}{\sigma_Y C} \qquad (5.12)$$

or:
where $c = 1.8$ is the constraint factor [130]. Then:

$$y_0 = \frac{P}{2\sigma_Y B c} \tag{5.13}$$

and:

$$R_0^2 = (R_0 - d)^2 + y_0^2 \tag{5.14}$$

so that:

$$d = R_0 - (R_0^2 - y_0^2)^{\frac{1}{2}} \tag{5.15}$$

The approximate plastic contact stiffness component is then given by:

$$k_{cp} = \frac{P}{d} \tag{5.16}$$

Now, $R_0 = 8mm$ at the incident bar/specimen interface, and

$R_0 = 1mm$ at the specimen/supports interface.

The resulting stiffness values are plotted in figure 5.8 as a function of impact load. As in the elastic problem, the contact stiffness at the supports is really made up of two components acting in parallel, so the required stiffness is:

$$k_{c2p} = 2k_{cp} \tag{5.17}$$

For convenience only the results for the magnesium alloy WE54 have been plotted in figure 5.8b; the equivalent results for ZCM 630-T6 are very similar. It is obvious that, while the assumption of perfect plasticity is an extreme one, the additional compliance caused by plastic effects, at the supports, in particular, could be considerable.

The contribution of this plastic contact stiffness component to the overall specimen behaviour is discussed further in section 5.8.

5.5. Use of the far-field, deep crack formula to estimate the J-integral in elasto-plastic power law materials.

In discussing the application of the Rice et al [28] deep crack estimate of the J-integral (equation 2.37) in section 2.2, the approach of Srawley [30] was described as a means of verifying the validity of far-field approximations in linear elastic and perfectly plastic materials. The same method can be applied to the KGS[1] fully plastic solutions described above. The work done U_p is simply:

$$U_p = \int_0^{u_{cp}} P \, du_{cp} \tag{5.18}$$

where, from equation (5.3):

$$P = P_0 \left[\frac{u_{cp}}{\alpha \epsilon_Y a h_3(a/W,n)} \right]^{1/n} \tag{5.19}$$

Substituting equation (5.19) in equation (5.18) and integrating gives:

$$U_p = \frac{n}{(n+1)} P_0 \left[\frac{1}{\alpha \epsilon_Y a h_3} \right]^{1/n} u_{cp}^{\frac{n+1}{n}} \tag{5.20}$$

From equation (2.41b), the ratio of the true J-integral,

[1] Kumar, German, and Shih [32]

as defined by equation (2.32), to the work done per unit area of net cross-section is:

$$\eta_p = \frac{(W - a)}{U_p}\left[\frac{\partial U_p}{\partial(W-a)}\right]_u = \left[\frac{\partial \ln U_p}{\partial \ln(W-a)}\right]_u \qquad (5.21)$$

where the u indicates partial differentiation at constant displacement. From equations (5.20) and (5.21) η_p can be rewritten as:

$$\eta_p = \lim_{\delta a \to 0} \ln\left[\frac{U_p(a+\delta a)}{U_p(a)}\right] \Big/ \ln\left[\frac{W - (a+\delta a)}{W - a}\right] \qquad (5.22)$$

which, from equation (5.20), is:

$$\eta_p = \lim_{\delta a \to 0} \ln\left[\frac{P_0(a+\delta a)}{P_0(a)}\left(\frac{h_3(a)}{h_3(a+\delta a)} \cdot \frac{a}{(a+\delta a)}\right)^{\frac{1}{n}}\right] \Big/ \ln\left[\frac{W - (a+\delta a)}{W - a}\right] \qquad (5.23)$$

But, from equation (5.4), $P_0 \propto (W - a)^2$, and so equation (5.23) becomes:

$$\eta_p = 2 + \lim_{\delta a \to 0} \frac{1}{n}\left[1 + \frac{\ln[h_3(a)/h_3(a+\delta a)]}{\ln[\{W - (a+\delta a)\}/(W - a)]}\right] \qquad (5.24)$$

In the limit of perfect plasticity, as $n \to \infty$, then $\eta_p \to 2$, but for finite n there will be a finite correction dependent on the gradient of the dimensionless function h_3 with respect to crack length. This function is tabulated in Kumar et al [32]. Figure 5.9a shows the function plotted against a/W for a range of values of n. For each value of n the function was fitted with a quadratic curve

and the limit defined by equation (5.24) evaluated. The results are plotted in figure 5.9b. For moderate strain hardening materials and crack lengths of around half the ligament it appears that equation (2.37) can overestimate the plastic component of the J-integral by up to 10%. This will be a much smaller fraction of the total J-integral (which includes the elastic component) and is effectively negligible except in the case of large scale plasticity.

5.6. How long after impact does it take a J-dominated field to become established?

Nakamura et al [49] have suggested that a J-dominant field is likely to have been established once the ratio of kinetic energy to strain energy has fallen below 1.0 (see discussion in section 2.4). They estimated the kinetic energy from Euler-Bernoulli beam theory and the elastic strain energy as $U = \frac{1}{2}Pu$, from which they derived a non-dimensional transition time t_T given by:

$$\frac{ct_T}{W} = 27 \qquad (5.25)$$

where c is the wavespeed (equation 3.7) and W the width of the specimen.

A similar estimate can be made using the derived values from the inertial modelling routine. The specimen

velocity $\dot{u}$ in the model is explicitly determined from the R-K-N iterations and so it is a simple matter to estimate the kinetic energy as:

$$T = \frac{1}{2} m' \dot{u}^2 \tag{5.26}$$

In the linear elastic case the strain energy within the specimen is given by:

$$U_e = \frac{1}{2} k_s (u - u')^2 = \frac{1}{2} \frac{P_2^2}{k_s} \tag{5.27}$$

or in the elasto-plastic range by:

$$U_p = \int_0^u P_2 \, d(u-u') \tag{5.28}$$

where u' is as defined in figure 4.1. In practice, very little energy was expended in plastic deformation over the loading range of interest and so equation (5.27) was considered sufficient to determine the strain energy. The ratio of kinetic energy to strain energy has been plotted for the steel specimens (figure 5.10) and for the magnesium alloy ZCM 630-T6 (figure 5.11) at high and low velocities. The transition time for all these cases is covered by the range:

$$39.6 \times 10^{-6} < t_T < 44.4 \times 10^{-6} \tag{5.29a}$$

or:

$$19.5 < \frac{ct_T}{W} < 21.3 \tag{5.29b}$$

for the magnesium alloy, and:

$$21.9 < \frac{ct_T}{W} < 23.0 \qquad (5.29c)$$

for the steel specimens (where data for En24 HC2 specimens has been used due to the linear nature of the analysis, but the results are expected to be equally valid for En24 HC3 specimens considering the low load levels attained before t_T). The difference between equations (5.29) and equation (5.25) is another indication of the reduced proportion of inertial loading in the Hopkinson pressure bar test compared with a simple drop-weight or pendulum test. Since all the times to fracture in the specimens tested were well in excess of the range defined in equation (5.29a) it is reasonable, by this criterion, to consider the J-dominant field to have been well established by these times and therefore that the crack initiations can sensibly be characterised by the J-integral.

Nakamura et al [49] also considered the bending moment definition of the strain energy (equation 2.38) and the difficulty of inferring the true bending moment at the crack tip from remote measurements at, say, quarter-span. From their finite element results they determined that inertial forces could contribute approximately 7% of the total bending moment at the transition time $t=t_T$ (compared with over 40% at $t=t_T/2$). The inertial modelling routine is designed to allow for this contribution, albeit in a

coarser manner than can be achieved with a two-dimensional finite element analysis, so that this objection to remote measurements is at least compensated for.

5.7. A loading rate parameter for elasto-plastic materials.

The approximation of the rate of change of stress intensity factor, $\dot{K}_I$, defined in equation (2.59) is useful because it is approximately constant in a linear elastic test. A similar parameter for elasto-plastic materials might appear to be $\dot{J}_I$, where:

$$\dot{J}_I = \frac{J_{Id}}{t_f} \tag{5.30}$$

but in a constant displacement rate test this would only be constant for a perfectly plastic material since, by equation (2.37), J is proportional to the strain energy. In fact, for materials with low strain hardening coefficient and limited ductility, equation (2.59) is probably more appropriate. It is therefore proposed to use the parameter $\dot{K}_{IJ}$ to characterise the effective loading rate in the magnesium alloy tests, where:

$$\dot{K}_{IJ} = \frac{1}{t_f}\left[\frac{EJ_{Id}}{(1-\nu^2)}\right]^{\frac{1}{2}} \tag{5.31}$$

from equation (2.34), although small scale yielding

conditions are not, of course, strictly applicable. Equation (5.31) is also used to characterise the loading rate in the En24 HC3 tests since it allows some comparison with loading rates in the En24 HC2 tests. However, with the amount of ductility observed in these tests it is no longer a consistent measure of loading rate and the values obtained must be treated with some caution.

5.8. Elasto-plastic analysis of the En24 HC3 tests.

The KGS[1] elasto-plastic algorithm presented in section 5.2 has not been validated at very high strain hardening coefficients (the h_3 functions are only tabulated up to $n = 20$). Although stress-strain measurements are not available for the En24 steel, the Ramberg-Osgood characterisations of the US equivalent steel AISI 4340, presented in section 5.3, suggest a strain hardening coefficient n for the HC1 and HC2 tempers in excess of 40. Thus it is not possible to re-analyse the room temperature En24 HC1 results in which the ligament was too small to permit a valid plane strain fracture toughness measurement. However, as shown in figure 5.4c, the 540°C temper (equivalent to the HC3 specimen batch) is characterised by $n = 23.3$, from which it is possible to obtain extrapolated estimates of the h_3 and h_1 functions

1 Kumar, German, and Shih [32]

in equations (5.2) and (5.3). It can be shown that small errors ($\sim$10%) in these extrapolations have a negligible effect on the results. For ease of calculation all h_3 and h_1 evaluations have been made for a/W = 0.5, a reasonable assumption for the case of limited plasticity. For large scale plastic effects in Charpy-size specimens the errors in h_3 and h_1 evaluations are very small compared with the difference between assuming a plane strain or plane stress solution (see below).

Plane strain solutions are presented for the three impact velocities in figure 5.12 and derived quantities tabulated in table 5.2. Large scale plasticity is evident and the KGS elasto-plastic algorithm tends to overestimate the forces generated. It is impossible to say with any confidence where crack initiation takes place on any of the traces in figure 5.12. The maximum specimen strain gauge (S3) readings are indicated (and values of the J-integral evaluated at these points) but the absence of any sharp features makes their interpretation as crack initiation events very tentative. In addition, the oscillations in the S3 signals indicate significant inertial loading even up to 100 x 10^{-6} s in the high impact velocity test (075 - figure 5.12c). The large shear lips (figure 3.36a) suggest the possibility of crack initiation and tunnelling at the centre of the crack front while considerable load is still carried by intact

ligaments near the surface. At the lowest impact velocity (V_0 = 2.5 m/s - figure 5.12a) it is probable that initiation takes place beyond the end of the force-time trace and the J-integral values quoted in table 5.2 are evaluated as minimum values at the end of the measurement interval. In fact, at this condition, the specimens did not fracture completely, the cracks arresting after just 1mm growth. At the highest impact velocity (V_0 = 5.7 m/s) the divergence of the measured force and the KGS elasto-plastic solution suggests that crack initiation has indeed occurred either at or some time just after the maximum S3 reading.

Two J-integral values are quoted in tables 5.2a, 5.3a, and 5.4a. One was evaluated using the far field formulation adapted for the inertial model (equation 4.59), the other from the KGS estimate given in equation 5.5. The agreement is within about 5% for all cases and is often much better. This is good considering that use of the KGS formulation requires interpolation (and even extrapolation in the case of En24 HC3 specimens) of both the h_3 and h_1 functions. The error is greatest in those specimens with the highest proportion of plasticity and is consistent with over-estimation caused by assuming η_p = 2 in the evaluation of the far-field J-integral. However, it could equally be due to interpolation error.

With such extensive ductility the assumption of plane

strain conditions may no longer be valid, in which case the solutions presented here should represent an upper bound. The lower bound solution would result from assuming plane stress conditions (figure 5.13). As expected the KGS solutions now underestimate the measured force traces, so confirming the possibility of such a loss of constraint. The resulting change in J-integral values (table 5.2) is only of the order of 10%, however, which is small given the uncertainty surrounding the identification of crack initiation.

The situation is made still more complicated if strain rate effects are included. At the loading rates realised in these tests, the data of Tanimura and Duffy [52] suggests that a stress elevation of 10% would be a reasonable estimate, an increase which would raise the KGS plane strain solution still further.

The KGS solutions shown in figure 5.12 are undamped, while the measured force oscillations display a marked degree of damping. As shown in appendix 2, it is a simple matter to include a viscous damping term in the inertial model. The somewhat inconclusive result is shown in figure 5.14 for the high velocity test (V_0 = 5.7 m/s) with a relative damping coefficient ζ = 0.05, where:

$$\zeta = \frac{c}{2m'w} \qquad (5.32)$$

Although the curve fitting is improved over the first two

inertial oscillations, the match breaks down around the time that yielding occurs. Of note is the considerable fall in the P_2 force level (figure 5.14c) which results in almost a halving of the J-integral (table 5.2).

The occurrence of some kind of damping in the impactor-specimen-support interaction is inevitable, although the type of damping and its magnitude is not obvious. Viscous damping was selected as the easiest to model and is presented here purely as an example of how the presence of damping might effect the parameters used to measure crack initiation. The inclusion of damping involves the dissipation of energy and so can have a critical effect on the value of the J-integral pertaining to the test.

Plasticity at the specimen supports was included in the contact stiffness by superposition of the iterated value of k_{sup} from equation (4.57) and the estimated plastic component (equation 5.17):

$$k_{suppl} = \left[\frac{1}{k_{sup}} + \frac{1}{k_{c2p}}\right]^{-1} \qquad (5.33)$$

The effect of including this algorithm is shown in figure 5.15. The small change in system compliance results in a decrease of 5% in the J-integral at the estimated moment of crack initiation (table 5.2). Since perfect plasticity has been assumed, this value represents over-compensation. Figure 5.15b indicates that the impactor load P_1 is

insensitive to the inclusion of the plastic component of contact stiffness at the supports.

5.9. Elasto-plastic analysis of the magnesium alloy tests.

The maximum specimen strain gauge (S3) reading for the magnesium alloy tests is more sharply defined than for the extremely ductile En24 HC3 results, but again sudden drops are rare, making the identification of crack initiation uncertain. Again the instant at which the maximum S3 reading occurs has been taken as that of crack initiation (figures 5.16, 5.17, 5.19, and 5.20) except in the case of two ZCM 630-T6 results (figure 5.18) where a sharp drop prior to the maximum reading does occur and yields more believable J-integral evaluations (table 5.3).

The model results are presented for each alloy in terms of the effect of varying test temperature at two different speeds. The overall frequency response and the magnitude of oscillation are better matched than was the case with the En24 HC3 specimens.

Test repeatability was less consistent than for the steel specimens. Results are presented for single tests where two very similar force-time traces were obtained. The results are summarised in tables 5.3 and 5.4 and in figure 5.21 which shows the variation of J_{Id} with test

temperature for the two alloys. In all cases the dynamic evaluations of the J-integral are larger than the static (room temperature) measurements provided by Magnesium Elektron Ltd. However, the ZCM 630-T6 specimens at the -75°C condition yield a J-integral only fractionally higher than the room temperature static value. A contributory factor was the wide range of iterated k_{sup} solutions (see tables 5.3a and 5.4a) caused by both low force levels and short times to either fracture or yielding. This observation points up the need to find ways to measure accurately both the compliance of the anvil and the specimen contact stiffness so that more consistent support stiffness values can be used. The errors in the k_{sup} evaluations, however, are not sufficient to explain the size of variation from static to dynamic J-integral evaluations. In the case of ZCM 630-T6 test 17 (figure 5.17c) and WE54 test 10 (figure 5.19b) the divergence of the measured and predicted forces at the indicated time of initiation suggests that crack initiation occurs somewhat earlier and the J-integral evaluations for these tests are probably too high. Thus the detection of crack initiation is the real problem. Figure 5.21 shows the large difference in J-integral evaluations that can result from changes in t_f estimates of the order of 20×10^{-6} s between "first drop" and maximum specimen strain gauge initiation criteria. Further problems which arise if the

crack velocity at initiation is very low are discussed below.

The minimum ligament sizes to give a J-dominant field (equation 2.29) are also shown in tables 5.3b and 5.4b. They are satisfied in all cases. The proportion of plasticity in the KGS J-integral evaluations (tables 5.3b and 5.4b) is small and the fracture surfaces (figures 3.37 and 3.38) are predominantly intergranular. There might therefore seem to be little necessity for using the elasto-plastic algorithm for these materials (although its use is justified by the fact that the ligament size restriction for valid K_{Ic} evaluations - equation 2.47 - is exceeded severalfold). Comparisons between the linear and elasto-plastic model results are given in figures 5.22 to 5.26. J-integral values (J_{Ide}) derived from the linear model are presented in tables 5.3b and 5.4b. These are generally larger (ie non-conservative) than the elasto-plastic values and so illustrate the importance of using the correct constitutive model in this kind of analysis.

Attempts to estimate the rate of crack growth were carried out on two ZCM 630-T6 specimens (figures 5.27 and 5.28) and two WE54 specimens (figure 5.29) in the manner described in section 4.12. For the ZCM 630-T6 specimens at two impact velocities a crack velocity of $\dot{a}$ = 25 m/s seems too low while $\dot{a}$ = 50 m/s models the data quite well. For the WE54 specimens $\dot{a}$ = 25 m/s seems suitable for both

impact velocities. Thus crack speed appears to be generally lower compared with the steel specimens and less dependent on impact velocity.

Since the P_2 force defined by equation (4.5) represents the bending load acting on the specimen, its behaviour with time might be expected to be similar to that of the surface stresses measured by the S3 strain gauge. This is true in terms of the initial time lag of approximately 20×10^{-6} s before the two signals rise and the fact that they both lag the P_1 and measured forces by a phase angle of about 180^{o} (see, for example, figure 5.12c), although the S3 signal is generally more oscillatory. For the crack growth predictions in figures 5.27 to 5.29 the force P_2 continues to rise for some time after initiation if the crack velocity is low enough. Since this occurs in tests where the assumed velocity fits the measured data (figures 5.28b and 5.29b) the implication is that the stresses measured at S3 could also have continued to rise after initiation and the J-integral values given above would then be non-conservative. Since errors in determining time to fracture have already been shown to result in very large changes in the magnitude of the J-integral (see figure 5.21) it is possible that slow crack velocity at fracture initiation may be responsible for much, if not all, of the apparent increase in toughness of the magnesium alloys with strain rate.

On the microstructural mechanics of fracture of magnesium alloys in general, Roberts [128] noted that high strain rates were not particularly detrimental. He reported that cracking begins microscopically at strains as low as one half those required to produce final fracture. Failure occurs in tension when these microcracks join by intergranular cracking. The intergranular fracture surfaces found with Magnesium Elektron ZCM 630-T6 and WE54 have already been presented in figures 3.37 and 3.38. The progression from tension to compression (and hence reduction in axial strain) across the ligament of the Charpy specimen may well therefore be responsible for the low crack velocities deduced from the force-time data.

TABLE 5.1. Ramberg-Osgood characterisation parameters from figures 5.4 and 5.5.

Material	σ_Y (MPa)	n	α
AISI 4340 (1) 315°C temper (R_c=48)	1740	48.5	0.241
AISI 4340 (1) 427°C temper (R_c=44)	1412	49.5	0.297
AISI 4340 (1) 540°C temper (R_c=38)	1137	23.3	0.369
Magnesium alloy ZCM 630-T6 (2)			
Curve A	125	7.8	0.36
Curve B	125	6.1	0.36
Mean (as plotted)		6.9	0.36
Magnesium alloy WE54 (2)			
Curve A	177	6.0	0.25
Curve B	177	6.7	0.25
Mean (as plotted)		6.3	0.25

Notes:

(1) Data from Chait [124].

(2) Data supplied by Magnesium Elektron Ltd. [125].

(3) The h_1 and h_3 functions [32] for the elasto-plastic algorithm were estimated as follows:

For n = 23.3 at a/W = 0.5: $h_1 \approx 0.042$, $h_3 \approx 0.130$

For n = 6.9 at a/W = 0.5: $h_1 = 0.504$, $h_3 = 1.69$

For n = 6.3 at a/W = 0.5: $h_1 = 0.558$, $h_3 = 1.91$ (plane strain)

For n = 23.3 at a/W = 0.5: $h_1 \approx 0.011$, $h_3 \approx 0.050$ (plane stress)

TABLE 5.2. Summary of results for En24 HC3 steel:
(a) inertial model stiffness parameters.

Temperature (^{o}C)		20
V_0 (m/s)		
2.5		Test 071
k_1	(N/m)	4.6×10^8
k_{sup}	(N/m)	1.64×10^8
a/W		.502+
k_s	(N/m)	3.92×10^7
4.2		Test 072
k_1		4.6×10^8
k_{sup}		1.77×10^8
a/W		.528
k_s		3.53×10^7
5.7		Test 075
k_1		5.2×10^8
k_{sup}		1.78×10^8
a/W		.491
k_s		4.11×10^7

N.B. + Mean value from En24 HC3 specimens (070, 072-075) since specimen preserved in deformed state.

TABLE 5.2. (cont) Summary of results for En24 HC3 steel: (b) J-integral toughness evaluations.

Temperature (^oC)		20
V_0 (m/s)		
2.5		Test 071
	t_f (s)	$>278.2 \times 10^{-6}$ (331.2×10^{-6})-
	J_{Id} (Jm^{-2})	$>116 \times 10^3$ (plane strain)
	J_{Id} KGS (Jm^{-2})	$>117 \times 10^3$ (plane strain)
	$\dot{K}_{IJ}$ ($MPam^{\frac{1}{2}}/s$)	(5.9×10^5)
	Ligament (mm)	(2.6)
	J_{Id} (Jm^{-2})	$>109 \times 10^3$ (plane stress)
	J_{Id} KGS (Jm^{-2})	$>108 \times 10^3$ (plane stress)
4.2		Test 072
	t_f	198.4×10^{-6}
	J_{Id} (eq. 4.59)	185×10^3 (plane strain)
	J_{Id} KGS (eq. 5.5)	175×10^3 (plane strain)
	$\dot{K}_{IJ}$ (eq. 5.31)	10.4×10^5
	Lig. (eq. 2.29)	3.9
5.7		Test 075
	t_f	111.8×10^{-6}
	J_{Id}	122×10^3 (plane strain)
	J_{Id} KGS	120×10^3 (plane strain)
	$\dot{K}_{IJ}$	15.0×10^5
	Ligament	2.7
	J_{Id}	114×10^3 (plane stress)
	J_{Id} KGS	109×10^3 (plane stress)
	J_{Id} (damped solution)	66×10^3 (plane strain)
	J_{Id} (plastic k_{sup})	117×10^3 (plane strain)

N.B. - Values quoted at $t_f = 278.2 \times 10^{-6}$ s - the last S1:S2 data point (S3 max at $t_f = 331.2 \times 10^{-6}$ s).

TABLE 5.3. Summary of results for Mg alloy ZCM 630-T6:
(a) inertial model stiffness parameters.

Temperature (°C)	-75	20	125
V_0 (m/s)			
2.4	Test 10	Test 04	Test 08
k_1 (x 10^8 N/m)	1.4	1.5	1.5
k_{sup} (x 10^8 N/m)	0.19	>10.0	>10.0
a/W	.516	.531	.524
k_s (x 10^6 N/m)	7.9	7.4	7.7
4.1	Test 15	Test 14	Test17
k_1	1.6	1.6	1.7
k_{sup}	5.0	>1.5	>5.0
a/W	.493	.501	.525
k_s	8.7	8.4	7.6

TABLE 5.3. (cont) Summary of results for ZCM 630-T6:
(b) J-integral toughness evaluations.

Temperature (^{o}C)	-75	20	125
V_0 (m/s)			
static J_{Ic} (Jm^{-2})		5505	
2.4	Test 10	Test 04	Test 08
t_f (us)	133.2	145.8	141.0
J_{Id} (Jm^{-2})	5943.	10852.	10071.
J_{Id} KGS	5809.	10341.	9663.
(J_{Idp} KGS)	(1139.)	(3939.)	(3439.)
$\dot{K}_{IJ}$ (x 10^5 $MPam^{\frac{1}{2}}/s$)	1.3	1.6	1.6
Ligament (mm)	1.2	2.2	2.0
J_{Ide}	5757.		11945.
"first drop" t_f		119.6	
J_{Id}		7412.	
$\dot{K}_{IJ}$		1.6	
4.1	Test 15	Test 14	Test 17
t_f	64.6	69.8	102.2
J_{Id} (eq. 4.59)	5770.	7179.	14056.
J_{Id} KGS (eq. 5.5)	5667.	7015.	13325.
(J_{Idp} KGS)	(1022.)	(1717.)	(6084.)
$\dot{K}_{IJ}$ (eq. 5.31)	2.6	2.7	2.6
Lig. (eq. 2.29)	1.2	1.4	2.8
J_{Ide}	6135.		
"first drop" t_f			82.2
J_{Id}			8896.
$\dot{K}_{IJ}$			2.6
J_{Ide}			9675.

TABLE 5.4. Summary of results for Mg alloy WE54:
(a) inertial model stiffness parameters.

Temperature (^{o}C)		-75	20	125
V_0 (m/s)				
1.5		Test 13	Test 10	Test 19
	k_1 (x 10^8 N/m)	1.2	1.1	1.1
	k_{sup} (x 10^8 N/m)	1.33	3.2	0.67
	a/W	.516	.497	.469
	k_s (x 10^6 N/m)	7.9	8.6	9.5
3.3		Test 15	Test 08	Test 18
	k_1	1.6	1.6	1.4
	k_{sup}	0.38	0.77	0.41
	a/W	.486	.482	.463
	k_s	7.2	8.1	9.7

TABLE 5.4. (cont.) Summary of results for WE54:
(b) J-integral toughness evaluations.

Temperature (°C)	-75	20	125
V_0 (m/s)			
static J_{Ic} (Jm^{-2})		2628	
1.5	Test 13	Test 10	Test 19
t_f (us)	206.0	269.2	>282.6+
J_{Id} (Jm^{-2})	8362.	16058.	>15705.
J_{Id} KGS	8247.	15770.	>15500.
(J_{Idp} KGS)	(758.)	(3692.)	(>3402.)
K_{IJ} (x 10^5 $MPam^{\frac{1}{2}}/s$)	1.0	1.0	(1.0)
Ligament (mm)	1.2	2.3	>2.2
J_{Ide}	8707.	17477.	
3.3	Test 15	Test 08	Test 18
t_f	94.6	109.8	112.2
J_{Id} (eq. 4.59)	6209.	11273.	10292.
J_{Id} KGS (eq. 5.5)	6088.	11082.	10099.
(J_{Idp} KGS)	(285.)	(1553.)	(1172.)
K_{IJ} (eq. 5.31)	1.9	2.2	2.0
Lig. (eq. 2.29)	0.87	1.6	1.5
J_{Ide}	6200.		10313.

N.B. + Values quoted at $t_f = 282.6 \times 10^{-6}$ s - the last S1:S2 data point (S3 max at $t_f = 318.2 \times 10^{-6}$ s).

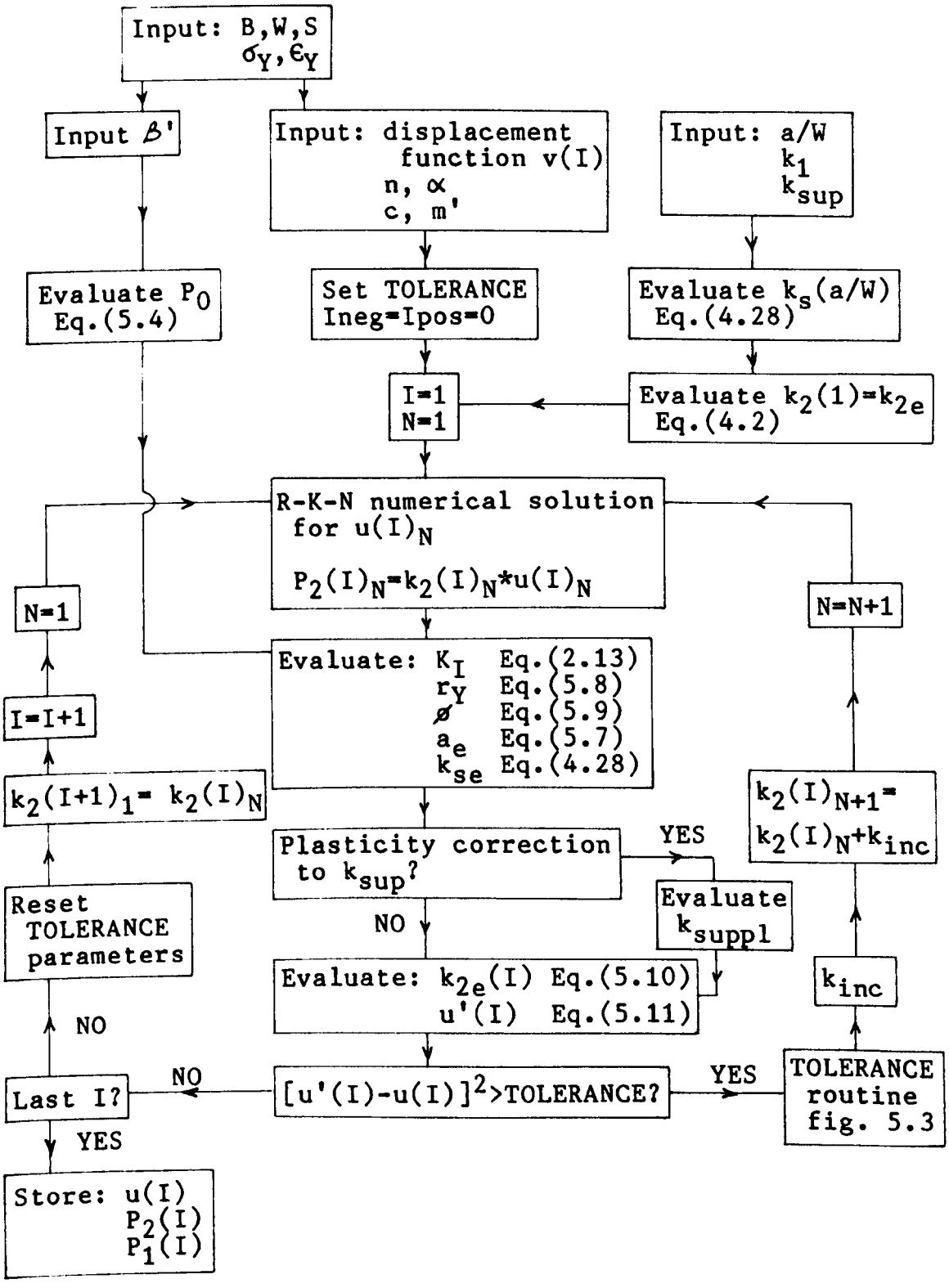

FIG. 5.1. Flow diagram of elasto-plastic inertial model solution technique.

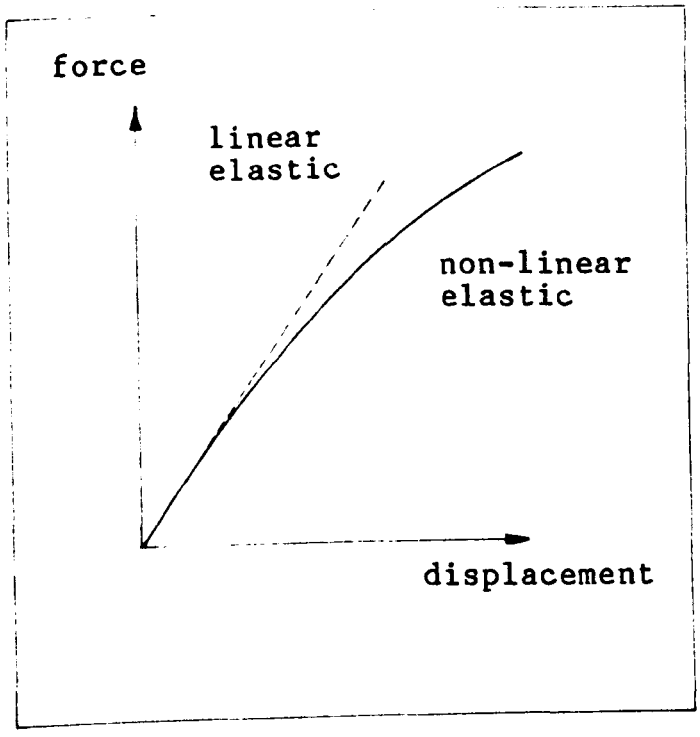

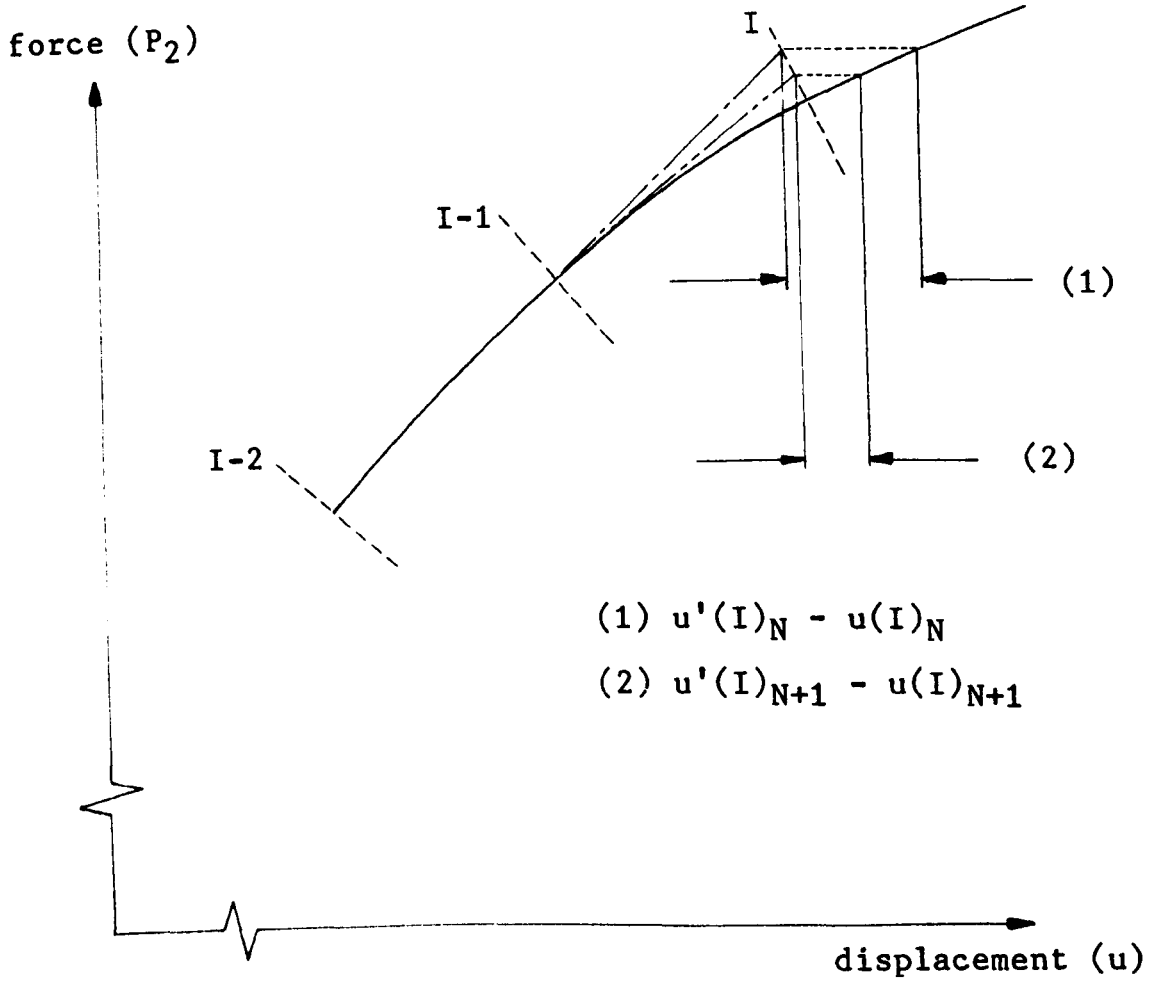

FIG. 5.2. Curve-fitting technique for material with a non-linear force-displacement curve (inset).

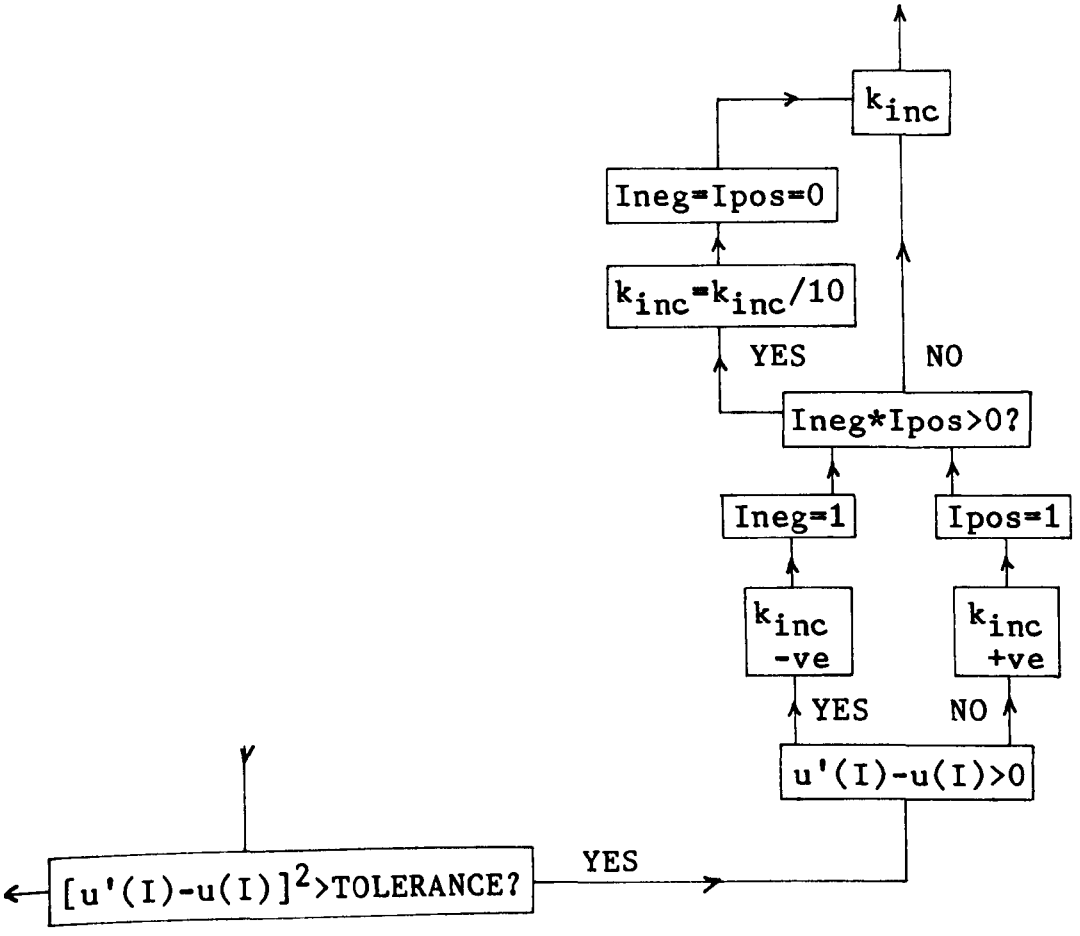

FIG. 5.3. TOLERANCE routine for elasto-plastic inertial model.

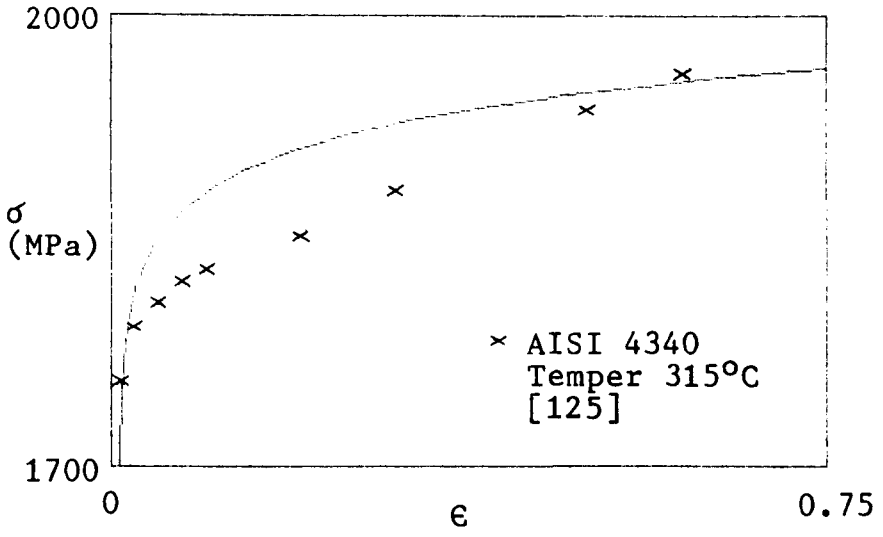

FIG. 5.4a.

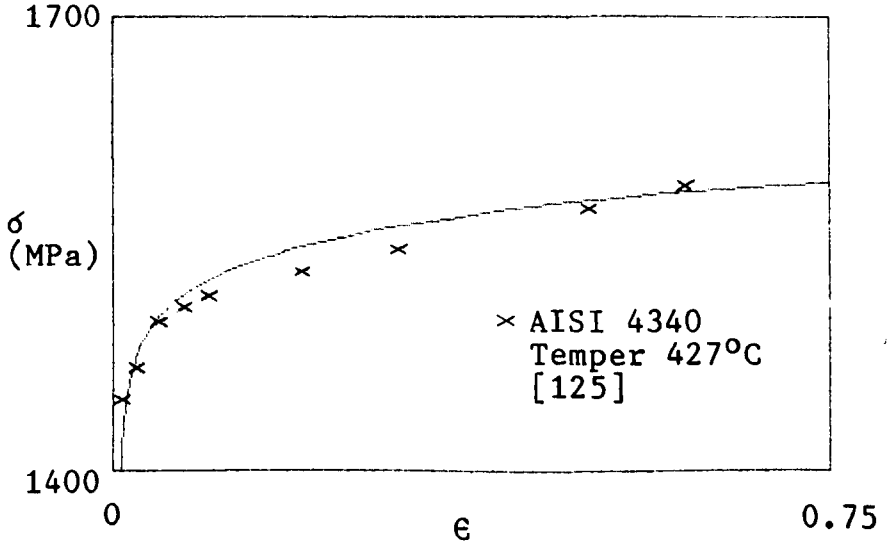

FIG. 5.4b.

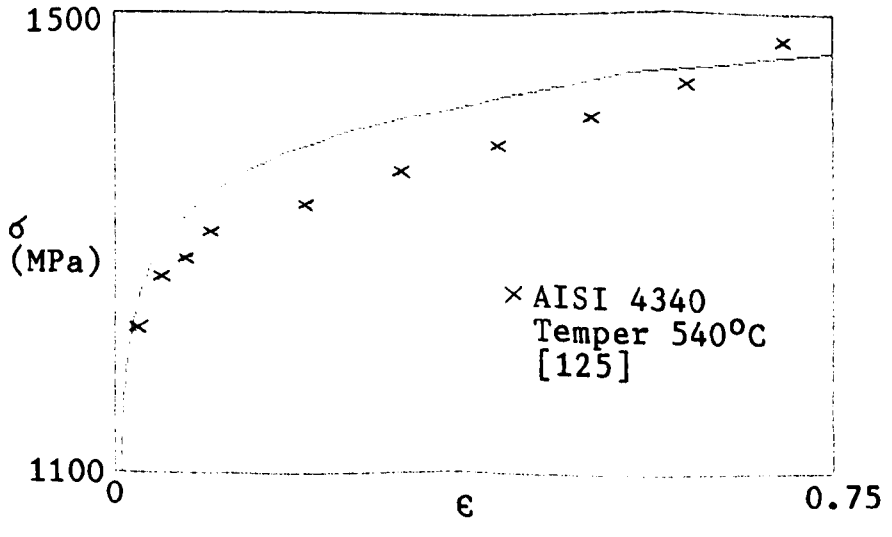

FIG. 5.4c.

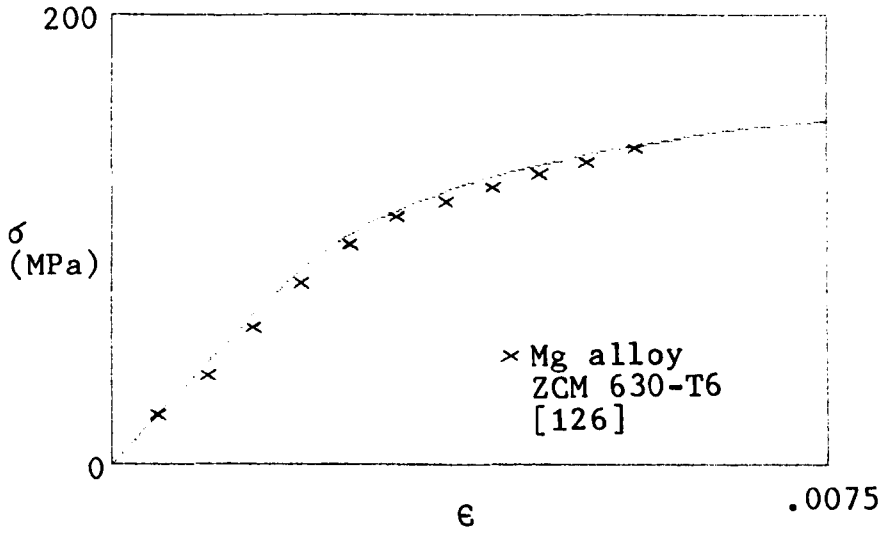

FIG. 5.5a

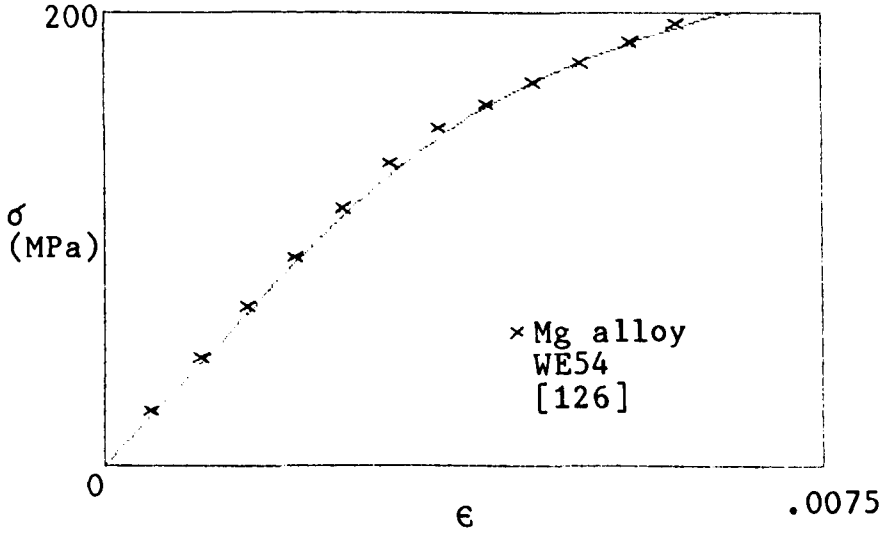

FIG. 5.5b.

FIG. 5.5. Ramberg-Osgood characterisations of the stress-strain behaviour of magnesium alloys ZCM 630-T6 ($n = 6.9$, $\alpha = 0.36$) and WE54 ($n = 6.3$, $\alpha = 0.25$).

Preceding page:

FIG. 5.4. Ramberg-Osgood characterisations of the stress-strain behaviour of three tempers of AISI 4340 steel:
(a) Temper 315°C : $n = 48.5$, $\alpha = 0.241$,
(b) Temper 427°C : $n = 49.5$, $\alpha = 0.297$
(c) Temper 540°C : $n = 23.3$, $\alpha = 0.369$

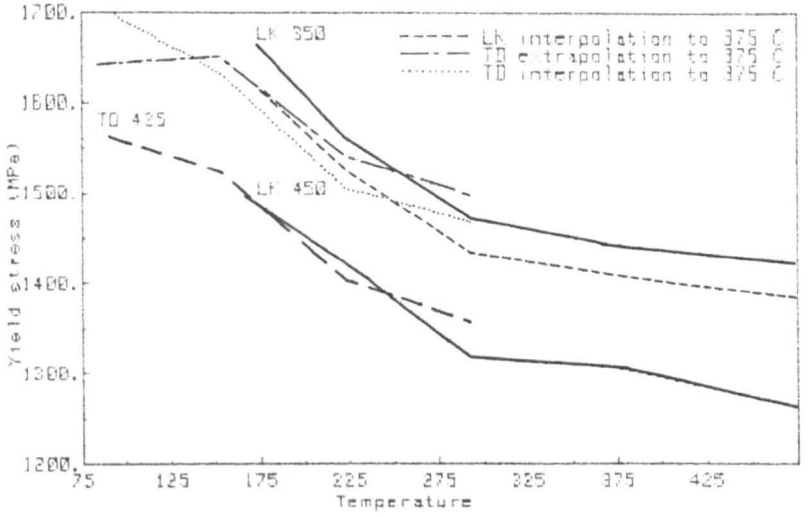

FIG. 5.6a.

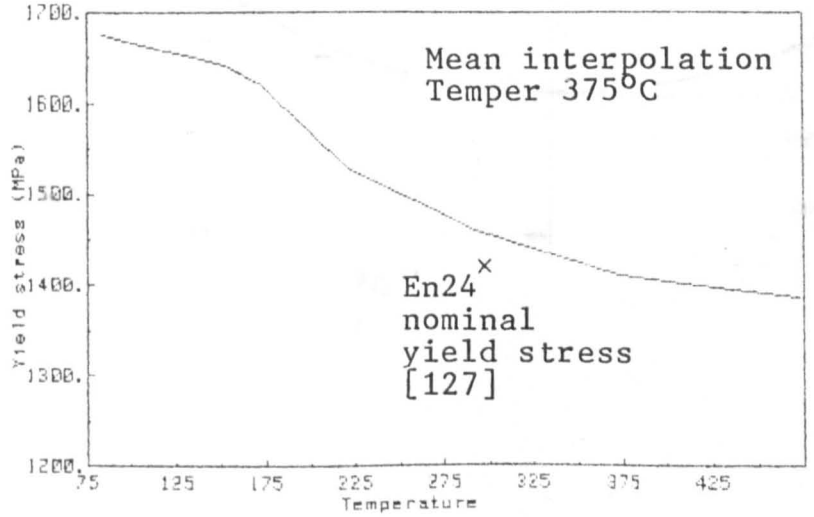

FIG. 5.6b.

FIG. 5.6. Yield stress-temperature data for AISI 4340 steel from:
(i) Lee and Kang [120] - tempers 350/450 °C
(ii) Tanimura and Duffy [52] - temper 425°C
showing mean interpolation for temper 375°C with nominal yield stress for En24 [127].

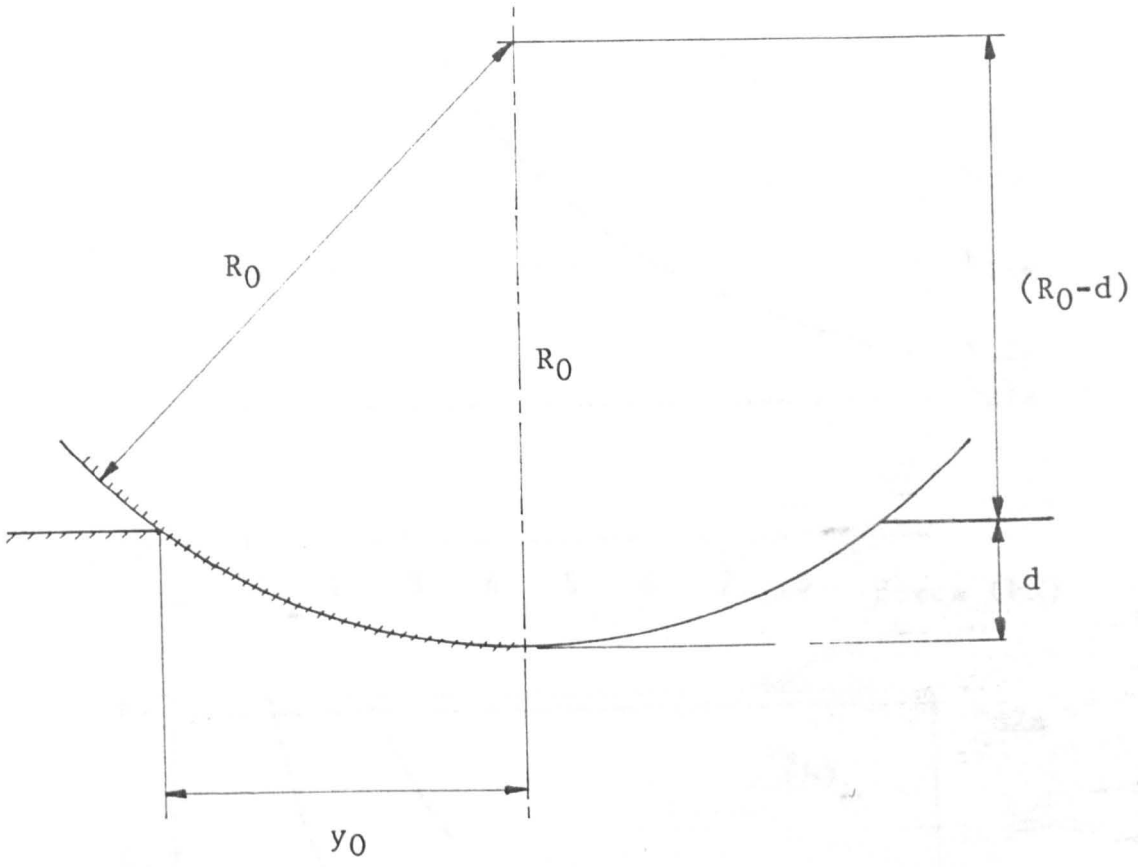

FIG. 5.7. Geometry for determination of the plastic component of contact stiffness.

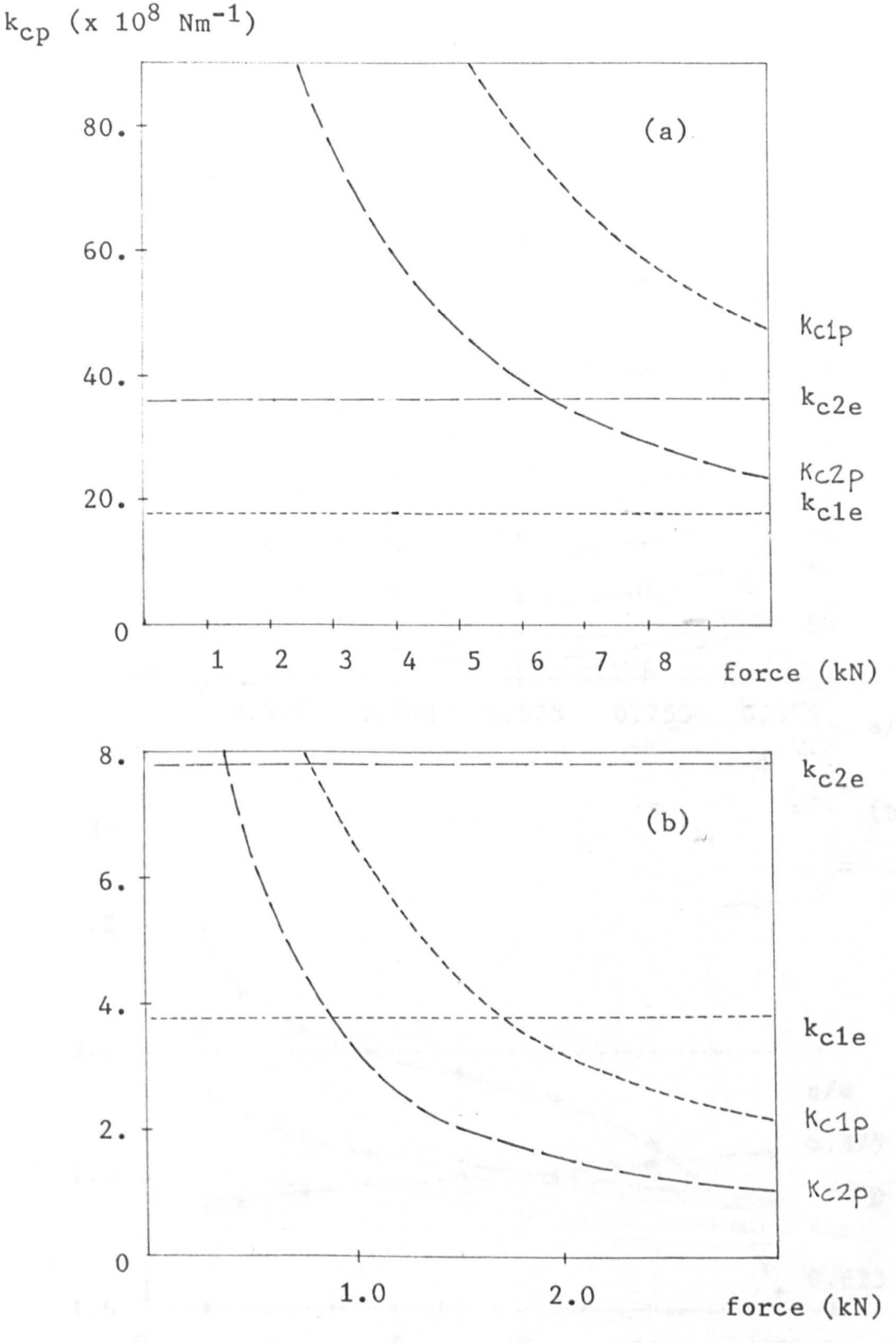

FIG. 5.8. Plastic components of contact stiffness for:
(a) En24 steel (σ_Y = 1500 MPa),
(b) Mg alloy WE54 (σ_Y = 177 MPa).

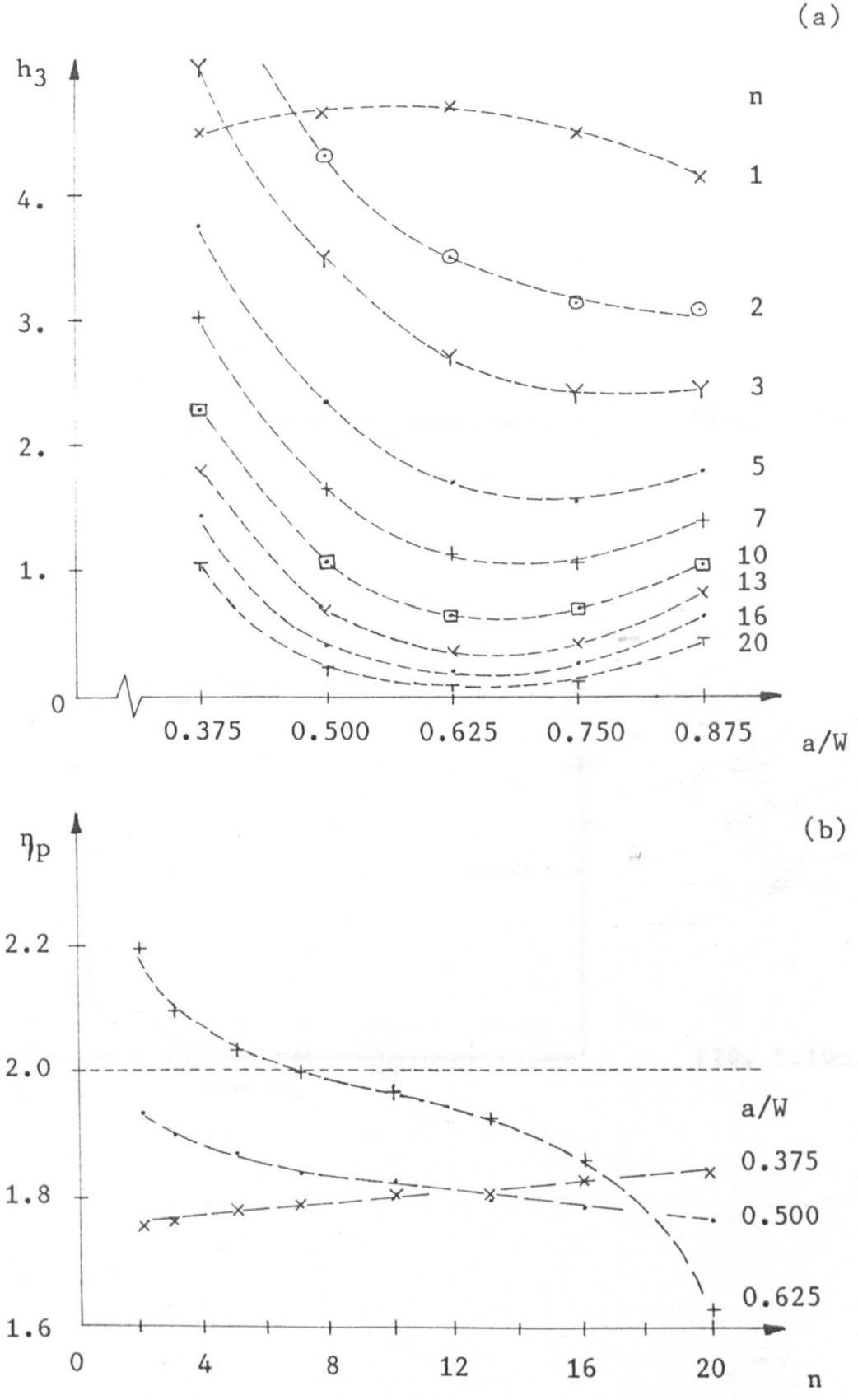

FIG. 5.9. h_3 [32] and η_p functions for elasto-plastic analysis.

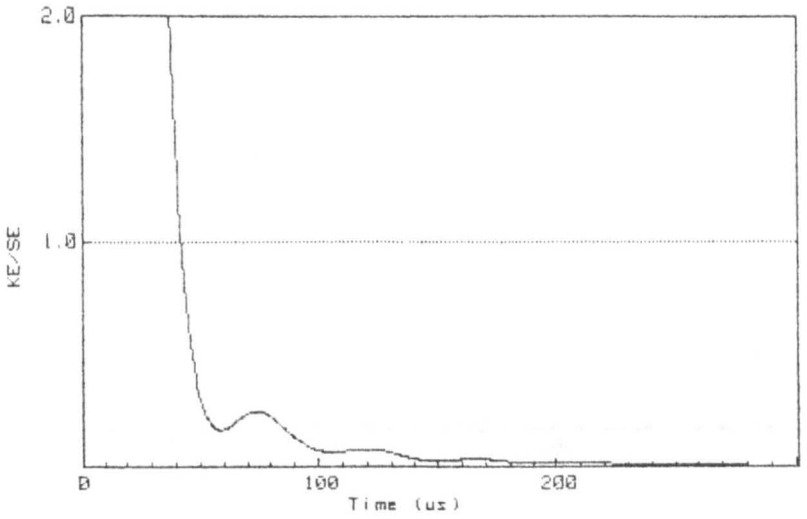

FIG. 5.10a.

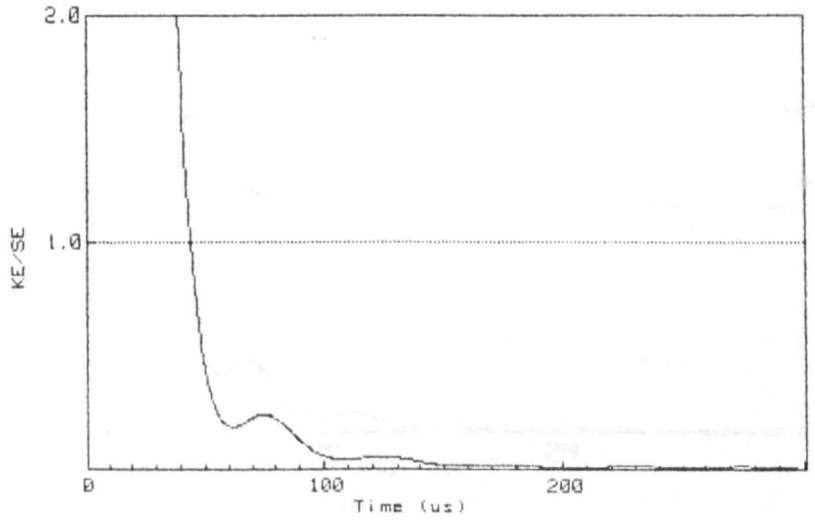

FIG. 5.10b.

FIG. 5.10. KE/SE v. time for En24 HC2 specimens:
(a) test 054 (V_0 = 4.2 m/s),
(b) test 060 (V_0 = 0.95 m/s).

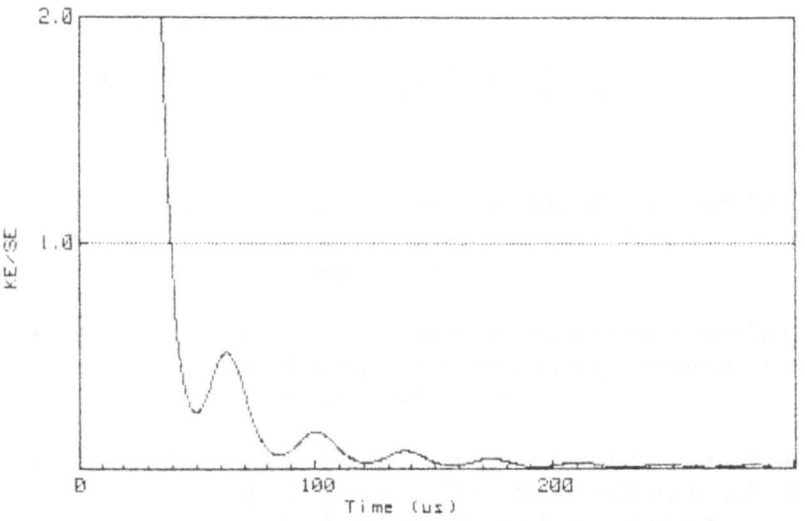

FIG. 5.11a.

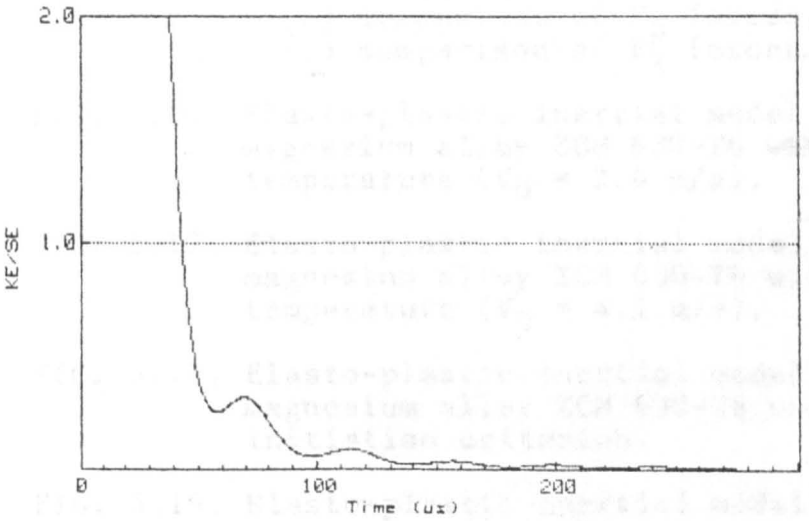

FIG. 5.11b.

FIG. 5.11. KE/SE v. time for Mg alloy ZCM 630-T6 specimens:
(a) test 14 (V_0 = 4.1 m/s),
(b) test 01 (V_0 = 1.2 m/s).

Titles for figures 5.12 to 5.20.

FIG. 5.12. Elasto-plastic inertial model results for En24 HC3 with increasing impact velocity (T = 20°C) - plane strain.

FIG. 5.13. Elasto-plastic inertial model results for En24 HC3 with increasing impact velocity (T = 20°C). - plane stress.

FIG. 5.14. Elasto-plastic inertial model results for En24 HC3 test 075: the effect of damping (ζ = 0.05):
(a) damped model result,
(b) comparison of F_p forces,
(c) comparison of P_2^p forces.

FIG. 5.15. Elasto-plastic inertial model results for En24 HC3 test 075: the effect of plasticity in the support contact stiffness:
(a) model result,
(b) comparison of F_p forces,
(c) comparison of P_2^p forces.

FIG. 5.16. Elasto-plastic inertial model results for magnesium alloy ZCM 630-T6 with increasing test temperature (V_0 = 2.4 m/s).

FIG. 5.17. Elasto-plastic inertial model results for magnesium alloy ZCM 630-T6 with increasing test temperature (V_0 = 4.1 m/s).

FIG. 5.18. Elasto-plastic inertial model results for magnesium alloy ZCM 630-T6 using "first drop" initiation criterion.

FIG. 5.19. Elasto-plastic inertial model results for magnesium alloy WE54 with increasing test temperature (V_0 = 1.5 m/s).

FIG. 5.20. Elasto-plastic inertial model results for magnesium alloy WE54 with increasing test temperature (V_0 = 3.3 m/s).

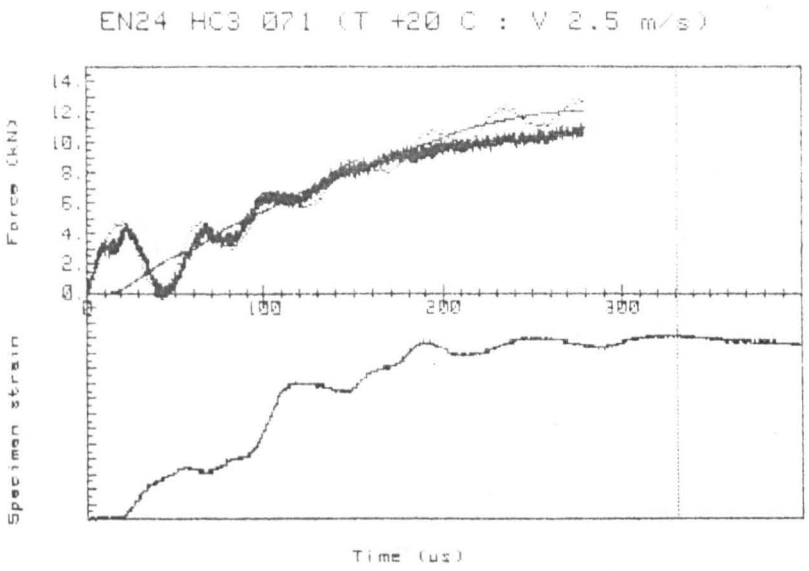

FIG. 5.12a.

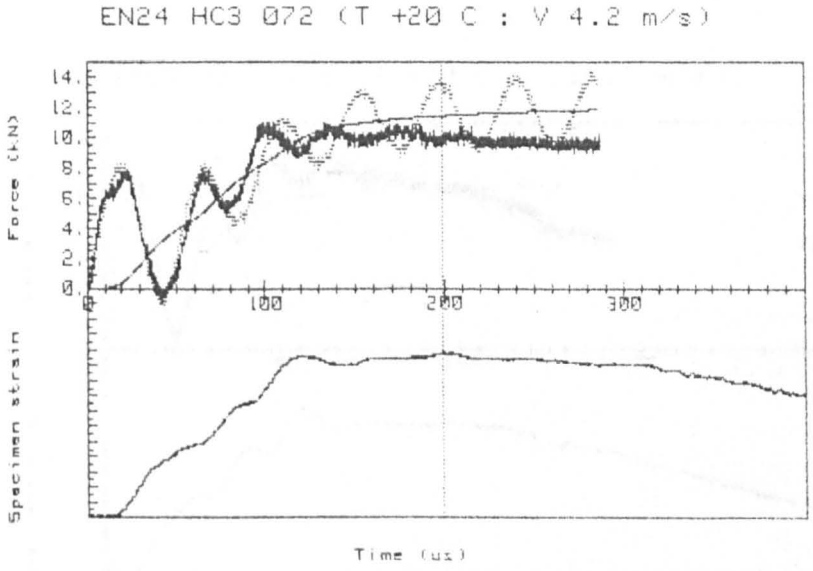

FIG. 5.12b.

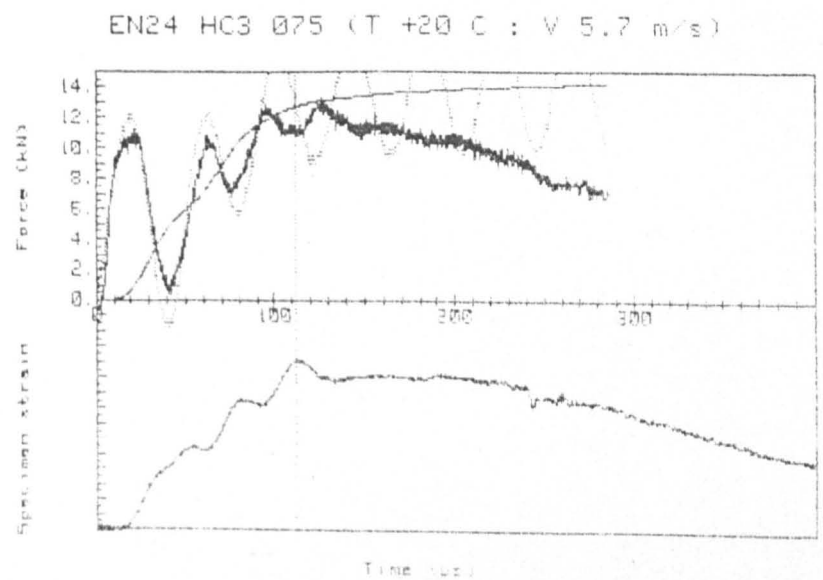

FIG. 5.12c.

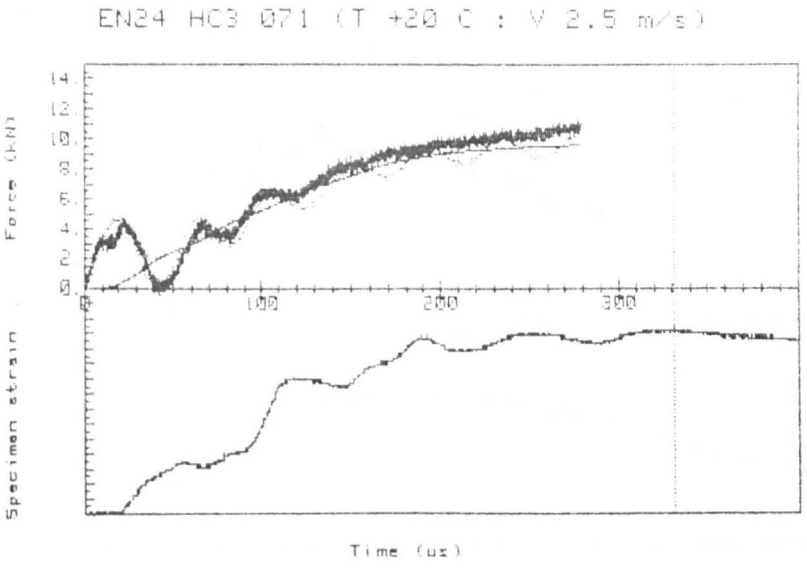

FIG. 5.13a.

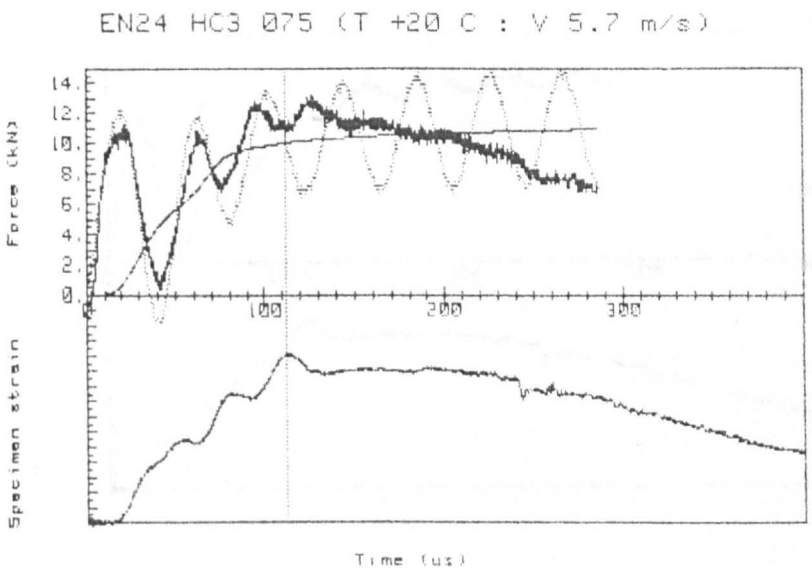

FIG. 5.13b.

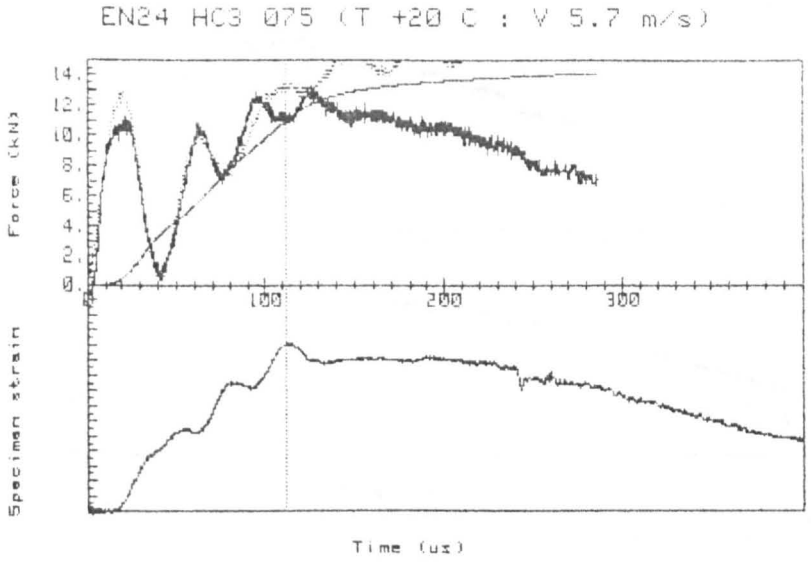

FIG. 5.14a.

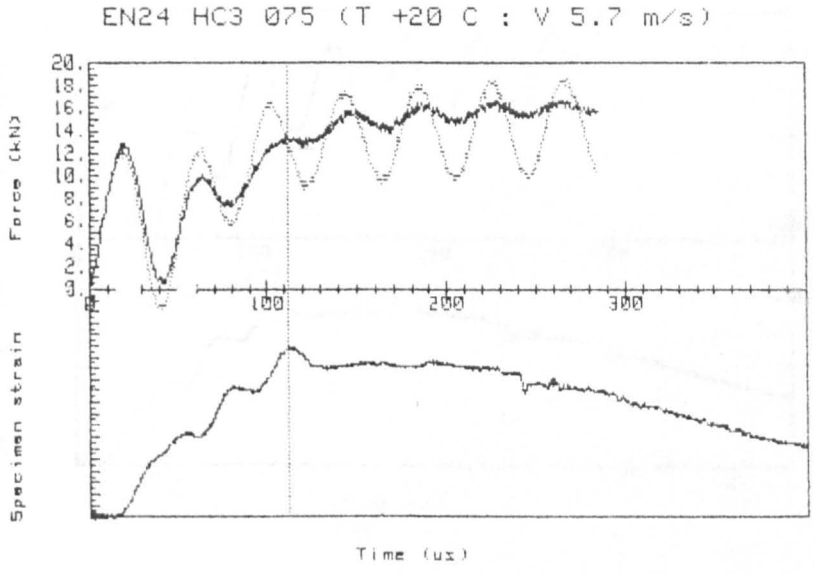

FIG 5.14b.

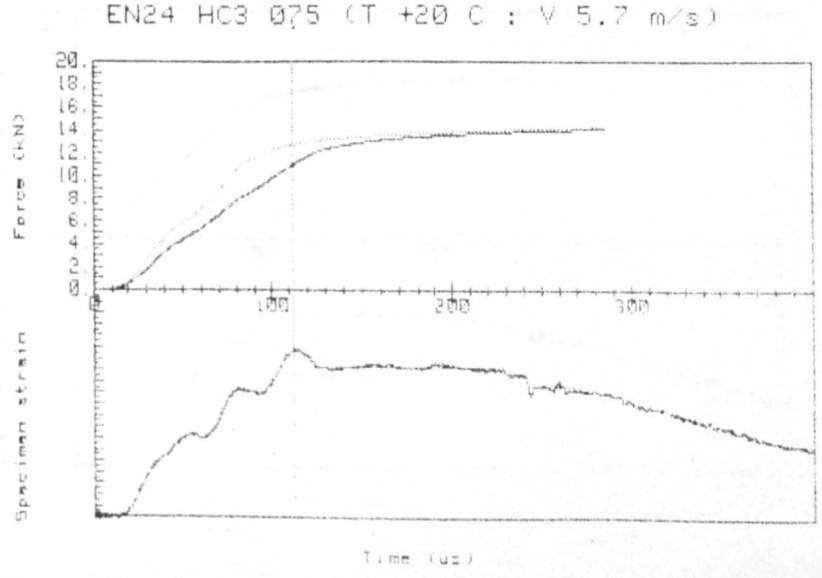

FIG. 5.14c.

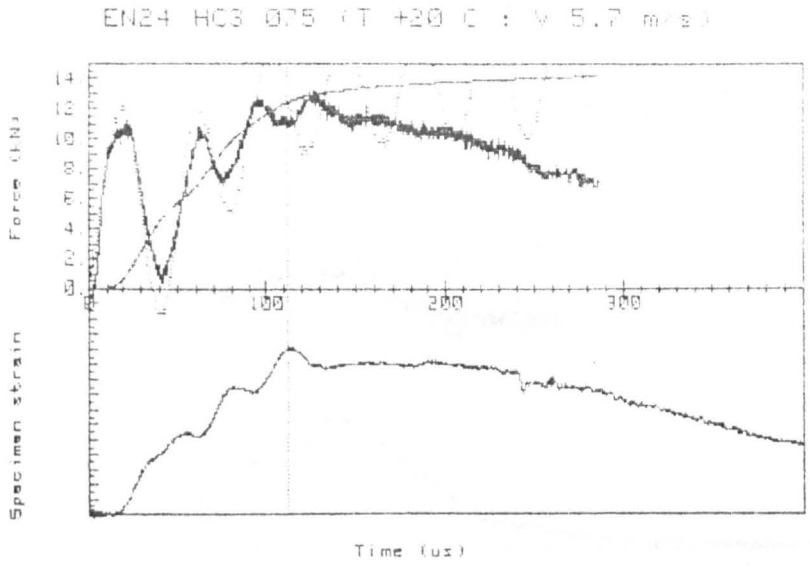

FIG. 5.15a.

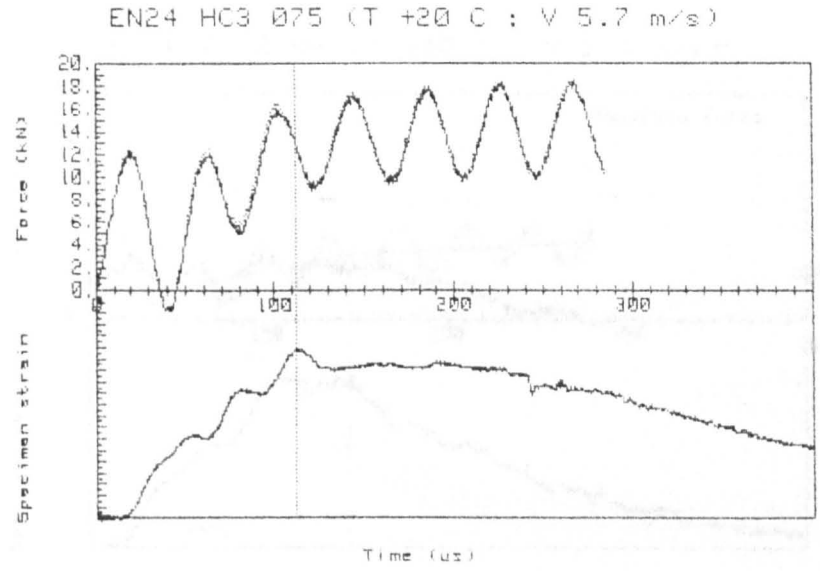

FIG. 5.15b.

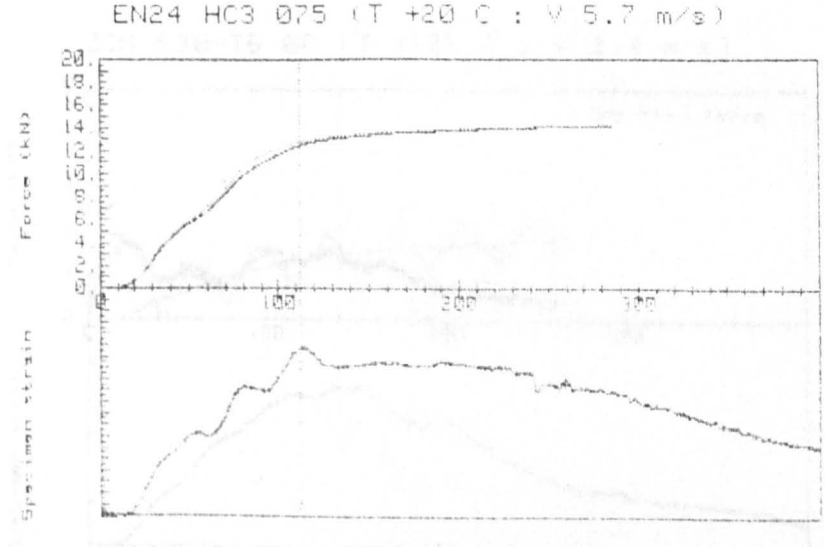

FIG. 5.15c.

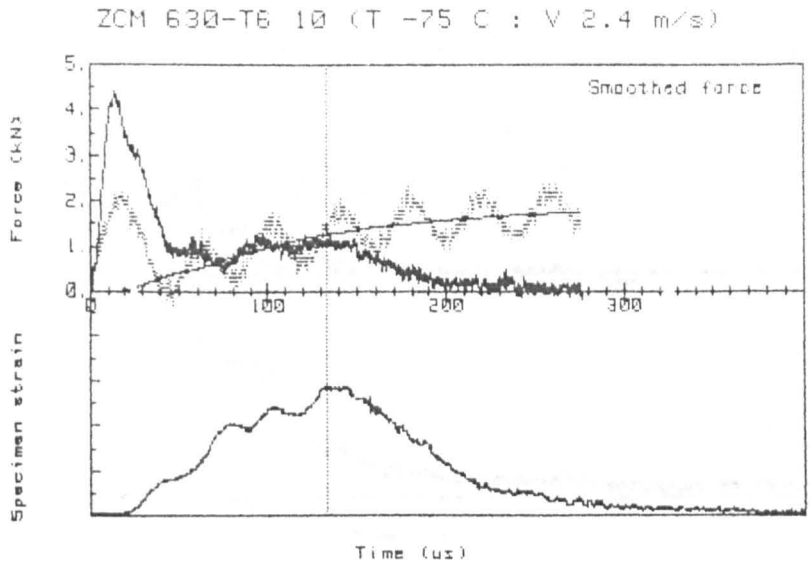

FIG. 5.16a.

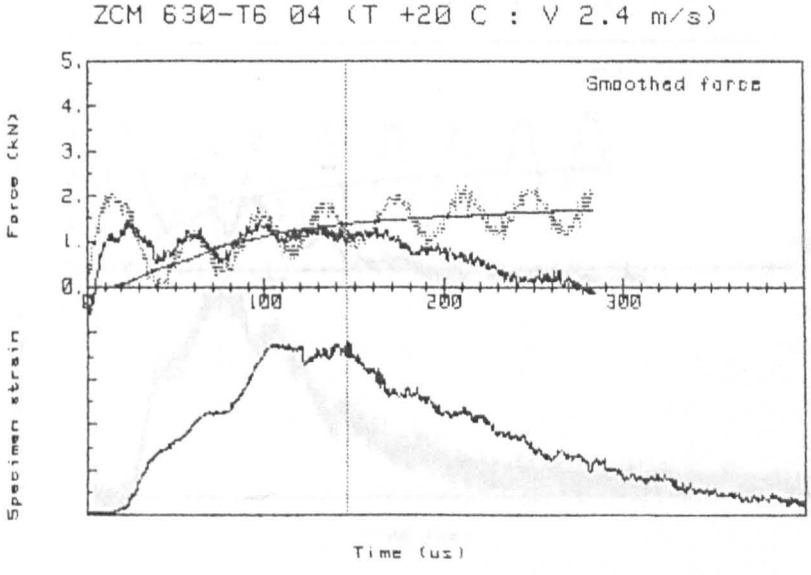

FIG. 5.16b.

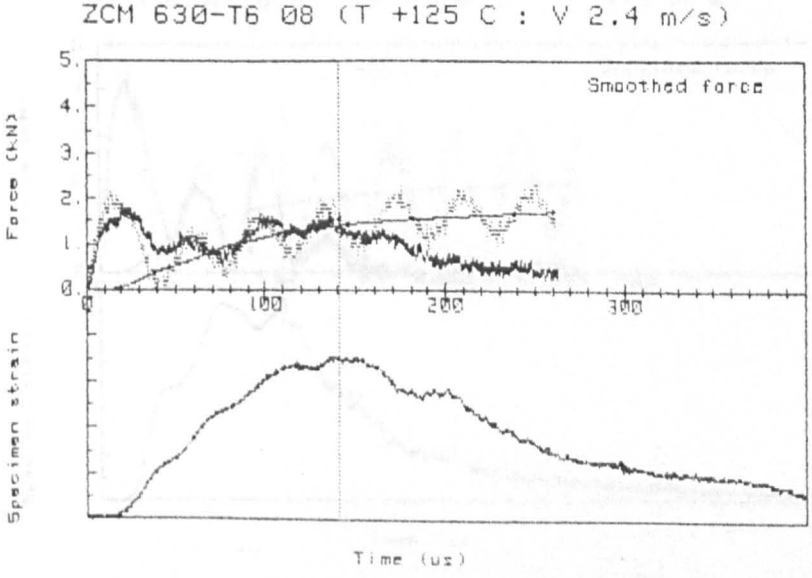

FIG. 5.16c.

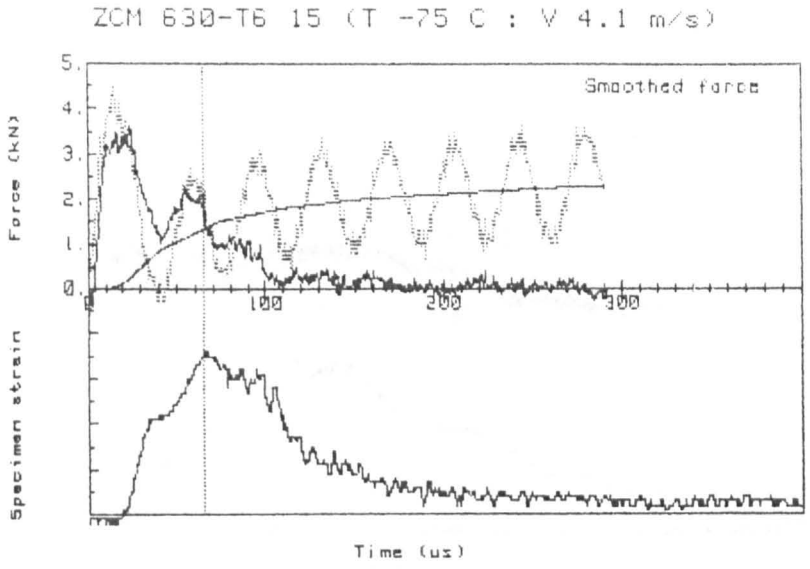

FIG. 5.17a.

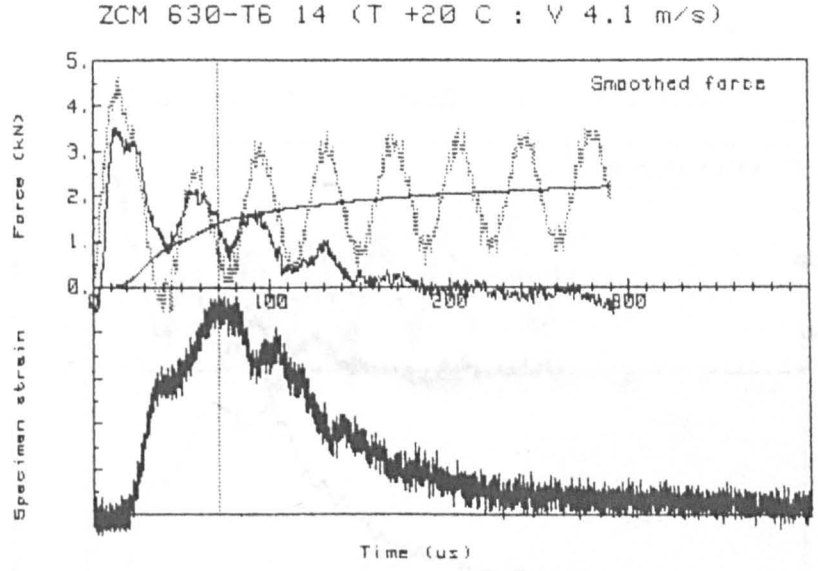

FIG. 5.17b.

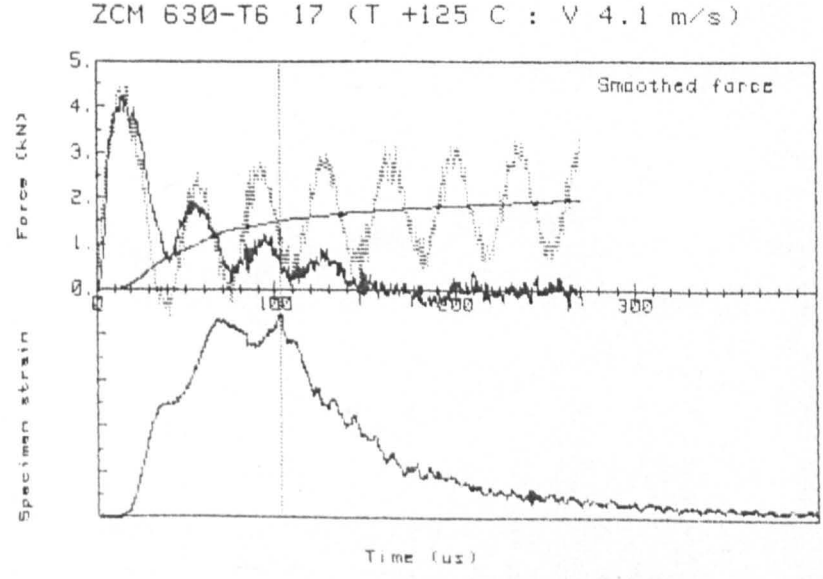

FIG. 5.17c.

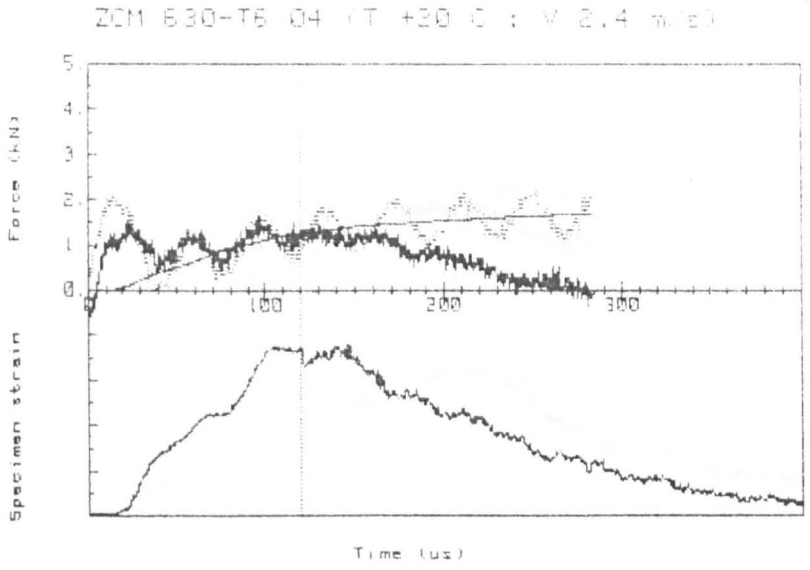

FIG. 5.18a.

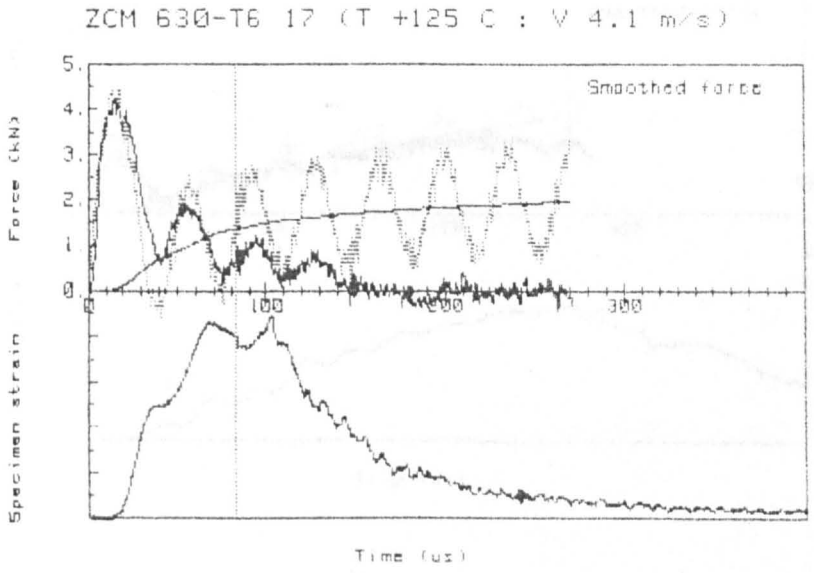

FIG. 5.18b.

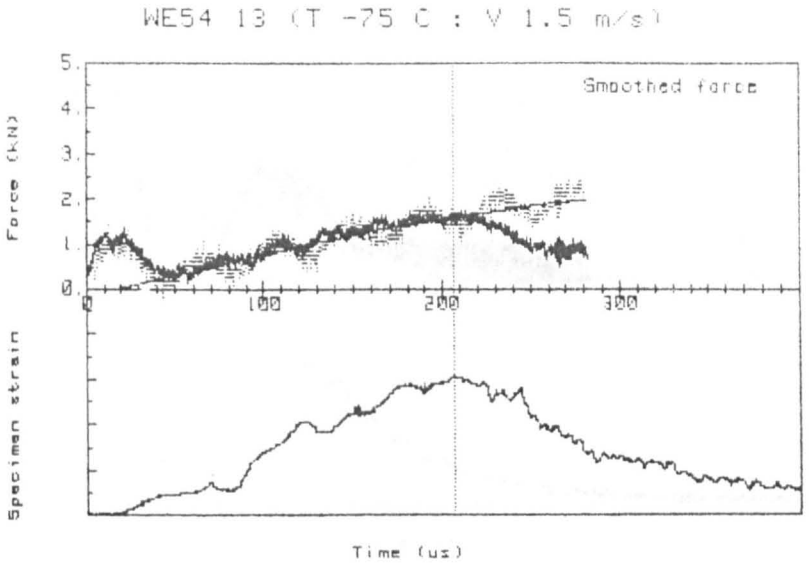

FIG. 5.19a.

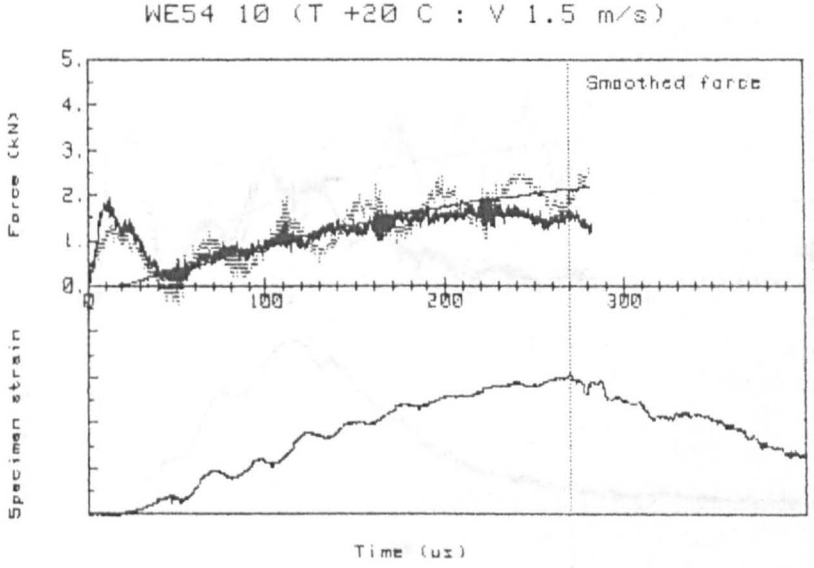

FIG. 5.19b.

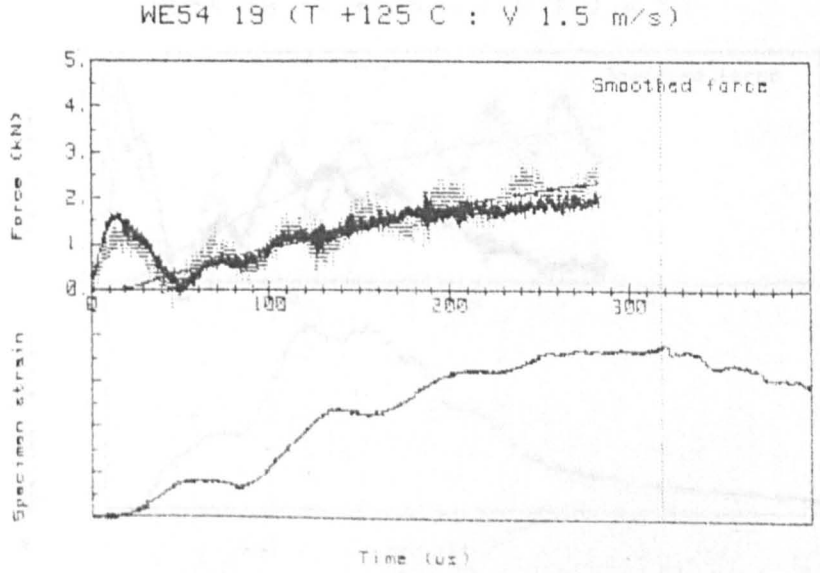

FIG. 5.19c.

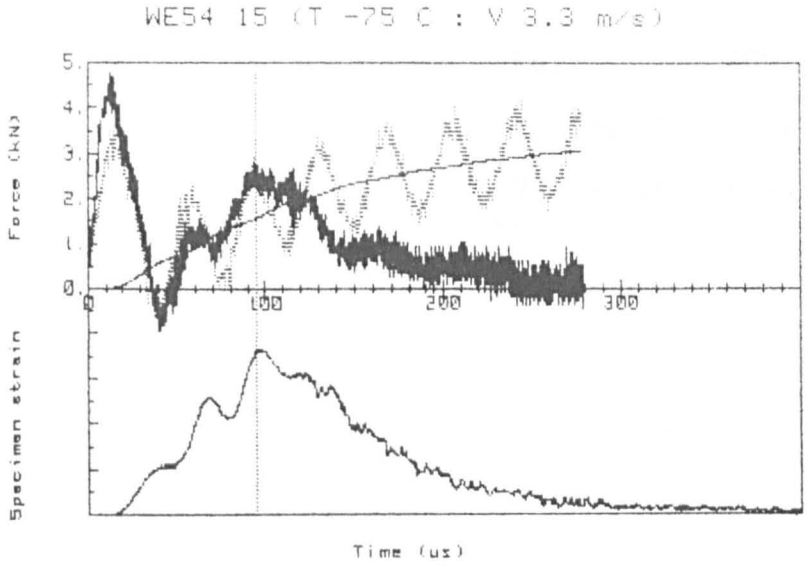

FIG. 5.20a.

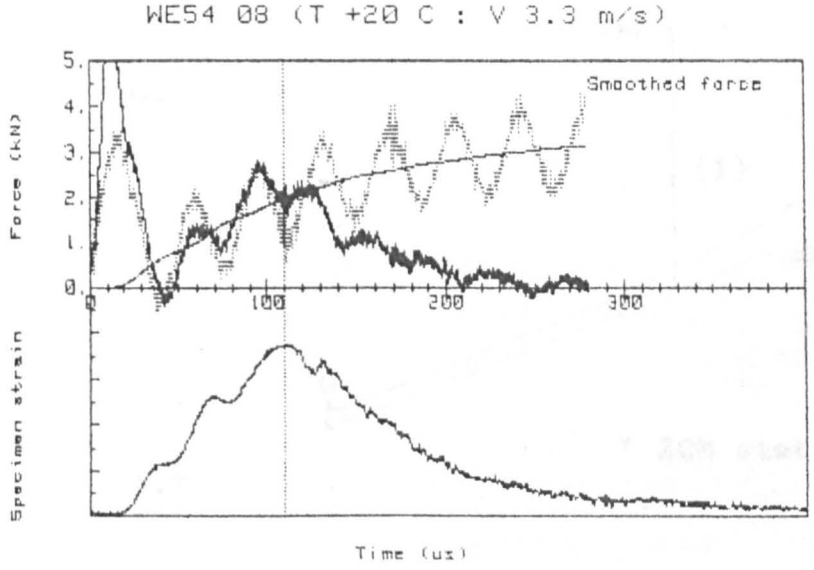

FIG. 5.20b.

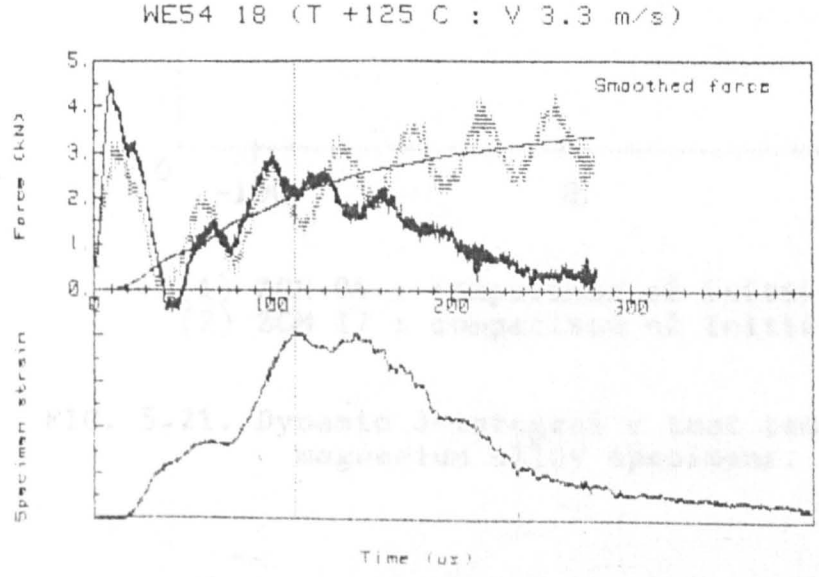

FIG. 5.20c.

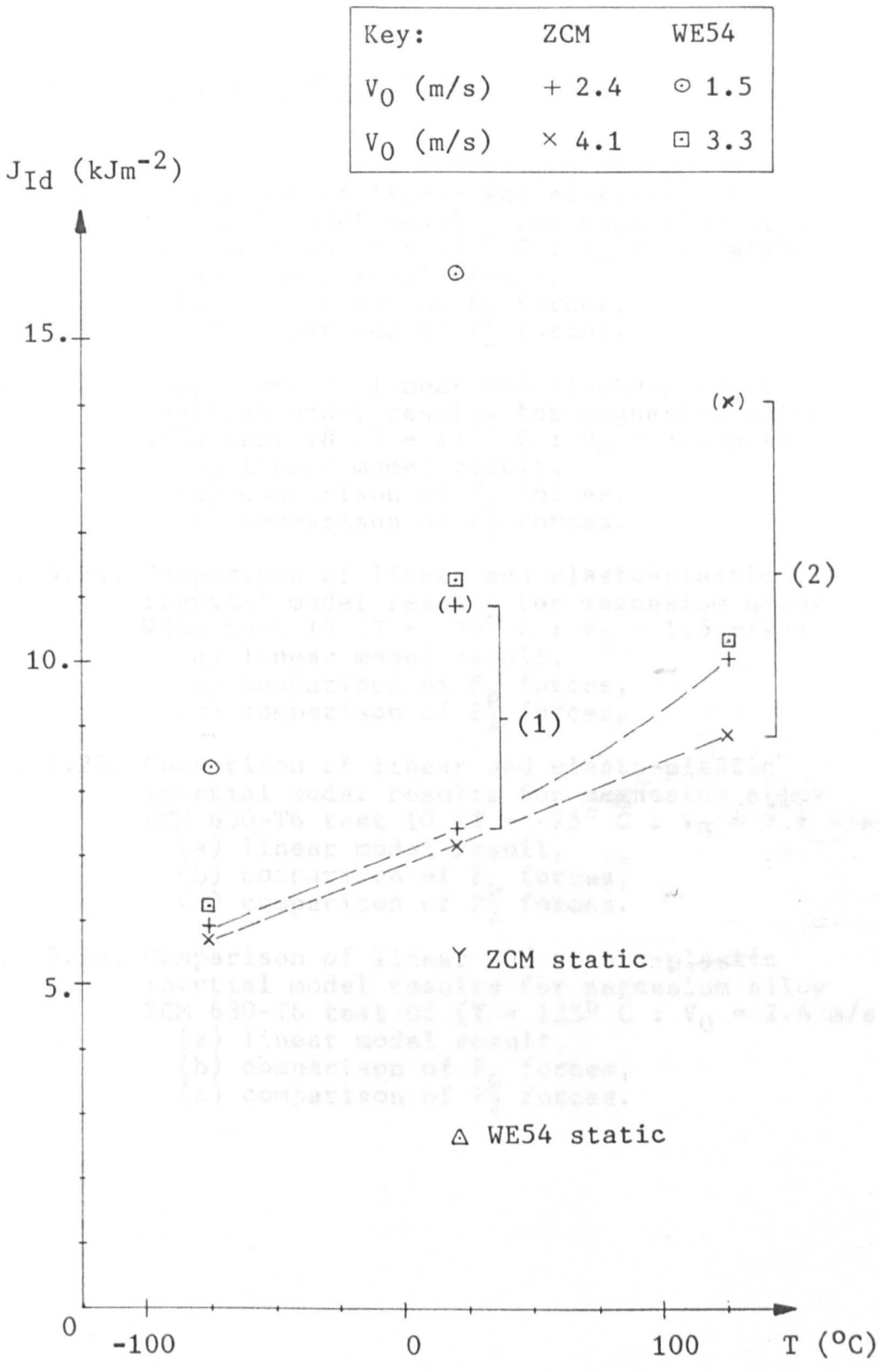

(1) ZCM 04 : comparison of initiation criteria
(2) ZCM 17 : comparison of initiation criteria

FIG. 5.21. Dynamic J-integral v test temperature for magnesium alloy specimens.

Titles for figures 5.22 to 5.26.

FIG. 5.22. Comparison of linear and elasto-plastic inertial model results for magnesium alloy WE54 test 15 ($T = -75^{o}$ C : $V_0 = 3.3$ m/s):
(a) linear model result,
(b) comparison of F_p forces,
(c) comparison of P_2^p forces.

FIG. 5.23. Comparison of linear and elasto-plastic inertial model results for magnesium alloy WE54 test 18 ($T = 125^{o}$ C : $V_0 = 3.3$ m/s):
(a) linear model result,
(b) comparison of F_p forces,
(c) comparison of P_2^p forces.

FIG. 5.24. Comparison of linear and elasto-plastic inertial model results for magnesium alloy WE54 test 13 ($T = -75^{o}$ C : $V_0 = 1.5$ m/s):
(a) linear model result,
(b) comparison of F_p forces,
(c) comparison of P_2^p forces.

FIG. 5.25. Comparison of linear and elasto-plastic inertial model results for magnesium alloy ZCM 630-T6 test 10 ($T = -75^{o}$ C : $V_0 = 2.4$ m/s):
(a) linear model result,
(b) comparison of F_p forces,
(c) comparison of P_2^p forces.

FIG. 5.26. Comparison of linear and elasto-plastic inertial model results for magnesium alloy ZCM 630-T6 test 08 ($T = 125^{o}$ C : $V_0 = 2.4$ m/s):
(a) linear model result,
(b) comparison of F_p forces,
(c) comparison of P_2^p forces.

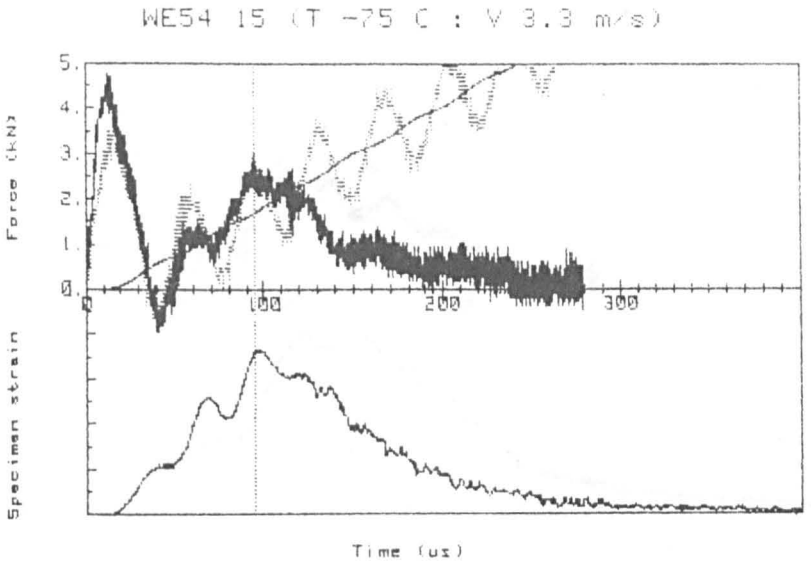

FIG. 5.22a.

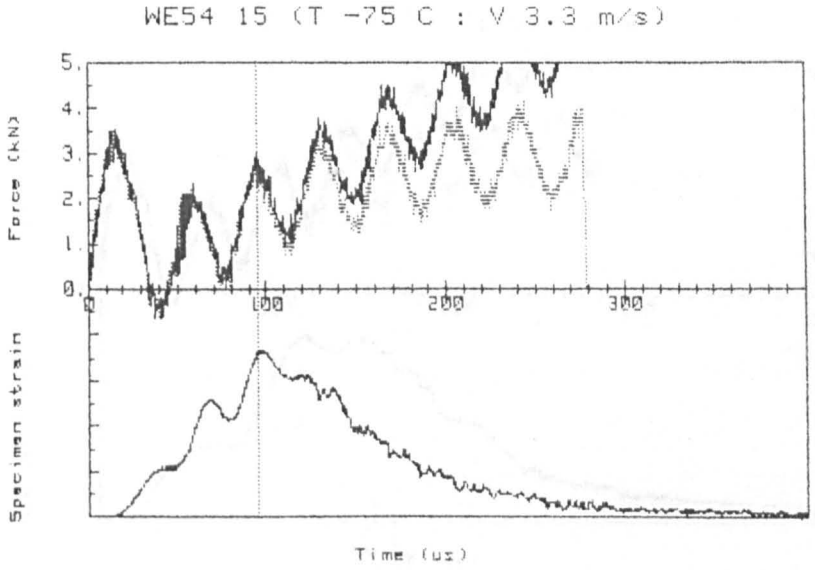

FIG. 5.22b.

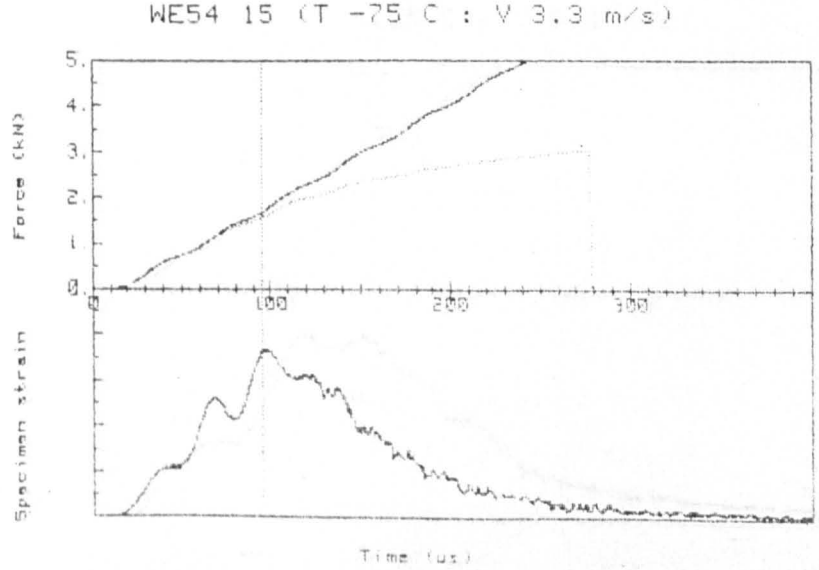

FIG. 5.22c.

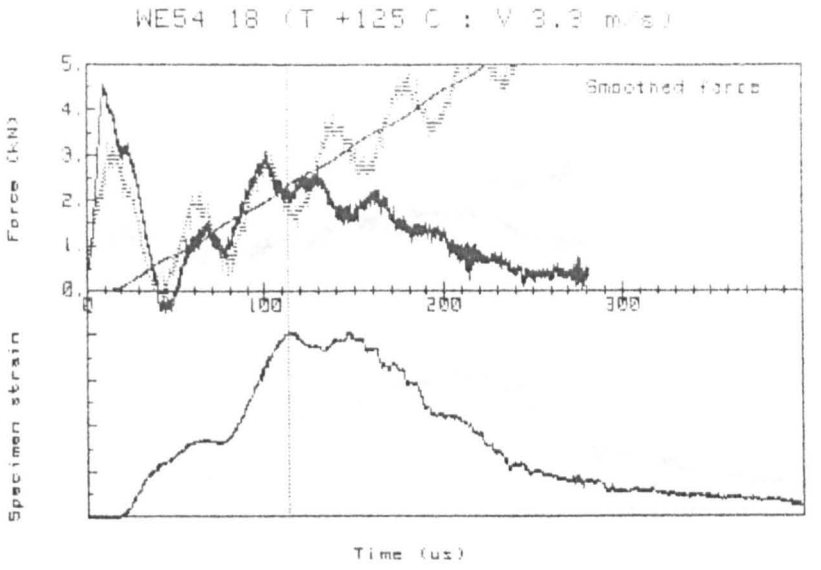

FIG. 5.23a.

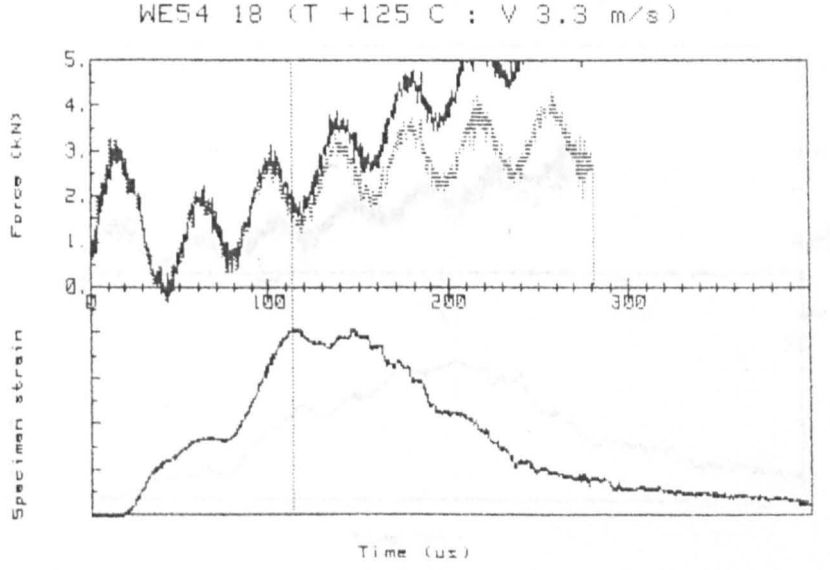

FIG. 5.23b.

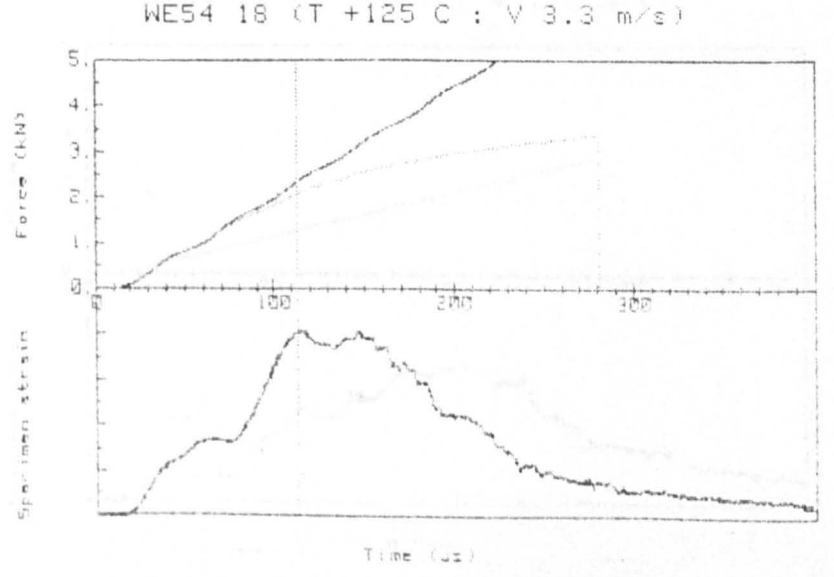

FIG. 5.23c.

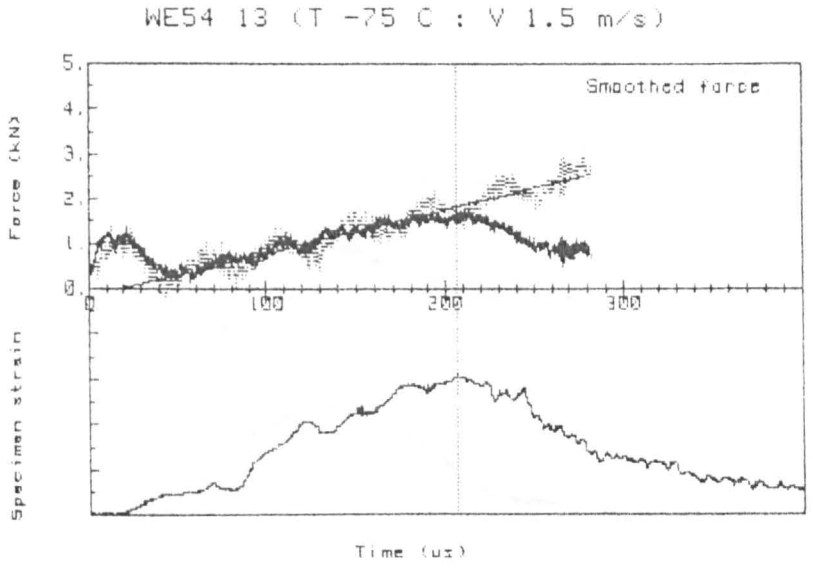

FIG. 5.24a.

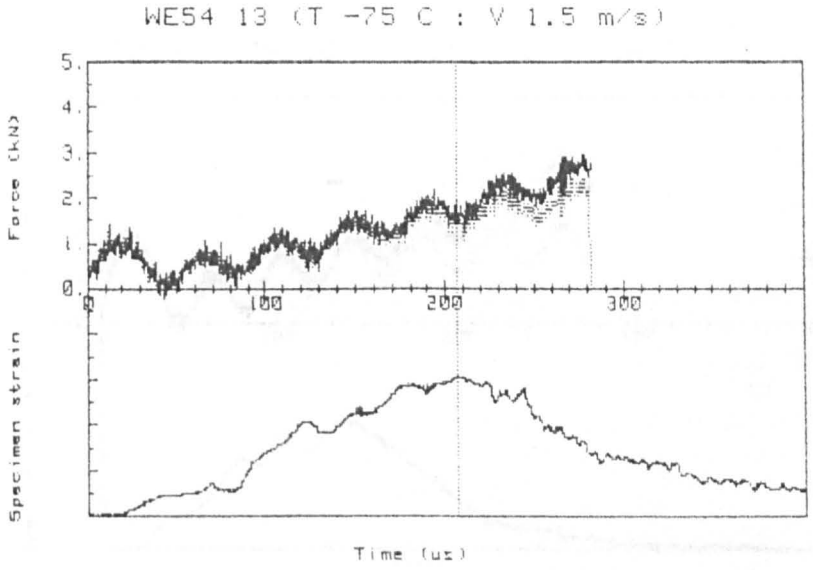

FIG. 5.24b.

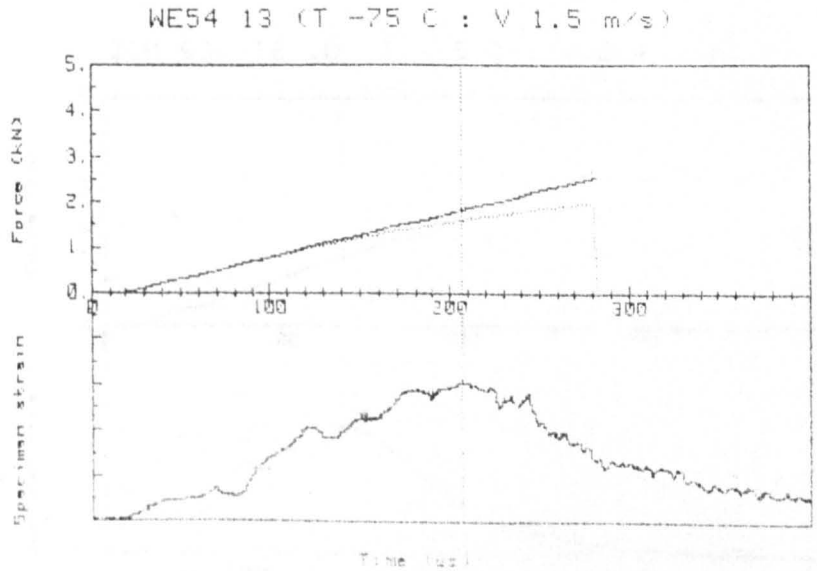

FIG. 5.24c.

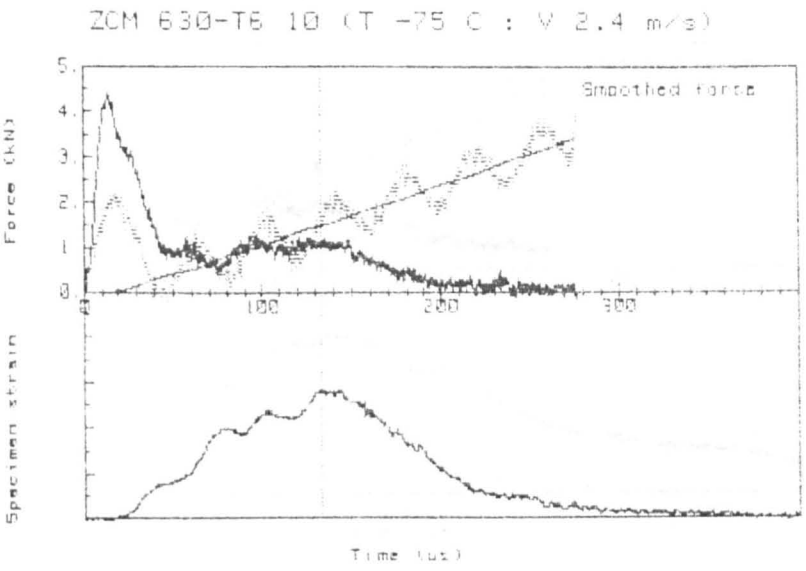

FIG. 5.25a.

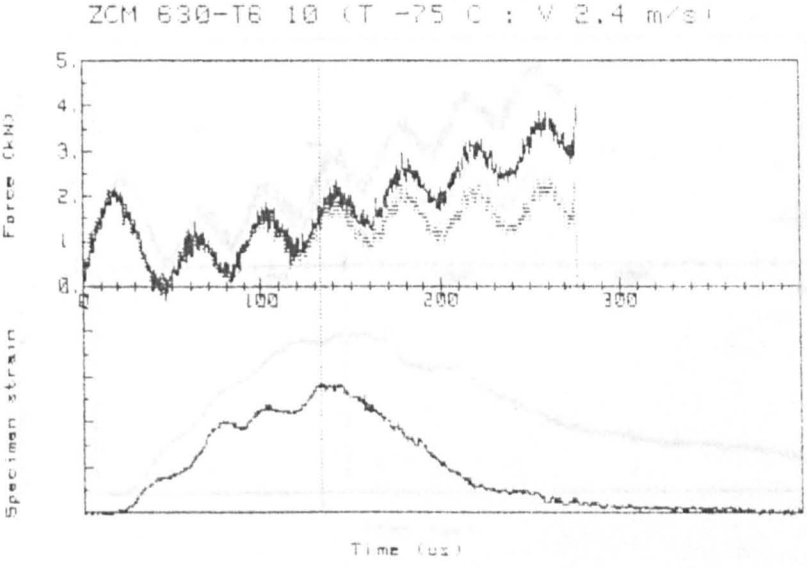

FIG. 5.25b.

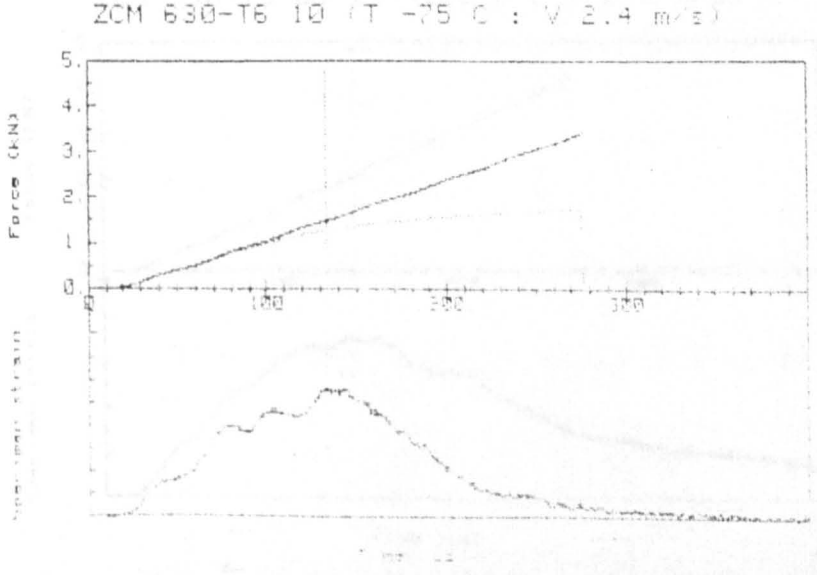

FIG. 5.25c.

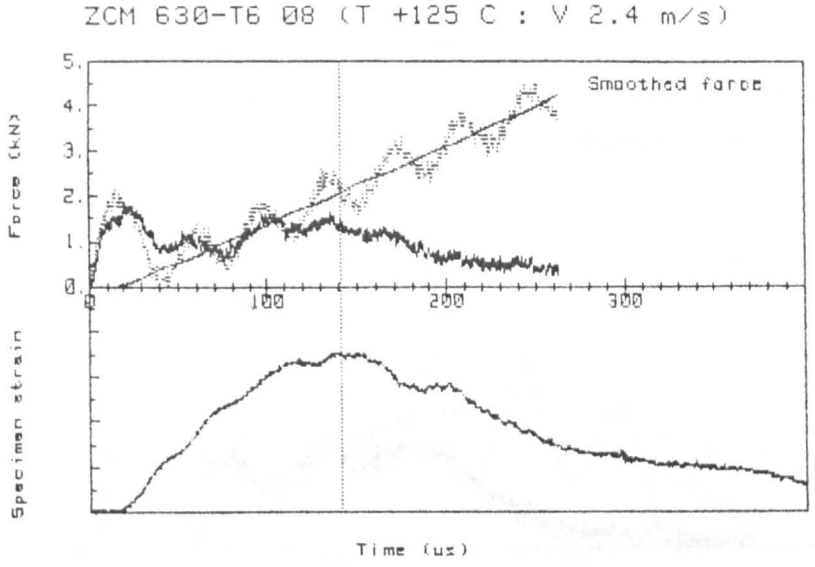

FIG. 5.26a.

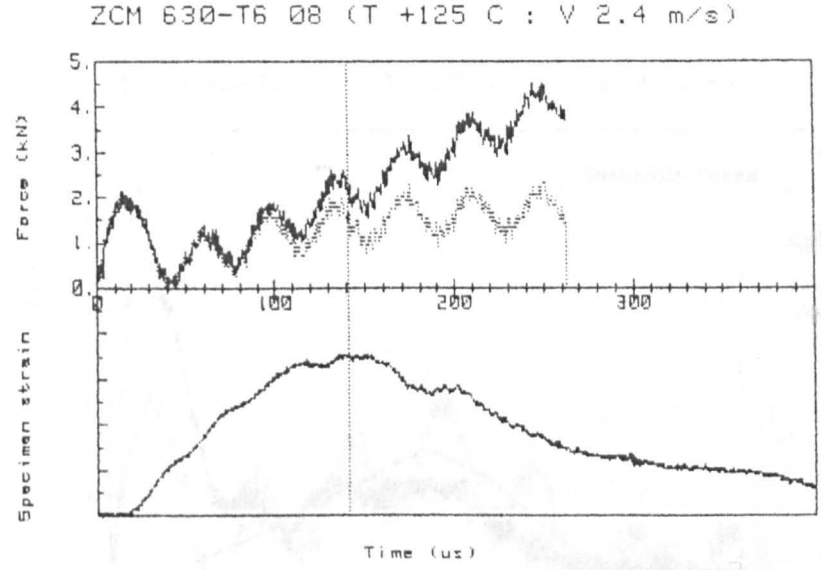

FIG. 5.26b.

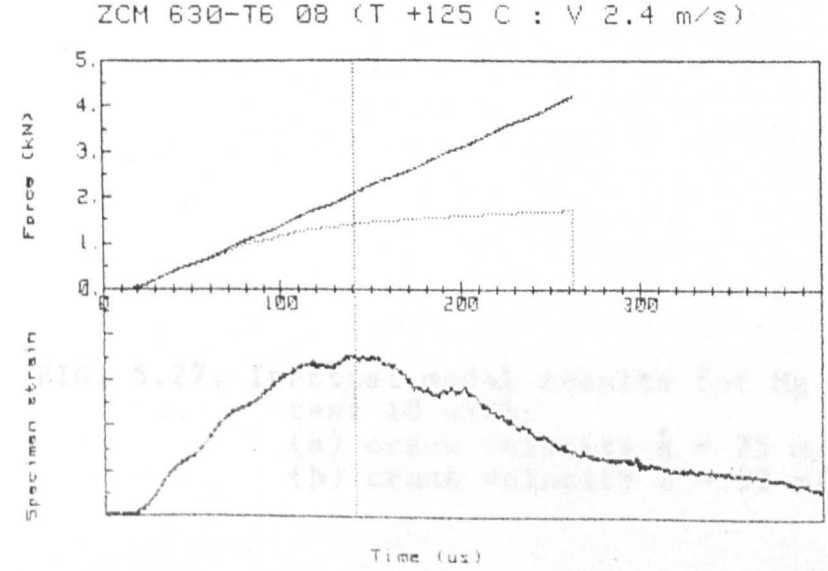

FIG. 5.26c.

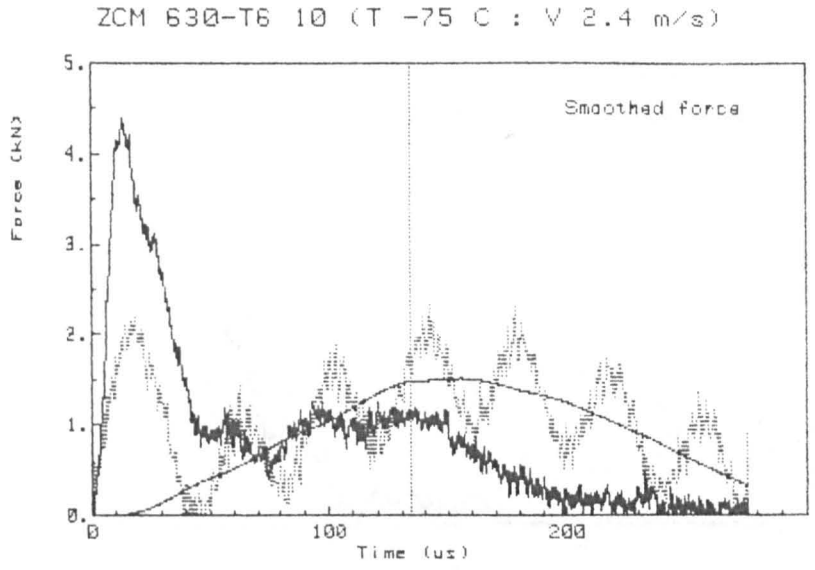

FIG. 5.27a.

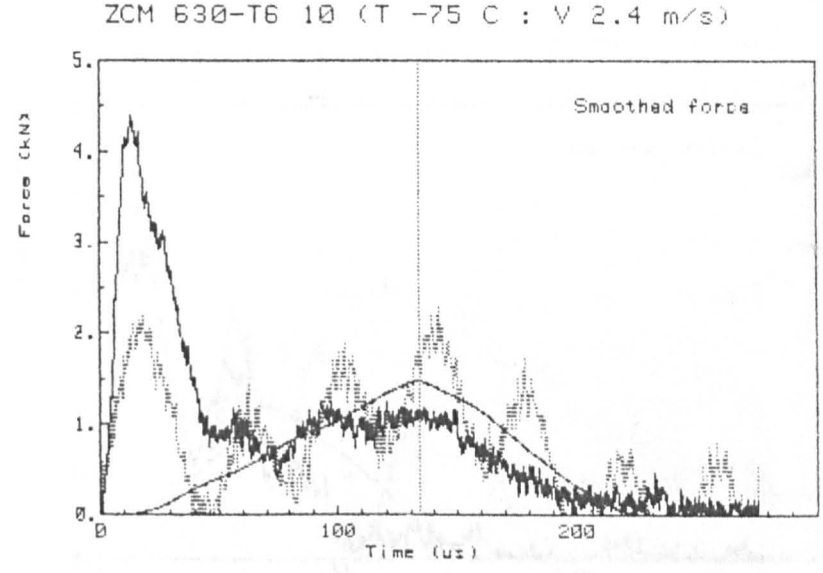

FIG. 5.27b.

FIG. 5.27. Inertial model results for Mg alloy ZCM 630-T6 test 10 with:
(a) crack velocity $\dot{a}$ = 25 m/s after init.,
(b) crack velocity $\dot{a}$ = 50 m/s after init.

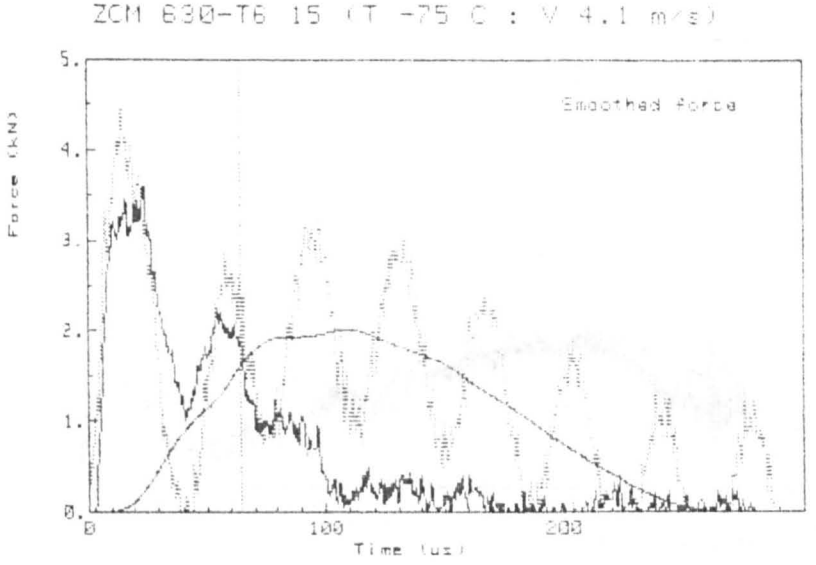

FIG. 5.28a.

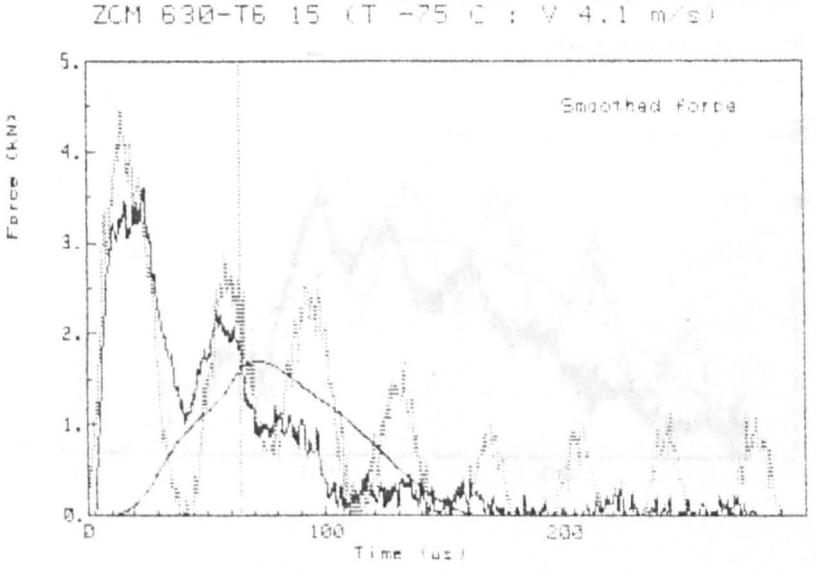

FIG. 5.28b.

FIG. 5.28. Inertial model results for Mg alloy ZCM 630-T6 test 15 with:
(a) crack velocity $\dot{a}$ = 25 m/s after init.,
(b) crack velocity $\dot{a}$ = 50 m/s after init.

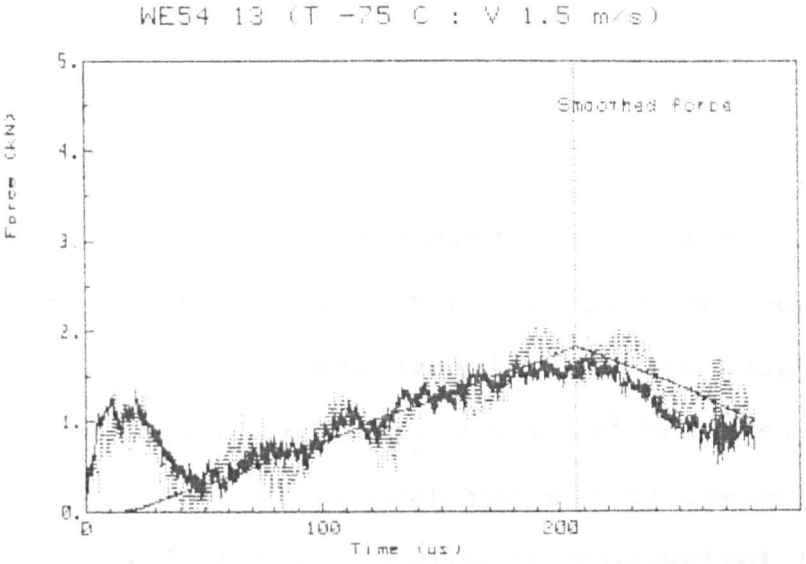

FIG. 5.29a.

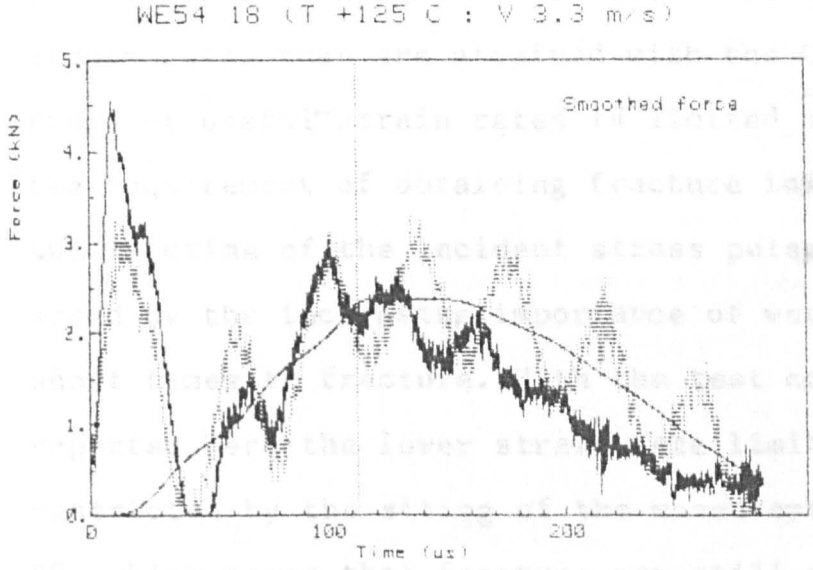

FIG. 5.29b.

FIG. 5.29. Inertial model results for Mg alloy WE54 with crack velocity $\dot{a}$ = 25 m/s after initiation for:
(a) test 13 (V_0 = 1.5 m/s),
(b) test 18 (V_0 = 3.3 m/s).

6. CONCLUSIONS.

The Hopkinson pressure bar loaded instrumented impact test on three point bend Charpy size specimens allows measurement of the dynamic fracture toughness of metals at high strain rates ($\dot{K}_I \sim 5 \times 10^5$ MPam$^{\frac{1}{2}}$/s). The inertial load component is much reduced by comparison with the standard Charpy pendulum or drop-weight test at the same nominal strain rate due to the finite rise time of the stress wave which loads the specimen. Thus the Hopkinson pressure bar technique can be used effectively at higher strain rates than are attained with the Charpy test. The range of useful strain rates is limited at low speed by the requirement of obtaining fracture initiation within the lifetime of the incident stress pulse and at high speed by the increasing importance of wave effects at short times to fracture. With the test configuration reported here the lower strain rate limit is further restricted by the siting of the measurement points S1 and S2, which means that fracture can still occur after measurements have ceased.

A lumped mass-spring model of the impact event has been used to account for the dynamic nature of the test. This approach is a compromise over a fully 3-dimensional finite element model of the loading bar, specimen, and supports. The inertia of both the specimen and the loading

system are explicitly included in the model and so truly dynamic toughness evaluations can be made. In particular, the load measured at the point of reflection of the incident bar is different from the load acting directly on the crack. Theoretical calculations of the stiffness of the profiled end section of the incident bar and the (linear elastic) stiffness of the contact zone with the specimen overestimate the "machine" stiffness compared with values derived from the experimental results. These differences are probably attributable to plastic deformation at the load points, possible out-of-squareness in the seating of the specimen, and, in the case of the support stiffness, the unknown contribution of the anvil.

The reliability of the derived fracture toughness results depends, firstly, on the accuracy of defining the instant of crack initiation and, secondly, on the efficiency with which the model represents the experiment. It is hypothesised that the latter can be determined by how well the derived impact force matches the measured force at the change of section of the incident bar up to the instant of crack initiation.

The model has also been used to demonstrate how the frequency of oscillations in the measured force-time trace depends on factors such as the ratio of impactor to specimen stiffness, the effective mass of the specimen, and the degree of "overhang" at the supports. The very

similar fracture toughness derivations from the full size and truncated specimens demonstrate how well the inertial (ie lumped mass-spring) model copes with different load characteristics.

Crack velocities have been estimated from the unloading rate of the measured force traces. In the En24 steel specimens these estimates ranged from 50 m/s to 250 m/s depending on impact velocity (and degree of plasticity), while for the magnesium alloys the crack velocities were approximately constant at 50 m/s for ZCM 630-T6 and 25 m/s for WE54 throughout the loading rate range. It is supposed that this difference in behaviour is related to the different material structures and modes of fracture (predominantly cleavage in the steel and intergranular in the magnesium alloys).

The effect of crack velocity on the derived specimen force (P_2) in the inertial model is critical. For rapid, brittle crack growth the force falls abruptly, in just the same way as the specimen strain gauge (S3) signal. However, at lower crack speeds it develops a "peak", sometimes continuing to rise after the assumed crack initiation. Again this behaviour is matched by the specimen strain gauge, suggesting that initiation may have occurred at low crack velocity some time earlier than indicated by the peak measurement. Thus the inertial modelling technique may be used to assess the limits of

specimen-mounted strain gauges in identifying crack initiation.

Even with relatively brittle crack initiation the S3 strain gauges sometimes measured sharp falls in strain with subsequent recovery and increase to a peak. In these cases comparison with the measured force in the incident bar shows that this "first drop" corresponds approximately to the peak measured load. It is proposed that sharp "first drop" features of this kind can be treated as crack initiation events.

Elasto-plastic specimen behaviour has been treated with a suitable algorithm based on power law strain hardening. For a ductile temper of En24 steel the algorithm resulted in an over-prediction of load if plane strain conditions were assumed. As expected, a second prediction based on the assumption of plane stress conditions bracketed the real measurement. It is not clear whether this result demonstrates a loss of constraint or is simply due to the over-stiff nature of the Ramberg-Osgood stress-strain characterisation used in the prediction. The amount of plasticity present in the specimens meant that identifying crack initiation from the S3 strain gauge traces was not really possible. J-integral values have been quoted for the maximum S3 reading, but it is not expected that these are accurate initiation values.

Using the same model for the magnesium alloy

specimens showed that few significant plastic effects occurred prior to crack initiation, although the plastic zone sizes computed from a linear analysis were too large to permit evaluation of valid plane strain fracture toughness measurements with Charpy size specimens.

Compositional changes in the two batches of En24 steel meant that these had to be treated as separate materials (in fact, the HC2 and HC3 steel lay outside the specification for En24 in their proportion of manganese). The relative change of toughness is the reverse of what might be expected from the relative changes in proportion of carbon and manganese, but is compatible with the increased amount of sulphur in the HC2 specimens. Small differences in heat treatment may also have contributed.

The En24 HC2 steel was tested under both quasi-static and dynamic loading conditions at room temperature. The measured rise in fracture toughness from 38 $MPam^{\frac{1}{2}}$ to 45-53 $MPam^{\frac{1}{2}}$ with increasing strain rate is not typical for this sort of material at these temperatures. From the increase of yield stress with strain rate, more brittle behaviour is expected. However, a corresponding increase in the critical cleavage stress with strain rate would explain the observed trend.

The increase of fracture toughness with test temperature in the transition zone is exactly as expected.

No significant trend in fracture toughness can be discerned over the (very limited) range of strain rates achieved in the tests.

The dynamic fracture toughnesses (as represented by J-integrals) of the magnesium alloys are also found to be higher than static values supplied by the manufacturers. In the case of the dynamic measurements, identification of crack initiation is not so clear cut as with the steel specimens. Slow crack velocities, implied by the shape of the force-time traces, may not have caused a drop in the S3 strain gauge measurements until some time after initiation. This hypothesis is supported by information from other sources on the microstructural mechanics of fracture in magnesium alloys and so it is possible that overprediction of the crack initiation time was responsible for most, if not all, the difference between static and dynamic measurements.

7. RECOMMENDATIONS FOR FURTHER WORK.

The most important shortcoming revealed by this study is in the identification of crack initiation. With strain gauges mounted on the specimen this becomes increasingly difficult as the degree of plasticity increases. Furthermore, if crack initiation occurs at low crack velocity in a displacement-controlled test of this kind, the accompanying drop in load may be too small to detect. Non-load-dependent techniques of crack detection are therefore required. Alternating current devices need to operate at higher frequencies than have been achieved to date if they are to be useful in this respect. A possible approach is the electromagnetic sensor briefly mentioned in section 3.6 if this can be used in the presence of considerable ductility.

It is desirable that the dynamic stress intensity factors derived from a lumped mass-spring analysis of the kind described in this thesis be compared with direct measurements using, say, the method of caustics. These are qualitatively similar, but this similarity needs to be quantified to give more confidence in the approach to analysis presented here.

It would be possible to extend the (limited) loading rate range of the Hopkinson pressure bar rig by increasing the S1/S2 strain gauge separation. This could be achieved

by moving the S1 strain gauge closer to the end of the bar or simply lengthening the incident bar. Further information about the loading of the specimen (including the possibility of specimen/support separation) could be obtained by replacing the solid anvil with two parallel output bars and measuring the transmitted component of the stress pulse.

It is important that specimens are prepared in single large batches so that vagaries of composition and heat treatment are minimised. Static tests should always be carried out on a given batch of specimens and ideally the rig should be modified so that these tests may be performed in situ with the same machine stiffness components.

The inertial modelling approach should be applied to as wide a range of materials as possible to improve the definition of the model components. This would entail using Hopkinson pressure bars of different cross-section (and, perhaps, material composition) to control the magnitude of forces generated at the loading section.

Greater understanding of the loading bar/specimen/support interaction could be obtained by further numerical modelling of the whole system. This may be feasible with the new transputers, although special care will need to be taken with the contact conditions.

8. REFERENCES.

1. WESTERGAARD, H. M., 'Bearing pressures and cracks', J. Appl. Mech., June 1939 (A49-A53).

2. KLEPACZKO, J. R., 'Loading rate spectra for fracture initiation in metals', Theor. and Appl. Fracture Mech., Vol. 1, 1984 (181-191).

3. ASTM E-399, 'Standard test method for plane strain fracture toughness of metallic materials', American Society for Testing and Materials (ASTM), 1983.

4. GLOVER, A. P., JOHNSON, F. A., RADON, J. C., and TURNER, C. E., 'Dynamic fracture toughness measurement by instrumented impact bend testing and compact K testing', in 'Dynamic Fracture Toughness', Welding Institute and ASM, 1976 (63-72).

5. WILLIAMS, J. G., and ADAMS, G. C., 'The analysis of instrumented impact tests using a mass-spring model', Int. J. of Fracture, Vol. 33, 1987 (209-222).

6. KANNINEN, M. F., and POPELAR, C. H., 'Advanced fracture mechanics', Oxford University Press, 1985.

7. IRWIN, G. R., 'Linear fracture mechanics, fracture transition, and fracture control', Eng. Fract. Mech., Vol. 1, 1968 (241-257).

8. GRIFFITH, A. A., 'The phenomena of rupture and flow in solids', Phil. Trans. of the Royal Society, Vol. A221, 1921 (163-198).

9. KNOTT, J. F., 'Fundamentals of fracture mechanics', Butterworth, 1973.

10. GROSS, B., and SRAWLEY, J. E., 'Stress intensity factors for three point bend specimens by boundary collocation', NASA TND-3092, 1965.

11. SRAWLEY, J. E., 'Wide range stress intensity factor expressions for ASTM E-399 standard fracture toughness specimens', Int. J. of Fracture, Vol. 12, 1976 (R475-R476).

12. ROOKE, D. P., and CARTWRIGHT, D. J., 'Compendium of stress intensity factors', HMSO, 1976.

13. MURAKAMI, Y., (Ed.), 'Stress intensity factors handbook', Committee on Fracture Mechanics, The Society of Materials Science, Japan, Pergamon Press, 1987.

14. TADA, H., PARIS, P. C., and IRWIN, G. R., 'The stress analysis of cracks handbook', Del Research Corporation, Hellertown, Pennsylvania, 1973.

15. SHIH, C. F., ANDREWS, W. R., and WILKINSON, J. P. D., 'Characterisation of crack initiation and growth with applications to pressure vessel steels', ICM 3, Vol. 3, 1979 (589-601).

16. RICE, J. R., 'A path independent integral and the approximate analysis of strain concentrations by notches and cracks', J. Appl. Mech., Vol. 35, 1968 (379-386).

17. RICE, J. R., and ROSENGREN, G. F., 'Plane strain deformation near a crack tip in a power law hardening material', J. Mech. Phys. Solids, Vol. 16, 1968 (1-12).

18. RAMBERG, W., and OSGOOD, W. R., 'Description of stress-strain curves by three parameters', NACA Technical Note No. 902, Washington, 1943.

19. HUTCHINSON, J. W., 'Singular behaviour at the end of a tensile crack in a hardening material', J. Mech. Phys. Solids, Vol. 16, 1968 (13-31).

20. HUTCHINSON, J. W., 'Fundamentals of the phenomenological theory of non-linear fracture mechanics', J. Appl. Mech., Vol. 50, 1983 (1042-1051).

21. SHIH, C. F., 'Relationship between the J-integral and the crack opening displacement for stationary and extending cracks', J. Mech. Phys. Solids, Vol. 29, 1981 (305-326).

22. McMEEKING, R. M., 'Finite deformation analysis of crack tip opening in elastic-plastic materials and implications for fracture', J. Mech. and Phys. Solids, Vol. 25, 1977 (357-381).

23. SHIH, C. F., and GERMAN, M. D., 'Requirements for a one parameter characterisation of crack tip fields by the HRR singularity', Int. J. of Fracture, Vol. 17, 1981 (27-43).

24. BEGLEY, J. A., and LANDES, J. D., 'The J-integral as a fracture criterion', in 'Fracture Toughness', Proc. of the 1971 National Symposium on Fracture Mechanics, Part II, ASTM STP 514, ASTM, 1972 (1-20).

25. LANDES, J. D., and BEGLEY, J. A., 'The effect of specimen geometry on J_{Ic}', in 'Fracture Toughness', Proc. of the 1971 National Symposium on Fracture Mechanics, Part II, ASTM STP 514, ASTM, 1972, (24-39).

26. ATKINS, A. G., and MAI, Y. W., 'Elastic and plastic fracture', Ellis Horwood, 1985.

27. PARIS, P. C., 'Discussion of "The J-integral as a fracture criterion"', following Ref. [24], ASTM STP 514, ASTM, 1972 (21-22).

28. RICE, J. R., PARIS, P. C., and MERKLE, J. G., 'Some further results of J-integral analysis and estimates', in 'Progress in Flaw Growth and Fracture Toughness Testing', ASTM STP 536, ASTM, 1973 (231-245).

29. SUMPTER, J. D. G., and TURNER, C. E., 'Method for laboratory determination of J_c', in 'Cracks and Fracture', ASTM STP 601, ASTM, 1976 (3-18).

30. SRAWLEY, J. E., 'On the relation of J_I to work done per unit uncracked area: "total" or component "due to crack"', Int. J. of Fracture, Vol. 12, 1976 (R470-R474).

31. GREEN, A. P., and HUNDY, B. B., 'Initial plastic yielding in notch bend tests', J. Mech. Phys. Solids, Vol. 4, 1956 (128-144).

32. KUMAR, V., GERMAN, M. D., and SHIH, C. F., 'Engineering approach for elastic-plastic fracture analysis', EPRI-NP-1931, General Electric Company, 1981.

33. HANCOCK, J. W., and COWLING, M. J., 'Role of state of stress in crack tip failure processes', Metal Science, 1980 (293-304).

34. McMEEKING, R. M., and PARKS, D. M., 'On criteria for J-dominance of crack tip fields in large scale yielding', in 'Elasto-Plastic Fracture', ASTM STP 668, ASTM, 1979 (175-194).

35. LIU, H. W., and ZHUANG, T., 'Plane strain crack tip field and a dual-parameter fracture criterion for non-linear fracture mechanics', Theor. and Appl. Fracture Mechanics, Vol. 7, 1987 (149-168).

36. KNOTT, J. F., 'Microscopic aspects of crack extension', in 'Advances in Elastic-Plastic Fracture Mechanics', ed. Larsson, L.H., Applied Science Publishers Ltd., London, 1980 (21-41).

37. RITCHIE, R. O., KNOTT, J. F., and RICE, J. R., 'On the relationship between critical tensile stress and fracture toughness in mild steel', J. Mech. and Phys. Solids, Vol. 23, 1973 (395-410).

38. RITCHIE, R. O., SERVER, W. L., and WULLAERT, R. A., 'Critical fracture stress and fracture strain models for the prediction of lower and upper shelf toughness in nuclear pressure vessel steels', Met. Trans. A, Vol. 10A, 1979 (1557-1570).

39. McCLINTOCK, F. A., and IRWIN, G. R., 'Plasticity aspects of fracture mechanics', in 'Fracture Toughness Testing and Its Applications', ASTM STP 381, ASTM, 1965.

40. RITCHIE, R. O., FRANCIS, B., and SERVER, W. L., 'Evaluation of toughness in AISI 4340 alloy steel austenitized at low and high temperatures', Met. Trans. A, Vol 7A, 1976 (831-838).

41. McCLINTOCK, F. A., 'A criterion for ductile fracture by the growth of holes', J. of Appl. Mech., Vol. 35, 1968 (363-371).

42. KALTHOFF, J. F., WINKLER, S., and BEINERT, J., 'The influence of dynamic effects in impact testing', Int. J. of Fracture, Vol. 13, 1977 (528-531).

43. NILSSON, F., 'Dynamic fracture theory', presented at the course 'Crack Dynamics in Metallic Materials', Int. Centre for Mechanical Sciences, Udine, Italy, Sept. 5-9 1988.

44. BROCK, L. M., JOLLES, M., and SCHROEDL, M., 'Dynamic impact over a subsurface crack: applications to the dynamic tear test', Trans. of ASME, 85-APM-17, 1985.

45. KANNINEN, M. F., 'A critical appraisal of solution techniques in dynamic fracture mechanics', in 'Proc. of the First International Conference on Numerical Methods in Fracture Mechanics', ed. Luxmoore, A.R., and Owen, D.R.J., Swansea, 1978.

46. NILSSON, F., 'Crack growth initiation and propagation under dynamic loading', Inst. Phys. Conf. Series No. 70, paper presented at 'Third Conference on Mechanical Properties at High Rates of Strain', Oxford, 1984.

47. KLEPACZKO, J. R., 'Dynamic crack initiation - experimental methods and results', presented at the course 'Crack Dynamics in Metallic Materials', Int. Centre for Mechanical Sciences, Udine, Italy, Sept. 5-9 1988.

48. MORAN, B., and SHIH, C. F., 'Crack tip and associated domain integrals from momentum and energy balance', Eng. Fract Mech., Vol. 27, 1987 (615-642).

49. NAKAMURA, T., SHIH, C. F., and FREUND, L. B., 'Analysis of dynamically loaded three point bend ductile fracture specimen', Eng. Fract. Mech., Vol. 25, 1976 (323-339).

50. WILLIAMS, J. G., 'The analysis of dynamic fracture using lumped mass-spring models', Int. J. of Fracture, Vol. 33, 1987 (47-59).

51. JONES, N., 'Structural aspects of ship collisions', in 'Structural Crashworthiness', ed. Jones, N., and Wierzbicki, T., 1983 (308-337).

52. TANIMURA, S., and DUFFY, J., 'Strain rate effects and temperature history effects for three different tempers of 4340 VAR steel', Int. J. of Plasticity, Vol. 2, 1986 (21-35).

53. HOFF, R., RUBIN, C. A., and HAHN, G. T., 'Strain rate dependence of the deformation at the tip of a stationary crack', in 'Fracture Mechanics 16th Symposium', ASTM STP 868, 1985 (409-430).

54. HOFF, R., RUBIN, C. A., and HAHN, G. T., 'High rate deformation in the field of a crack', in 'Material Behaviour Under High Stress and Ultra High Loading Rates', ed. Mescall, J., and Weiss, V., Proc. 29th Sagamore Army Materials Conference, Plenum Press, 1983.

55. ASTM STP 563, 'Instrumented Impact Testing', American Society for Testing and Materials, 1974.

56. WELDING INSTITUTE AND ASM, 'Dynamic Fracture Toughness', Welding Inst. and ASM, 1976.

57. WULLAERT, R. A., (ed.), 'CSNI Specialist Meeting on Instrumented Pre-cracked Charpy Testing', Electric Power Research Inst., Palo Alto, California, 1981.

58. ASTM E-23, 'Standard methods for notched bar impact testing of metallic materials', American Society for Testing and Materials (ASTM), 1982.

59. SERVER, W. L., 'General yielding of Charpy V notch and pre-cracked Charpy specimens', J. of Eng. Mat. and Tech., Vol. 100, 1978 (183-187).

60. SERVER, W. L., 'Impact three point bend testing for notched and pre-cracked specimens', J. of Testing and Evaluation, Vol. 6, 1978 (29-34).

61. IRELAND, D. R., 'Procedures and problems associated with reliable control of the instrumented impact test', in 'Instrumented Impact Testing', ASTM STP 563, ASTM, 1974 (3-29).

62. KOBAYASHI, A. S., RAMULU, M., and MALL, S., 'Impacted notch bend specimens', J. of Pressure Vessel Tech., Vol. 104, 1982 (25-30).

63. IYER, K. R., and MICLOT, R. B., 'Instrumented Charpy testing for determination of the J-integral', in 'Instrumented Impact Testing', ASTM STP 563, ASTM, 1974 (146-165).

64. KOBAYASHI, T., 'Analysis of impact properties of A533 steel for nuclear reactor pressure vessel by instrumented Charpy test', Eng. Fract. Mech., Vol. 19, 1984 (49-65).

65. NICHOLAS, T., 'Instrumented impact testing using a Hopkinson bar apparatus', AFML-TR-75-54, Air Force Materials Laboratory, 1975.

66. TSUKADA, H., IWADATE, T., TANAKA, Y., and ONO, S., 'Static and dynamic fracture toughness behaviour of heavy section steels for nuclear pressure vessels', in '4th International Conference on Pressure Vessel Tech.' Vol. 1, I. Mech. E., 1980 (369-374).

67. NGUYEN-DUY, P., LAPOINTE, A., and FLAMAND, J., 'Determination of the fracture toughness of two C-Mn steels for different temperatures and loading rates', in 'Proc. of the Int. Symposium on Fracture Mechanics', ed. Tyson, W.R., and Mukherjee, B., Winnipeg, 1987.

68. MALL, S., KOBAYASHI, A. S., and LOSS, F. J., 'Dynamic fracture analysis of notched bend specimens', in 'Crack Arrest Methodology and Applications', ASTM STP 711, ASTM, 1980 (70-85).

69. BOHME, W., and KALTHOFF, J. F., 'The behaviour of notched bend specimens in impact testing', Int. J. of Fracture, Vol. 20, 1982 (R139-R143).

70. KALTHOFF, J. F., 'On the measurement of dynamic fracture toughnesses - a review of recent work', Int. J. of Fracture, Vol. 27, 1985 (277-298).

71. GALLAGHER, R. H., 'A review of finite element techniques in fracture mechanics', in 'Proc. of the First International Conference on Numerical Methods in Fracture Mechanics', ed. Luxmoore, A.R., and Owen, D.R.J., Swansea, 1978.

72. HENSHELL, R. D., and SHAW, K. G., 'Crack tip elements are unnecessary', Int. J. for Num. Meth. in Engineering', Vol. 9, 1975 (495-509).

73. BARSOUM, R. S., 'On the use of isoparametric finite elements in linear fracture mechanics', Int. J. for Num. Meth. in Engineering', Vol. 10, 1976 (25-37).

74. OWEN, D. R. J., and FAWKES, A. J., 'Engineering fracture mechanics: numerical methods and applications', Pineridge Press Ltd., 1983.

75. NAKAMURA, T., SHIH, C. F., and FREUND, L. B., 'Elastic-plastic analysis of a dynamically loaded circumferentially notched round bar', Eng. Fract. Mech., Vol. 22, 1985 (437-452).

76. TVERGAARD, V., and NEEDLEMAN, A., 'Effect of material rate sensitivity on failure modes in the Charpy V-notch test', J. Mech. Phys. Solids, Vol. 34, 1986 (213-241).

77. NORRIS, D. M., and MARSTON, T. U., 'Dynamic analysis of the Charpy V-notch test', in 'CSNI Specialist Meeting on Instrumented Precracked Charpy Testing', ed. Wullaert, R.A., Electric Power Research Inst., Palo Alto, California, 1981 (2.35-2.49).

78. NISHIOKA, T., PERL, M., and ATLURI, S. N., 'An analysis of dynamic fracture in an impact test specimen', J. of Pressure Vessel Tech., Vol. 105, 1983 (124-131).

79. NAKAMURA, T., SHIH, C. F., and FREUND, L. B., 'Three dimensional transient analysis of a dynamically loaded three point bend ductile fracture specimen', Office of Naval Research, ONR0365/3, 1986.

80. KLEPACZKO, J. R., 'Fracture initiation under impact', Int. J. Impact Eng., Vol. 3, 1985 (191-210).

81. KLEPACZKO, J. R., 'Initiation of fracture at different loading rates, an attempt at modelling based on dynamic plasticity', J. de Physique, 1985 (C5.245-250).

82. KLEPACZKO, J. R., 'Discussion of a new experimental method in measuring fracture toughness initiation at high loading rates by stress waves', J. Eng. Mat. and Tech., Vol. 104, 1982 (29-35).

83. KRABIELL, A., and DAHL, W., 'Influence of strain rate and temperature on the tensile and fracture properties of structural steels', in 'Advances in Fracture Research', ed. Francois, D., Vol. 1, Cannes, 1981 (393-400).

84. MARANDET, B., PHELIPPEAU, G., and SANZ, G., 'Experimental determination of dynamic fracture toughness by J-integral method', in 'Advances in Fracture Research', ed. Francois, D., Vol. 1, Cannes, 1981 (375-383).

85. COSTIN, L. S., and DUFFY, J., 'The effect of loading rate and temperature on the initiation of fracture in a mild, rate-sensitive steel', J. Eng. Mat. and Tech., Vol. 101, 1979 (258-264).

86. RICE, J. R., and LEVY, N., 'Local heating by plastic deformation at a crack tip', in 'Physics of Strength and Plasticity', ed. Argon, A.S., MIT Press, 1969 (277-293).

87. COSTIN, L. S., DUFFY, J., and FREUND, L. B., 'Fracture initiation in metals under stress wave loading conditions', in 'Fast Fracture and Crack Arrest', ASTM STP 627, ASTM, 1977 (301-318).

88. COSTIN, L. S., DUFFY, J., and FREUND, L. B., 'Dynamic fracture initiation: a comparison of two experimental methods', J. Eng. Mat. and Tech., Vol. 101, 1979 (168-172).

89. HOMMA, H., SHOCKEY, D. A., and MURAYAMA, Y., 'Response of cracks in structural materials to short pulse loads', J. Mech. Phys. Solids, Vol. 31, 1983 (261-279).

90. GIOVANOLA, J. H., 'Investigation and application of the one point bend impact test', in 'Fracture Mechanics 17th Symposium', ASTM STP 905, ASTM, 1986 (307-328).

91. COX, T. B., and LOW, J. R., 'An investigation of the plastic fracture of AISI 4340 and 18 Nickel-200 grade maraging steels', Met. Trans., Vol. 5, 1974 (1457-1470).

92. BILEK, Z., 'The dependence of the fracture toughness of high strength steel on crack velocity', Scr. Metal., Vol. 12, 1978 (1101-1106).

93. HOPKINSON, B., 'A method of measuring the pressure produced in the detonation of high explosives or by the impact of bullets', Phil. Trans. Roy. Soc. A, Vol. 213, 1914 (437-456).

94. KOLSKY, H., 'An investigation of the mechanical properties of materials at very high rates of loading', Proc. Phys. Soc., Vol. B62, 1949 (676-700).

95. TANAKA, K., and KAGATSUME, T., 'Impact bending test on steel at low temperatures using a split Hopkinson bar', Bulletin of the JSME, Vol. 23, 1980 (1736-1744).

96. YOKOYAMA, T. and KISHIDA, K., 'Measurement of dynamic fracture initiation toughness by a novel impact three point bend test technique using Hopkinson pressure bars', in 'Proc. of Int. Conf. on Impact Loading and Dynamic Behaviour of Materials', Bremen, 1987.

97. RUIZ, C., and MINES, R. A. W., 'The Hopkinson pressure bar: an alternative to the instrumented pendulum for Charpy tests', Int. J. of Fracture, Vol. 29, 1985 (101-109).

98. MINES, R. A. W., and RUIZ, C., 'The dynamic behaviour of the instrumented Charpy test', J. de Physique, Vol. 46, 1985 (C5.187-196).

99. HOLISTER, G. S., 'Experimental stress analysis', Cambridge University Press, 1967.

100. JOHNSON, W., 'Impact strength of materials', Edward Arnold, 1972.

101. IRELAND, D. R., 'A review of the proposed standard method of test for impact testing precracked Charpy specimen of metallic materials', in 'CSNI Specialist Meeting on Instrumented Precracked Charpy Testing', ed. Wullaert, R.A., Electric Power Research Inst., Palo Alto, California, 1981.

102. MICRO-MEASUREMENTS, 'Strain gauge installations with M-Bond 43-B, 600, and 610 adhesive systems', Instruction Bulletin B-130-10, Micro-Measurements Division, Measurements Group Inc., Raleigh, NC 27611, USA, 1979.

103. VENKATASUBRAMANIAN, T. V., and UNVALA, B. A., 'An AC potential drop system for monitoring crack length', J. Phys. E. Sci. Instrum., Vol. 17, 1984 (765-771).

104. UNVALA, B. A., private communication, January 1988.

105. OKUMURA, N., VENKATASUBRAMANIAN, T. V., UNVALA, B. A., and BAKER, T. J., 'Application of the AC potential drop technique to the determination of R-curves of tough ferritic steels', Eng. Fract. Mech., Vol. 14, 1981 (617-625).

106. MACGILLIVRAY, H., and CANNON, D., 'Project to develop a standard method of fracture toughness testing at very high loading rates', Progress Report 1, Dept. of Trade and Industry, November 1987.

107. SPIES, F. A., 'Instrumented impact testing machine for determining impact fracture toughness by the impact response curve method', Amsler Otto Wolpert Werke GMBH, Ludwigshafen, W. Germany, 1987.

108. SAVAGE, K., private communication, January 1988.

109. McPARLAND, S., private communication, May 1988.

110. NASH, G. E., 'An analysis of the forces and bending moments generated during the notched beam impact test', Int. J. of Fracture Mechanics, Vol. 5, 1969 (269-286).

111. NASH, G. E., 'Bending deflections and moments in a notched beam', Eng. Fract. Mech., Vol. 3, 1971 (139-150).

112. KISHIMOTO, K., AOKI, S., and SAKATA, M., 'Simple formula for dynamic stress intensity factor of pre-cracked Charpy specimen', Eng. Fract. Mech., Vol. 13, 1980 (501-508).

113. CROUCH, B. A., and WILLIAMS, J. G., 'Modelling of dynamic crack propagation behaviour in the three point bend impact specimen', J. Mech. Phys. Solids, Vol. 36, 1988 (1-13).

114. KREYSZIG, E., 'Advanced Engineering Mathematics', Wiley, 1979.

115. KISHIMOTO, K., KURODA, M., AOKI, S, and SAKATA, M., 'Simple formulas for dynamic fracture mechanics parameters of elastic and viscoelastic three point bend specimens based on Timoshenko's beam theory', in 'Proc. 6th Int. Conf. Fracture', Vol. 5, 1984 (3177-3184).

116. WILLIAMS, J. G., private communication, October 1988.

117. TSE, F. S., MORSE, I. E., and HINKLE, R. T., 'Mechanical Vibrations: Theory and Applications', 2nd edition, Allyn and Bacon, 1978.

118. LYNN, P., and INGRAFFEA, A. R., 'Transition elements to be used with quarter point crack tip elements', Int. J. Num. Meth. in Engineering, Vol. 12, 1978 (1031-1036).

119. TIMOSHENKO, S. P., and GOODIER, J. N., 'Theory of elasticity', 3rd edition, McGraw-Hill, 1982.

120. LEE, W. S., and KANG, I. C., 'Tensile properties and fracture behaviour of AISI 4340 steel as a function of test temperature', J. of the Korean Inst. of Metals, Vol. 24, 1986 (115-123).

121. DIETER, G. E., 'Mechanical Metallurgy', 2nd edition, McGraw-Hill, 1976.

122. GOLDMAN, N. L., and HUTCHINSON, J. W., 'Fully plastic crack problems: the centre-cracked strip under plane strain', Int. J. of Solids and Structures, Vol. 11, 1975 (575-591).

123. ILYUSHIN, A. A., 'The theory of small elastic-plastic deformations', Prikadnaia Matematika i Mekhanika, P.M.M., Vol. 10, 1946 (347).

124. FORD, H., and LIANIS, G., Agnew. Math. Phys., Vol. 8, 1957 (360-382) - as referenced by Ref. [32].

125. CHAIT, R., 'Factors influencing the strength differential of high strength steels', Met. Trans., Vol. 3, 1972 (365-371).

126. MAGNESIUM ELEKTRON LTD., private communication, December 1988.

127. THE MOND NICKEL COMPANY LTD., 'The mechanical properties of nickel alloy steels', 3rd edition, The Mond Nickel Company Ltd.

128. ROBERTS, C. S., 'Magnesium and its alloys', Wiley, 1960.

129. CASE, J., and CHILVER, A. H., 'Strength of Materials and Structures', 2nd edition, Arnold, 1971.

130. ATKINS, A. G., and FELBECK, D. K., 'Mutual indentation hardness in service failure analysis', CME, June 1974, (78-83).

APPENDIX 1 : The relationship between the loading rate parameters, $\dot{\epsilon}$ and $\dot{K}_I$.

Assuming the von Mises yield criterion, the size of the plastic zone in the direction $\theta = 0$ can be determined from equations (2.6a) and (2.6b) to be:

$$r_Y = \frac{(1 - 2\nu)^2}{2\pi} \left[\frac{K_I}{\sigma_Y}\right]^2 \qquad \text{(A1.1a)}$$

for plane strain and:

$$r_Y = \frac{1}{2\pi} \left[\frac{K_I}{\sigma_Y}\right]^2 \qquad \text{(A1.1b)}$$

for plane stress.

The stress field is described by equation (2.1) so that:

$$\sigma_{22} = \sigma_{11} = \frac{K_I}{(2\pi r)^{\frac{1}{2}}} \qquad \text{at } \theta=0 \qquad \text{(A1.2)}$$

and the equivalent strain is:

$$\epsilon_{22} = \frac{1}{E}[\sigma_{22} - \nu(\sigma_{11} + \sigma_{33})] \qquad \text{(A1.3)}$$

Substituting for plane strain and plane stress conditions respectively, equations (A1.2) and (A1.3) give:

$$\epsilon_{22} = \frac{K_I}{E(2\pi r)^{\frac{1}{2}}} (1 - 2\nu)(1 + \nu) \qquad \text{(A1.4a)}$$

or:

$$\epsilon_{22} = \frac{K_I}{E(2\pi r)^{\frac{1}{2}}} (1 - \nu) \qquad \text{(A1.4b)}$$

Differentiating both sides of equations (A1.4a) and (A1.4b) with respect to time gives the strain rate, $\dot{\epsilon}_{22}$, perpendicular to the axis of the crack. At the edge of the plastic zone, $r = r_Y$, and so, substituting from equations (A1.1a) and (A1.1b) the relationship between strain rate and the rate of change of the stress intensity factor, $\dot{K}_I$, at that point is:

$$\dot{\epsilon}_{22} = \frac{\sigma_Y}{EK_I} \dot{K}_I (1 + \nu) \qquad \text{(A1.5a)}$$

for plane strain and:

$$\dot{\epsilon}_{22} = \frac{\sigma_Y}{EK_I} K_I (1 - \nu) \qquad \text{(A1.5b)}$$

for plane stress. Of course, the strain rates will be higher within the plastic zone itself while the rate of change of stress intensity factor will be constant for a given loading condition.

APPENDIX 2 : Solution of the governing equation for the linear elastic lumped mass-spring model.

The equation to be solved (equation 4.3 with the inclusion of a damping term) is:

$$m'\ddot{u} + c\dot{u} + (k_1 + k_2)u = k_1 v \qquad \text{(A2.1)}$$

where u and v are functions of time, $\dot{u}$ is the first derivative with respect to time, $\ddot{u}$ is the second derivative, m' is the equivalent mass, c is the coefficient of damping, and k_1 and k_2 are the system stiffness values defined in equations (4.1) and (4.2). Equation (A2.1) can be rewritten as:

$$\ddot{u} = -\left[\frac{(k_1 + k_2)}{m'}\right]u - \left[\frac{c}{m'}\right]\dot{u} + \left[\frac{k_1}{m'}\right]v \qquad \text{(A2.2)}$$

which is of the form:

$$\ddot{u} = [\text{Const1}]u + [\text{Const3}]\dot{u} + [\text{Const2}]v \qquad \text{(A2.3)}$$

where:

$$\text{Const1} = -\frac{(k_1 + k_2)}{m'} \qquad \text{(A2.4a)}$$

$$\text{Const2} = \frac{k_1}{m'} \qquad \text{(A2.4b)}$$

$$\text{Const3} = -\frac{c}{m'} \qquad \text{(A2.4c)}$$

The Runge-Kutta-Nystrom method (see, for example, [114]) solves initial value problems of the form:

$$\ddot{u} = f(t,u,\dot{u}) \quad u(t_0) = u_0 \quad \dot{u}(t_0) = \dot{u}_0 \qquad \text{(A2.5)}$$

The solution requires the auxiliary quantities:

$$A_n = (h/2)\ f(t_n, u_n, \dot{u}_n)$$

$$= (h/2)\ [\text{Const1}.u_n + \text{Const2}.v_n + \text{Const3}.\dot{u}_n]$$

$$B_n = (h/2)\ f(t_n + h/2, u_n + b_n, \dot{u}_n + A_n)$$

$$\text{where } b_n = (h/2)(\dot{u}_n + A_n/2)$$

$$C_n = (h/2)\ f(t_n + h/2, u_n + b_n, \dot{u}_n + B_n)$$

$$D_n = (h/2)\ f(t_n + h, u_n + d_n, \dot{u}_n + 2C_n)$$

$$\text{where } d_n = h\ (\dot{u}_n + C_n)$$

whence the new values of displacement and velocity are:

$$u_{n+1} = u_n + h\ (\dot{u}_n + K_n) \qquad \text{(A2.6)}$$

$$\text{where } K_n = (A_n + B_n + C_n)/3$$

$$\dot{u}_{n+1} = \dot{u}_n + K_n^* \qquad \text{(A2.7)}$$

$$\text{where } K_n^* = (A_n + 2B_n + 2C_n + D_n)/3$$

h is the step length (typically 0.4×10^{-6} s in the analysis of the HPB results reported here, since values of v are available every 0.2×10^{-6} s). The method is fourth order.

The initial values for u and $\dot{u}$ in the HPB loading system are zero.

The accuracy of the numerical algorithm was proved by comparison with the analytic results for both step velocity and ramp velocity inputs.

APPENDIX 3 : Evaluation of equivalent specimen mass for variously loaded cracked and uncracked beams.

A3.1. Simply supported uncracked beam.

In the following analysis simple beam theory is used to derive an estimate of the equivalent point mass m' for the three point bend specimen subjected to a dynamic force P at its midspan. Shear forces are neglected and so the midpoint deflection is (from equation 4.23):

$$u_{nc} = \frac{PS^3}{48EI} \qquad \text{(A3.1)}$$

This is also the deflection of the equivalent point mass which, therefore, has the associated stiffness:

$$k = \frac{P}{u_{nc}} = \frac{48EI}{S^3} \qquad \text{(A3.2)}$$

and a natural frequency of vibration w given by:

$$w^2 = \frac{k}{m'} \qquad \text{(A3.3)}$$

The deflection of any point, distance x from the end of the beam, at time t is given by:

$$u = f(x)e^{iwt} \qquad \text{(A3.4)}$$

where:

$$f(x) = \frac{P}{EI}\left[\frac{x^3}{12} + \frac{S^2x}{16}\right] \qquad \text{for } 0 < x < \frac{S}{2} \qquad \text{(A3.5)}$$

which can be derived from the bending moment equation

(see, for example, [129]):

$$M = -\frac{Px}{2} = EI\,\frac{d^2f}{dx^2} \tag{A3.6}$$

Rayleigh's method (see, for example, [117]) then estimates the frequency w of the fundamental mode as:

$$w^2 = \frac{\int_0^S EI\,[f''(x)]^2\,dx}{\int_0^S \rho A\,[f(x)]^2\,dx} = \frac{\int_0^{S/2} EI\,[f''(x)]^2\,dx}{\int_0^{S/2} \rho A\,[f(x)]^2\,dx} \tag{A3.7}$$

by symmetry.

Substituting equation (A3.5) in (A3.7) and comparing with equation (A3.3) results in the determination of the equivalent mass as:

$$m' = \frac{17}{35}m = 0.49m \tag{A3.8}$$

where $m = \rho AS$.

A3.2. Simply supported cracked beam.

Nash [110,111] has applied a normal mode technique to a cracked beam to derive the following expression for the deflection of the beam at any point x/S:

$$u_y\left(\frac{x}{S},t\right) = \frac{Y_i\left(\frac{x}{S}\right)\,Y_i\left(\frac{1}{2}\right)}{w_i W_i}\int_0^t F(\eta)\,\sin w_i(t-\eta)\,d\eta \tag{A3.9}$$

for initial conditions $u_y(x/S,t) = \dot{u}_y(x/S,t) = 0$. $Y_i(x/S)$ is a shape function and W_i a distributed mass function,

both of which are defined in [110]. w_i is the frequency of the i'th mode. Considering, then, only the first mode the deflection becomes:

$$u_y(\tfrac{x}{S},t) = \frac{Y_1(\tfrac{x}{S})\ Y_1(\tfrac{1}{2})}{w_1 W_1}\ f(t) \qquad \text{(A3.10)}$$

and the distributed particle velocity is:

$$\dot{u}_y(\tfrac{x}{S},t) = \frac{Y_1(\tfrac{x}{S})\ Y_1(\tfrac{1}{2})}{w_1 W_1}\ f(t) \qquad \text{(A3.11)}$$

Comparing the kinetic energy of the equivalent point mass m' with the kinetic energy of the full beam gives:

$$\tfrac{1}{2}m'\ [\dot{u}_y(\tfrac{1}{2})]^2 = \int_0^{\frac{1}{2}} \rho AS\ [\dot{u}_y(\tfrac{x}{S})]^2\ d(\tfrac{x}{S}) \qquad \text{(A3.12)}$$

whence:

$$m' = \frac{2\rho AS}{Y_1{}^2(\frac{1}{2})} \int_0^{\frac{1}{2}} Y_1{}^2(\tfrac{x}{S})\ d(\tfrac{x}{S}) \qquad \text{(A3.13)}$$

which can be computed to give:

$$m' = 0.38m \qquad \text{(A3.14)}$$

where $m = \rho AS$.

A3.3. Simply supported uncracked beam with midspan constraint.

The equation of motion for the transverse vibration of an Euler-Bernoulli beam (equation 4.11) is:

$$EI \frac{\partial^4 u}{\partial x^4} + \rho A_0 \frac{\partial^2 u}{\partial t^2} = 0 \qquad \text{(A3.15)}$$

Assuming harmonic solutions of the form:

$$u = f(x)e^{iwt} \qquad \text{(A3.16)}$$

equation (A3.15) becomes:

$$\frac{\partial^4 f}{\partial x^4} - \frac{\rho A_0}{EI} w^2 f(x) = 0 \qquad \text{(A3.17)}$$

Equation (A3.17) has solutions of the form:

$$f(x) = A\sin\lambda x + B\cos\lambda x + C\sinh\lambda x + D\cosh\lambda x \qquad \text{(A3.18)}$$

where:

$$\lambda^4 = \frac{\rho A_0}{EI} w^2 \qquad \text{(A3.19)}$$

For a beam constrained at midspan (see figure 4.2) the boundary conditions are:

$$\begin{aligned} &\text{(i) at } x = 0, \text{ displacement } u = 0, \\ &\text{(ii) at } x = 0, \text{ bending moment } EI \frac{\partial^2 u}{\partial x^2} = 0 \\ &\text{(iii) at } x = S/2, \text{ slope } \frac{\partial u}{\partial x} = 0 \\ &\text{(iv) at } x = S/2, \text{ shear force } EI \frac{\partial^3 u}{\partial x^3} = \frac{k_1}{2} u \end{aligned} \qquad \text{(A3.20)}$$

Substituting these boundary conditions (A3.20) in (A3.18) produces the frequency equation:

$$\frac{k_1}{2} [\tan(N_m) - \tanh(N_m)] + 2EI \left[\frac{N_m}{(S/2)}\right]^3 = 0 \qquad \text{(A3.21)}$$

where $N_m = \lambda S/2$. From equation (A3.19):

$$w^2 = \frac{EI}{\rho A_0} \lambda^4 = \frac{EI}{\rho A_0} \left[\frac{N_m}{(S/2)}\right]^4 \qquad \text{(A3.22)}$$

Solutions to equation (A3.21) have been computed numerically for various values of constraint stiffness k_1 and the corresponding values of natural frequency calculated from equation (A3.22).

The stiffness of the unnotched beam is given by equation (A3.2) and then the equivalent mass (equation 4.14) is:

$$m' = \frac{k_1 + k_2}{w^2} \qquad \text{(A3.23)}$$

Values of m' and the first natural frequency are given in table 4.1 for various values of the ratio k_1/k_2 and the limiting solutions and their consequences discussed in section 4.3.